

G.D. Conway (Ed.)

**Proceedings of the 7th International
Reflectometry Workshop for
Fusion Plasma Diagnostics (IRW7)
Garching, 9th - 12th May, 2005**

IPP II/9
June 2005



Max-Planck-Institut
für Plasmaphysik



Proceedings of the 7th International Reflectometry Workshop for Fusion Plasma Diagnostics (IRW7)

May 9th - 12th, 2005

*Max-Planck-Institut für Plasmaphysik
Euratom-Association IPP, Garching, Germany*

**organised in co-operation with the
International Atomic Energy Agency (IAEA)**

Edited by G.D.Conway

IRW7 International Advisory Committee

M.E.Manso (IST) – Chair
F.Clairet (CEA)
G.D.Conway (IPP) – Local organizer
A.J.H.Donne (FOM)
E.Doyle (UCLA)
E.Gusakov (IOFFE)
K.Kawahata (NIFS)
A.Mase (U.Kyushu)
V.Vershkov (Kurchatov)
G.Vayakis (ITER) – ITPA/RWG
G.Mank (IAEA)

Local organizing committee

G.D.Conway
L.Scoones

Contents

| | page |
|--|------|
| <i>Workshop participants</i> | v |
| <i>Editorial - G.D.Conway</i> | 1 |
| <i>Automatic electron density measurements with microwave reflectometry during high density H-mode discharges on ASDEX Upgrade</i> A.Silva, P.Varela, L.Cupido, M.Manso, L.Meneses, L.Guimaraes, G.Conway, F.Serra and the ASDEX Upgrade Team | 3 |
| <i>Recent development of microwave reflectometer for density profile and fluctuation measurements on LHD</i> T.Tokuzawa, K.Kawahata, S.Sakakibara, S.Yamamoto and the LHD Experimental Group | 8 |
| <i>A frequency sweeping heterodyne reflectometer in the Hanbit mirror</i> S-H.Seo | 12 |
| <i>An Ultrashort pulse reflectometry for LHD plasmas</i> Y.Kogi, A.Mase, M.Ignatenko, K.Uchida, K.Kudo, K.Nishiyama, H.Hojo, K.Kawahata, Y.Nagayama and T.Tokuzawa | 13 |
| <i>Adaptive window length calculation for automatic spectrogram analysis of broadband reflectometry data</i> P.Varela, A.Silva, M.Manso and the ASDEX Upgrade Team | 21 |
| <i>Recent progress with high-resolution FM profile reflectometer measurements on DIII-D</i> L. Zeng, E.J. Doyle, G. Wang, W.A. Peebles and T.L. Rhodes | 25 |
| <i>Profile reflectometry on MAST</i> G.Cunningham, T.Edlington, A.Silva and L.Meneses | 30 |
| <i>Measurements localization in poloidal correlation reflectometry</i> E.Z.Gusakov and A.Yu.Popov | 34 |
| <i>2D full wave simulation of poloidal and radial sensitivity of reflectometer and estimation of density fluctuations absolute level</i> D.A.Shelukhin, V.A.Vershkov, S.V.Soldatov and A.O.Urazbaev | 39 |
| <i>Remarks on the asymmetry of the angular response in X-mode reflectometry observed in numerical simulations</i> E.Holzhauer and E.Blanco | 45 |
| <i>Doppler reflectometry studies using a two-dimensional full-wave code</i> E.Blanco, T.Estrada, S.Heuraux and J.Sanchez | 49 |
| <i>Doppler reflectometry spectra simulations with velocity shear layer</i> F.da Silva, S.Heuraux and M.Manso | 53 |
| <i>Consideration of Doppler reflectometry in Born approximation</i> V.V.Bulanin, A.V.Petrov and M.V.Yefanov | 58 |

| | |
|---|-----|
| <i>Nonlinear effects in Doppler reflectometry, analytical theory & numerical simulations</i> E.Z.Gusakov, S.Heuraux, F.da Silva and A.V.Surkov | 62 |
| <i>Observation of coherent plasma flow perturbations using Doppler reflectometry on ASDEX Upgrade</i> G.D.Conway, B.Scott, J.Schirmer, M.Reich, A.Kendl and the ASDEX Upgrade Team | 66 |
| <i>Radial correlation Doppler reflectometry</i> J.Schirmer, G.D.Conway, H.Zohm, W.Suttrop, E.Holzhauser and the ASDEX Upgrade Team | 70 |
| <i>Doppler backscattering on Tore Supra: perpendicular velocity profile and k-spectrum in high ICRH experiments</i> P.Hennequin, C.Honore, A.Truc, A.Quemeneur, C.Fenzi-Bonizec, C.Bourdelle, X.Garbet, G.T.Hoang and the Tore Supra Team | 74 |
| <i>Quasi-optical Gaussian beam tracing to evaluate Doppler backscattering conditions</i> C.Honoré, P.Hennequin, A.Truc and A.Quemeneur | 81 |
| <i>Status of the microwave imaging reflectometer at TEXTOR</i> M.J.van de Pol, E.Mazzucato, H.K.Park, T.Munsat, C.W.Domier, N.C.Luhmann Jr., I.G.J.Classen, A.J.H.Donne and the TEXTOR Team | 85 |
| <i>Simulation of optical and synthetic imaging using microwave reflectometry</i> G.J.Kramer, R.Nazikian and E.Valeo | 89 |
| <i>Identification of local Alfvén wave resonances with reflectometry as a diagnostic tool in tokamaks</i> A.G.Elifimov, R.M.O.Galvao, L.F.Ruchko, M.E.C.Manso and A.A.Ivanov | 90 |
| <i>Experimental studies of the registration of Alfvén wave resonances in the TCABR tokamak by frequency scanning reflectometry</i> L.F.Ruchko, R.M.O.Galvao, A.G.Elifimov, J.I.Elizondo, E.Sanada, Yu.K.Kuznetsov, A.M.M.Fonseca, V.Bellintani Jr., A.N.Fagundes, I.C.Nascimento, W.P.de Sa, C.A.F.Varandas, M.Manso, P.Varela and A.Silva | 96 |
| <i>Further development of reflectometry diagnostics for measurement of Alfvén cascades on the JET tokamak</i> S.Hacquin, S.Sharapov, B.Alper, D.Borba, C.Boswell, J.Fessey, L.Meneses, M.Walsh and the JET EFDA Contributors | 100 |
| <i>FM-CW reflectometry for MHD activity measurements on Tore Supra</i> F.Clairet, S.Heuraux, G.Leclert and L.Vermare | 104 |
| <i>Radial behavior of density fluctuations deduced from FM-CW reflectometry data on Tore Supra</i> S.Heuraux, L.Vermare, F.Clairet, G.Leclert and F.da Silva | 109 |
| <i>Correlation reflectometry measurements of turbulence in T-10 tokamak</i> V.A.Vershkov, D.A.Shelukhin, S.V.Soldatov and A.O.Urazbaev | 113 |
| <i>Fluctuation measurements in TJ-II using a broadband fast hopping reflectometer</i> T.Estrada, E.Blanco, L.Cupido, M.E.Manso and J.Sanchez | 119 |

| | |
|--|-----|
| <i>Density and fluctuation profiles obtained with the D-band reflectometer in Tore Supra</i> A.Sirinelli, R.Sabot, J-C.Giacalone and F.Clairet | 123 |
| <i>Fluctuation measurements at TEXTOR during operation of dynamic ergodic divertor</i> A.Krämer-Flecken, S.Soldatov, H.R.Koslowski, M.Lehnen, Y.Liang, V.Vershkov, R.Wolf, O.Zimmermann and the TEXTOR Team | 126 |
| <i>Initial density fluctuation measurements using fixed-frequency quadrature reflectometers on DIII-D</i> G.Wang, W.A.Peebles, T.L.Rhodes, E.J.Doyle, N.A.Crocker, X.Nguyen, L.Zeng, S.Kubota, G.R.McKee, M.A.VanZeeland | 132 |
| <i>A new spectral analysis to study pellet triggered ELMs from broadband reflectometry at ASDEX Upgrade</i> L.Fattorini, M.E.Manso, P.T.Lang and the ASDEX Upgrade Team | 137 |
| <i>Scaling and inverse scaling of ASDEX Upgrade reflectometer data</i> M.Abel, G.D.Conway, H.Zohm and the ASDEX Upgrade Team | 143 |
| <i>A dual source reflectometer for density profile and fluctuations measurements in Tore Supra</i> R.Sabot, A.Sirinelli, J.M.Chareau, F.Clairet, J.C.Giacalone, L.Vermare, P.Hennequin, S.Heuraux and G.Leclert | 148 |
| <i>A user friendly interface for a fast wave solver in realistic plasma geometry</i> R.Nazikian | 152 |
| <i>Reflectometry for Wendelstein 7-X</i> M.Hirsch, E.Holzhauer and H-J.Hartfuss | 153 |
| <i>Frequency hopping millimeter-wave reflectometry in ASDEX Upgrade</i> L.Cupido, S.Graça, L.Meneses, J.Santos, M.Manso and F.Serra | 158 |
| <i>JET density profile reflectometer, new design</i> L.Meneses, L.Cupido, A.A.Ferreira, M.Manso and L.Guimaraes | 162 |
| <i>Coherent signal generation and detection for millimeter wave reflectometry systems</i> L.Cupido, L.Meneses and A.A.Ferreira | 166 |
| <i>Status and plans for reflectometry in ITER</i> G.Vayakis, C.Walker and the ITER International Team and Participant Teams | 170 |

Editorial

G.D.Conway (IPP) – June 2005

The seventh International Reflectometry Workshop for Fusion Plasma Diagnostics (IRW7) was held at the Max-Planck-Institut für Plasmaphysik in Garching, Germany from May 9th to 12th, 2005. The meeting was organized in cooperation with the International Atomic Energy Agency (IAEA).

The International Reflectometry Workshop (IRW) series is the main biennial forum for the fusion plasma reflectometry community to present and review the latest experimental results, new technological developments and advances in the area of theory and numerical simulation codes applied to microwave and millimetre-wave reflectometry for diagnosing fusion plasmas. The workshop series began as an IAEA Technical Committee Meeting on Microwave Reflectometry for Fusion Plasma Diagnostics with the first meeting held at JET (Joint Undertaking), England in March 1992. Workshops have subsequently been held approximately every two years since.

Contributions to the workshop come from all areas of plasma microwave and millimetre-wave reflectometry and radar, specifically experimental applications such as density profile measurements, plasma position control, density fluctuations and turbulence measurements, as well as modelling, simulation and diagnostic response characterization etc. Basic techniques, from simple homodyne circuits, through to advanced systems such as imaging and Doppler reflectometry and other novel techniques are also covered.

This latest workshop was attended by 43 reflectometry specialists from around the world, including USA (4), Japan (2), Russia (3), France (6), Portugal (10), Germany (9), Italy (1), The Netherlands (1), Spain (2), UK (1) and ITER/EFDA (2). For the first time the workshop also had representatives from Korea (1) and Brazil (1). Numerous local scientists from the ASDEX Upgrade project (~5), ITER and EFDA teams (2) based at the IPP site also participated in various sessions of the workshop. A list of registered participants is included in these proceedings.

In total, 40 oral papers (20 minute duration plus 10 minutes for questions) were presented in 8 consecutive sessions over three and a half days, making this the largest and longest workshop in the series to date. On the last day, the workshop was followed by a meeting of the ITPA specialist working group on reflectometry (RWG) to discuss issues and progress in the design of ITER reflectometer diagnostics. This meeting was also well attended.

The workshop proceedings, published here as an IPP laboratory report, contains 37 papers (plus 2 abstracts) in roughly the order of presentation, grouped according to the session topics. The actual sessions were: (i) Density profile measurements (chair: F.Clairet, 7 papers), (ii) Code, theory and simulations (chair: G.J.Kramer, 3 papers), (iii) Doppler reflectometry – simulations & experiments (chair: M.Hirsch, 8 papers), (iv) Microwave imaging (chair: E.J.Doyle, 2 papers), (v) 3 sessions on Fluctuation measurements (chairs: T.Tokuzawa, R.Nazikian & G.Vayakis, 15 papers) and finally (vi) Hardware developments (chair: G.D.Conway, 5 papers). Each session was followed by a 45 minute summary and discussion period, led by the session chairman. The discussions were vigorous and forthright. It is hoped that that written summaries of the discussions can be included in future proceedings as they would provide a record of the current dynamics in the reflectometry field.

The number of papers per topic, nevertheless, gives a good indication of the current trends within the field. Compared to previous workshops there has been a substantial increase in the level of interest in fluctuation measurements with density profile measurements remaining constant. Profile measurements are now generally perceived as almost routine employing a relatively mature

technique. Reflectometry density profiles are in some cases now viewed as more robust than those from the more standard Thomson scattering diagnostics. This is progress indeed! Most recent development work has concentrated on just two measurement techniques: Fast swept FM systems (operational on ASDEX Upgrade, Tore Supra, DIII-D, MAST, Hanbit mirror, and in design for KSTAR) and Ultrashort pulse reflectometers (2 systems on the LHD stellarator and additional systems on the GAMMA 10 mirror device and SSPX spheromak). AM profile systems are also in operation on Alcator C-Mod and the TJ-II stellarator, although they were not reported at this workshop. The current emphasis is now on improving profile reliability, radial coverage or extent (particularly to the tokamak core) and the processing speed of an ever increasing amount of data.

Fluctuation measurements are finding renewed interest, particularly in the study of MHD and fast particle modes. The localized core measurement of Alfvén cascades is a specific example with major applications to ITER. There is also a growing trend of cross-over measurements, for example extracting information on fluctuations and turbulence from the FM-swept group-delay data. Two examples are reported here from Tore Supra measurements. Fixed probing frequency measurements, however, remain the bedrock technique for plasma density turbulence and correlation studies. Although significant progress has been made in the simulation and modelling of the fixed frequency reflectometer response function, the final step of extracting an absolute density fluctuation level $\delta n/n$ and an associated correlation length from the phase and amplitude fluctuations remains problematic and application dependent.

The new area of Doppler reflectometry and plasma velocity measurements has seen an explosive growth in the last couple of years. There has been much analytic and 2D full-wave simulation work on the Doppler concept which has now placed this technique on a firm footing. Several groups are actively engaged in Doppler measurements and the results presented here demonstrate the ability of Doppler reflectometry to provide high resolution radial electric field profiles and associated shearing, together with E_r fluctuations. It is expected that this new technique will have an increasing impact on the wider fusion community in the coming years.

The second new area of development, Microwave Imaging Reflectometry, has unfortunately been mired by a degree of controversy. In attempting to establish the technique, certain claims have been made by some proponents which undermine the perception of traditional single line-of-sight antenna fluctuation measurements. Although a sense of perspective has hopefully been restored, unnecessary damage has been caused. MIR (based on large-lens optical imaging) attempts to capture two-dimensional time-frame pictures (in the poloidal and toroidal directions) of density turbulence at a specified radial location – just like a photographic picture. However, like a camera, optical MIR also experiences similar limitations, such as restricted depth of field, spatial/temporal resolution, and optical aberrations etc. Nevertheless, impressive results have been obtained, as reported here from the TEXTOR diagnostic. Also reported are simulation studies on both optical and synthetic imaging, which show not just the limitations of imaging but also demonstrate the possibilities of alternative techniques such as single-antenna synthetic aperture and multi-antenna measurements. This work points the way towards tomographic reflectometer reconstruction of density fluctuations. Despite the challenges it is expected that a wealth of new information can be provided by imaging techniques.

Finally, each workshop brings forward new hardware and software developments. Hardware falls into two categories: Front-end, which deals with antennas and transmission line design; and back-end, concerning the reflectometer transmitter/receiver electronics and control. In the first category, in addition to several talks, 2 posters on Doppler developments on AUG and antenna systems on JET were presented. These illustrate two areas of relevance for ITER: concept testing and performance modelling. The report on the status of ITER reflectometer designs nevertheless highlights that it will remain the driving force in hardware development. This applies equally to the back-end where demand is expected to push component performance and availability.

Workshop participants

Brazil

Artur Elfimov Institute of Physics, University of São Paulo, Brazil
Email:

France

Frédéric Clairet Association EURATOM-CEA, Cadarache
Email:

Pascale Hennequin Laboratoire de Physique et Technologie des Plasmas, École Polytechnique
Email:

Stephane Heuroux LPMIA, CNRS 7040 Université Henri Poincaré, Nancy
Email:

Cyrille Honoré Laboratoire de Physique et Technologie des Plasmas, École Polytechnique
Email:

Roland Sabot Association EURATOM-CEA, Cadarache
Email:

Antonie Sirinelli Association EURATOM-CEA, Cadarache
Email:

Germany

Markus Abel Institut für Physik, Universität Potsdam
Email:

Garrard Conway Max-Planck-Institut für Plasmaphysik, Euratom-Association IPP, Garching
Email:

Matthias Hirsch Max-Planck-Institut für Plasmaphysik, Euratom-Association IPP Greifswald
Email:

Eberhard Holzhauser Institut für Plasmaforschung, Universität Stuttgart
Email:

Andreas Krämer-Flecken Institut für Plasmaphysik, Forschungszentrum Jülich, Euratom Associatio
Email:

Jasmine Schirmer Max-Planck-Institut für Plasmaphysik, Euratom-Association-IPP, Garching
Email:

Bruce Scott Max-Planck-Institut für Plasmaphysik, Euratom-Association-IPP, Garching
Email:

Carolin Troester Max-Planck-Institut für Plasmaphysik, Euratom-Association-IPP, Garching
Email:

Dietmar Wagner Max-Planck-Institut für Plasmaphysik, Euratom-Association-IPP, Garching
Email:

Italy

Alessandro Simonetto CNR - Istituto di Fisica del Plasma, Milano
Email:

ITER / EFDA

Christian Ingesson EFDA - CSU, Garching, Germany
Email:

George Vayakis ITER NAKA JWS, Naka, Ibaraki, Japan
Email:

Japan

Yuichiro Kogi ASTEC, Kyushu University, Kasuga
Email:

Tokihiko Tokuzawa National Institute for Fusion Science, Toki
Email:

Korea

Seong-Heon Seo Operation and Research Division, Korea Basic Science Institute, Daejeon
Email:

The Netherlands

Marc van de Pol FOM-Institute for Plasma Physics Rijnhuizen, Association Euratom-FOM
Email:

Portugal

Luis Cupido Centro de Fusão Nuclear, Associação Euratom, Instituto Superior Técnico
Email:

Luca Fattorini Centro de Fusão Nuclear, Associação Euratom, Instituto Superior Técnico
Email:

André Ferreira Centro de Fusão Nuclear, Associação Euratom, Instituto Superior Técnico
Email:

Sílvia da Graça Centro de Fusão Nuclear, Associação Euratom, Instituto Superior Técnico
Email:

Sebastien Hacquin Centro de Fusão Nuclear, Associação Euratom, Instituto Superior Técnico
Email:

Luis Meneses Centro de Fusão Nuclear, Associação Euratom, Instituto Superior Técnico
Email:

Fernando Serra Centro de Fusão Nuclear, Associação Euratom, Instituto Superior Técnico
Email:

António Silva Centro de Fusão Nuclear, Associação Euratom, Instituto Superior Técnico
Email:

Filipe da Silva Centro de Fusão Nuclear, Associação Euratom, Instituto Superior Técnico
Email:

Paulo Varela Centro de Fusão Nuclear, Associação Euratom, Instituto Superior Técnico
Email:

Russia

Victor Bulanin St. Petersburg State Polytechnical University, St. Petersburg
Email:

Evgeniy Gusakov Ioffe Physico-Technical Institute, St. Petersburg
Email:

Dimitry Shelukhin Nuclear Fusion Inst., Russian Research Centre Kurchatov Institute, Moscow
Email:

Spain

Emilio Blanco Laboratorio Nacional de Fusión, Asociación Euratom-CIEMAT, Madrid
Email:

Teresa Estrada Laboratorio Nacional de Fusión, Asociación Euratom-CIEMAT, Madrid
Email:

United Kingdom

Geof Cunningham Euratom/UKAEA Fusion Association, Culham Science Centre, Abingdon
Email:

U.S.A.

Edward Doyle Dept. of Electrical Eng. & PSTI, University of California, Los Angeles
Email:

Gerrit Kramer Princeton Plasma Physics Laboratory, Princeton
Email:

Raffi Nazikian Princeton Plasma Physics Laboratory, Princeton
Email:

Guiding Wang Dept. of Electrical Eng. & PSTI, University of California, Los Angeles
Email:

Automatic electron density measurements with microwave reflectometry during high-density H-mode discharges on ASDEX Upgrade

A. Silva¹, P. Varela¹, L. Cupido¹, M. Manso¹, L. Meneses¹, L. Guimarães¹, G. Conway², F. Serra¹ and the ASDEX Upgrade Team²

¹*Centro de Fusão Nuclear, Associação EURATOM / IST, Instituto Superior Técnico, Av. Rovisco Pais, P-1049-001 Lisboa, Portugal*

²*Max-Planck-Institut für Plasmaphysik, EURATOM Association, Boltzmannstr. 2, D-85748 Garching, Germany*

I - Current status of the microwave reflectometry system on ASDEX Upgrade

The first antennas of the ASDEX Upgrade microwave reflectometer system were brought in-vessel by the summer 1991. Since then new channels have been added and several modifications and improvements were made to get better or add additional measuring capabilities. The system has four O-mode channels for measuring electron density profiles and fluctuations on the High Field Side (HFS sectors 5 & 6) covering the density range 0.3×10^{19} to $6.66 \times 10^{19} \text{ m}^{-3}$ (see Figure 1).



Figure 1 – HFS and LFS in-vessel antennas setup on sector 5 & 6.

At the Low Field Side (LFS sector 6) there are five O-mode channels for profiles (see Figure 1) and fluctuation measurements covering the density range 0.3×10^{19} to $12.4 \times 10^{19} \text{ m}^{-3}$. There are two X-mode channels in the frequency range 35 to 73 GHz for electron density profiles. The Q band channel (35 to 50 GHz) is not operational due to a damaged waveguide that could not be repaired during the last summer vacuum break. On sector 5 there are two O-mode channels fully dedicated to electron density fluctuation measurements in the range 3×10^{19} to $6.66 \times 10^{19} \text{ m}^{-3}$.

With the memory limitations of the current acquisition system 3066 density profiles can be calculated for the HFS and LFS with a repeating rate of $35 \mu\text{s}$ in single sweep or combined in bursts. Simultaneous measurements of density profiles and fluctuations are possible at the LFS. A frequency calibration signal is available for each band every 10 sweeps.

II – Hardware improvements during summer 2004

During the summer vacuum break of 2004 several enhancements were made to improve or extend the capabilities of the system.

A special design W band microwave power amplifier was include after the passive frequency multiplier and the transmitted power was boosted from 0dBm to 10dBm. This extended the measuring range of the upper band giving the ability to the system to follow interesting plasma phenomena like pedestal formation on high density plasmas.

On FM-CW reflectometry accurate frequency calibration is an important subject due to the fact that errors will affect the quality of the reconstructed electron density profiles. With fast sweeping sources, sophisticated and fast electronic involved the risks of frequency deviation are always present. They can be a consequence of thermal or post-tuning drifts, hysteresis, and aging or a combination of all these. The problem can be more relevant if the microwave sources don't have a linear frequency characteristic. Aware of this problem we

have included since the beginning of the implementation of the system a dynamic calibration circuit based on frequency markers referenced to a precision 500 MHz source, that can provide a calibration curve with up to 25 points. But this was not sufficient to reproduce in detail the tuning characteristic of the Hyperabrupt Tuned Oscillators (HTO). This lack of detail can be clearly observed on the bumps present on the evolution of the beat frequency curve of a reflection at a metallic mirror, which must be constant. In fact we can use this information to recover the detailed calibration curve. Equation 1 shows that it is possible to recover the real probing frequency step from the phase shift of a reflection at a mirror placed at well known distance.

$$f_b = \frac{\Delta\varphi}{2\pi} \cdot \frac{1}{t_{sample}} \quad (1)$$

$$\Delta F = f_b \cdot \frac{t_{sample}}{t_{delay}} \Rightarrow \Delta F = \frac{\Delta\varphi}{2\pi} \cdot \frac{1}{t_{delay}}$$

On the ASDEX Upgrade system this is only available during vacuum breaks. We can overcome this major drawback of the method if we use a well calibrated coaxial line.

A line like this with $t_{delay}=14.1643$ ns was added to the existing markers circuit as shown in red in Figure 2.

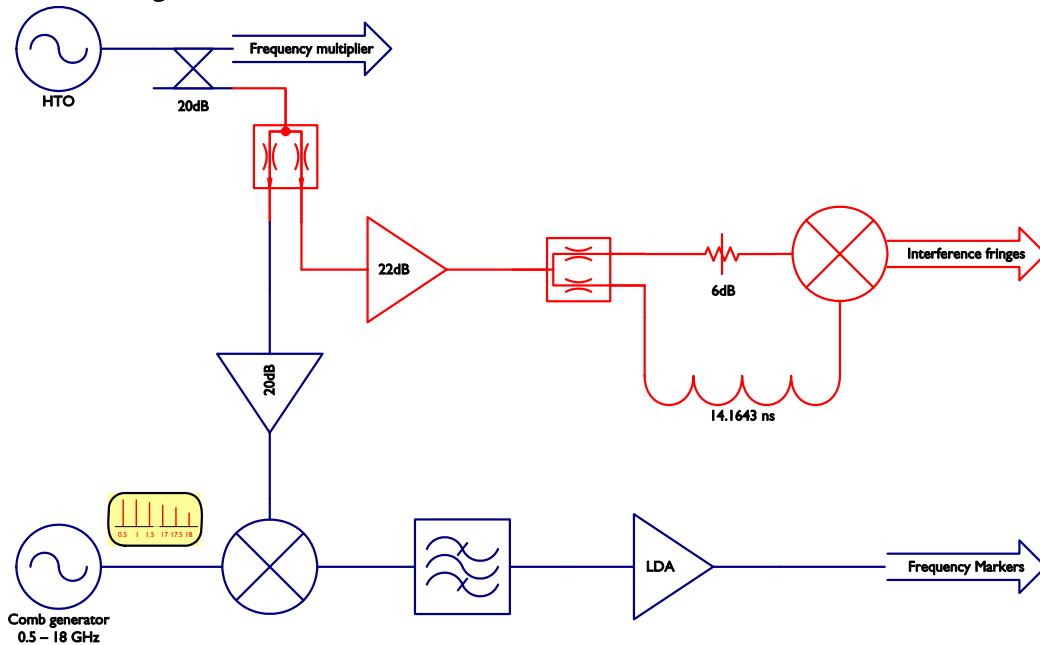


Figure 2 - Complete frequency calibration circuit.

The output of the interference signal and the frequency markers are shown in Figure 3(a) and (c). The instantaneous phase evolution of the signal in Figure 3(a) is obtained by *Hilbert Transform* [1] and the resulting frequency step as an outcome of using Equation 1 is shown in Figure 3(b). It is clear that the markers can not account for the fast changes of the tuning sensitivity of the HTO like the one that takes place around 21 μ s.

To get a complete calibration curve one start frequency must be given and we use one of the frequency markers. The resulting calibration curve is shown in Figure 4. In this way a better frequency linearization is obtained with the possibility to have a new calibration for each band every 10 sweeps during plasma operation.

With the new frequency calibration a new microwave contribution to the group delay was obtained for all density profile channels, improving band matching and profile inversion precision.

The V X-mode antenna was modified to correct a construction error and the radiation pattern is now the expected one.

The firmware of all of the eight control boards was upgraded to use a high level language, like the one used in the fluctuations monitor control system. This makes the communication more robust.

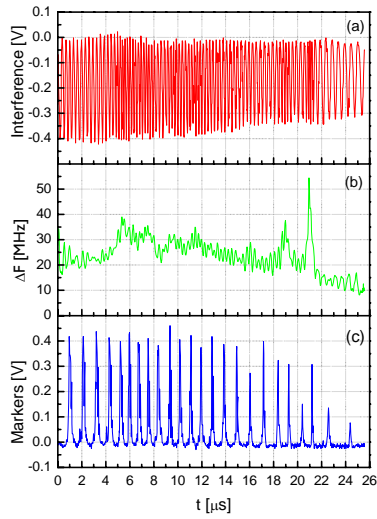


Figure 3 - a) Interference signal. b) Frequency step from the interference signal. c) Frequency markers signal.

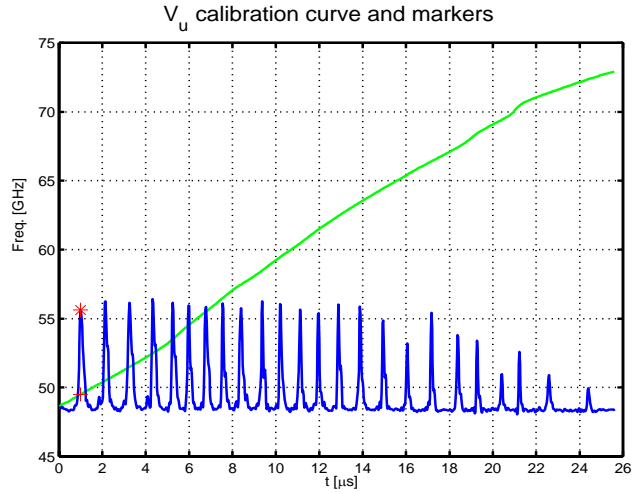


Figure 4 - Markers signal (blue) with the chosen marker for start frequency (red) and the resulting calibration curve (green).

Frequency hopping was added to the fluctuation monitor channels and is now possible to use several frequency steps that can be programmed independently for both channels during one shot.

III – Comparison with lithium beam and different density ranges

It is important to compare with other electron density diagnostics to validate and discard the existence of possible errors, although sometimes this could be difficult due to quite different time resolutions or physical positions around the torus. In this case we have compared with the lithium beam in the scrape-off-layer region. There is good agreement between the two diagnostics in terms of gradient and position (Figure 5). Reflectometry uses a linear initialization for the non measured profile up to $0.3 \times 10^{19} \text{ m}^{-3}$ but this can be improved if X-mode could be used to give the missing information. During the next long vacuum break much effort will be placed in repairing and optimizing the Q band X-mode channel.

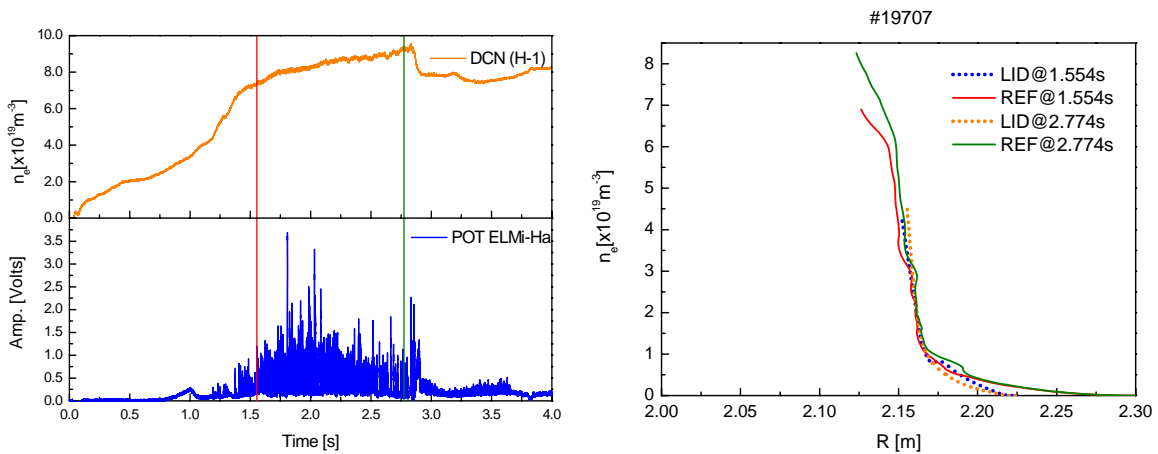


Figure 5 - Comparison with lithium beam for two time instants in shot #19707.

Reflectometry can measure in a reasonable range of different electron densities as shown in Figure 6. A flat gradient can limit plasma core access.

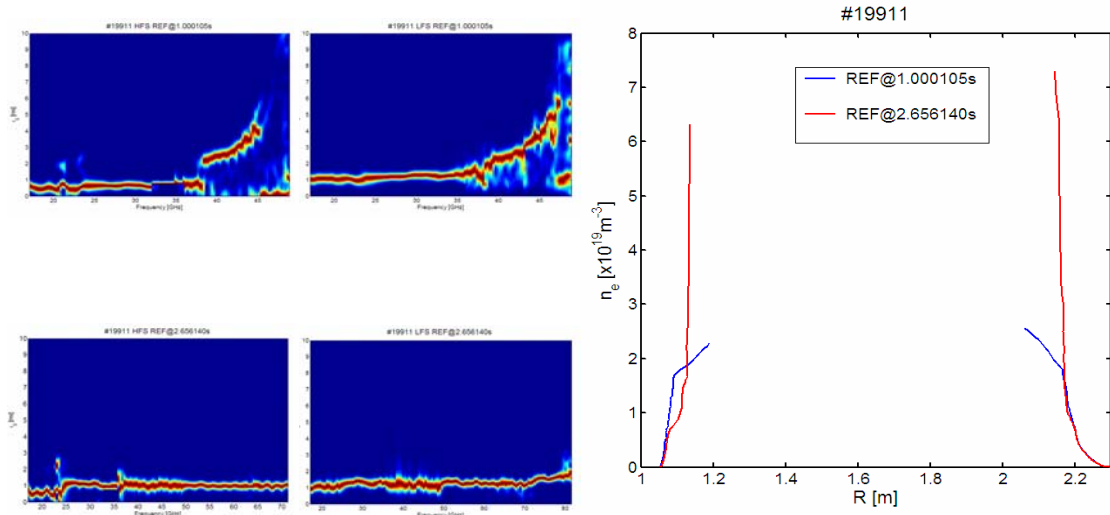


Figure 6 - Group delay for the HFS and LFS in two different plasma regimes and the resulting electron density profiles in shot #19911.

IV – ELM's and profile relaxation

Due to its high time resolution reflectometry is particularly suitable to analyze fast transient plasma phenomena like Edge Localized Modes (ELM). Instead of making the profile inversion for all time instants we have chosen to select a density layer on each band and to follow the related time evolution of the group delay (Figure 7).

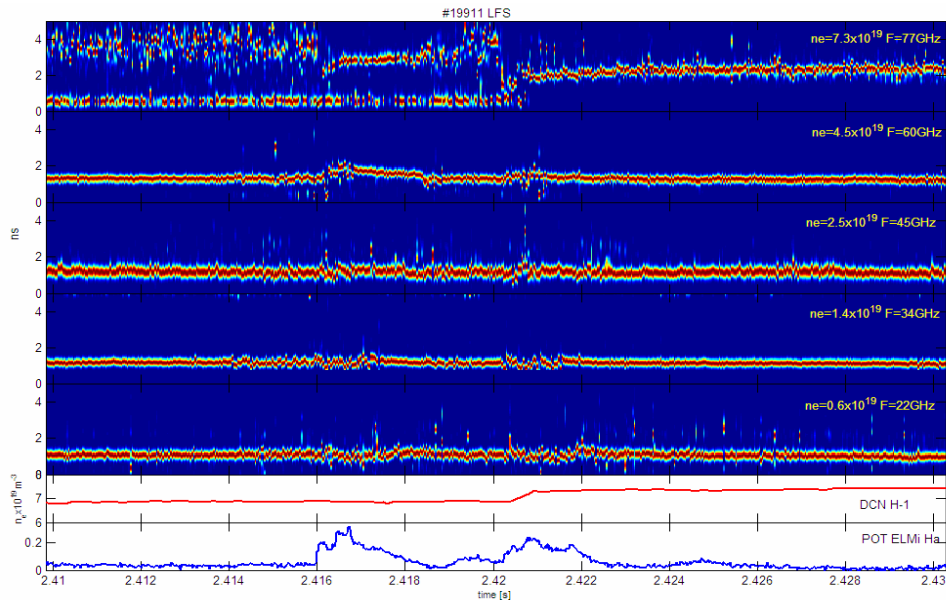


Figure 7 - Group delay evolution at the LFS for five different density layers. Related DCN and H_{α} time traces.

Between 2.41 s and 2.43 s of shot #19911 there is a natural ELM ($t \approx 2.416$ s), a pellet ($t \approx 2.419$ s) and a pellet induced ELM ($t \approx 2.420$ s). For the density $7.3 \times 10^{19} \text{ m}^{-3}$ (W band) the reflection is very weak until the ELM occurs. At this time we have a clear evolution of the group delay that increases also on the other high density layers (4.5×10^{19} and $2.5 \times 10^{19} \text{ m}^{-3}$) and a decrease for the lower density layers (1.4×10^{19} and $0.6 \times 10^{19} \text{ m}^{-3}$) revealing the presence of a profile pivot point between 1.4×10^{19} and $2.5 \times 10^{19} \text{ m}^{-3}$. The profile recovers the initial shape around 2.4185s some 3 ms after the start of the ELM. This is consistent with previous results [2] [3]. At 2.419s a pellet is injected that induces an increase of the mean density as shown by the DCN signal and this can also be clear observed by the evolution of group delay related to the density layer $7.3 \times 10^{19} \text{ m}^{-3}$ with a clear reflection overcoming the spurious reflection present around 0.5 ns. The induced ELM shows a similar behavior to the natural one. The same effects are observed at the HFS (see Figure 8), but in this case it is clearly observed the perturbation of the group delay around 2.4195s at the lower density layer

$(0.6 \times 10^{19} \text{ m}^{-3})$ induced by pellet. The pellet injector is located at the HFS just a few centimeters below our antennas.

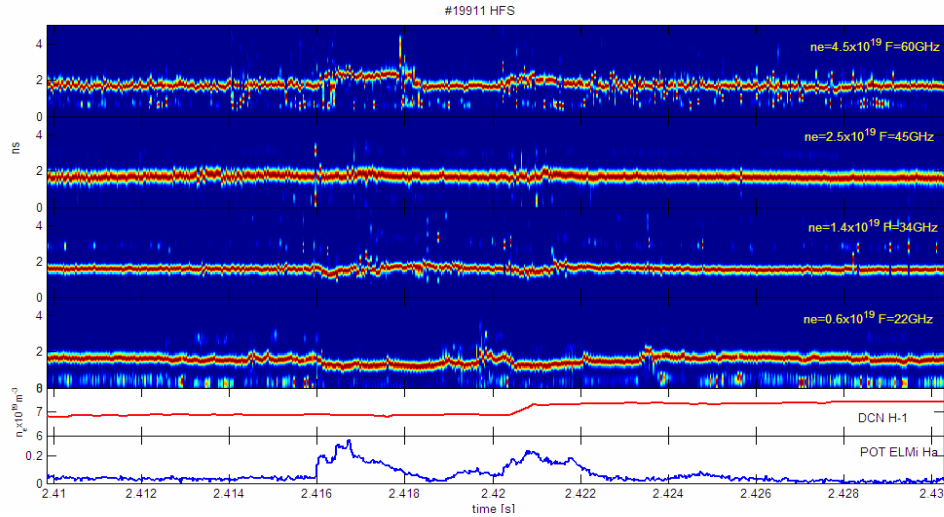


Figure 8 - Group delay evolution at the HFS for four different density layers. Related DCN and H_{α} time traces.

V – Summary and future work

The new frequency calibration method improved profile inversion precision and is available during plasma operation.

The W band channel is now routinely measuring and can give input to edge pedestal studies on high density discharges.

Much effort will be placed on repairing the hardware and analyzing the X mode signals to provide a better initialization for the O-mode channels.

The specifications for a new acquisition system with larger memory and better dynamic response are on paper. Commercial or dedicated solutions are under study.

[1] A. B. Carlson. *Communication Systems – An Introduction to Signals and Noise in Electrical Communication*. McGraw-Hill, New York, third edition, 1986.

[2] P. Varela. *Automatic time-frequency analysis for plasma density profile evaluation from microwave reflectometry*. PhD thesis, Universidade Técnica de Lisboa, Instituto Superior Técnico, 2002.

[3] I. Nunes. *Edge density studies of ELMy H-modes in ASDEX Upgrade using reflectometry*. PhD thesis, Universidade Técnica de Lisboa, Instituto Superior Técnico, 2004.

This work has been carried out within the framework of the Contract of Association between the European Atomic Energy Community and “Instituto Superior Técnico”, and has also received financial support from “Fundação para a Ciência e a Tecnologia” and “PRAXIS XXI”.

Recent Development of Microwave Reflectometer for Density Profile and Fluctuation Measurements on LHD

T. Tokuzawa¹, K. Kawahata¹, S. Sakakibara¹, S. Yamamoto²
and LHD Experimental Group¹

¹ *National Institute for Fusion Science, Toki 509-5292, Japan*
² *Osaka University, Suita 565-0871, Japan*

1. Introduction

Several types of microwave reflectometer have been installed to Large Helical Device (LHD [1]) for measuring the electron density profile and fluctuation [2, 3]. Recently we have been developing a new type of reflectometer which is used an ultrashort sub cycle pulse. It is called as an ultrashort pulse reflectometer [4]. An ultrashort pulse has broad band frequency components in a Fourier-space. It means one ultrashort pulse can take the place of a broad band microwave source. Also this ultrashort pulse reflectometer is categorized in the type of a time-of-flight (TOF) measurement system. This TOF measurement has the advantage which we can easily distinguish between the ordinary polarized wave and the extraordinary polarized wave in the reflected wave, because each cut-off position is separated in the plasma. Currently this ultrashort pulse reflectometer operates on ten channels using filter banks and a super heterodyne detection system for measuring the edge density profile and slow plasma oscillation. Also we have been developing the multi-channel heterodyne fixed frequency reflectometer which measures the density and magnetic fluctuation in the core region [5]. When the extraordinary polarized microwave is launched, the frequency spectrum of the reflected signal is found to be similar with that of the magnetic probe signal. By using this reflectometer it is quite easy to observe MHD phenomena such as Alfvén eigenmodes [6]. In this paper we present these two reflectometer systems and some experimental results.

2. Ultrashort pulsed radar reflectometer

The schematic of ultrashort pulsed radar reflectometer is shown in Fig. 1. An impulse of -2.2 V, 23 ps full-width half-maximum is used as a source. To extract the desired probing range of the frequency, we utilize a Ka-band rectangular waveguide. When the impulse is launched into the waveguide, it is transformed to the chirped wave including broad frequency

components. It is caused by the dispersion effect of the electromagnetic wave in the waveguide. The output chirped wave from the waveguide is amplified by a power amplifier and then is launched into the plasma. The incident wave reflects back from the cut-off layers corresponding to each frequency component. The

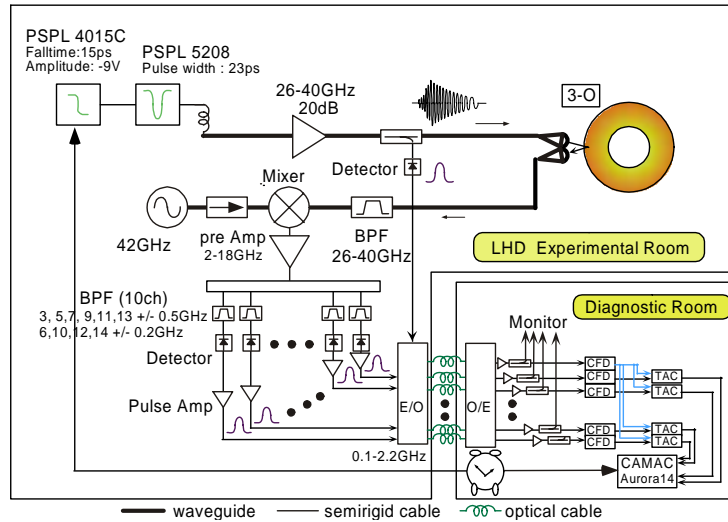


Figure 1 Schematic of ultrashort pulsed radar reflectometer

The reflected wave is mixed with 42 GHz continuous wave of the local oscillator. The output from the mixer is amplified by the intermediate frequency (IF) amplifier (2 – 18 GHz) and then divided to ten. Each IF signal is filtered by band pass filters which the centre frequencies are 3, 5, 6, 7, 9, 10, 11, 12, 13, 14 GHz and they correspond to 39, 37, 36, 35, 33, 32, 31, 30, 29, 28 GHz, respectively, in the incident frequency components. The ten signals are detected by the Schottky barrier diode detectors to obtain the reflected signal pulses. The reflected pulses are amplified by pulse amplifiers and led to constant fraction discriminators (CFD). A part of the incident wave is extracted with a directional coupler and is detected to obtain the reference pulse. Both the reference pulse as the start signal and the reflected pulse as the stop signal are led to the time-to-amplitude converter (TAC). The output voltage of TAC is proportional to the time difference between the start and the stop signal. The spatial ambiguity estimated from the TAC output has been tested and defined lower than 6 mm.

By using the ordinary wave the measured flight time of each frequency pulse reflected from the plasma has been described by $\tau_p(\omega_0) = \left(\frac{\delta\phi(\omega)}{\delta\omega} \right)_{\omega=\omega_0} = \frac{2}{c} \int_{r_a}^{r_c(\omega_0)} \left(1 - \frac{\omega_{pe}^2(x)}{\omega_0^2} \right)^{-1/2} dx$, with r_a the edge of the plasma, c the velocity of the light, ω the probing frequency, ω_{pe} the plasma frequency, ω_0 the plasma frequency corresponding to the critical density, and $r_c(\omega_0)$ the position where the plasma frequency equals the probing frequency, respectively. The result of the time evolution of TOF measurement is shown in Fig. 2. The delay time is defined by the travelling time from the assumed plasma edge to each cut off layer. When the corresponding cut-off layer is generated in the plasma, each reflected wave is observed in order. By using

Abel inversion the position of the reflecting layer is given by

$$r_c(\omega_0) = \frac{c}{\pi} \int_0^{\omega_0} \tau(\omega) / \sqrt{\omega_0^2 - \omega^2} d\omega.$$

Figure 3 shows the time evolution of the reconstructed density profile. In this inversion the cubic spline interpolation is used for connecting the data points between the lowest frequency cut-off layer and the assumed plasma edge.

3. Fluctuation Measurement System

The heterodyne reflectometer system is utilized for the fluctuation measurement [5]. Currently the system has three channels of fixed frequencies of 78, 72, 65 GHz. In LHD the real-time data acquisition system has been able to be utilized and the sampling rate is up to 10 MSample/sec by using a compactPCI based digitizer [7]. The system is very convenient to observe MHD phenomena such as energetic particle driven Alfvén eigenmodes [6], launching the extraordinary polarized wave. In Fig. 4 the temporal behaviour of the reflectometer signal of 78 GHz and magnetic probe signal and these power spectra are shown. Coherent spectra of around 8 and 16 kHz are caused by low-*n* mode oscillation. In the range of 100~150 kHz there are a lot of coherent mode. These

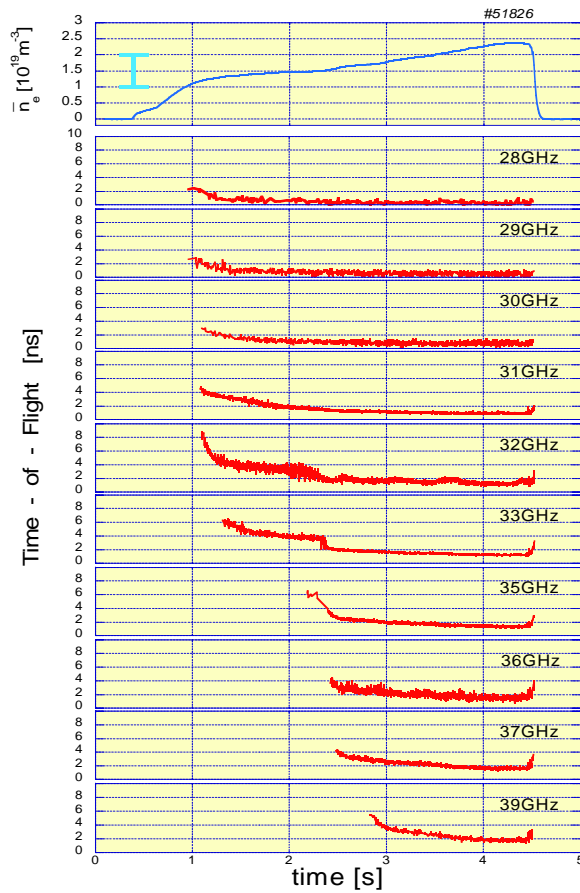


Figure 2 Time evolution of averaged electron density and Time-of-flight of each frequency reflected signal

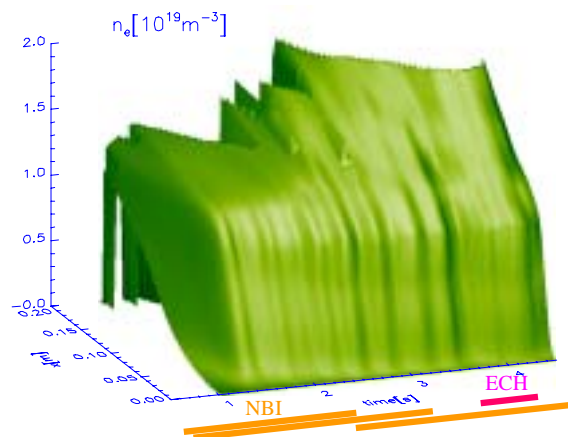


Figure 3 Time evolution of the reconstructed density profile

Coherent spectra of around 8 and 16 kHz are caused by low-*n* mode oscillation. In the range of 100~150 kHz there are a lot of coherent mode. These

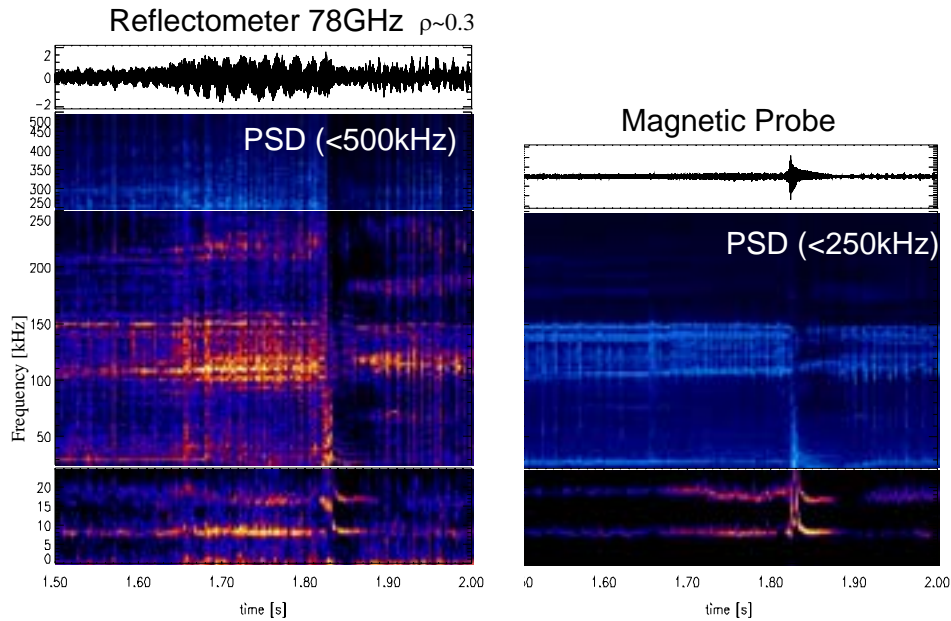


Figure 4 Time evolution of reflectometer signal and frequency spectrum (Left) and these of magnetic probe (right)

mode are identified the $n=1$ (n :toroidal mode number) mode by the magnetic probe analysis. Also on the reflectometer signal it is observed higher mode around 230 kHz. Just after $t=1.82$ s MHD-burst is occurred and these frequency components are rapidly disappeared and then passing 0.02s these mode are revived. It may be caused that the distribution of high energy particle is changed by such a MHD-burst. Therefore reflectometer is easy to be utilized to study the MHD phenomena.

Acknowledgements

This work was partially supported by a Grand-in-Aid for Young Scientists (B) (No.15760625, 2003) from the Japan Society for the Promotion of Science to one of the authors (TT).

References

- [1] O. Motojima *et al.*, Nucl. Fusion **43**, 1674 (2003)
- [2] T. Tokuzawa *et al.*, Rev. Sci. Instrum. **74**, 1506 (2003)
- [3] K. Tanaka *et al.*, NIFS-PROC-49, 88 (2001)
- [4] T. Kaneba *et al.*, Rev. Sci. Instrum. **75**, 3846 (2004)
- [5] T. Tokuzawa *et al.*, 31st EPS Conf. P5-114 (2004)
- [6] S. Yamamoto *et al.*, IAEA Conf. EX/5-4Rb(2004).
- [7] H. Nakanishi *et al.*, Fusinon Eng. Design **66-68** 827(2003).

A frequency sweeping heterodyne reflectometer in the Hanbit mirror

Seong-Heon Seo

Operation and Research Division, Korea Basic Science Institute, Daejeon 305-333, Korea

E-mail: shseo@kbsi.re.kr

A frequency sweeping heterodyne reflectometer is being developed for the density profile measurement of the Hanbit mirror. It consists of three Voltage Controlled Oscillators (VCO's). The frequency range of VCO's are 4-8 GHz, 8-12 GHz, and 12-18 GHz, respectively. Plasma density in the range between $0.2 \times 10^{12} \text{ cm}^{-3}$ and $4 \times 10^{12} \text{ cm}^{-3}$ can be measured by sweeping the VCO's frequencies simultaneously. Each VCO's output is mixed with a 30 MHz local oscillator's output to generate an up-converted probing wave to form a heterodyne reflectometer. A phase comparator is used to measure the phase of the Intermediate Frequency (IF) signal. To avoid phase jump, the relative phase measurement technique is applied. The design of the reflectometer, the signal analysis technique, and the preliminary result of the plasma density profile measurements will be presented.

An Ultrashort-Pulse Reflectometry for LHD Plasmas

Y. Kogi, A. Mase, M. Ignatenko, K. Uchida, K. Kudo, K. Nishiyama, H. Hojo¹,

K. Kawahata², Y. Nagayama², T. Tokuzawa²

KASTECC, Kyushu University, Kasuga 816-8580, Japan

¹*Plasma Research Center, University of Tsukuba, Tsukuba 305-8577, Japan*

²*National Institute for Fusion Science, Toki 509-5292, Japan*

We have applied an ultrashort-pulse reflectometer (USRM) to large helical device (LHD) plasmas for density profile measurement. This system can be controlled and monitored from remote site (Kyushu University) by using ultra wideband science information network (super-SINET) that ideal bandwidth reaches up to 1 Gbps. As a result of the measurement, we have confirmed reflection wave from the plasma, and succeeded to reconstruct density profiles corresponding to two plasma operation condition by means of SRA method. Applicability of microwave imaging reflectometry (MIR) for the case of mirror device was numerically studied. The questions concerning radial localization of measurements, optimal position of optical system and imaging properties of MIR system were considered. The high curvature of the plasma cutoff layer and a relatively small distance from the plasma to the port are known to improve the performance of a conventional reflectometer. Nevertheless in the case of density fluctuations with wide wavenumber spectrum and large amplitude, the imaging reflectometry shows better results than the conventional one.

I-1. INTRODUCTION OF USRM MEASUREMENT

Ultrashort pulse reflectometer (USRM) systems for density profile measurement are applicable in wide electron density range such as from inductively coupled plasma (ICP)⁴ to fusion experimental plasma¹⁻³. Since the propagation duration of probing beam inside plasma is less than a few nano seconds, the signal obtained by the USRM system is hardly influenced by density fluctuations. Since a sampling scope is utilized for a detection system in the present experiment, which takes about 10 ms to acquire a set of waveform, plasma density must be fixed during the measurement. However, utilizing the sampling scope will provide us cost effective solution to reconstruct precise density profile by means of signal record analysis method (SRA)⁵. Furthermore, the injection of an impulse enable us to measure a density profile over a wide spatial region since it contains broad-band frequency range inside an impulse. We report here the USPR system, application of the system to the large helical device (LHD), and remote operation system utilizing super-SINET.

I-2. USRM SYSTEM AND REMOTE OPERATION SYSTEM ON LHD

Figure 1 shows the USPR system on LHD. An impulse generator (Picosecond Labs Model 4015C) is utilized as a source, which transmits Gaussian impulses. The pulse width, height, and repetition rate of the impulse are 22 ps, 3 V, and 1 MHz, respectively. The pulse is fed to 30 cm section of a waveguide and chirped inside the waveguide. Bandwidth of the chirped pulse ranges from 7 GHz up to 20 GHz. The chirped pulse is then fed to an active doubler after passing through a 15 m low-loss coaxial cable. The active doubler doubles the frequency component

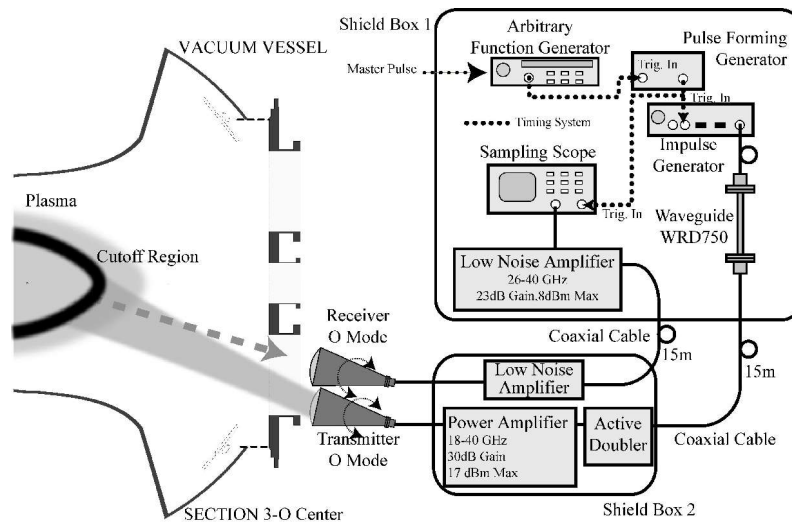


Figure 1 Schematic diagram of the USRM system on LHD

of the chirped pulse. The frequency range is between 26 GHz to 40 GHz. Then the chirped pulse is fed to a power amplifier with a gain of 30 dB and 1dB compression point of 17 dBm, and then transmitted to a plasma in the ordinary (O) mode by a conical horn antenna located at bottom port of section 3-O. The reflected wave from the plasma is received by another conical horn located at the same port. The signal is amplified by a low-noise amplifier, and further amplified by another low-noise amplifier after passing through a 15 m low-loss coaxial cable. The signal is then digitized by a sampling scope with equivalent sampling frequency of 250 GHz. In this measurement condition, it takes about 10 ms to acquire an array of 1024 data points with 2 times average. The impulse generator is controlled by a timing system. The timing system consists of an arbitrary function generator and a pulse-forming generator. The arbitrary function generator receives a master pulse, whose time is synchronized with plasma sequence, and transmits rectangular waves during the plasma operation. The frequency and duty cycle of the rectangular wave are 1 MHz and 50%, respectively. This rectangular wave is fed to a pulse-forming generator as a trigger. The pulse-forming generator transmits rectangular pulse with a moderately short pulse width less than 10 ns and rapid rise and fall time less than 100 ps at each trigger time. This rectangular pulse is fed to the impulse generator and the sampling scope as a trigger. In order to avoid affection of magnetic materials to helical magnetic field, most instruments of the USRM system are kept 10 m away from vacuum vessel of LHD. The directly recorded signal is analyzed and reconstructed by means of SRA method⁵.

Remote control system using super science information network (super-SINET) has been introduced to the USRM system since 2003 as shown in Fig. 2. This network is promoted by National Institute for Informatics (NII). Bandwidth of the main backbone and branch line is 10 Gbps and 1 Gbps, respectively. The control client can operate the control server by using this network. The general purpose interface bus (GPIB) card is installed in the control server. The remote console, which has graphical user interface (GUI) as shown in Fig. 3, is prepared to control the instruments of USRM via GPIB. The operations such as adjustment of supply voltage fed to amplifiers and the doubler, timing control of the impulse, data acquisition and monitoring, adjustment of transmitter and receiver angle can be performed from the remote site (Kyushu University).

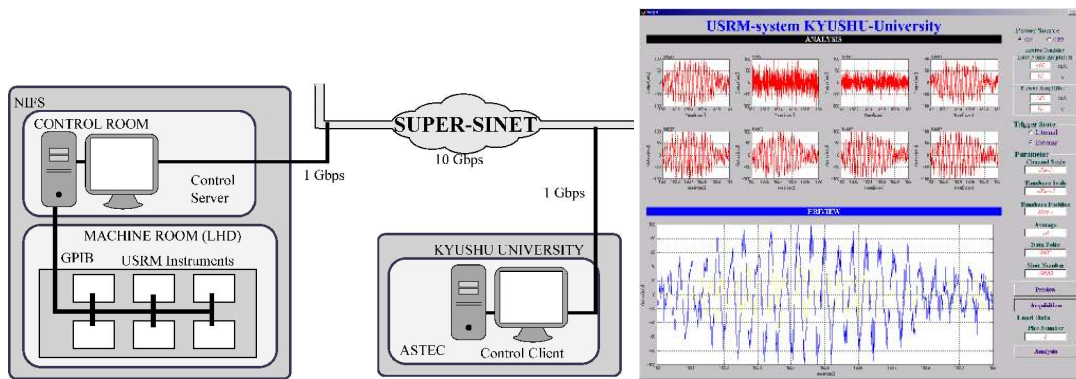


Figure 2 Remote control system by super-SINET Figure 3 GUI control application

I-3. RESULTS OF THE MEASUREMENT

Figure 4 shows operational sequence of heating systems (a), time evolution of stored energy of the plasma (b), and electron density by FIR(c). The plasma is generated from 0.5 second, and density reaches $1.5 \times 10^{19} \text{ m}^{-3}$ at 2.0 second, which corresponds to the cutoff frequency of 35 GHz. Figure 5 shows an output signal observed by the sampling scope. Each figure corresponds to measurement time denoted in Fig. 4(b,c) as four gray lines and t1-t3 from top figure to bottom one. In the Fig. 5(a), we can confirm the reflected wave from the diagonal vacuum vessel from 186 ns to 187 ns when the plasma does not exist (t1). Figure 5(b,c) are the signals when the plasma exists. Two types of trace, which color is gray and black, indicate the raw observed signals and bandpass-filtered signals by 2nd order digital Butterworth filter, respectively. Frequency range of the bandpass filter is between 26 and 40 GHz, which corresponds to bandwidth of incident frequency. Noise level observed in Fig. 5(b,c) increases obviously compared to Fig. 5(a). This noise is considered to be detected due to interference of other microwave diagnostic systems and electron cyclotron emission. By using the bandpass filter, we successfully confirm reflection from the plasma as shown in Fig. 5(c). We can attribute the signal received around 178 ns to reflection from the plasma since the detection time is 10 ns former than that from the vacuum wall. However, we can not observe any obvious reflection in this temporal range as shown in Fig. 5(b), even though the value of the plasma density at t2 and t3 are almost same. As we describe above, it takes 10 ms to acquire a trace of data by using the sampling scope. From this reason, the cutoff layer should freeze during 10 ms in order to measure the reflected wave keeping its phase information. Plasma density at t2 changes rapidly during the measurement as shown in Fig. 4(c). We can not observe the obvious reflected waves since the cutoff layer moves back and forth at t2. While, we can observe them at t3 since the cutoff layer seems to freeze during the measurement as shown in Fig. 4(c). Fig. 6 shows preliminary results of density reconstruction by means of SRA method in the case of two plasma operations. It is confirmed that density profile is expanding to outside in high density operation regime compared to low one. We are scheduled to take more data to investigate reliability of our system in the next experimental cycle.

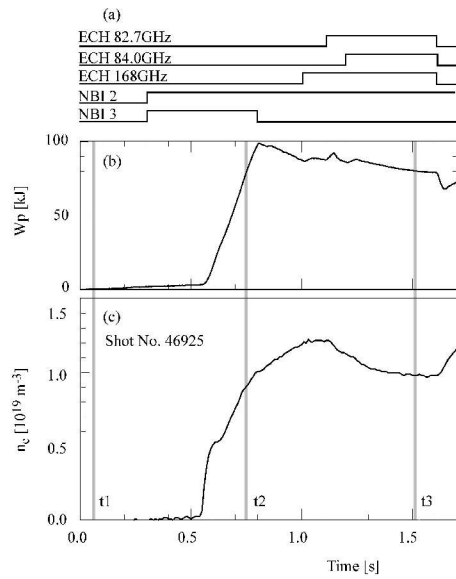


Figure 4 Time evolution of the heating systems (a), stored energy (b) and electron density (c)

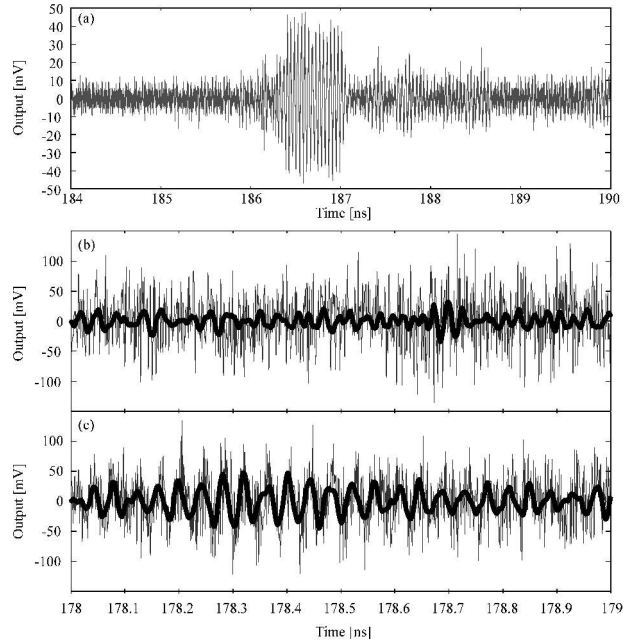


Figure 5 Reflection wave form at each measurement time

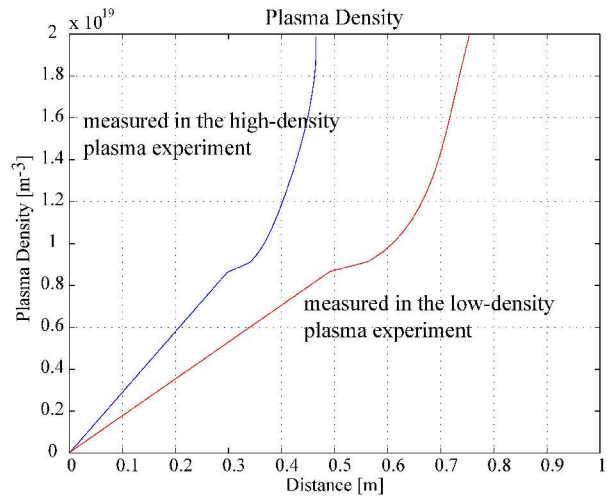


Figure 6 Density profiles reconstructed by the SRA method

II-1. INTRODUCTION OF NUMERICAL STUDY OF MICROWAVE IMAGING REFLECTOMETER

The microwaves reflected from cutoff layer inside the plasma bear information about plasma parameters. Microwave reflectometry utilizes the reflected signal for plasma density profile and fluctuations measurements. In spite of long term usage and popularity of the method, extracting information from reflectometer signal is a challenge up to nowadays, since scattering by random fluctuations leads to complicated interference pattern far from a cutoff ⁶ As a possible solution, an imaging concept was suggested in order to project the signal near the cutoff to the receiving plane outside the plasma, and the feasibility of the method was proven for a wide range of density fluctuation parameters ^{7,8}. An experimental and theoretical study was recently presented by Munsat *et al.* ⁹

where the authors performed laboratory characterization of an imaging reflectometer system by using a metal reflector with sinusoidal corrugations. The reflector was used as an approximation to the reflection by a plasma cut-off layer with turbulent fluctuations. The authors found that for the long wavelength, small amplitude corrugations both the conventional (without optics) and MIR systems accurately measure the target surface shape. For the shorter wavelength and/or higher amplitude, the conventional system was able to accurately reproduce the surface shape close to the target only. In contrast to conventional reflectometry, the imaging configuration was able to measure the shape of corrugations even far from the surface. All the parameters related to plasma and the machine geometry were selected in the original papers such as to correspond to tokamaks. We perform a numerical study of the MIR system in order to assess the feasibility of the method and to estimate possible obstacles and complications arising when microwave imaging reflectometry is applied to a smaller scale low density fusion device, such as the GAMMA 10 tandem mirror device.

II-2. NUMERICAL MODEL

The model employed in this study takes into account a free-space propagation of the launched microwaves, a phase front correction by the optical system, and a reflection from the plasma (Fig. 7). It comprises analytical and numerical (FDTD) solutions of 2D Maxwell's equations in vacuum and the equation for the induced current density \mathbf{j}

$$\frac{\partial \mathbf{B}}{\partial t} = -\nabla \times \mathbf{E}, \quad (1)$$

$$\frac{\partial \mathbf{E}}{\partial t} = c^2 \nabla \times \mathbf{B} - \frac{1}{\epsilon_0} \mathbf{j}, \quad (2)$$

$$\frac{\partial \mathbf{j}}{\partial t} = \epsilon_0 \omega_{pe}^2 \mathbf{E} - \omega_{ce} \mathbf{j} \times \mathbf{b}_0, \quad (3)$$

where \mathbf{B} , \mathbf{E} are the signal magnetic and electric fields respectively, c is the speed of light in vacuum, ϵ_0 is the permittivity of vacuum, ω_{pe} , ω_{ce} are the electron plasma frequency and cyclotron frequency, and \mathbf{b}_0 is a unit vector in the direction of the external magnetic field. Plasma parameters are included in the current density equation (3). Plasma profile is assumed in an exponential form:

$$n(r) = n_0 \exp(-r^2/\Delta_r^2) \quad \text{with } n_0 = 2 \times 10^{12} \text{ cm}^{-3} \text{ and } \Delta_r = 10 \text{ cm}. \quad (4)$$

External magnetic $B_0 = 0.45 \text{ T}$ is directed normally to the simulation plane. For the modelled parameters the cutoff layer is located at 10.3 cm. The random fluctuations $\delta n/n$ were generated as a sum of N modes with random amplitudes δn_{oi} and uniformly distributed phases ϕ_{θ_i} , ϕ_{r_i} similar to reference 10:

$$\frac{\delta n}{n} = \frac{2\gamma}{\sqrt{N}\sigma} \sum_{i=1}^N \delta n_{oi} \cos(k_{\theta_i}(r_c \theta - v_\theta t) + \phi_{\theta_i}) \times \cos(k_{r_i} r + \phi_{r_i}). \quad (5)$$

Here γ is a root-mean-square (RMS) amplitude of random fluctuations, σ is a standard deviation of δn_{oi} , r_c is a radius of normal incidence cutoff layer, $v_\theta = 6 \text{ km/s}$ is a rotation speed. The amplitude δn_{oi} has a Gaussian shape

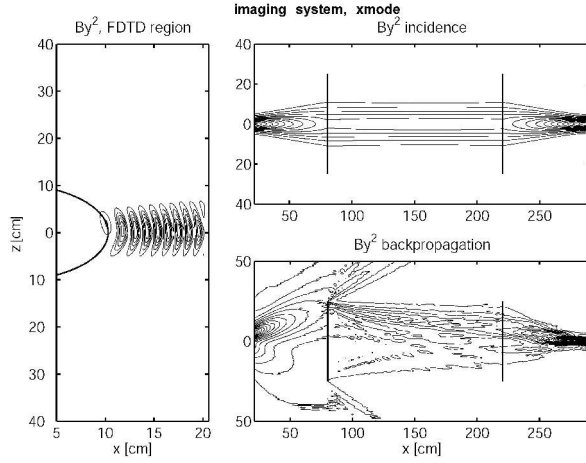


Figure 7 Distribution of incident and reflected fields in the analytical and FDTD regions. The cutoff layer is shown with a solid line in the FDTD region.

$$\delta n_{oi} \propto \exp\left(-\frac{(k_{\theta i} - k_{\theta 0})^2}{\Delta k_{\theta}^2} - \frac{(k_{r i} - k_{r 0})^2}{\Delta k_r^2}\right)$$

With $k_{\theta i}$, $k_{\theta 0}$ and Δk_{θ} , and $(k_{r i}$, $k_{r 0}$ and Δk_r) being the

poloidal (radial) wavenumbers, the shift of a wavenumber spectrum and spectral width respectively.

The imaging optics considered in this paper consists of a confocal two-lenses optical system. The two identical lenses with correction of spherical aberration have zero widths and focus distances $f_1=f_2=70\text{cm}$. Such a system transmits an image of the source with an enlargement factor equal to unity¹¹. In order to check the imaging properties of the different size optics, a Gaussian signal with sinusoidal phase was generated and numerically projected through the optics in vacuum. The system with lenses of 100cm size reproduced the shape of amplitude and phase perfectly (Fig.8), while small size optics distorted the signal. Reflections from wall of the chamber and from the port window are not taken into account.

II-3. RESULTS OF THE SIMULATION

As it was shown in Fig.8, the simulated large lenses optical system can project microwave signal without distortions within a region of $-6\text{cm} < z < 6\text{cm}$. The optical system thus restores a spacial distribution of density fluctuations as shown in Fig. 9(a). In order to check the imaging property of the simulated system in more details we put a single density disturbance of the amplitude 1% near the cutoff, shifted optics from cutoff by 3cm and recorded the z-profile of received signal. The reflectometer signal phase fluctuations profile transmitted by optics of 50cm size are found unable to reproduce the shape of density fluctuations at all (Fig. 9(b)). Large lenses system revealed a better performance and projected the image of density fluctuations within the area of $3\text{cm} < z < 3\text{cm}$ without strong distortion. It can be explained by the high curvature of reflecting cutoff layer, which leads to a spread of the reflected signal over a wide angle. Small size optics miss huge part of scattered waves and thus appear to be unable to build an image. Even 100cm size optics is able to restore density fluctuations profile in the narrow region only. The rotation of the plasma in a mirror device can be utilized to create a time image of the fluctuations in the cutoff point illuminated by the microwave beam. The time dependent phase fluctuations of the imaging reflectometer replicate the shape of density fluctuations at the cutoff as it is shown in Fig.10(a). In order to compare the time imaging properties of a conventional and MIR systems, a scattering from density

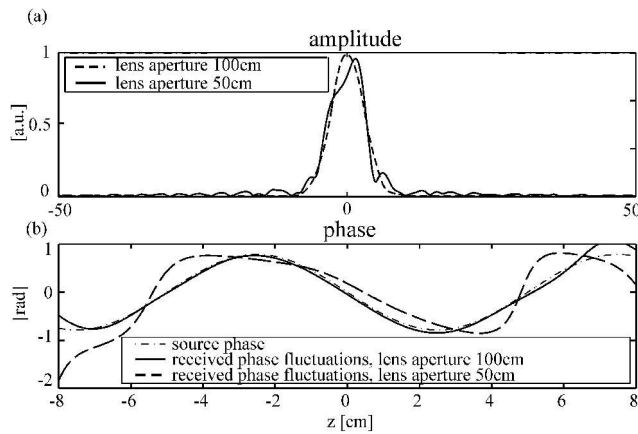


Figure 8 (a) Amplitude and (b) phase of the signal projected by the two-lenses confocal system. Optical system with large lenses transmits signal better than that with small lenses.

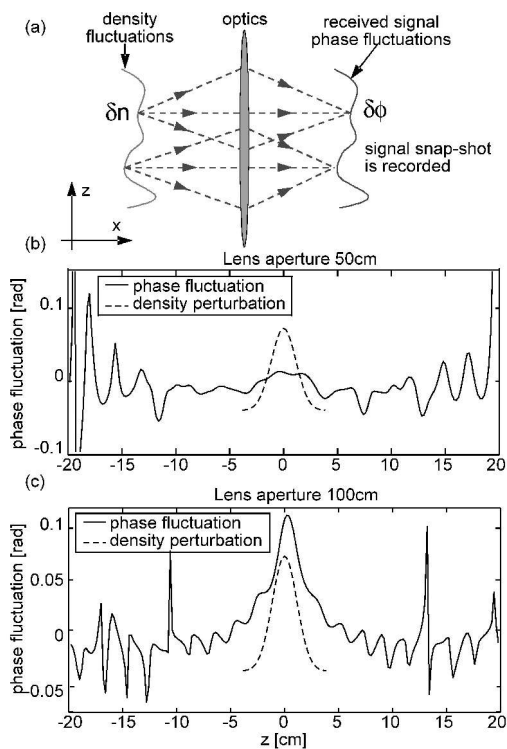


Figure 9 (a) Principle of space imaging, (b), (c) phase fluctuations of the reflectometer signal transmitted by optics of 50 & 100cm respectively.

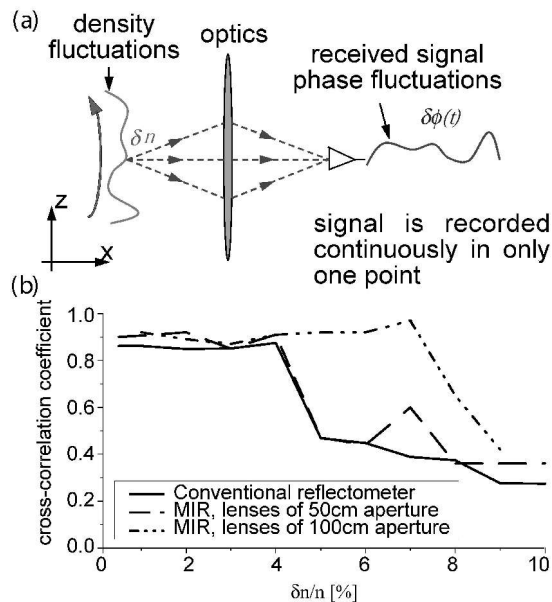


Figure 10 (a) Principle of time imaging, (b) Cross-correlation coefficient between the fluctuations of the received signal phase and the shape of density fluctuations as a function of fluctuation amplitude.

fluctuations with a wide wavenumber spectrum was simulated. Antenna of conventional reflectometer was located at $x=60\text{cm}$, which was close to the port window. As an estimation of imaging properties we used cross correlation coefficient between the fluctuations of the received signal phase and the shape of density fluctuations (Fig. 10(b)). At small fluctuation levels all the system show relatively high cross-correlation coefficient, but in the case of large fluctuations it was only the imaging system with large aperture optics which could reproduce properly the fluctuation shape.

III. SUMMARY

In summary, USRM diagnostics with remote operation system has been applied to LHD plasmas in order to measure density profiles. As a result of the measurement, we have successfully confirmed the reflections from the cutoff layer when the plasma is sustained in steady state. And we have succeeded to reconstruct the density profiles by means of SRA method. We also confirmed followings in the MIR simulation study. For the geometry of GAMMA 10 tandem mirror device the conventional reflectometer shows high performance even without any optics as far as fluctuation spectrum measurements are concerned. Possible reasons for that are the high curvature of the cutoff layer^{12,13}, relatively low working frequency and the small distance from the cutoff to the receiving antenna. On the other hand a high cutoff curvature is an obstacle to the application of MIR system to the mirror device due to the spread of the reflected microwaves over a wide angle. As a result, only a large aperture optics is able to image the density fluctuation with a reasonable accuracy. For the case of tokamak devices the size of the required imaging optics can be reduces due to smaller plasma curvature in a reflecting layer and higher working frequencies.

ACKNOWLEDGMENTS

This work was performed as a collaborating research program at National Institute for Fusion Science. The part of this work was also supported by Effective Promotion of Joint Research with Industry, Academia, and Government in Special Coordination Funds for Promoting Science and Technology, MEXT.

REFERENCES

1. Y. Roh *et al.*, Rev. Sci. Instrum. **72**, 332 (2001)
2. S. Kubota *et al.*, Rev. Sci. Instrum. **70**, 1042 (1999)
3. A. Mase *et al.*, J. Plasma Fusion Res. **78**, 439 (2002).
4. Y. Kogi *et al.*, Rev. Sci. Instrum. **74**, 1510 (2003)
5. L. G. Bruskin *et al.*, Jpn. J. Appl. Phys., Part 1 **40**, 705 (2001)
6. R. Nazikain *et al.*, Phys. Plasmas, **8**, p.1840 (2001).
7. E. Mazzucato, Rev. Sci. Instrum., **69**, p.1691 (1998).
8. E. Mazzucato, Nucl. Fusion, **41**, p.203 (2001).
9. T. Munsat *et al.*, Plasma Phys. Control. Fusion, **45**, 469 (2003).
10. L.G. Bruskin *et al.*, Plasma Phys. Control. Fusion, **45**, 1227 (2003)
11. E.G. Steward, Fourier Optics: An Introduction, Allis Horwood Ltd, (1983).
12. Y. Lin *et al.*, Plasma Phys. Control. Fusion, **43**, L1 (2000).
13. L.G. Bruskin *et al.*, Plasma Phys. Control. Fusion, **44**, 2305 (2002).

Adaptive window calculation for automatic spectrogram analysis of broadband reflectometry data

P. Varela¹, A. Silva¹, M. Manso¹, and the ASDEX Upgrade Team²

¹*Associação EURATOM/IST, Instituto Superior Técnico, 1049-001 Lisboa, Portugal*

²*MPI für Plasmaphysik, EURATOM/IPP Association, D-85740 Garching, Germany*

Abstract

Electron density profiles of fusion plasmas may exhibit large variations due to different operating regimes as well as fast changes due to transient plasma phenomena (e.g. ELMs), which modify the frequency content of broadband reflectometry signals. For this reason, the evaluation of the density profile based on the spectrogram technique usually requires: (i) the use of conservative sizes of the window of analysis, in order to cope with the large/fast data variations, or (ii) direct user intervention to match the window size to the data content. In the first case, accuracy is reduced, while in the second, the need for user intervention prevents the fully automatic evaluation of the density profile. Here we present the application of a new technique that uses a time-frequency energy concentration measure in order to estimate the optimum window length. In this way, the spectrogram analysis may be automatically adapted to the frequency content of the data in each window, increasing the time-frequency resolution in cases where the frequency exhibits fast/large variations, as for example just inside the pedestal region of H-mode plasma profiles. The application to test signals and simulated profile data shows the importance of the new technique in improving the accuracy of automatically evaluated density profiles. The advantages of the technique versus its computing requirements are also discussed.

1 Introduction

Broadband reflectometry as a diagnostic of the electron density profile of fusion plasmas as reached a level where profile availability to the physics community is of crucial importance for the full establishment of the diagnostic technique. In this context, automatic data evaluation procedures play a major role, since they allow the density profiles to be routinely available – depending on the characteristics of the diagnostic (e.g., the amount of data to be processed, available computing power, etc.) the profiles might even be available immediately after each shot. However, the automatic evaluation of the density profile from broadband data faces a major problem: due to profile modifications the frequency content of the reflected signals (directly related to the group delay of the probing waves) varies significantly which requires adjustments of the data processing parameters, that vary depending on the specific technique used in the evaluation.

In the case of the spectrogram analysis used to evaluate the profile data on ASDEX Upgrade, the parameter to be adjusted is the length of the window of analysis. By varying the size of the spectrogram window, it is possible to adjust the time-frequency resolution to a specific feature of the signal being analysed. However, in cases where the frequency content exhibits fast/large variations along the sweep a fixed-length analysis window is often not adequate to provide the required time-frequency resolution. In these cases, the evaluation of the density profile based on the spectrogram technique requires: (i) the use of large windows, in order to cope with the fast data variations, or (ii) direct user intervention to match the size of the window to the data. In the first case, accuracy is reduced, while in the second, user intervention disables the fully automatic evaluation of the data.

Here, we report on the application of a new technique that allows the length of the window of analysis to be automatically adjusted to the frequency content of the signals being analysed. This is achieved through the use of an energy concentration measure in the time-frequency plane. This measure is applied at each time sample to a given set of possible lengths of the window of analysis, in order to determine the optimum window length. The technique, first proposed in [1], is based on the assumption that the optimum window length (the one that results in good time-frequency localization and high resolution) is the one which provides the higher time-frequency concentration.

2 The adaptive spectrogram

2.1 Basic principles

Adaptive time-frequency representations require a means of determining an appropriate window length (in the case of the spectrogram analysis) or kernel function (in the case of other distributions) without extensive a-priori knowledge of the characteristics of the signal being analysed. The adaptive spectrogram technique presented here optimizes the length of the window of analysis for each time slice by maximizing a short-time measure of time-frequency concentration defined as

$$C(t, p) = \frac{\iint_{-\infty}^{+\infty} |D_p(\tau, \Omega)w(\tau - t)|^4 d\tau d\Omega}{\left(\iint_{-\infty}^{+\infty} |D_p(\tau, \Omega)w(\tau - t)|^2 d\tau d\Omega\right)^2}. \quad (1)$$

In the above, $D_p(\tau, \Omega)$ is the spectrogram distribution and $w(\tau)$ is a one-dimensional concentration window centered at $\tau = 0$. The optimal time-varying window length is thus defined as $p^*(t) = \operatorname{argmax}_p C(t, p)$. Notice that the ratio of the L_4 and the L_2 norms of the spectrogram used in the concentration measure favors peaky distributions that place as much signal energy into as small a region of time-frequency as possible.

The implemented algorithm works as follows. The short-time concentration is computed for discrete values p_i , $i = 1, \dots, P$ of the window length. The resulting concentration measures $C(t, p_i)$ represent samples of $C(t, p)$. An estimate of the optimal window length $p^*(t)$ is then obtained by taking the maximum value of $C(t, p_i)$. Once the optimal window length $p^*(t_0)$ is computed at time t_0 , the time slice $D_{p^*(t_0)}(t_0, w)$ of the adaptive spectrogram can be computed with window length $p^*(t_0)$.

The algorithm can be implemented more efficiently by rewriting $C(t, p)$ in terms of the quantities

$$c_2(\tau, p) = \int_{-\infty}^{+\infty} |D_p(\tau, \Omega)|^2 d\Omega \quad \text{and} \quad c_4(\tau, p) = \int_{-\infty}^{+\infty} |D_p(\tau, \Omega)|^4 d\Omega$$

and taking advantage of the localization effect of $w(\tau)$. More details of the implementation can be found in [1].

2.2 Application example

In order to evaluate the performance of the new technique we applied it to the test signal shown in figure 1(a). The signal has 256 samples and is composed of three diracs (located at samples 10, 20, and 250), a sum of two fixed-frequency signals (limited to between samples 45 and 95), a fixed-frequency signal modulated by a gaussian pulse (centered at sample 129), and a linear chirp with frequencies going from $f = 0.05$ at $n = 157$ to $f = 0.3$ at $n = 220$.

Figures 1(b)–(d) show the spectrogram distribution computed with window lengths of 5, 15, and 41 samples respectively. As can be observed, the small window is able to clearly localize the dirac pulses but fails to reproduce the other frequency components. Using a larger window enable us to recognize the existence of the other frequency components although the time-frequency resolution is rather poor. In addition, the dirac pulses are also poorly resolved. Finally, a large window is able to resolve all the components except the dirac pulses, due to the resulting poor time resolution.

Figure 1(e) shows the adaptive spectrogram distribution of the test signal computed using the technique described in 2.1. As can be observed, the adaptive spectrogram is able to resolve all frequency components with good time-frequency resolution throughout the signal. The corresponding evolution of the optimum window length is shown in figure 1(f). As expected, a small window was used in the region where the diracs are present, providing good time resolution. As soon as the sum of two frequencies is detected a large window is used in order to provide the necessary frequency resolution. A smaller window is used between samples 157 and 220 in order to resolve the frequency evolution of the linear chirp component.

3 Application to simulated profile data

For the ASDEX Upgrade broadband reflectometer, the application of the adaptive spectrogram to the automatic evaluation of density profiles has a major impact in suppressing the need to adapt the window length to the characteristics of the reflected signals. This is especially true during sudden changes in the profile gradient such as the ones occurring just inside the pedestal region in H-mode plasmas, during ELMs or due to changes in plasma density. Currently, the

window length is (manually) fixed at 256 samples for the K, Ka, and Q channels and 128 for the V and W channels, where the pedestal region is expected to be in medium and high density H-mode plasmas respectively. Although adequate for most cases, this setup does not provide good time-frequency resolution in the low/medium density part of the discharges (such as before the L-H transition) where the profile flattening might occur in the Q and even in the Ka channels. In these cases it would be best to use smaller window lengths in order to provide enough time-frequency resolution to resolve the profile flattening.

To evaluate the effect of using a large window of analysis in the region where the gradient is changing rapidly we used V-band data obtained from a simulated profile of the form

$$n_e(r) = (1 - (r/a)^n)^m \quad (2)$$

with $n = 2$ and $m = 4$. The raw signal is shown in figure 2. As expected, the beat frequency exhibits a sudden increase due to the profile flattening above $f = 70$ GHz. The spectrograms shown in figures 2(b)–(d) were computed with 64, 128, and 256 samples respectively. As can be observed, a large analysis window leads to an unacceptable decrease in the time and frequency resolution in the region where the beat frequency is changing fast. As a result, the spectrogram distribution is unable to reproduce the correct frequency behaviour. The corresponding adaptive spectrogram is shown in figure 2(e) while the evolution of the window length across the signal is depicted in figure 2(f). In the region where the beat frequency is changing slowly the adaptive technique estimated a large window providing essentially frequency resolution. As soon as the beat frequency starts to increase the window becomes smaller and smaller to provide the necessary time resolution. Notice also the clear improvement in frequency resolution in the range below 70 GHz due to the use of a larger window.

From these results one can conclude that the adaptive spectrogram is an efficient technique to automatically adapt the length of the window of analysis to accommodate for possible beat frequency changes in broadband reflectometry data.

4 Discussion

The adaptive spectrogram technique allow us to automatically adapt the window length parameter to the characteristics of the reflectometry signals. By matching the window of analysis to the local time-frequency properties of the signals, both time and frequency resolutions can be simultaneously and independently improved. As such, large/fast beat-frequency variations induced by profile changes may be resolved, directly improving the accuracy of the inverted profile. However, as expected, extra performance doesn't come without a price: the adaptive spectrogram requires about six times the computation time of a fixed-window spectrogram. Due to this additional computational effort, the use of this technique in the routine evaluation of density profiles on ASDEX Upgrade will be limited to the frequency band "containing" the profile flattening (the so-called last band). This alone represents a major improvement in the accuracy of level-1 profiles (profiles computed with a minimum of data processing effort) since it provides a means for adapting the data analysis parameters to changes in the electron density throughout the discharge.

Acknowledgments

This work has been carried out in the framework of the Contract of Association between European Atomic Energy Community and "Instituto Superior Técnico", Financial support was also received from "Fundação para a Ciência e Tecnologia" and "Programa Operacional Ciência, Tecnologia e Inovação do Quadro Comunitário de Apoio III".

References

- [1] D. L. Jones and R. G. Baraniuk, "A simple scheme for adapting time-frequency representations", *IEEE Transactions on Signal Processing*, Vol. 42, No. 12, Dec. 1994.

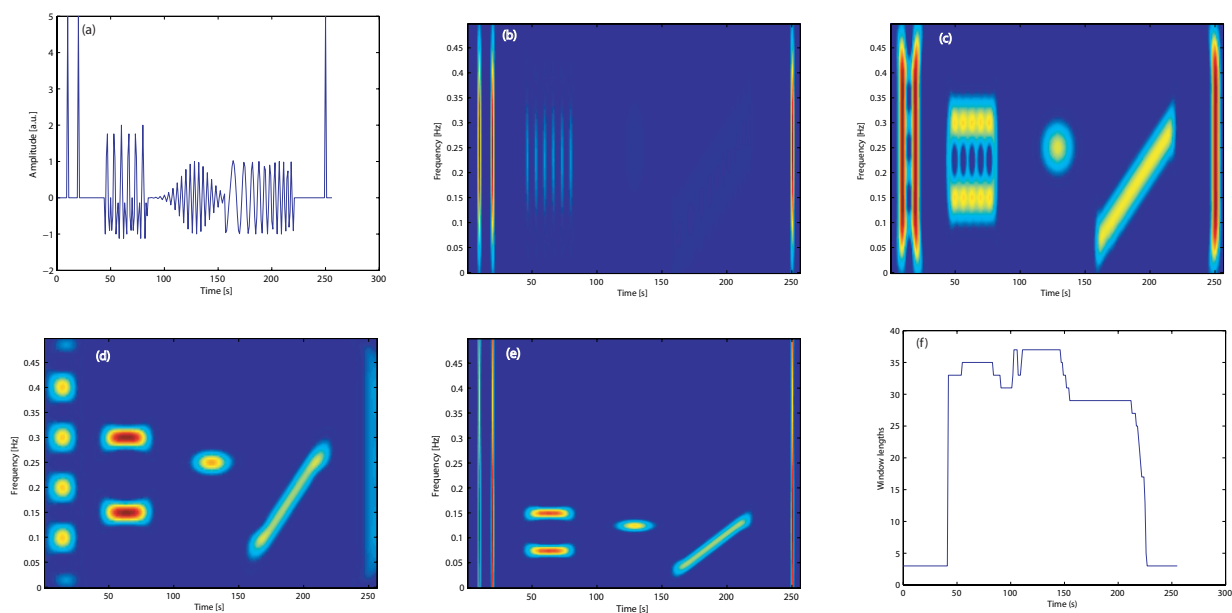


Figure 1: Application of the adaptive spectrogram technique to a test signal: (a) test signal, (b) 5 samples window, (c) 15 samples window, (d) 41 samples window, (e) adaptive spectrogram, and (f) window length evolution.

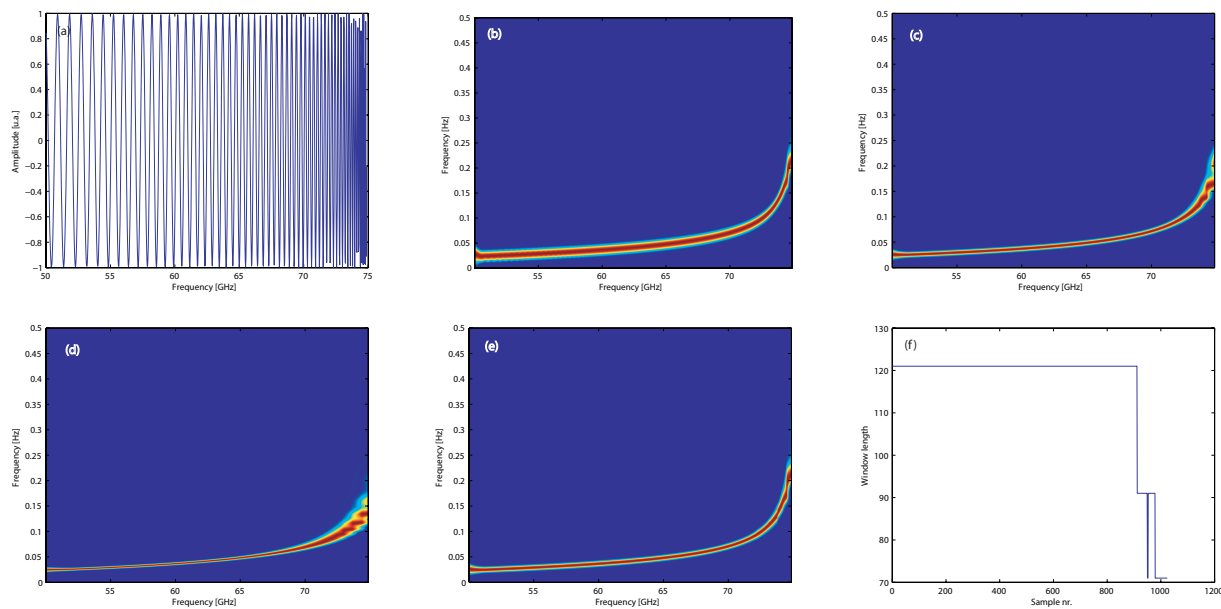


Figure 2: Application to simulated V-band data in the profile flattening region: (a) simulated signal, (b) 64 samples window, (c) 128 samples window, (d) 256 samples window, (e) adaptive spectrogram, and (f) window length evolution.

Recent progress with high-resolution FM profile reflectometer measurements on DIII-D*

L. Zeng, G. Wang, E.J. Doyle, W.A. Peebles and T.L. Rhodes

Department of Electrical Engineering and Plasma Science and Technology Institute
University of California, Los Angeles
California 90095, USA

Abstract

Hardware and software advances continue to be incorporated in the high-resolution FM-CW density profile reflectometry system on DIII-D. A novel dual-polarization measurement technique was utilized, to expand the density coverage $0-6.4 \times 10^{19} \text{ m}^{-3}$ continuous, and with a time resolution of $\geq 10 \text{ } \mu\text{s}$ and spatial resolution of $\geq 4 \text{ mm}$. The high memory-depth PC-based data-acquisition system has been expanded to 6 digitized channels. A new between-shot automatic profile analysis capability has recently been implemented, taking 4-5 minutes to automatically analyze X-mode profiles between discharges and storing profiles into the DIII-D MDSplus database. System capabilities are illustrated using results from a variety of areas such as L-H transition and pedestal physics, ELM dynamics, plasma-wall interaction studies, disruptions and ITB studies.

1. Introduction

Profile reflectometry has been widely used in fusion study for density profile measurement, and is planned for profile measurement as well as edge location control on ITER. Because of its high time and spatial resolution, it is also successfully employed to investigate some plasma MHD instabilities [1,2], as well as edge localized modes (ELMs). Currently, the major emphasis of work with the high-resolution FM profile reflectometer system on DIII-D has transitioned from development of the hardware and measurement capabilities to physics utilization. Despite this change in emphasis, both hardware and software advances continue to be incorporated in the system. These advances include a full solid state system, simultaneous O/X- mode launch,

*Work supported by the U.S. Department of Energy under DE-FG03-01ER54615 and DE-FC02-04ER54698.

increased fast digitizing capability, and a new between-shots automatic profile analysis. These advances are described in detail below.

2. System Hardware Upgrades: Dual-polarization Technique

Since the IRW6 meeting in May 2003, a novel dual-polarization measurement technique has been utilized in our profile reflectometry system, in which O- and X-mode polarizations are simultaneously launched from a common solid-state microwave source. In addition, the frequency coverage has been expanded from Q-band (32-50 GHz) to V-band (50-72 GHz) [3]. This increase in frequency coverage (using high performance solid-state microwave sources) has expanded the density coverage from $0-3.1 \times 10^{19} \text{ m}^{-3}$ in 2003 [4], with an unmeasured gap, to $0-6.4 \times 10^{19} \text{ m}^{-3}$ continuous. The system now possesses good time ($\geq 10 \text{ } \mu\text{s}$) and spatial resolution ($\sim 4 \text{ mm}$). The system consists of two sub-systems (Q-band and V-band). A schematic of one sub-system is shown in Figure 1. The probe microwave beams are generated by a solid-state source which can sweep full frequency band in as little as $10 \text{ } \mu\text{s}$, and which is launched at 45° polarization into the plasma. This serves to couple to both O- and X-mode waves. Microwaves are simultaneously reflected from both the X-mode right hand cutoff frequency layer and the O-mode electron plasma frequency layer. Simultaneously, the reflected O- and X-mode waves are received by the two orthogonal horns, and mixed with local beams separately. With this approach, the range in density that can be measured is expanded.

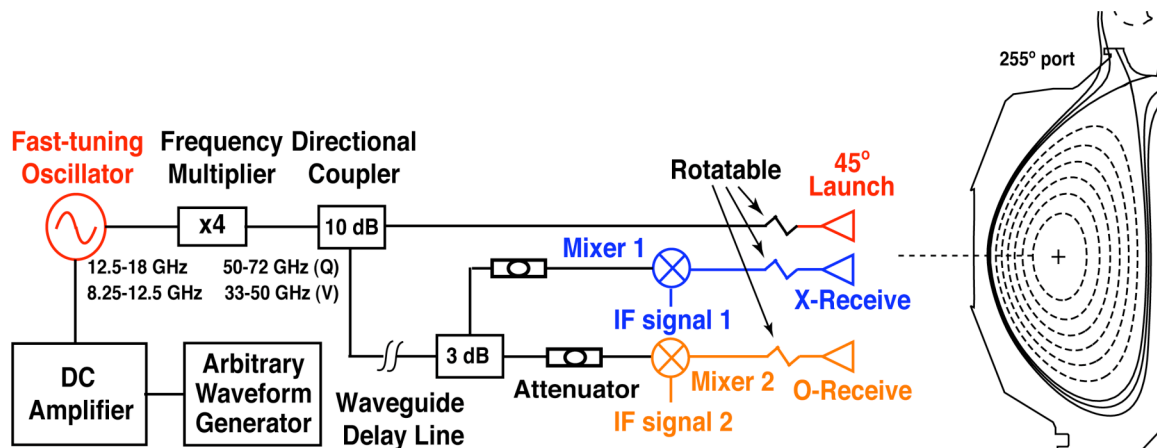


Figure 1 a schematic of profile reflectometry system on DIII-D

3. Analysis Improvements and X-mode Profile Between-shots Analysis

The data acquisition system has been upgraded by using three high memory-depth Gage CS 12100 PC-based data acquisition boards, with high sampling rate (50 MHz in dual-channel mode) and with large on-board memory (512 MB/board, maximum total 1.5GB/shot). This high performance system can be operated either in continuous digitization for a maximum 2.56 s data coverage at 50 MHz, or in “Burst” data acquisition mode with ~ 1 ms duration data bursts every 5-10 ms for up to 6 s.

In order to quickly analyze the large volume of data, a between-shot profile analysis capability has been implemented. The new analysis is based on a previous analysis program, employing digital complex demodulation (CDM) [5] and other techniques [6]. By simultaneously using ten Linux-based computers (Dual-Xeon 2.66 GHz processors, 2 GB RAM each), analysis of X-mode profiles every 5-10 ms throughout the whole discharge takes 4-5 minutes, completing well before the next discharge. Profile data is stored in the DIII-D MDSplus database and is ready for viewing between-shots after ~ 10 minutes. An example of between-shots X-mode profile analysis is shown in Figure 2. The density contours (total of 800 profiles), with 4 s data coverage and 5 ms time resolution, are shown in Figure 2(a), where the color curves represent different density layers. It is clearly observed that the inner density layers move inward during the application of electron cyclotron current drive (ECCD) and during locked modes occur later. The measured density decreases are consistent with the CO₂ line average density measurement shown in Figure 2(b).

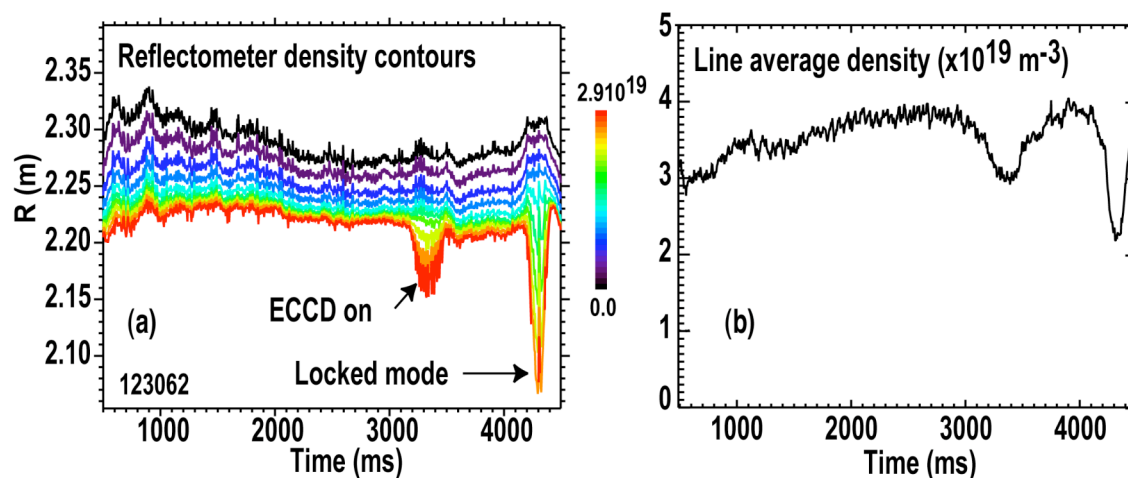


Figure 2, an example of between-shot profile analysis, reflectometer density contours (a), and line average density (b)

4. Comparison Between Diagnostics and an Example of Selected Physics Applications

Currently, the physics applications of profile reflectometer measurements include plasma-wall interaction studies, ELM dynamics, L-H transition and pedestal evolution. In plasma-wall interaction studies, good agreement in the edge density profile is found between different diagnostics on DIII-D as shown in Figure 3, where the black circles are Thomson scattering data, the red squares are Langmuir probe data and blue diamonds represent reflectometer profile measurements for shot 120350 at 4150 ms.

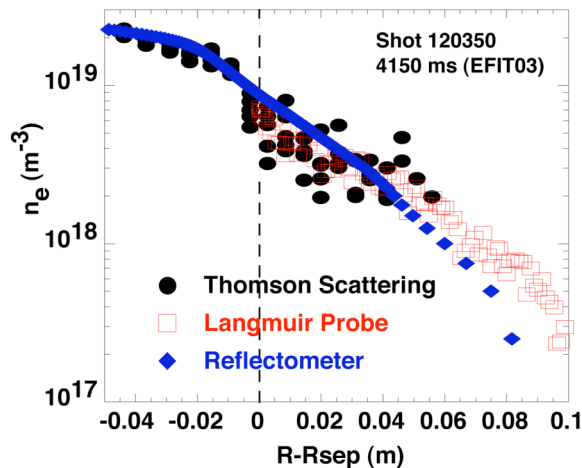


Figure 3, edge profile measurement comparison among reflectometer, Langmuir probe and Thomson scattering

A detailed example of the density profile dynamic evolution through a single Type-I ELM is shown in Fig. 4. The ELM timing is shown by a divertor D_α signal, Fig. 4(a), where the numbers and vertical lines represent the times for the density profile sequence shown in Fig. 4(b). In Fig. 4(b), profile 1 is taken just before the ELM onset, and shows a typical H-mode edge pedestal with steep gradient. At the onset of the ELM, profile 2 shows an increase in SOL density, with the density at the top of the pedestal slightly reduced. At the time of the ELM crash (profile 3), about 100 μs later, the SOL profile has expanded radially outward to the vessel wall, where there is a relatively large density rise of $\sim 2 \times 10^{18} \text{ m}^{-3}$. During the recovery phase, profile 4 shows the pedestal gradually rebuilding, and SOL density reducing. The final profile in the sequence, 5, shows a return to a well-defined edge pedestal several ms after the ELM onset. Thomson scattering data obtained at the same time as reflectometer profile 5 are shown via points with error bars, showing good agreement

between the two measurements. The illustrated evolution of the pedestal and SOL density profiles demonstrates that the density rise observed in the SOL is directly linked to the pedestal loss during the ELM.

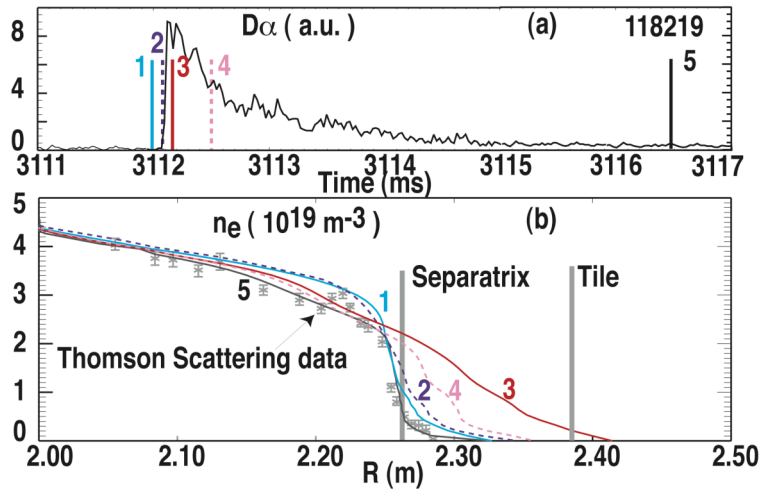


Figure 4, (a) $D\alpha$ signal with times for (b) indicated and (b) density profile dynamic evolution through a single Type-I ELM for shot 118219,

5. Summary

Both hardware and software upgrades continue to be incorporated in the DIII-D FM density profile reflectometer system. The density coverage has been expanded, 0- $6.4 \times 10^{19} \text{ m}^{-3}$, using simultaneous dual polarization launch. New between-shot profile analysis capability has been implemented, and X-mode profiles are stored in an MDSplus database. The increased system capability has expanded the range of physics issues which can be addressed, e.g. plasma-wall interaction studies, ELM dynamics, L-H transition and pedestal evolution.

References

- [1] L. Zeng, et al, J. Nucl. Mater. **337-339**, 742-746 (2005)
- [2] L. Zeng, et al, Plasma Physics Control. Fusion, **46**, A121 (2004)
- [3] G. Wang, et al., Rev. Sci. Instrum. **75**, 3800 (2004).
- [4] G. Wang, et al, proceedings of the 6th International Reflectometry Workshop (2003)
- [5] K.W. Kim et al, Rev. Sci. Instrum. **66**, 1229 (1995)
- [6] G. Wang et al, Rev. Sci. Instrum. **74**, 1525 (2003)

PROFILE REFLECTOMETRY ON MAST

G. Cunningham[†]

T. Edlington[†]

A. Silva[‡]

L. Meneses[‡]

[†]EURATOM/UKAEA Fusion Association, Culham Science Centre, Abingdon, Oxon, OX14 3DB, UK

[‡]Associação EURATOM/IST, Centro de Fusão Nuclear, Instituto Superior Técnico, 1049-001 Lisboa, Portugal

The ‘Mega Ampere Spherical Tokamak’ (MAST), has a typical plasma volume $\simeq 7m^3$ and aspect ratio 1.3 to 1.4. It is equipped with a broad range of diagnostics including a high resolution, single pulse, Ruby laser TS system with 284 radial points, and a lower spatial resolution Nd:YAG system with 19 radial points (presently being upgraded), running at 200Hz. These are complemented by a scanning reflectometer, primarily intended for fast density profile measurement, and technically similar to the one on AUG (Silva [1]), except that there are only 3 channels and they are all on the low field side of the plasma. A schematic drawing of one channel is shown in figure 1, and the specifications are as follows.

| | K band | Ka band | U band |
|--------------------------|-----------|-----------|---------|
| Frequency range (GHz) | 17.6-26.7 | 26.4-40.1 | 39.3-55 |
| Source power (dBm) | +22 | +19 | +12 |
| Detector bandwidth (MHz) | 7 | 20 | 7 |

The characteristic features of this design are that a single antenna is used for transmit and receive, the two signals being split by a 3dB coupler inside the vacuum, and the reference signal comes from an adjustable pin located in the antenna throat. The virtues of this arrangement are that the antenna can be mounted normal to all the flux surfaces (MAST usually runs with up/down symmetric, DND plasmas, and the antennas are on the mid-plane), and that first order reflections from the vacuum windows do not reach the detector.

The RF sources are ‘hyper-abrupt tunable oscillator’ (HTO) type, multiplied up to give a fast sweep over each waveband. In the typical configuration, the sources are swept across their range in $20\mu s$ followed by $5\mu s$ settling time. A burst of about 5 such sweeps is followed by an interval of about 2ms for operation at fixed, though programmable, frequency. The signals are digitised at 50MHz and the fast ADC has enough memory for about 600 sweeps (eg. 120 bursts of 5 sweeps each). In parallel with this ‘fast’ signal acquisition there is a second ‘slow’ channel, having additional gain (with reduced bandwidth), which is digitised at 0.5MHz, for plasma turbulence studies. The HTOs are driven with linear ramps from a waveform generator, itself programmed using GPIB. All the modules are synchronised using a sophisticated programmable pulse generator, and all the data acquisition system apart from the waveform generator is mounted in a single VME crate and controlled using a single-board PC under Linux. The crate is fairly close to the MAST vessel (inside the radiation shield wall), and communicates to the outside world using fibre-optic Ethernet.

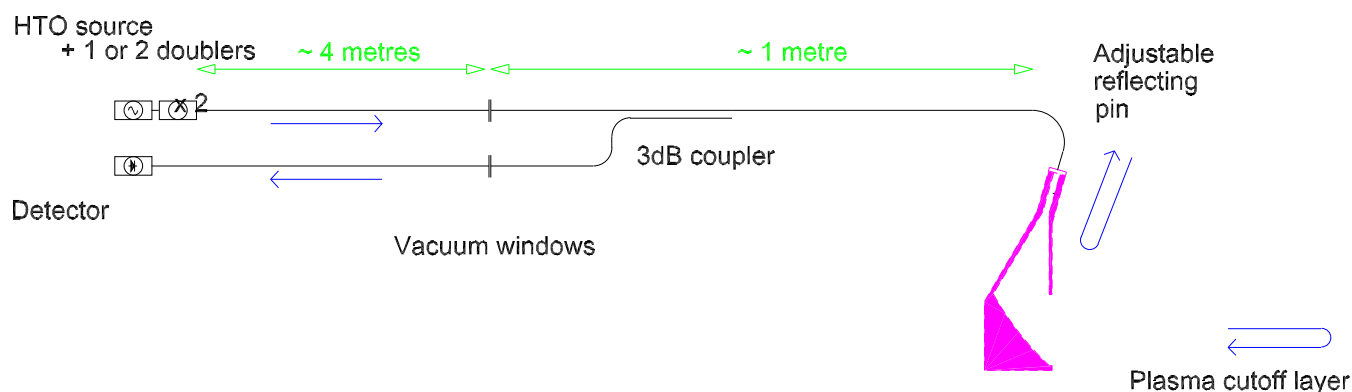


Figure 1: Schematic of the MAST reflectometer (one channel only is shown)

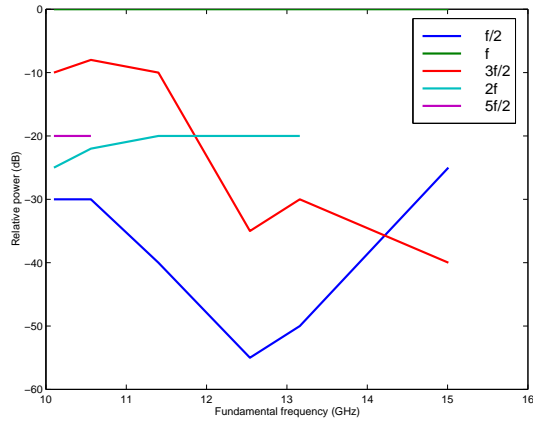


Figure 2: HTO sideband spectra, relative to the fundamental, showing high level of sideband emission. This unit has been replaced.

During the first period of operation of this system it proved impossible to get understandable fringes from the U band channel under any plasma conditions, including ELM-free H mode. At first this was thought to be due to spurious reflections in the waveguides, but after a long investigation this was found not to be the main problem. The actual problem was that the HTO oscillator was generating significant levels of sidebands, especially $\frac{3}{2}f$ in the lower part of the band, which was only -10dB below the fundamental, as can be seen in figure 2. This was enough to cause significant contamination of the fringes. This HTO has now been replaced, although the new one only reaches 13.5GHz so the upper limit of the system is reduced from 60 to 54GHz. It is thought likely that the modulation seen in the lower third of the Ka band, which is more apparent in the analysed data, results from a similar problem although it is less severe.

The reason for the observed decrease in fringe intensity towards the lower end of each frequency band is still unclear. The most likely candidate seems to be losses in the ex-vessel waveguides, and these are presently being replaced in the hope of improving the signal.

Raw signals Inspection of the raw signals (not shown here) shows a number of features:

- The K and Ka band signals are strong though still somewhat variable from sweep to sweep,
- The U band is much weaker and more variable when the plasma is in L mode,
- In an H mode plasma the U band signal is much stronger,
- All 3 channels have weaker signals at the low frequency end of their band than at the high frequency end,
- The lower third of the Ka band shows strong amplitude modulation.

Data reduction - approaching Bayesian analysis

The detected signal is the difference frequency f_d between the two signals, one from the plasma cut-off and the other from the reference pin. The difference arises from the fact that the probe frequency f_p is sweeping, and the difference in the two optical paths, so

$$f_d = \frac{df_p}{dt} \cdot \delta t = \frac{df_p}{dt} \cdot \int \frac{\lambda(x)}{c} dx$$

where δt is the ‘group delay’ and λ is the refractive index.

Thus the main task of data reduction is to measure f_d as accurately as possible and over as short a time scale as possible. In this type of reflectometer there is no ‘intermediate frequency’, so phase detection is not possible, and the number of cycles of f_d (the number of ‘fringes’) is fairly small, typically 20-50 in this case, so it is important to ensure that efficient use is made of the data available. In the past ‘zero crossing’ was used to measure f_d , but in recent years most workers (Varela [2] for example) have progressed to the ‘spectrogram’ method which is preferable in that it uses the entire waveform rather than just the region close to the zero crossing, although it does ignore the phase information.

Spectrograms can be seen in figure 3, upper. It is apparent that (a) there is a certain amount of low frequency noise, and (b) there are some localised artifacts, for example in the U band at about $17\mu s$, 3.8MHz. Both of these can largely be removed by making a similar spectrogram for a plasma-less shot, and subtracting it, as seen in figure 3, lower. Having done this, it is usually adequate to simply take the highest point in each spectrogram slice as the peak.

Now, if our final plasma density profile is to be of value to a physicist, then *it is not enough simply to make a ‘best estimate’ of the density profile*, we must also provide some indication as to how trustworthy this estimate is. In many situations such a confidence estimator can be provided by the estimate of the ‘error’ in the measurement, and this is appropriate when the errors are fairly small, random, and normally distributed. With the data we have here this is clearly not going to be the case - there *are* errors in the ‘best estimate’ but the more serious problem is that the measurement itself is liable to come and go, and to be contaminated by spurious signals. In this case it will be more profitable simply to make an estimate of the ‘confidence level’ for each measurement of $\delta t(f_p)$ in our spectrogram. The best way of calculating this ‘confidence level’ is still under investigation, but at present it is based on the peaked-ness of the peak itself, and the height of the peak compared with the standard deviation in the background.

Such a confidence estimator is also useful in dealing with another situation seen here in the Ka band, where distortion of the signal leads to a substantial second harmonic of f_d in the spectrogram. If such a peak appears at a reasonable confidence level, then its frequency can be used to improve the estimate of the frequency of the fundamental. By these means we are able to

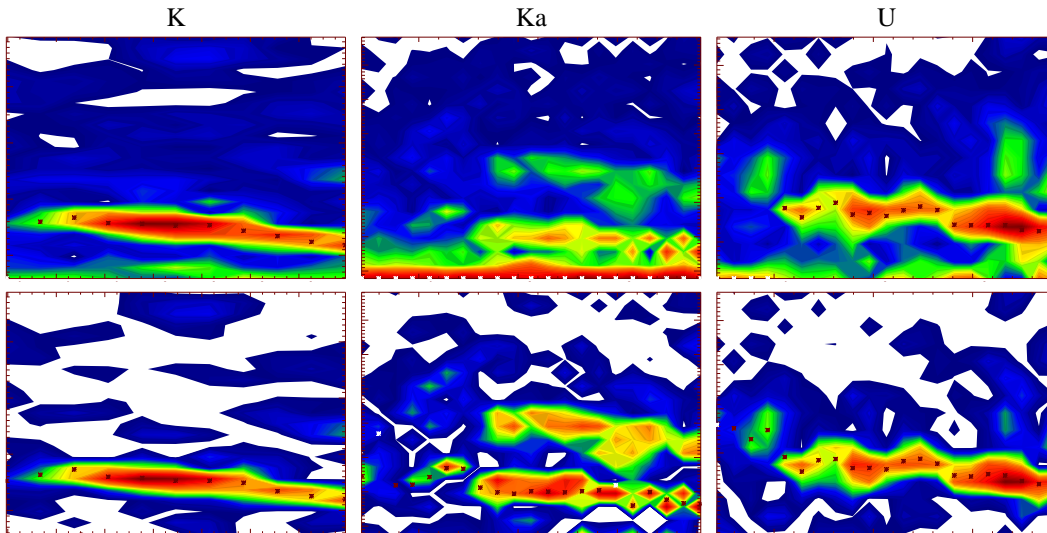


Figure 3: Spectrograms for single sweeps, (upper) before and (lower) after background subtraction. The vertical axis is f_d , the horizontal is time during the sweep.

derive well behaved profiles without having to invoke continuity in either space or time, so that our confidence estimator remains meaningful.

Time resolved profiles. There does remain a problem in that there is no conventional way of displaying ‘confidence’ instead of error bars, so at present we are just omitting measurements which fall below a certain confidence threshold from our final plot. Typical results can be seen in figure 4, this shot has density increasing steadily and enters ELM-free H mode at 0.234s. In the left hand plot all the profiles are shown irrespective of the ‘confidence’ in each data point, while in the right hand plot a cut-off is applied to eliminate data with low confidence. Clearly more work remains to be done as there is still an amount of obviously faulty, spiky, data, but the method is largely successful in eliminating the unreliable data when the cut off layer is far from the antenna, or perhaps non-existent. The rapid steepening of the density profile on entry to H mode is clear, as is the corrupt data in the lower third of the Ka band.

Another set of data which illustrates the fast recording capability of the system is seen at figure 5, which is an H mode shot with ELMs at 0.220, 0.223, 0.226s, etc., these data were recorded with the reflectometer sweeping continuously, the sweeps being grouped into bursts of 4 sweeps each for analysis. In this case the ‘confidence’ level is generally high but falls just at the deepest point of each ELM, nevertheless some good data remain within each ELM. Clearly further study is needed here to determine the optimal confidence indicator and the proper, quantitative, confidence level. In these data there is also apparent a certain consistent ‘ripple’ in the delay with respect to f_p , and this suggests that the calibration needs further attention.

Conclusion

The MAST reflectometer is now in working order and producing useful data especially for H mode plasmas. There remain certain weaknesses especially in the U band signal strength, and these are being addressed at present. With regard to data reduction, it is believed that it is important not only to make a ‘best estimate’ of the time-resolved density profile, but also to indicate the confidence level in that estimate. Initial use of a simplified Bayesian approach to data reduction is proving very powerful and promises to give the confidence indicator required.

Acknowledgements

This work is funded jointly by the UK Engineering and Physical Sciences Research Council and EURATOM. The reflectometer electronics and antennas, and the fast ADC, were built by IST Lisbon.

References

- [1] A. Silva et al. Ultrafast broadband frequency modulation of a CW reflectometry system to measure density profiles on ASDEX upgrade. *Review of Scientific Instruments*, 67(12), 1996.
- [2] P. J. G. Varela. *PhD thesis, Automatic time-frequency analysis for plasma density profile evaluation from microwave reflectometry*. Universidade Tecnica de Lisboa, Instituto Superior Tecnico, 2002.

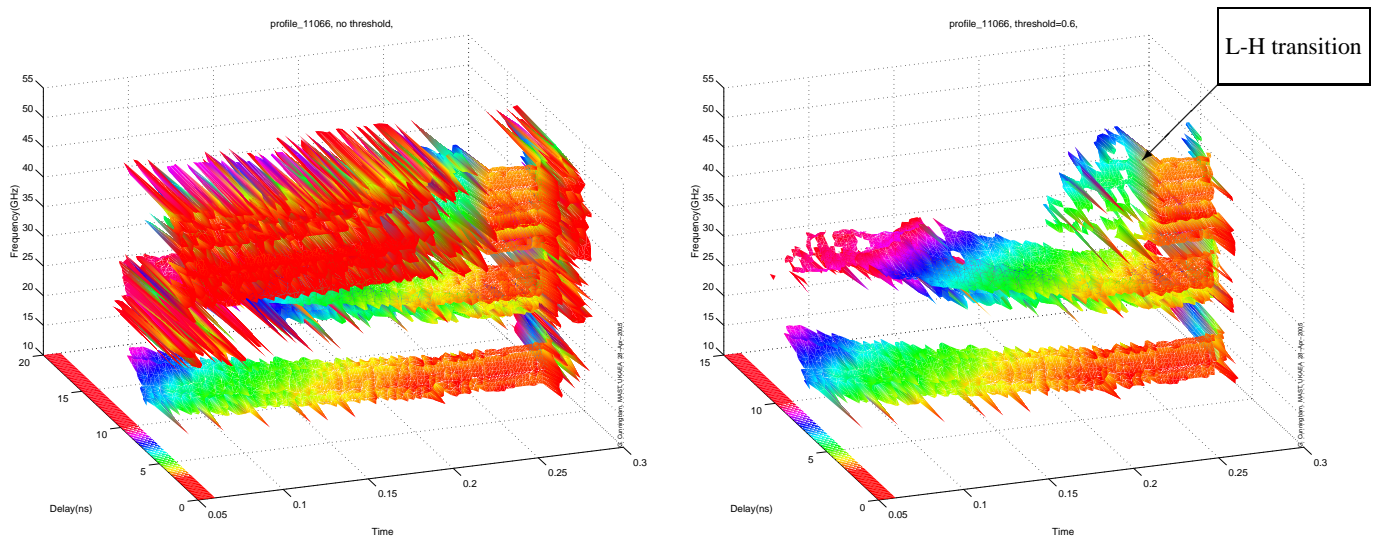


Figure 4: Complete time-resolved profiles (prior to Abel inversion) shown before and after application of a threshold on the ‘confidence’ level. Application of the threshold is largely effective at removing the unreliable data when the cutoff layer is far from the antenna. The surface is coloured by the group delay.

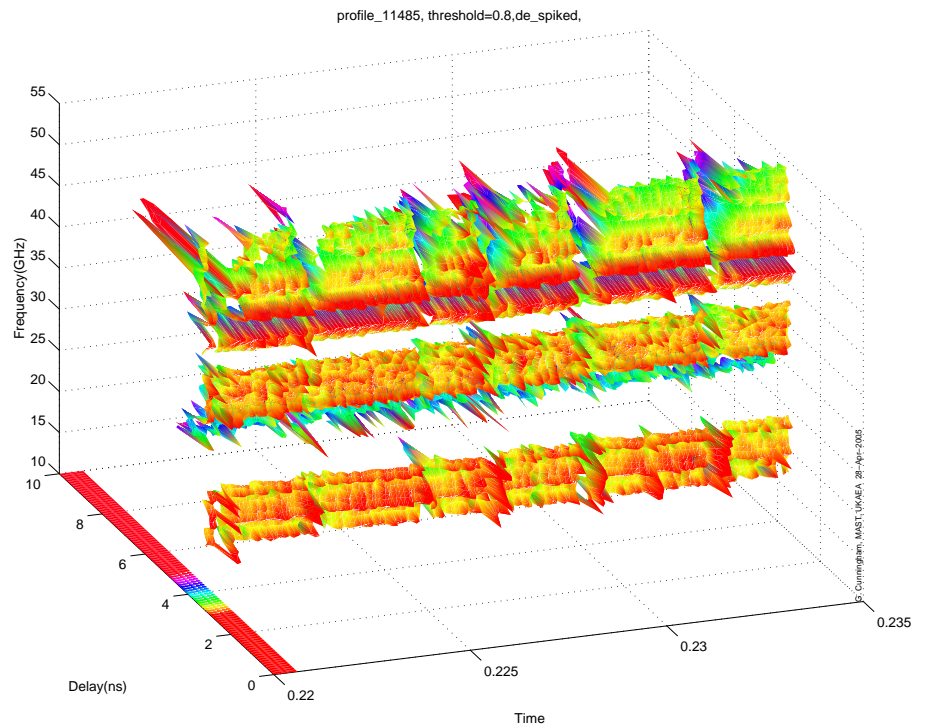


Figure 5: A time-resolved profile for an ELMy H mode discharge recorded by continuous sweeping. The ELMs at 0.220, 0.223, 0.226s etc. are clearly measurable despite the loss of confidence at the deepest point of each ELM.

Measurements localization in Poloidal Correlation Reflectometry

Gusakov E Z, Popov A Yu

Ioffe Institute, St-Petersburg, Russia

Introduction

Poloidal correlation reflectometry (PCR) utilizing microwave plasma probing by several poloidally separated antennae is used nowadays for plasma rotation diagnostics and turbulence analysis [1]. The poloidal rotation velocity (PRV) $V(r)$ is determined in this technique from

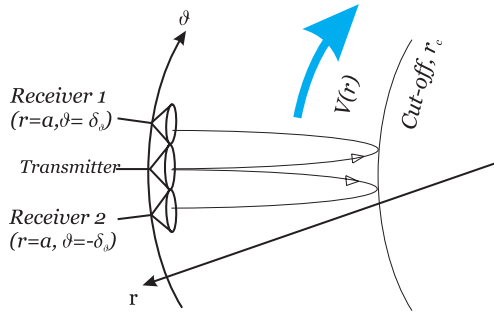


Figure1 Poloidal correlation reflectometry experimental scheme

the temporal shift τ_{cor} of the maximum of the cross correlation function of scattered signals in two poloidally separated channels $V(r_c) = \delta_\theta a / (\tau_{cor} r_c)$ (see Fig1 for the diagnostic scheme and notations used). The localization of measurements and their interpretation is usually based in PCR on the assumption that the microwave scattering off long scale fluctuations dominating in the turbulence spectra occurs in

the cut-off layer. This assumption being correct in respect to backscattering, however fails in the case of small angle scattering or forward scattering, which is possible all over the probing wave trajectory. In spite of the fact the forward scattering is enhanced in the vicinity of cut off [2], this localization is not sufficient to guarantee the suppression of the volume contribution to the PCR signal for all density profiles. In the present paper the localization of PCR is treated analytically for arbitrary density and turbulence profiles. The 3D WKB approach is used to calculate the reflectometry signal and cross correlation function in cylindrical geometry for Gaussian turbulence spectrum and accounting for the diffraction effects.

General approach

The analysis is performed in the cylindrical geometry taking into account the curvature effects. The 1D background plasma density $n_0(r)$ distribution is assumed. The density fluctuations $\delta n(\vec{r}, t) = n(\vec{r}, t) - n_0(r)$, characterized by the correlation function

$$\langle \delta n(\vec{r}, t) \delta n(\vec{r}', t') \rangle = \delta n^2(R) \cdot \exp \left[-\frac{(r-r')^2}{l_{cr}^2} - \frac{((\theta-\theta')a - V(R)\tau)^2}{l_{c\theta}^2} \right],$$

where $\vec{r} = (r, \vartheta, z)$, $R = r + r'/2$, $\tau = t - t'$, are supposed small, satisfying the Born approximation, whereas the turbulence radial correlation length satisfies condition $l_{cr} > (c^2(a - r_c)/\omega^2)^{1/3}$, allowing to neglect backscattering far from the cut off. Under above assumptions the incident O mode wave field in plasma can be represented as a superposition of WKB modes propagating at different angles. In particular, at the receiving antennae with the accuracy to the first order in density perturbation amplitude one obtains the following expression for the reflected wave:

$$E(\vartheta, z, t) = \frac{1}{(2\pi)^2} \sum_m \int \tilde{E} \exp(i\phi_r(m, k_z, t)) dk_z$$

with $\phi_r(m, k_z, t)$ being WKB phase consisting of the unperturbed term $\varphi_0(m, k_z, t)$ given in paraxial approximation by the expression

$$\varphi_0(m, k_z, t) = 2 \int_a^{r_c} k(r) dr' + m^2 d_\vartheta^2(0)/2a^2 + k_z^2 d_z^2(0)/2 + m\vartheta + k_z z - \frac{\pi}{2},$$

where $k(r) = \frac{\omega}{c} \sqrt{1 - n(r)/n_c}$, $d_\vartheta^2(r) = 2 \int_r^{r_c} \frac{a^2}{r'^2} \frac{dr'}{k(r')}$ and $d_z^2(r) = \frac{2c^2}{\omega^2} \int_r^{r_c} k(r') dr'$, $n_c = n_0(r_c)$

and the phase perturbation

$$\delta\varphi = -\frac{\omega^2}{2c^2} \cdot \left(\int_a^{r_c} \frac{\delta n(r', \theta^-(r'), z^-(r'), t)}{n_c} \frac{dr'}{k(r')} + \int_a^{r_c} \frac{\delta n(r', \theta^+(r'), z^+(r'), t)}{n_c} \frac{dr'}{k(r')} \right)$$

calculated along the unperturbed trajectory that comes to the point (ϑ, z) and is given by relations $\theta^\pm = \vartheta - m [d_\vartheta^2(0) \pm d_\vartheta^2(r)]/2a^2$, $z^\pm = z - k_z [d_z^2(0) \pm d_z^2(r)]/2$. The upper and lower signs in the above equations correspond to the parts of the ray trajectory after and before the reflection from the cut off surface. Both the probing and the receiving antennae beams are assumed to be Gaussian with equal the poloidal and toroidal width

$$E_0(\vartheta, z) = \sqrt{\frac{a}{\pi\rho^2}} \exp\left(-\frac{a^2\vartheta^2}{2\rho^2} - \frac{z^2}{2\rho^2}\right) = 2\sqrt{\frac{\pi\rho^2}{a}} \int \frac{dm}{2\pi} \frac{dk_z}{2\pi} \exp\left(-\frac{m^2\rho^2}{2a^2} - \frac{k_z^2\rho^2}{2}\right).$$

The expression for the scattering power in the standard reflectometer case can be represented as

$$P_s = P_i \frac{\omega^4 l_{cr}}{c^4} \frac{\int_a^{r_c} \frac{\delta n^2[r]}{n_c^2} \frac{dr}{Q^2(r)}}{\sqrt{1 + \frac{d_z^4(0)}{4\rho^4}} \sqrt{1 + \frac{d_\vartheta^4(0)}{4\rho^4}} \sqrt{1 + \frac{2\rho_g^2}{l_{c9}^2}}} \quad (1)$$

where P_i is a probing power and the scattering efficiency $1/Q^2(r)$ takes an explicit form

$$\frac{1}{Q^2(r)} = \begin{cases} \frac{1}{k^2(r)}, & r - r_c \gg l_{cr} \\ \left[\frac{c^2}{\omega^2} \frac{\sqrt{\pi} \tilde{L}_n}{l_{cr}} \exp\left(-\frac{(r-r_c)^2}{2l_{cr}^2}\right) I_0\left(\frac{(r-r_c)^2}{2l_{cr}^2}\right) \right], & r - r_c \leq l_{cr}, L = \left(\frac{d \ln n_0}{dr}\right)_{r=r_c}^{-1} \end{cases} \quad (2)$$

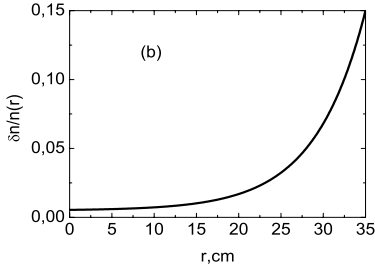
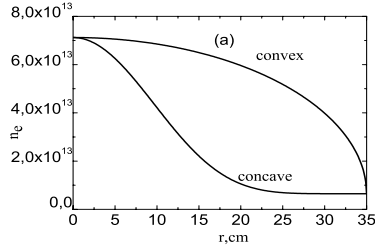


Figure 2 (a) background density profiles (convex and concave); (b) density fluctuation level profile

It increases as $1/k^2(r)$ in the cut off vicinity, however this singularity is a weak one and does not provide the only input to the integral. In the case of linear density profile and homogeneous turbulence this so called logarithmic singularity results in substantial contribution of the plasma volume to the signal (1). In this case the scattered signal is related to the density perturbation by the following simple expression

$$\delta n(r_c) = n_c \sqrt{\frac{P_s}{P_i}} \left[\frac{\sqrt{\pi} l_{cr} L_n \left[\ln\left(\frac{8L_n}{\pi l_{cr}}\right) + 0.71 \right]}{\sqrt{1 + \frac{d_g^4(a)}{4\rho^4}} \sqrt{1 + \frac{d_z^4(a)}{4\rho^4}} \sqrt{1 + \frac{2\rho^2}{l_{cg}^2}}} \frac{\omega^2}{c^2} \right]^{-1/2} \quad (3)$$

which can be used for reconstruction of turbulence distribution from the fluctuation reflectometry data. This

expression accounts for the contribution of the plasma volume to the signal, however neglects the density profile nonlinearities and turbulence inhomogeneity, which can be very strong at the edge. Relation

(3) is used below in figure 3 for reconstruction of the turbulence distribution from measurements performed at variable probing frequency in the case of plasma

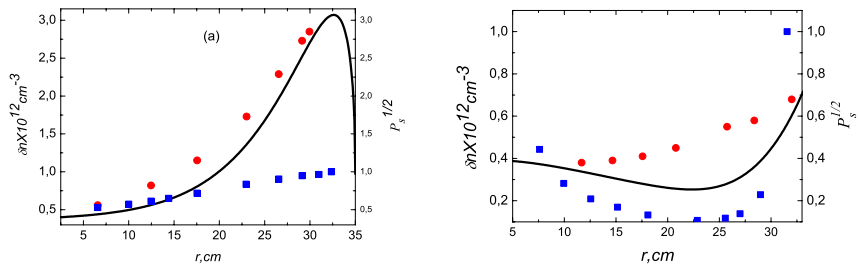


Figure 3 Density fluctuation reconstruction (solid line – original turbulence distribution, blue squares – reflectometry signal, red circles –according to (3)). (a) the case of convex density profile; (b) the case of concave density profile.

density and turbulence profiles shown in figure 2. The following values of correlation length and geometric parameters were used: $l_{cr} = 1\text{ cm}$, $l_{cg} = 2\text{ cm}$, $\rho = 1\text{ cm}$, $a\delta_g = 2\text{ cm}$. As it is seen

in figure 3, the fluctuation reflectometry signal dependence on the cut off position (blue points) does not give an adequate approximation for the turbulence distribution for both profiles. On contrary, expression (3) in the case of concave profile provides a fairly good reconstruction of the turbulence in wide spatial zone. In the case of convex density profile the reconstruction is less perfect, however it can be used as a zero order approximation for the iteration procedure based on (1).

The CCF of two signals can be obtained explicitly as

$$CCF_{12}(\tau) \approx \frac{P_i}{\sqrt{P_{s1}P_{s2}}} \frac{\sqrt{\pi}l_{cr}}{\sqrt{1+\frac{d_g^4(0)}{4\rho^4}} \sqrt{1+\frac{d_z^4(0)}{4\rho^4}}} \frac{\omega^4}{4c^4} \int_{r_c}^a \frac{dr}{Q^2(r)} \frac{\delta n^2(r)}{n_c^2} (S_{12}^{++} + S_{12}^{--} + 2S_{12}^{+-}), \quad (4)$$

where $S_{12}^{++}(r, \tau) + S_{12}^{--}(r, \tau)$ and $2S_{12}^{+-}(r, \tau)$ are the contributions of different (incident-incident, reflected-reflected and incident-reflected) branches of two rays trajectories to the correlation function. These contributions are expressed in terms of elementary functions, in particular

$$S_{12}^{+-} = \frac{\frac{l_{c,g}}{\rho_g} \exp\left\{-\frac{2\delta_g^2 \rho_g^2}{4\rho_g^4 + d_g^4(a)}\right\}}{\sqrt{1 + \frac{l_{c,g}^2}{2\rho_g^2} + \frac{d_g^4(r)}{4\rho_g^4 \left(1 + \frac{d_g^4(a)}{4\rho_g^4}\right)}} \exp\left\{\frac{\left(r\delta_g \left[1 + \frac{d_g^4(r)d_g^4(a)}{4\rho_g^4 \left(1 + \frac{d_g^4(a)}{4\rho_g^4}\right)}\right] - V(r)\tau\right)^2}{2\rho_g^2 \left(1 + \frac{l_{c,g}^2}{2\rho_g^2} + \frac{d_g^4(r)}{4\rho_g^4 \left(1 + \frac{d_g^4(a)}{4\rho_g^4}\right)}\right)}\right\} \quad (5)$$

As it is pointed out by (4) the scattering efficiency (2) enters the CCF expression, thus providing some cut off localisation to the PRV measurements. However, as in the case of the

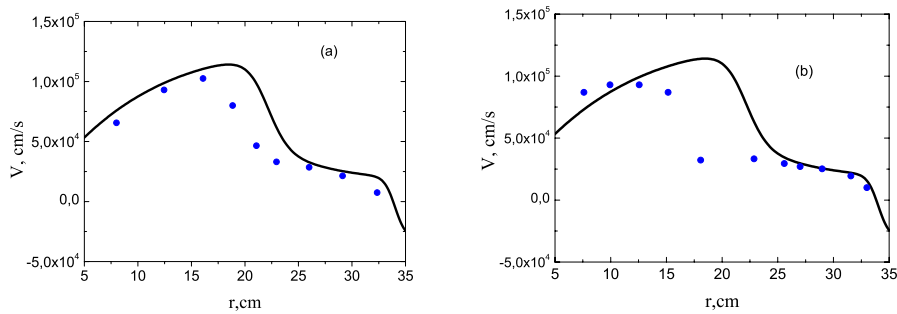


Figure 4 Velocity profile reconstruction (solid line – original profile, circles - profile extracted from PCR; (a) and (b) – correspond to convex and concave density profiles).

reflectometry signal, it does not suppress completely the volume contribution, which can, in principle, decrease the locality of the PCR technique. An example of velocity profile reconstruction from the PCR data for density profiles of fig.2 are shown in figure 4. As it is seen there, reconstruction of the velocity profile from PCR data under cut off localisation assumption is more reliable in the case of convex profile, however even in this case the localisation of strong velocity shear region is not perfect. A more reliable velocity profile can be obtained from the PCR experimental data as a result of iteration procedure based on (4) and (5).

Conclusions

Simple explicit analytical expressions for the poloidal correlation reflectometry signal and cross correlation function accounting for probing wave diffraction in realistic 3D experimental geometry are given for arbitrary plasma density and turbulence profiles. It is shown that the reflectometry signal and turbulence spatial distributions can be very different. The simple method for the density perturbation reconstruction from the experimental data is proposed, however it is shown that for the concave density profile its accuracy decreases. The accuracy of simplified method of poloidal velocity determination from the PCR data can be as well affected by contribution of the plasma volume to the reflectometry signal for some density profiles and velocity distributions. The obtained explicit expressions for the PCR characteristics provide the effective theoretical tool for determination of the turbulence level and velocity distribution from the experimental data for arbitrary density profiles.

The work was supported by RFBR grant 04-02-16534; NWO-RFBR grants 047.016.015, Scientific School grant 2159.2003.2 and INTAS grants INTAS-01-2056.

References

1. V.A. Vershkov, S.V. Soldatov, D.A. Shelukhin et al. (2003) *Proc. 30th Conf. Control. Fusion Plasma Phys.* **ECA 27A** P-2.56
2. E.Z.Gusakov, A.V. Surkov (2004) *Plasma Phys. Control. Fusion* **46** 1143–1162

2D full wave simulation of poloidal and radial sensitivity of reflectometer and estimation of density fluctuations absolute level.

D.A. Shelukhin, V.A. Vershkov, S.V. Soldatov, A.O. Urazbaev

Nuclear Fusion Institute, Russian Research Center “Kurchatov Institute”, Moscow, Russia

I. Introduction

A lot of attention is devoted to the investigations of plasma transport now. Recent theories claim the turbulent transport as the reason of an anomalous transport in tokamak plasma. The main instabilities that should be the responsible for the transport in plasma core are Ion Temperature Gradient (ITG) instability¹ and Dissipative Trapped Electron Mode (DTEM)². The character poloidal wave numbers for these instabilities are $k_{\perp} \times \rho_i \sim 1$ that give the character poloidal size of instabilities about 1 cm.

It was shown experimentally that reflectometry is a very sensitive to small-scale perturbations of plasma density³. Application of the correlation reflectometry technique allows to measure of character size of turbulence and its velocity. Yet non-locality of reflectometry measurements significantly complicates the interpretation of results.

This paper devoted to attempts to reveal the possibility of using reflectometry as a diagnostic for the measurements of the local parameters of density fluctuations. It became possible with the development of analytical methods as well as 2D full wave codes. The first part of the paper dealing with the 2D simulation of the O-mode reflectometry measurements in real T-10 experiments geometry and the rest of the paper related to the comparison of results of simulations with full wave codes and analytical approaches. The obtained results are discussed in conclusions.

II. 2D full wave simulation of reflectometry measurements.

One of the most important topics in reflectometry simulation is the set of perturbed density field. It was used the model proposed for the simulation of reflectometry at plasma periphery⁴. Due to this approach, the stochastic density field is calculated as:

$$\tilde{n}_e(r, \phi, t) = \langle n_e(r, \phi) \rangle + \sum \delta n_e(r, \phi, t) \quad (\text{II.1})$$

where r is the minor radius, ϕ – poloidal angle and t – time. The first term corresponds to the time-averaged density profile, the second one – to density perturbations. The density perturbations are given by superposition of stochastically independent fluctuations:

$$\delta n_e(r, \phi, t) = n_0 \times T(t) \times R(r) \times \Phi(\phi, t) \quad (\text{II.2})$$

$$T(t) = \left(\exp\left(-\frac{(t-t_0)}{t_{\text{decay}}}\right) - \exp\left(-\frac{(t-t_0)}{t_{\text{rise}}}\right) \right) \times H(t-t_0) \quad (\text{II.2.1}) \quad R(r) = \exp\left(-\left(\frac{(r-r_0)}{\Delta_r}\right)^2\right) \quad (\text{II.2.2})$$

$$\Phi(\phi, t) = \exp\left(-\left(\frac{(\phi - (\phi_0 + \Omega_{\perp} \cdot (t-t_0))) \cdot r_0}{\Delta_{\perp}}\right)^2\right) \times (a + b \cdot \cos(k_{\perp} \cdot (\phi - (\phi_0 + \Omega_{\perp} \cdot (t-t_0))) \cdot r_0)) \quad (\text{II.2.3})$$

The first term is the amplitude of single perturbation, second one is time evolution of single perturbation, third and fourth – radial and poloidal shapes of perturbations. The perturbation is appears in time moment t_0 with center situated at position r_0 , ϕ_0 , and has character time of rise t_{rise} and decay t_{decay} . Character radial and poloidal size are characterized by Gaussian width Δ_r and Δ_{\perp} . Plasma supposed to rotate in poloidal direction with angular velocity Ω_{\perp} . Coefficients a and b give relative amplitudes of Broad Band (BB) and Quasi Coherent (QC) oscillations amplitude in spectra respectively. The poloidal wave number for QC fluctuations is k_{\perp} . Values of perturbation parameters were chosen close to the experimental ones and varied along the minor radius.

| Parameter | Simulation | Expression | Estimation |
|-----------------------|-------------------------|--|------------|
| Δ_r^{BB} | 0.7 cm | $\Delta_r^{BB} \approx \Delta_r^{QC} / 3$ | - |
| Δ_{\perp}^{BB} | 0.7 cm | $\Delta_{\perp}^{BB} = 2 / \Delta(Y_{2D}^{BB}(k_{\perp}))$ | 0.61 cm |
| Δ_r^{QC} | 0.7 cm | $\Delta_r^{QC} \approx \lambda_{\perp}^0 / 3\sqrt{2}$ | - |
| Δ_{\perp}^{QC} | 4.0 cm | $\Delta_{\perp}^{QC} = 2 / \Delta(Y_{2D}^{QC}(k_{\perp} - k_{\perp}^0))$ | 3.8 cm |
| λ_{\perp}^0 | 2.1 cm | $\lambda_{\perp}^0 = 2\pi / k_{\perp}^0$ | 2.1 cm |
| v | 2.46×10^5 cm/s | $v = \Delta x / \Delta \tau$ | - |
| μ | - | (III.7) | 0.35 |
| σ_n/n | 0.75 % | (III.10) | 0.81 % |

Table 1. Character parameters of turbulence at the reflection radius in 2D full wave simulations, expressions used in estimations of these parameters from experimental signal spectra and values parameters estimated from simulated specter

reflectometry frequency $F = 37$ GHz that corresponds to reflection at normalized minor radius $\rho = 0.65$, character length of plasma permittivity profile $L_e = (d(\ln(n_e))/dr)^{-1} = 16$ cm, fraction of QC oscillation was 15 %, the turbulence parameters are shown in Table 1.

Locality of reflectometry was characterized by the cross-correlation coefficient between received electric field vector $\tilde{E}(t)$ and perturbed local density:

$$\gamma(r, \varphi) = \frac{\langle \tilde{E}(t) \times \tilde{n}_e(r, \varphi, t) \rangle}{\langle \tilde{E}(t) \rangle \times \langle \tilde{n}_e(r, \varphi, t) \rangle} \quad (\text{II.4})$$

The contour plots of this coefficient, calculated for all three poloidally separated antennas, are shown in Figure 1. The confidence level is 0.06% and determined by a limited length of data sequences. One should note that coherency maxima are laid at the reflection radius, shown by the horizontal black lines. The poloidal positions of coherency maxima are in good agreement with the positions of reflection spots for all three horns (black vertical lines). This means that reflectometry measurements have a good locality in both radial and poloidal directions and could allow providing the fluctuations size and velocity measurements.

The experimental radial correlation function is shown on Figure 2 a. The measurements was made in T-10 tokamak, discharge parameters were $I_p = 155$ kA, $B_T = 2.0$ T, $\langle n_e \rangle = 2.5 \times 10^{19} \text{ m}^{-3}$, reflection occurred at $\rho = 0.65$. The radial correlation reflectometry

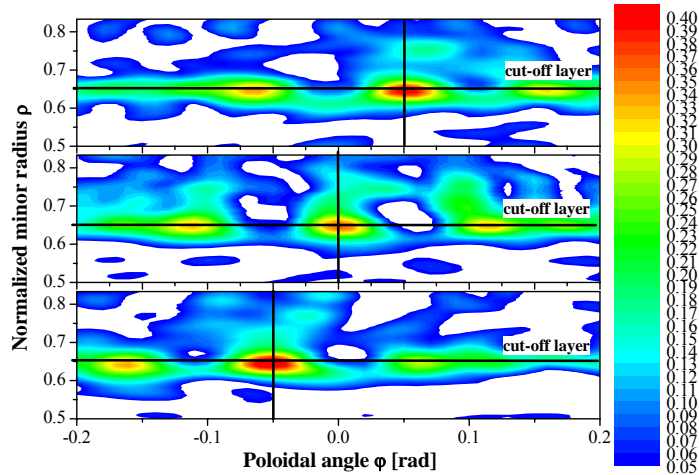


Figure 1. Contour plots of correlation coefficient between scattered electric field and local density.

This stochastic plasma density field was re-calculated in plasma permittivity field that was used in full wave simulation. High effective 2D full wave electromagnetic code Tamic Rτ Analyzer was used to calculate the propagation and scattering of electromagnetic waves from plasma⁵. The T-10 plasma and antenna array geometry were used in simulations. Electromagnetic wave launched from the central horn and reflected signals from all three poloidally separated horns were analyzed.

The most of simulations were made using the following parameters:

reflectometry frequency $F = 37$ GHz that corresponds to reflection at normalized minor radius $\rho = 0.65$, character length of plasma permittivity profile $L_e = (d(\ln(n_e))/dr)^{-1} = 16$ cm, fraction of QC oscillation was 15 %, the turbulence parameters are shown in Table 1.

Locality of reflectometry was characterized by the cross-correlation coefficient between received electric field vector $\tilde{E}(t)$ and perturbed local density:

$$\gamma(r, \varphi) = \frac{\langle \tilde{E}(t) \times \tilde{n}_e(r, \varphi, t) \rangle}{\langle \tilde{E}(t) \rangle \times \langle \tilde{n}_e(r, \varphi, t) \rangle} \quad (\text{II.4})$$

The contour plots of this coefficient, calculated for all three poloidally separated antennas, are shown in Figure 1. The confidence level is 0.06% and determined by a limited length of data sequences. One should note that coherency maxima are laid at the reflection radius, shown by the horizontal black lines. The poloidal positions of coherency maxima are in good agreement with the positions of reflection spots for all three horns (black vertical lines). This means that reflectometry measurements have a good locality in both radial and poloidal directions and could allow providing the fluctuations size and velocity measurements.

The experimental radial correlation function is shown on Figure 2 a. The measurements was made in T-10 tokamak, discharge parameters were $I_p = 155$ kA, $B_T = 2.0$ T, $\langle n_e \rangle = 2.5 \times 10^{19} \text{ m}^{-3}$, reflection occurred at $\rho = 0.65$. The radial correlation reflectometry

technique was obtained by simulation of wave propagation at the different probing frequencies on the same turbulent density field. Turbulence properties were as shown in Table 1, except only BB fluctuations were used. The results are shown in Figure 2 b) as red points and approximating curve. Radial cross-correlation function of density perturbation at the reflection radius is shown on the same plot as green curve. The parameters of turbulence were used to compare the experimental

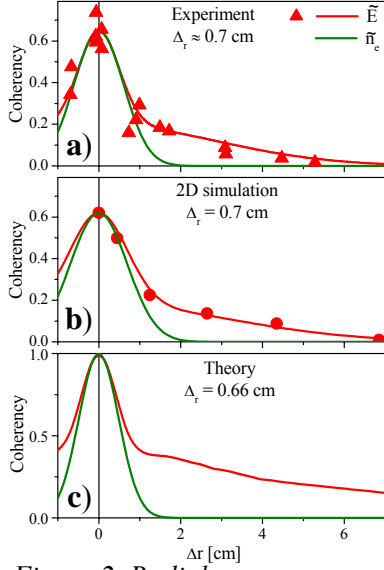


Figure 2. Radial cross-correlation functions of reflectometry signals obtained in experiment (a), due to results of 2D simulation (b) and theoretical predictions (c).

results with analytic estimations⁶. Radial cross-correlation function was calculated to using the same turbulence parameters as in 2D simulation (Figure 2 c).

It is clearly seen that experimental, simulated and theoretical radial cross-correlation functions of reflectometry signals are in reasonable coincidence. Each function contains some core that presents the cross-correlation function of a density perturbations and long tail that arise from small angle scattering. Both simulation and theory justify the fact that reflectometry has a good radial locality and could give estimation of perturbation radial size.

Other important topic is the turbulence spectra measurements. Size of reflection spot could significantly exceed the fluctuations size. It could lead to decrease of reflectometry sensitivity to perturbations with small spatial size. Typical experimental spectra in T-10 discharge is shown in Figure 3 a. The parameters was $I_p=200\text{kA}$, $B_T=2.5\text{ T}$, $\langle n_e \rangle = 2 \times 10^{19}\text{ m}^{-3}$, reflection occurred at $\rho=0.65$. One could see that spectra has a complex structure and contains Low Frequency (LF) and QC oscillations maxima that are superimposed on BB background.

First simulation run was made using BB turbulence only (Fig. 3 b). The simulated spectra of the reflected signal (red) and spectra of density fluctuations at the reflection radius (green) are in good agreement. This leads to conclusion that at least for BB oscillations reflectometry sensitivity is not important for interpretation of measurement results.

Second run used both BB and QC perturbation in random density field (Fig. 3 c). It is clearly seen that contrast of QC fluctuation peaks is significantly higher in spectra of local density rather than in spectra of reflected signal. Therefore, reflectometry has a limited sensitivity to QC oscillations and this fact should be taken into account in data processing.

Simulation of the poloidal correlation properties of turbulence shows that not only experimental and simulated turbulence spectra but also poloidal cross-phase and poloidal coherence are in good quantitative and qualitative agreement. It should be especially note that the slope poloidal velocity calculated from slopes of experimental and simulated cross-phase are coincide with the poloidal velocity of turbulence at the reflection radius. This leads to conclusion that estimation of poloidal velocity using the poloidal correlation could give the correct results.

III. Estimation of the relative amplitude of density perturbations

The results of 2D simulation of reflectometry showed that reflectometry has a rather good radial locality and sensitivity to perturbations with character sizes that are predicted for ITG and DTEM. It is possible to reconstruct the density fluctuations level at reflection point.

The simplest case will be considered. Let us suppose that O-mode reflectometry signal reflected from

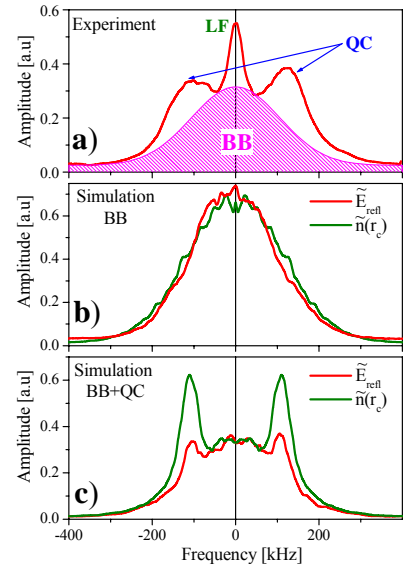


Figure 3. Experimental specter of reflectometry signal (a). Spectra of simulated signals (red) and local densities (green) in the case of pure BB (b) and BB and QC (c) oscillations.

the plasma with linear density and plasma permittivity profile with character length L_ε . It was shown that in 1D geometric optics approach spectral power of radial correlation function of density perturbation Γ_n and signal phase Γ_ϕ are related by the following equation⁷:

$$\Gamma_\phi(k_r) = 2\pi \frac{k_0^2 L_\varepsilon}{|k_r|} [C^2(w) + S^2(w)] \Gamma_n(k_r) \quad (\text{III.1})$$

where $k_0 = 2\pi/\lambda_0$ is the wave number of incident electromagnetic wave, $C(w)$ and $S(w)$ – Fresnel integrals⁸ and $w = \sqrt{2|k_r|L_\varepsilon}/\pi$. In

a case of Gaussian, radial shape of perturbation the power spectrum of radial correlation function has a Gaussian form with character width $\Delta_r^{cor} = \Delta_r \times \sqrt{2}$. Integration of both part of equation (III.1) using Gaussian spectra form leads to the following relation between the amplitude of phase fluctuation σ_ϕ and relative amplitude of density perturbations σ_n/n :

$$\sigma_\phi = \left\langle |\tilde{\phi}|^2 \right\rangle^{1/2} = 4\pi K_1 \left(\frac{\Delta_r^{cor}}{L_\varepsilon} \right) \frac{\sqrt{L_\varepsilon \Delta_r^{cor}}}{\lambda_0} \frac{\sigma_n}{n_{cr}} \quad (\text{III.2})$$

Coefficient K_1 is of order of unity and depends only on the ration of character size of turbulence and permittivity profile length. Numerical integration was used in a wide range of parameter to obtain the following approximation:

$$K_1 \left(\frac{\Delta_r^{cor}}{L_\varepsilon} \right) = \sqrt{\int_0^\infty \frac{[C^2(w) + S^2(w)]}{w} \exp\left(-\frac{\pi^2 w^4}{16} \left(\frac{\Delta_r^{cor}}{L_\varepsilon}\right)^2\right) dw} \approx \sqrt{0.25 \ln\left(\frac{L_\varepsilon}{\Delta_r^{cor}}\right) + 0.58} \quad (\text{III.3})$$

This approximation is similar to derived analytically, but numerical coefficient are different.

1D full wave simulation was used to verify derived expressions. Density perturbations had uniform distribution with $\sigma_n/n = 0.5\%$. The results are presented in Figure 4 as a comparison of the phase perturbation of simulated signal with the theory predictions. One could see that in a case of weak turbulence with uniform distribution 1D geometric optics approach could give a good estimation of the perturbation amplitude at reflection radius.

The estimation of reflectometry sensitivity to perturbations with high poloidal wave number k_\perp could be made using phase screen model⁹. The perturbations of density at the reflection surface are considered in this case as a perturbation of electric field on a phase screen, situated at effective optical distance from launched and receiving horns d . Let us suppose that plasma has a poloidal cross-section with center in origin of coordinates, incident beam has a Gaussian distribution of electric field with effective size w and front curvature of beam when it incident on plasma is r_b . If plasma permittivity profile is linear and horns situated in horizontal plane at z_0 , the distance from horns to phase screen is equal $d = (z_0 - r_s) + L_\varepsilon$, where r_s is the radius of reflection surface. Electric field in this case has a following distribution on the phase screen:

$$E_s(\xi) = \frac{1}{\sqrt{2\pi}w} \exp\left(-\frac{\xi^2}{2w^2}\right) \times \exp\left(\frac{ik_0\xi^2}{\rho_{eff}}\right) \times \exp[i\sqrt{2}\sigma_\phi \cos(k_\perp\xi + \theta)] \times \left(1 - 2\frac{\xi^2}{\rho_{max}^2}\right) \quad (\text{III.4})$$

$$\rho_{eff} = \left(\frac{\rho_b}{(\rho_b + L_\varepsilon)^2} + \frac{1}{\rho_s}\right)^{-1} \quad (\text{III.4.1})$$

$$\rho_{max} = \left(\frac{1}{\rho_c} + \frac{1}{\rho_b + L_\varepsilon}\right)^{-1} \quad (\text{III.4.2})$$

The first term is the distribution of the electric field in incident beam, second one arises from the curvature of the plasma surface and beam front, third one is the modulation of electric

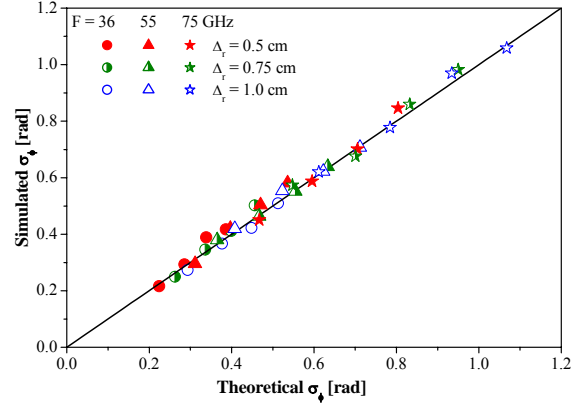


Figure 4. Comparison of simulated phase perturbations with theory predicted

field by the harmonic density perturbations and last one is the attenuation of the field due to oblique incidence on the reflection surface. The electric field in receiving horn can be calculated using Fresnel-Huygens formula. In weak turbulence regime with $\sigma_\phi \ll 1$ and $k_\perp \ll k_0$ after averaging over $-\pi < \theta < \pi$, the estimated relative perturbation of electric field in receiving horn is give by the following integral:

$$\frac{\sigma_{2D}(k_\perp)}{\sigma_{2D}(0)} = F_{12}(k_\perp) = \int_{-\frac{\rho_{\max}}{\sqrt{2}}}^{\frac{\rho_{\max}}{\sqrt{2}}} \frac{1}{\sqrt{2\pi w}} \exp\left(-\frac{\xi^2}{2w^2}\right) \times \exp\left(\frac{ik_0\xi^2}{\rho_{\text{eff}}}\right) \times \cos(k_\perp\xi) \times \exp\left(\frac{ik_0\xi^2}{2d}\right) \times \left(1 - 2\frac{\xi^2}{\rho_{\max}^2}\right) d\xi \quad (\text{III.5})$$

We take into account also that in small k_\perp limit perturbation of electric field tends to the value of phase perturbation in 1D approach. If the radius of the reflection surface significantly exceeds the beam width and $L_\varepsilon \rightarrow 0$, equation resulted in analytical estimation.

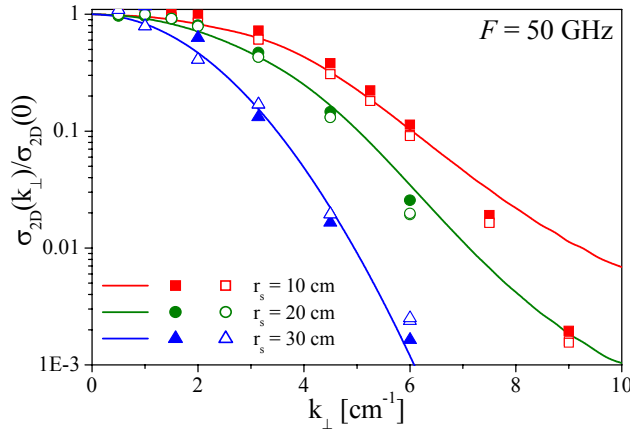


Figure 5. Reflectometer sensitivity to density perturbations according to 2D simulation (points) and phase screen model (curves)

frequency spectra could be re-calculated in k_\perp spectra (Fig. 6). Using the perturbation shape (II.2.3) it is possible to estimate the character spatial size of turbulence (Tab. 1). The experimental specter (black) in this case can be presented as a sum of statistically independent QC (red) and BB (green) components:

$$Y_{2D}(k_\perp) = \sqrt{(1 - \mu)Y_{2D}^{BB}(k_\perp)^2 + \mu Y_{2D}^{QC}(k_\perp)^2} \quad (\text{III.6})$$

where μ is the effective fraction of QC in signal. The value of μ could be estimated as:

$$\mu = \frac{\kappa^2}{1 + \kappa^2} \quad (\text{III.7.1}) \quad \kappa = 2 \frac{\Delta_\perp^{BB}}{\Delta_\perp^{QC}} \frac{Y_{2D}^{QC}(k_\perp^{\max})}{F_{12}(k_\perp^{\max})Y_{2D}^{BB}(0)} \quad (\text{III.7.2})$$

where $Y_{2D}^{QC}(k_\perp^{\max})$ and $Y_{2D}^{BB}(0)$ are the amplitudes of QC and BB components in spectra. If Y_{2D} is the experimental specter of turbulence and Y_{1D} is specter in a limit of infinite probing frequency, they are related as:

$$Y_{2D}(k_\perp) = Y_{1D}(k_\perp) \cdot F_{12}(k_\perp) \quad (\text{III.8})$$

The effective correction for limited reflectometer sensitivity calculated as follows:

$$K_2 = \sqrt{\frac{\int_{-\infty}^{\infty} Y_{1D}(k_\perp)^2 dk_\perp}{\int_{-\infty}^{\infty} (Y_{1D}(k_\perp) \cdot F_{12}(k_\perp))^2 dk_\perp}} \quad (\text{III.9})$$

The level of density perturbations is estimated according to (III.2) taking into account the different radial scale length of BB and QC oscillations. In a case of statistically independent fluctuations, it leads to following equations:

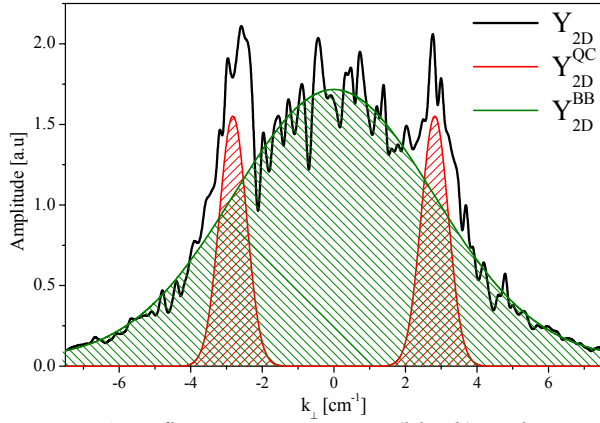


Figure 6. Reflectometer spectra (black) and its BB (green) and QC components (red)

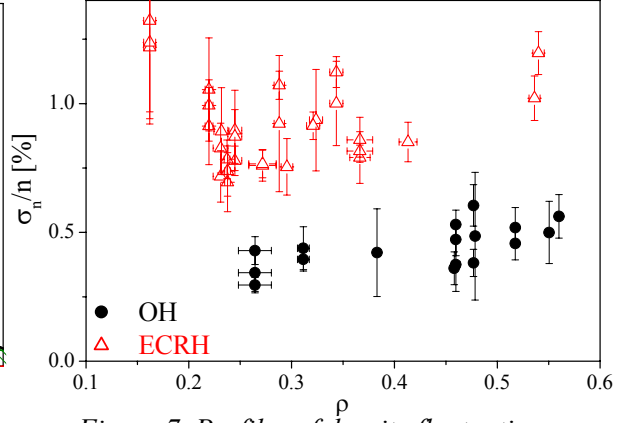


Figure 7. Profiles of density fluctuations amplitude in Ohmic (black) and ECRH (red) discharges in T-10 tokamak

$$\frac{\sigma_n}{n_{cr}} = \frac{1}{4\pi} \frac{\lambda_0}{\sqrt{L_\epsilon \Delta_r^{eff}}} K_2 \sigma_\phi \quad (III.10) \quad \Delta_r^{eff} = \left[\left(\frac{(1-\mu)}{\Delta_{r,cor}^{BB}} \left(\frac{1}{K_1(\Delta_{r,cor}^{BB})} \right)^2 + \frac{\mu}{\Delta_{r,cor}^{QC}} \left(\frac{1}{K_1(\Delta_{r,cor}^{QC})} \right)^2 \right) \right]^{-1} \quad (III.10.1)$$

Parameter Δ_r^{eff} has a sense of effective radial length of perturbations.

This approach was used to estimate fluctuations parameters from the reflectometer signals, obtained in 2D simulations. The density fluctuations parameters in this case are known and it is possible to compare them with the estimated ones (Tab. 1). One could see reasonable agreement between simulation parameters and estimations.

The method was used to estimate turbulence level in T-10 discharges with Ohmic and ECR heating. The results are shown in Figure 7. The level of density perturbations is increased in ECRH discharges in accordance with confinement degradation. It should be noted that K_2 coefficient slightly varied along the minor radius and its value was close to unity. Therefore, reflectometer sensitivity to high k_\perp does not effect on the measurements.

IV. Conclusions

The using of reflectometry as a method of turbulence measurements was considered by means of 2D simulation and various analytical approaches. It was found that in a case of weak turbulence both simulations and theory shows good locality of this method. Both simulation and phase screen model estimations shows that reflectometry has a good sensitivity to perturbations with k_\perp up to $k_0/3$. Therefore, reflectometry can measure spatial size, velocity and relative amplitude of fluctuations at the reflection radius.

Authors would like to thank Dr. E.Z. Gusakov and Dr. V.V. Bulanin for the fruitful discussions. This work was supported by grants: Scientific School 1608.2003.2, NWO-RFBR 047.016.015, RFBR 04-02-17562, RFBR 04-02-17567 and INTAS 2001-2056.

¹ M.Z. Tokar *et al*, 2000, Phys. Rev. Lett., 84, 895

² J. Weiland, H. Nordman, Nuclear Fusion, 31, (1991), 390

³ V.A. Vershkov *et al*, 1999, RSI, V. 70, N. 3, 2903.

⁴ V.A. Vershkov *et al*, Proc. of 30th EPS Conference Contr. Fus. and Plasma Phys., St. Petersburg, Russia, 2003, EC, Vol. 27A (2003), P-2.56.

⁵ K.N. Klimov *et al*, Proceedings of 2000 International Conference on Mathematical Methods in Electrodynamics Theory, Vol. 1, Kharkov, Ukraine, September, 12–15, 2000, p 128.

⁶ E.Z. Gusakov *et al* Plasma Physics Control Fusion, 44 (2002) p.2327

⁷ E. Mazzucato, R. Nazikian, RSI **66**, 1237 (1995).

⁸ M. Abramowitz, L. Stegun, Handbook of Mathematical Functions, Dover, New York, 1968

⁹ Y. Lin, R. Nazikian *et al*, Plasma Phys. Cont. Fusion, **43** (2001), L1-L8

Remarks on the asymmetry of the angular response in x-mode reflectometry observed in numerical simulations

E. Holzhauer, E. Blanco*

Institut für Plasmaforschung, Universität Stuttgart, Pfaffenwaldring 31
70565 Stuttgart, Germany

*Laboratorio Nacional de Fusión por Confinamiento Magnético,
Asociación Euratom-CIEMAT, Av. Complutense, 22 28040 Madrid, Spain

Theory

If an electromagnetic wave with x-mode polarisation is incident at an oblique angle θ with the background density gradient the propagation is not symmetric with respect to the angle θ [1].

$$\frac{d^2 E_y}{ds^2} + p(s) \frac{dE_y}{ds} + q(s) E_y = 0, \quad s = k_0 x$$

where

$$p(s) = \frac{d}{ds} (w_p^2) \frac{\sin^2 \theta_0}{(w^2 - w_h^2) \left(\cos^2 \theta_0 - \frac{w_p^2}{w^2 - w_c^2} \right)}$$

$$q(s) = 1 - \frac{w_p^2}{w^2} \frac{w^2 - w_p^2}{w^2 - w_h^2} - \sin^2 \theta_0 - \frac{d}{ds} (w_p^2) \frac{w_c}{w} \frac{\sin \theta_0 \cos^2 \theta_0}{(w^2 - w_h^2) \left(\cos^2 \theta_0 - \frac{w_p^2}{w^2 - w_c^2} \right)}$$

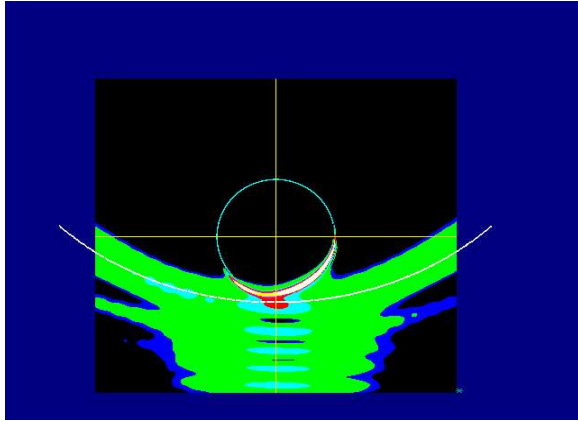
The asymmetry depends on the following parameters:

- (i) the density gradient length,
- (ii) the magnitude and sign of the angle of propagation θ ,
- (iii) the magnitude and sign of the static magnetic field B,
- (iv) the difference between wave frequency and uh-frequency.

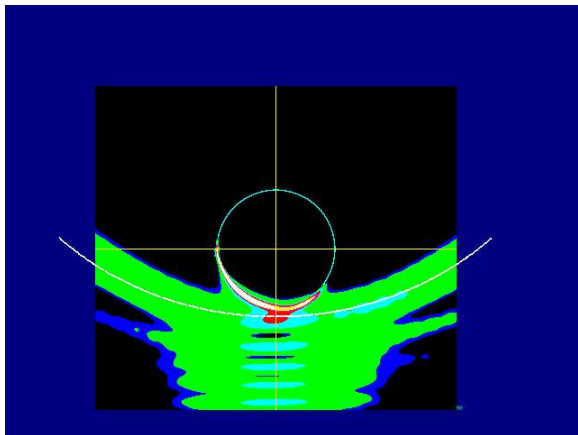
Simulation

Full wave solutions for x-mode reflectometry are calculated using a FDTD (Finite-Difference-Time-Domain) numerical code. Examples illustrating the effect of the asymmetry term are given for both Standard reflectometry and Doppler reflectometry. In the case of Standard reflectometry the asymmetry becomes noticeable for strongly focused beams with their correspondingly large angular spectrum. The same result is obtained for a wave with large beam waist (= small divergence) or a plasma with strong curvature.

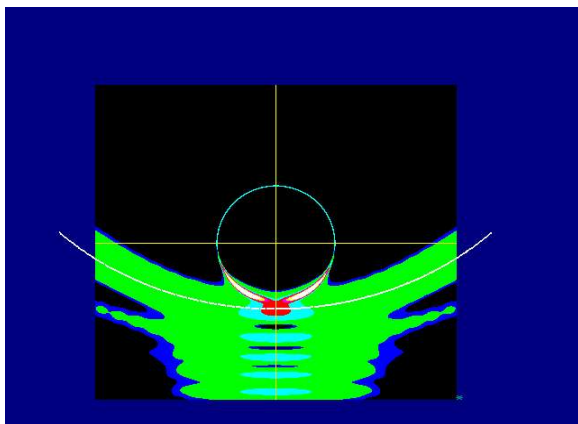
The first example is for a laboratory experiment with $f_0/f_{ce} = 10$, with f_{ce} the electron-cyclotron frequency and f_0 the probing microwave frequency. These conditions are typical for helicon plasma discharges [2]. In this case the right-hand cut-off frequency lies close to the upper-hybrid resonance and the asymmetry is expected to be pronounced in this regime.



(a) positive magnetic field



(b) negative magnetic field



(c) zero magnetic field

Fig. 1: Plot for the rms-value of the electric field demonstrating the dependence of the asymmetry on magnetic field.

Absorption at the uh-resonance (e.g. collisions) or conversion into Bernstein waves must also be taken into account. Here a small amount of numerical viscosity provides damping of the uh-resonance. Plasma parameters are similar to those in the linear *VINETA* experiment at IPP in Greifswald [2]. Fig.1 shows the rms-field in the poloidal plane of the cylindrical plasma. The circle around the centre indicates the radial position of the o-mode cut-off. As can be seen uh-resonance and o-mode cut-off lie very close together. The transmitter antenna is situated at the bottom of the discharge chamber.

If the magnetic field $B = 0$ the resonance is seen to be symmetric at the radius of the o-mode cut-off. This case without magnetic field provides a check on the accuracy of the numerical code.

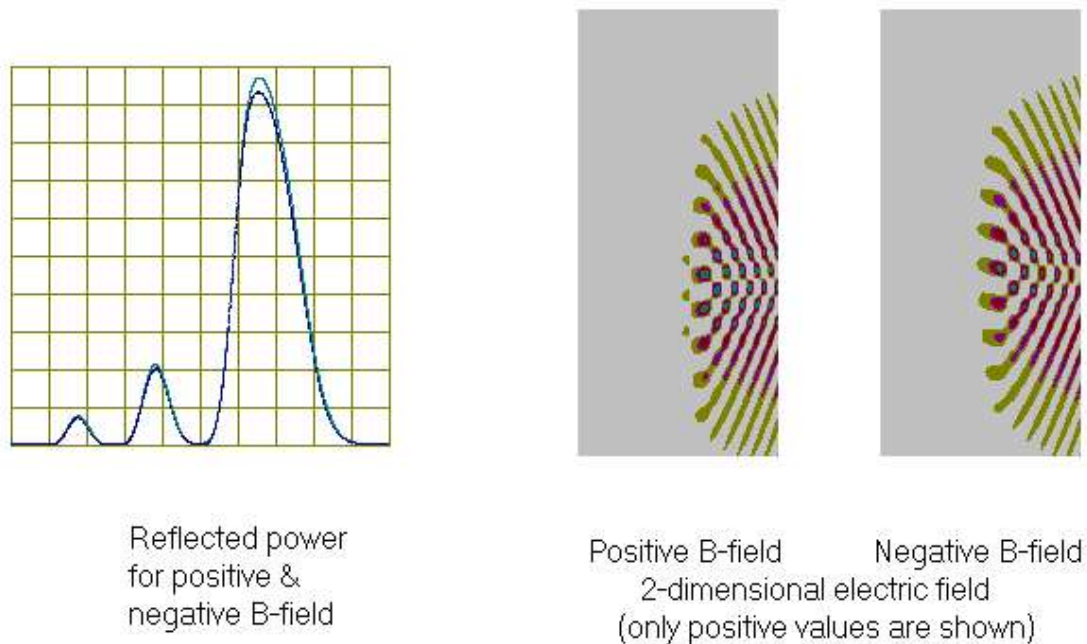


Fig.2 : Doppler reflectometer (tilt angle 14 deg., $f_0/f_{ce} = 1.5$).

For x-mode reflectometers in fusion plasmas (stellarator, tokamak) the cyclotron frequency usually is close to the probing frequency. In this case the right-hand cut-off frequency lies sufficiently far from the upper-hybrid resonance and thus the asymmetry is not expected to be pronounced in this regime.

The second example is for the case of a Doppler reflectometer with tilt angle 14 deg. and $f_0/f_{ce} = 1.5$ as shown in Fig. 2. The difference in the electric field distribution mainly shows up in the phase of the electric field close to cut-off. The reflected power is almost independent of the asymmetry effects in eqn. (1).

The third example demonstrates the asymmetry effect for the standard reflectometer on the TJ-II stellarator at CIEMAT with $f_0/f_{ce} = 1.5$. The transmitter horn antenna is situated on the left boundary of the plot.

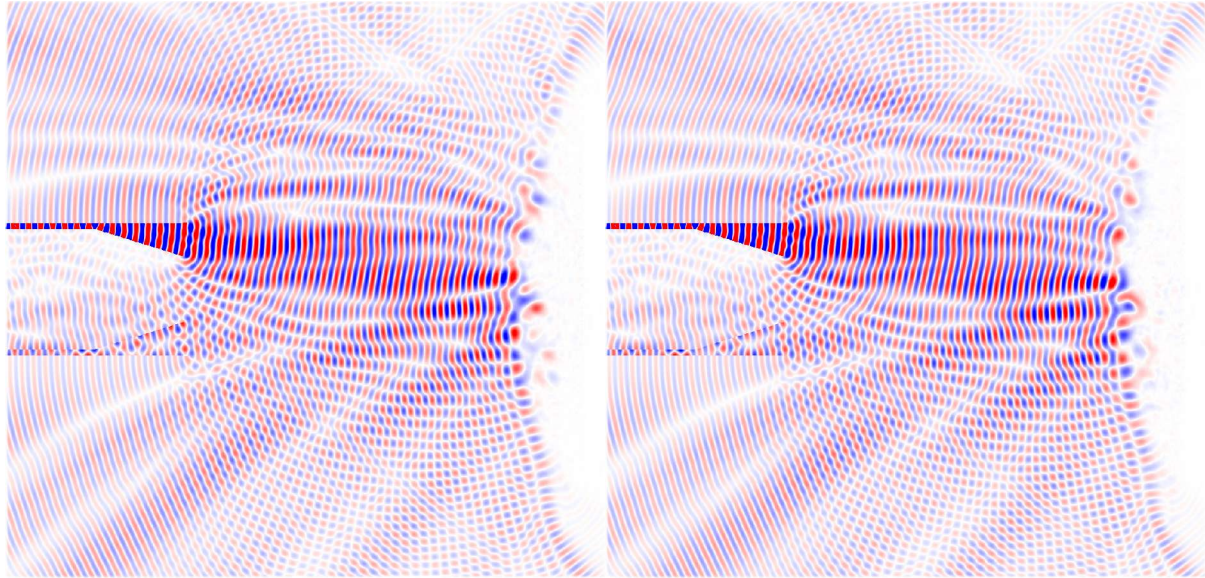


Fig.3: Snapshot for Standard reflectometer on TJ-II with turbulence.
 (a) positive B-field (b) negative B-field

Similar to the case of the Doppler reflectometer the difference in the electric field distribution mainly shows up in the phase of the electric field close to cut-off.

Conclusion

The asymmetry is pronounced if the upper-hybrid frequency is close to the probing microwave frequency. If part of the incident wave can tunnel through the x-mode cut-off and reach the position of the upper-hybrid resonance (via reflection as slow x-mode) then absorption at this resonance (e.g. collisions) or conversion into Bernstein waves must also be taken into account. For fusion relevant parameters the reflected power is almost independent of the asymmetry effects in eqn. (1) which mainly show up in the phase of the electric field.

References

- [1] R.B. White, F.F. Chen *Plasma. Physics* **16** 565 (1974)
- [2] C. Schröder, *Ph.D. Thesis* Universität Greifswald (2003)

Doppler reflectometry studies using a two-dimensional full-wave code

E. Blanco, T. Estrada, S. Heuraux* and J. Sánchez

Laboratorio Nacional de Fusión por Confinamiento Magnético. Asociación Euratom-CIEMAT, Av. Complutense 22, 28040 Madrid, Spain

*LPMIA UMR 7040, UHP Nancy I, BP 239, 54506 Vandoeuvre Cedex, France

A two-dimensional full-wave numerical code in the extraordinary mode of propagation has been developed to simulate reflectometry. Realistic plasma shape and magnetic field distribution are introduced in the code using the theoretical magnetic surfaces of TJ-II, while density profile and turbulence characteristics are extrapolated from those obtained experimentally.

The code has been used to study the viability of the Doppler reflectometry technique to determine the perpendicular rotation velocity of the density fluctuations in TJ-II. The numerical results obtained modifying the plasma geometry allow us to conclude that the shape of the TJ-II plasmas (cut-off layers with high curvature) makes the optimization of the Doppler reflectometer difficult. Additionally, simulation results support the possibility to perform reflectometry at large tilt angles and therefore to characterizing turbulence with high wave-numbers keeping the spatial localization of the measurement.

Two-dimensional full-wave code

A two-dimensional full-wave code has been developed to simulate the propagation of waves in turbulent and magnetised plasmas. The code considers propagation in the extraordinary mode of polarization. A detailed description of the code can be found in

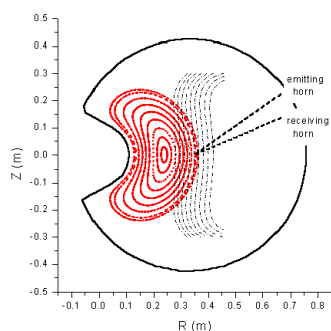


Figure 1: TJ-II plasma shape and constant magnetic field lines.

[1]. The numerical solution of Maxwell's equations is obtained using the Finite-Difference Time-Domain [2] technique. The medium size of TJ-II and the probing frequencies involved (33 – 50 GHz) make possible the simulations in a realistic period of time.

The realistic plasma shape and magnetic field distribution [3] are introduced in the code using the theoretical magnetic surfaces of TJ-II.

Two independent waveguides and horns are implemented, emitting and receiving ones.

The density distribution has been implemented superimposing a density perturbation to a steady density profile similar to the experimental one [4]. The density perturbation is given by the expression:

$$n_e(x, y, t) = \langle n_e(x, y) \rangle + \delta n_e(x, y, t)$$

$$\delta n_e(x, y, t) = \sum \sum a(k_x, k_y) \sin(k_x x + k_y (y - v_p t) + \phi_{random}(x, y, t))$$

The k -spectrum is fit by a Gaussian function written as $\exp(-(k_x^2 + k_y^2)/k_w^2)$ with a spectral width $k_w = 540 \text{ m}^{-1}$. Finally, the plasma perturbation rotates in the perpendicular direction at a velocity $v_p = 3 \text{ km/s}$.

Numerical results

To illustrate the results two examples are displayed in figure 2; it is shown the spectra of the complex amplitude signal $Ae^{i\phi}$ obtained for antennas tilt angle of 18° and 30° . In both cases the spectra are shifted to negative frequencies indicating the existence of

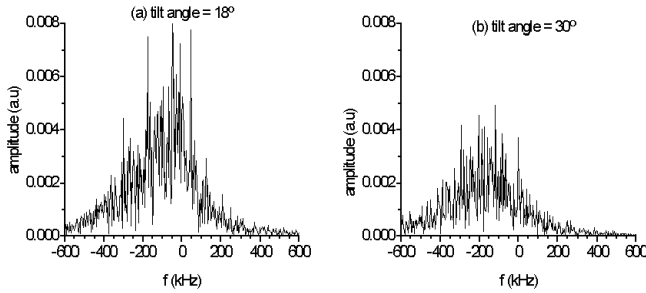


Figure 2: Complex amplitude spectra for TJ-II plasma at two different tilt angles. The frequency of the wave is 40 GHz.

rotating structures. However no clear separation exists between the reflected and backscattered signals and therefore it is not possible to extract information about the magnitude of the rotation velocity of the fluctuations.

This result is a consequence of a poor spectral resolution. An estimation of the wave-number resolution can be made from geometrical considerations (figure 3).

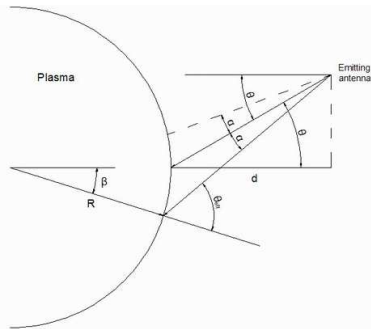


Figure 3: Geometry of the plasma cut-off layer and spot size.

The effective incident tilt angles range between $\theta_{eff,max} \approx \theta + \alpha + \beta$ and $\theta_{eff,min} \approx \theta - \alpha - \beta$, being θ the antenna tilt angle, α the 3dB half beam-width and β the angle due to the cut-off layer curvature. Taking into account that the 3dB half beam-width is $\alpha = 10^\circ$ (spot diameter close to 5 cm) and the plasma curvature radius at the cut-off layer is about $R = 20 - 25 \text{ cm}$, the increment in the tilt angle due to

the plasma curvature is $\beta \approx 6^\circ$. The corresponding spectral resolution $\Delta k_\perp/k_\perp (= \Delta f/f_D)$ estimated as $(\sin \theta_{eff,max} - \sin \theta_{eff,min})/\sin \theta$ is about 0.9 for $\theta = 30^\circ$ and still worse 1.5 for $\theta = 18^\circ$.

The results for a plasma slab, are illustrated in figure 4. From these spectra it is possible to separate the backscattered signal from the reflected one and therefore to extract information about the perpendicular velocity. However, the perpendicular rotation velocity estimated from the maximum in the Doppler frequency structure is lower than the turbulence rotation.

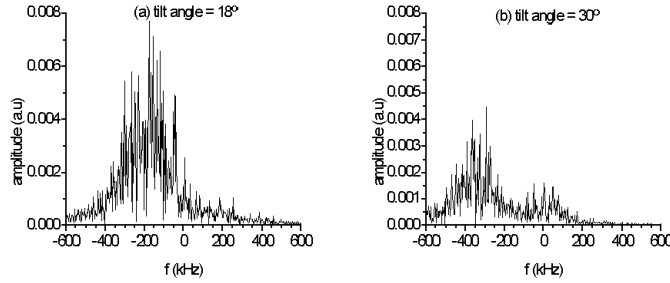


Figure 4: Complex amplitude spectra for slab plasma at two different tilt angles. The frequency of the wave is 40 GHz

This discrepancy can be partially explained in terms of the different amplitude of high and low fluctuation wave-numbers.

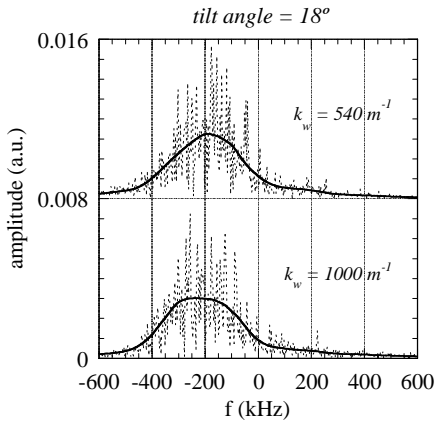


Figure 5: Complex amplitude spectra for a slab plasma and two different spectral widths. The frequency of the wave is 40 GHz.

To study this effect we have modified the spectral width while keeping fixed the other parameters. As an example figure 5 displays the complex amplitude spectra for a slab plasma with tilt angle 18° and two different spectral widths $k_w = 540 \text{ m}^{-1}$ and 1000 m^{-1} . It is observed that the shape of Doppler frequency structure changes to a more symmetric one (with respect to $f_D \approx 250 \text{ kHz}$) when the wave-number spectra are broader.

These simulations points to the possibility to measure turbulence with high wave-numbers keeping the spatial localization of the measurement. We have estimated the enhancement factor of the electric field in two cases: $\theta = 0^\circ$ and $\theta = 30^\circ$ for a probing frequency of 40 GHz. Two examples are shown in figure 6 for two different density

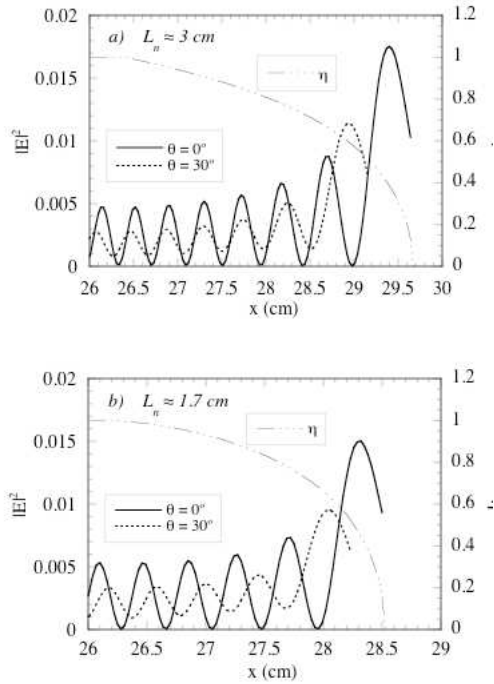


Figure 6: Electric field of the probing wave for normal $\theta = 0^\circ$ and oblique $\theta = 30^\circ$ incidence and, two different density scale length. Also, it's shown the refraction index

profiles with scale lengths at the cut-off layer $L_n \approx 3$ and 1.7 cm, and two different tilt angles. This figure shows the spatial variation of the electric field at zero tilt angle and at tilt angle $\theta = 30^\circ$, together with the refraction index. The enhancement factor of the electric field when approaching the cut-off depends on the density gradient scale length [5]; it changes from about 4 to about 3 when L_n decreases from 3 cm to 1.7 cm. Besides, the enhancement factor is almost unchanged when comparing normal ($\theta = 0^\circ$) and oblique ($\theta = 30^\circ$) incidence; consequently its contribution to the spatial localization of the measurement remains.

Acknowledgments:

We would like to acknowledge C Hidalgo for fruitful discussions. This work has been partially funded by the Spanish Ministry of Science and Technology under project FTN2003-04431.

References

- [1] Blanco E, Heurax S, Estrada T, Sánchez J and Cupido L 2004 Rev. Sci. Instrum **75** 3822
- [2] Yee K S 1966 IEEE Trans. Antennas Propag. **14** 302
- [3] Alejaldre C et al. 1999 Plasma Phys. Control. Fusion **41** A539
- [4] Hidalgo C, Pedrosa M A, Castellano J, van Milligen B, Jiménez J A, Fraguas A L and Sánchez E 2001 Plasma Phys. Control. Fusion **43** A313
- [5] White R B and Chen F F (1974) Plasma Physics **16** 565

Doppler reflectometry spectra simulations with velocity shear layer

F. da Silva, [†]S. Heuraux, and M. Manso

*Associação EURATOM/IST–Centro de Fusão Nuclear
Instituto Superior Técnico, 1046-001 Lisboa, Portugal*

[†]*Laboratoire de Physique des Milieux Ionisés et Applications, Unité du CNRS 7040
Université Henri Poincaré, Nancy 1, BP 239, 54506 Vandœuvre Cedex, France*

Abstract

Doppler reflectometry is able to provide information on plasma poloidal rotation from the frequency shift of the backscattered spectrum at oblique plasma probing. It is usually assumed that the Doppler effect is due to the fluctuation rotation at cut-off vicinity. Full-wave modeling of the Doppler reflectometry signal is performed in a slab plasma geometry with a given shear velocity layer with inhomogeneous turbulence having realistic wavenumber spectrum and radial distribution. The first part of the presentation is devoted to the description of the code and to a short recall of the developed tools needed to simulate Doppler reflectometry. The advantages and limitations of the simulations will be also discussed.

1 Introduction

The reflectometry simulation code used in this work has been originally build for CWFMB broadband reflectometry for profile evaluation [1]. Here it will be used for Doppler simulations and we will discuss further on some modifications made to perform this task.

2 Characteristics of the code

Considering a cold plasma approximation on two dimensions (x - y plane) without gradients in the perpendicular direction ($\partial/\partial z = 0$) with the external magnetic field (plasma field \mathbf{B}_0) taken along the z -direction, the current density flow \mathbf{J} is restricted to the same direction. The response of \mathbf{J} to the electric field \mathbf{E} accounts for plasma effects. Considering a transversal magnetic propagation (TM) (E_z, B_x, B_y) and using a FDTD Yee scheme [2] we obtain for the O-mode, for the electric field $\mu_0 \varepsilon_0 (\partial t E_z)_{i,j}^n = (\partial x B_y - \partial y B_x - \mu_0 J_z)_{i,j}^n$ and for the magnetic field $(\partial t B_x)_{i,j+1/2}^{n+1/2} = -(\partial y E_z)_{i,j+1/2}^{n+1/2}$; $(\partial t B_y)_{i+1/2,j}^{n+1/2} = (\partial x E_z)_{i+1/2,j}^{n+1/2}$. The equation for the current density is $(\partial t J_z)_{i,j}^{n+1/2} = e^2/m_e (n_e E_z)_{i,j}^{n+1/2}$, where e is the electron charge, m_e the electron mass and n_e the electronic density.

3 Plasma model

Coupling between the electromagnetic wave and the plasma is taken into account by the current density, J_z , which depends on the plasma density n_e . The density $n_e(\mathbf{r}, t)$ is in general a function of space and time since the code allows time evolution of the density profile due to modifications of the base plasma $n_{e0}(\mathbf{r}, t)$ on time, coherent plasma modes $\delta n_{eMOD}(\mathbf{r}, t)$ and turbulence $\delta n_{eTRB}(\mathbf{r}, t)$: $n_e(\mathbf{r}, t) = n_{e0}(\mathbf{r}, t) + \delta n_{eMOD}(\mathbf{r}, t) + \delta n_{eTRB}(\mathbf{r}, t)$. The plasma has a generic density profile across elliptical iso-density lines. Turbulence is modeled as a sum of modes with random phase according to the scheme proposed in [3]. The density perturbation at each point obeys to $\delta n_{eTRB} = \sum_{i=i_m}^{i_M} \sum_{j=j_m}^{j_M} A(i, j) \cos [k_x(i)x + k_y(j)y + \varphi(i, j)]$.

The amplitude $A(i, j)$ is chosen in agreement with experimental data [4] and may be modified during the simulation to accommodate several plasma scenarios. Keeping the same amplitude spectrum and varying $\delta n_{e_{TRB}}$ with time allows the setting of several turbulence *snapshots* with the same spectral conditions.

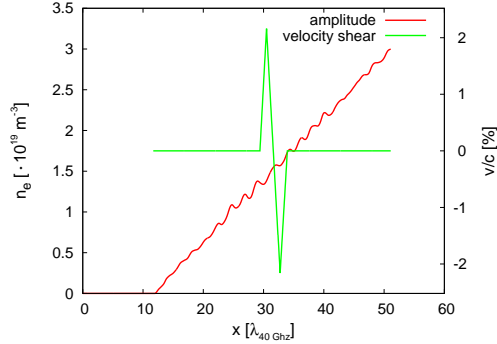


Figure 1: Radial cut of density profile with velocity shear profile superimposed.

The shear model is implemented imposing, on the original *static* matrix, a shear velocity profile (see Fig. 1). The columns of the original turbulence matrix on the shear region are shifted poloidally, each column sliding at a speed given by the velocity shear imposed. The process is illustrated in Fig. 2: The columns of the original turbulence matrix $\delta n_{e_{TRB}}$ (top left), as the simulation runs its course, slide with a velocity given by the shear profile (Fig. 1). Its effect on the turbulence structure is shown on Fig. 2 (bottom left). This model for velocity shear implies a modification of the angular wavenumber spectrum (k -spectrum) on the shear layer (both poloidal and radially). On Fig. 2 the original spectrum (top right) and the spectrum at iteration 50×10^3 are shown. The deformation on the shear zone reflects the elongation of the turbulent structures along the poloidal direction and the radial squeezing as the matrix columns are slid. This choice of model has been made to improve drastically the computation time.

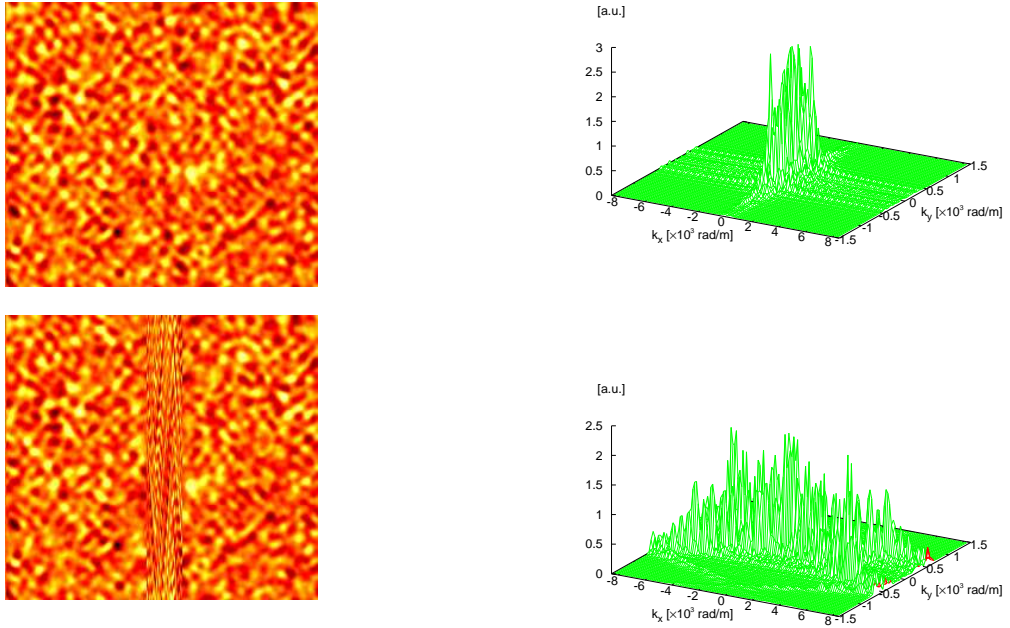


Figure 2: Original turbulence matrix $\delta n_{e_{TRB}}$ (top left) and the amplitude k -spectrum (top right). Matrix of turbulence at iteration 50×10^3 (bottom left) and the modified spectrum at the shear region (bottom right).

4 Classic reflectometry versus Doppler reflectometry setups

The code is usually run using a monostatic setup (one antenna used both for emission and reception). The emitting structure (antenna/waveguide) is obtained imposing the electric field on the structure to null, $E_z = 0$. The signal is excited in the waveguide as a TE₁₀ waveguide mode using a Unidirectional Transpar-

ent Source (UTS) [5] which allows unidirection injection of the probing wave (towards the plasma) while allowing the returned wave to be pick-up beyond the injection point separated from the source excitation. In Fig. 3, a monostatic setup for a 2D H-plane horn with a half power beam width of $\approx 30^\circ$ appears on the left. The Doppler effects using this setup will be due to *lateral* probing of the plasma through the relatively large antenna radiation pattern. The response of the direct reflection of the plasma (density iso-surfaces at $\pi/2$ with the axis of the antenna) is much strong than the Doppler effects.

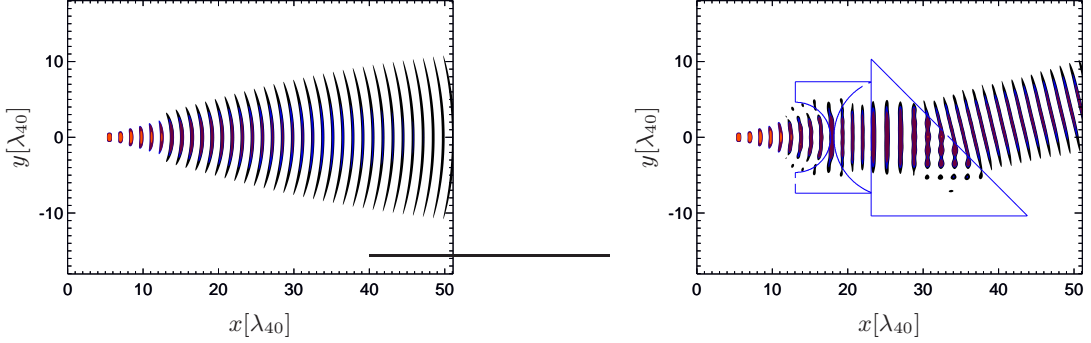


Figure 3: *Classic* reflectometry antenna setup (left) and Doppler setup with a converging lens and prism to launch beams with a high directivity (right).

To adopt the code to an angular plasma probing several possibilities could be envisaged: (i) Antenna forming an angle with the plasma other than $\pi/2$; (ii) Plasma forming an angle with an *horizontal* antenna; (iii) Use of an optical system. The antenna with an angle would be quite simple to implement but we would lose the UTS as it is implemented (the waveguide aligned with the grid points) or would require a much more complex reformulation of the UTS implementation to adapt it. The plasma forming an angle with the antenna would maintain the use of the UTS but calculations performed on the plasma matrix would become very time consuming since the plasma iso-density lines would not be aligned with the columns (poloidal direction) and lines (radial direction) of the matrix. The use of an optical system, as shown on Fig. 3 (right), to probe the plasma appears as the solution more fast to implement. It is also extremely easy to implement on the code requiring almost no modifications since we opt for a *plasma optical system*. The same code subroutine used to perform calculations on the *true plasma* region is used to calculate propagation on the lens region. It is only a matter of including the plasma optics on the same matrix were the plasma is defined. Furthermore, the code stability continues to hold. The first two solutions would present an additional problem: due to the fact that the antenna radiation pattern is somewhat large (to obtain a narrow diagram on 2D is a quite daunting task [6]) the plasma will be simultaneously probed with different angles and consequently the antenna will be integrating the response of a continuum of plasma angular wavenumbers. The use of a lens allows the emission of a non-diverging beam with a planar wavefront which will respond to a single wavenumber according to the injection angle chosen by the prism. The same impulsive response (IR) technique used to implement the UTS [5] is used to eliminate the spurious reflection from the lens and prism. The beam used has a width of $14.7 \lambda_{40 \text{ GHz}}$ and the optics have a plasma frequency of $f_{pe} = 20 \text{ GHz}$.

5 Results

The procedure used to process the results was to collect the backscattered signal on the waveguide (separated from the probing wave due to UTS) and performing an FFT. Eight runs with different instances of the *start* matrix are made and an average of all FFTs is performed to obtain the *final* FFT result. Simulations were made for different fixed frequencies, 34, 35, 36 and 40 GHz, probing the regions where the shear is maximum, where it passes through null, the maximum counter-shear and finally a region beyond the shear region. The 8-runs averaged FFT for this different frequencies are shown on Fig. 4 for probing angles of 7° and 15° .

The poloidal velocity used with 15° ($v_{pol}/c = 0.054$) was 1.5 times higher than the one used with 7° ($v_{pol}/c = 0.036$), which accounts for the difference on the magnitude of the Doppler shifts appearing on Fig. 4. These are *code velocities* which would correspond to *real velocities* of 21.6 Km and 32 Km. With this rescaling of velocities the Doppler shifts would be reduced from the GHz (*code*) to around 2 MHz (*real*).

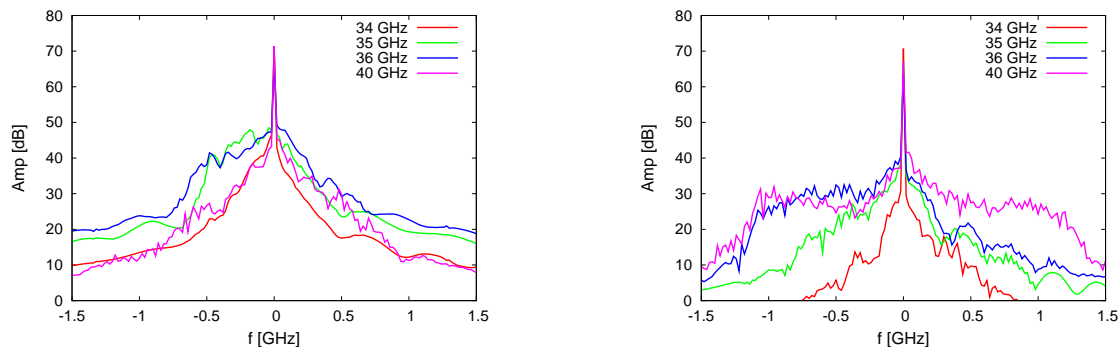


Figure 4: Averaged spectra of returned signals probed at 7° (left) and 15° (right).

6 Discussion

The code and its *Doppler adaptations* have proved adequate to study the effects of Doppler in general and the problem of a shear layer in particular. The use of the *plasma optics* together with the UTS and the IR correction technique can be a useful tools to obtain a probing beam to perform Doppler studies and it was also used in a study of nonlinear effects in Doppler reflectometry to compare the results of analytical theory and simulation [7]. The shear model used is a good starting point for reflectometry simulations on this subject where very few studies exist but clearly needs improvements in particular on the spectral modifications induced. This should be the subject of further modeling. The spectral analysis techniques can also be the object of further refinement.

Acknowledgements

This work, supported by the European Communities and *Instituto Superior Técnico*, has been carried out within the Contract of Association between EURATOM and IST. Financial support was also received from *Fundação para a Ciência e Tecnologia* in the frame of the Contract of Associated Laboratory. The views and opinions expressed herein do not necessarily reflect those of the European Commission, IST and FCT.

References

- [1] F. da Silva, M Manso, A. Silva, and ASDEX Upgrade Team. Simulation of reflectometry density changes using a 2D full-wave code. *Review of Scientific Instruments*, 72(1):311–314, January 2001.
- [2] K. S. Yee. Numerical solution of initial boundary value problems involving Maxwell’s equations in isotropic media. *IEEE Transactions on Antennas and Propagation*, 14:302–307, 1966.
- [3] S. Heuraux, S. Hacquin, F. da Silva, F. Clairet, R. R. Sabot, and G. Leclert. Radial wave-number spectrum of density fluctuations deduced from reflectometry phase signals. *Review of Scientific Instruments*, 74(3):1501–1505, March 2003.

- [4] P Devynck, X Garbet, C Laviron, J Payan, S K Saha, F Gervais, P Hennequin, A Quemeneur, and A Truc. Localized measurements of turbulence in the TORE SUPRA tokamak. *Plasma Physics and Controlled Fusion*, 35(1):63–76, January 1993.
- [5] F. da Silva, S. Heuraux, S. Hacquin, and M. Manso. Unidirectional transparent signal injection in finite-difference time-domain electromagnetic codes—application to reflectometry simulations. *Journal of Computational Physics*, 203(2):467–492, 2005.
- [6] F. da Silva, S. Heuraux, N. Lemoine, C. Honoré, P. Hennequin, M. Manso, and R. Sabot. Global full-wave simulation of the tore-supra doppler reflectometer. *Review of Scientific Instruments*, 75(10):3816–3810, Oct 2004.
- [7] E. Z. Gusakov, S. Heuraux, F. da Silva, and A. V. Surkov. Nonlinear effects in the Doppler reflectometry (analytical theory and numerical simulations). This workshop.

Consideration Doppler reflectometry in Born approximation

V.V.Bulanin, A.V.Petrov, M.V.Yefanov

St.Petersburg State Polytechnical University, St.Petersburg, 195251, Russia

Doppler reflectometry is now extensively employed as an effective tool for plasma rotation measurements in toroidal devices [1]-[5]. The method is based on deriving of the rotation velocity from the Doppler frequency shift of backscattered radiation expected under an oblique incidence of microwave beam onto cutoff surface. It is assumed, that fair radial resolution of the diagnostics occurs due to microwave field enhancement in the vicinity of the cutoff. To verify this assumption 2D simulation of O-mode microwave backscattering was carried out in Born approximation. This simulation is valid only for small amplitude of fluctuations [6]. Nevertheless the considered simulation allows to reasonably determine a range of diagnostic parameters to proceed, if necessary, with a full-wave analysis. Developed 2D code is applicable for arbitrary radial profiles of background plasma density and for the scattering from any size and shape of plasma density fluctuations. The computation can be performed for any antenna tilt angle and for any phase and amplitude distribution of electric field across the antenna mouth.

An approach to numerical integration

In a frame of Born approximation it is possible to introduce spatial weighting function $W(\mathbf{r})$ which links directly an output signal $I(t)$ of IQ detector with plasma density fluctuations $\delta n(\mathbf{r},t)$ [4].

$$I(t) = \eta \int \delta n(\mathbf{r}, t) W(\mathbf{r}) d^2r \quad W(\mathbf{r}) = \langle E_i(\mathbf{r}, t) E_a(\mathbf{r}, t) \rangle \quad (1)$$

Where: η is a dimensional constant; E_i is electric field of incident beam and E_a is electric field of imaginary radiation launched into the plasma via receiving antenna; an averaging is performed over microwave period. The weighting function is computed with a full electric field of probing beam in a free space represented as a superposition of poloidal modes of convergent and divergent cylindrical waves.

$$E_i(r, \varphi, t) = \sum_{m=-\infty}^{+\infty} \left(\dot{E}(m) H_m^{(2)}(r) + \dot{A}(m) H_m^{(1)}(r) \right) \exp(im\varphi - i\omega t) \quad (2)$$

Here: $H_m^{(1)}(r), H_m^{(2)}(r)$ are Hankel functions; $E(m)$ is m – spectrum of the incident beam obtained with use of prescribed distribution of electric field across the antenna mouth. The electric field in plasma is given by:

$$E_i(r, \varphi, t) = \sum_m \dot{P}(m) F_m(r) \exp(im\varphi - i\omega t) , \quad (3)$$

where: $F_m(r)$ is a solution of one-dimensional wave equation. The complex spectra $A(m)$ and $P(m)$ are found by equalizing the vacuum electric field to the electric field on plasma

boundary. The imaginary electric field E_a of receiving antenna beam was obtained in a similar way.

Spatial and wave number resolutions

To quantitatively estimate spatial and wave number resolutions the two models of plasma density fluctuations have been employed given the weighting function is computed. The fluctuations are represented by a superposition of either variously directed plane waves of random phases with specified wave number k_{\perp} or various poloidal modes. The fluctuations are localized in Gaussian shape layer at radius r_0 . The first model

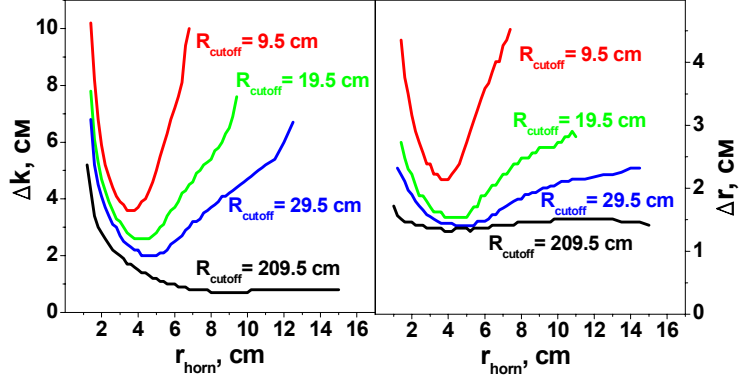


Fig.1 Plot of spatial Δr and wave number Δk resolutions against antenna size. Width of Gaussian layer is 1 cm. Model of isotropic plasma fluctuations is applied

represents isotropic plasma turbulence with correlation length of about reciprocal wave number k_{\perp} . The superposition of the poloidal modes is more relevant to plasma drift turbulence in tokamak plasma. The squared response $\langle I^2(r_0, k_{\perp}) \rangle$ or $\langle I^2(r_0, m) \rangle$ is calculated with use of expression (1) being averaged over different realizations with various sets of the random phases. The both radial Δr and wave-number Δk resolutions were taken at a half maximum of the 2D functions $\langle I^2(r_0, k_{\perp}) \rangle$ or $\langle I^2(r_0, m) \rangle$. With use of such an approach the influence of the cutoff curvature on the resolution has been studied. In Fig. 1 antenna size (r_{horn}) dependence of the k-resolution is shown for various radius of the cutoff surface R_{cutoff} . Qualitatively similar dependences were lately obtained with use of phase screen model [4]. The optimal antenna size corresponding to minimum of the wave number resolution is evidently seen for a moderate cutoff curvature. The increasing of the cutoff radius is followed by the improvement of the k-resolution. It is important that the spatial resolution has also a minimum at the same antenna size.

Improvement of Doppler reflectometry resolution

The observed degradation of the diagnostics resolution at lower cutoff curvature explicitly depends on width of the incident beam m -spectrum $E(m)$, as the eigenfunctions $F_m(r)$ are strongly dependent on poloidal number m . The width Δm of the m -spectrum is given in paraxial approximation for Gaussian beam by

$$(\Delta m)^2 = r_{\text{horn}}^2 \left(\frac{r_a}{R} + 1 \right)^2 + \frac{4r_a^2}{r_{\text{horn}}^2}, \quad (4)$$

where: r_a is radial coordinate of the antenna and R is radius of wave front at antenna mouth. The width of the m -spectrum has got a minimum at the antenna size corresponding to the minimum of the spatial and k -resolutions observed in Fig.1. On the other hand Δm has also got a minimum regarding radius R . The minimum condition is satisfied at $R_{\min} = -r_a$. Therefore, it is natural to expect the

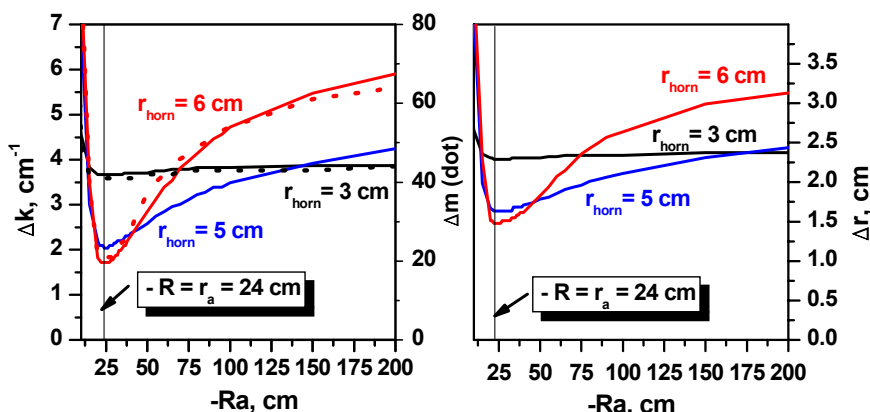


Fig.2 Spatial and wave number resolutions as a function of wave front radius Ra for various size antennas.

improvement of resolutions at the concave wave front at antenna mouth. This has been checked by computation of the resolutions as a function of the wave front radius. The results are shown in Fig.2. The m -spectrum width Δm is also plotted here by dotted lines. The essential improvement of the resolutions occurred for the convergent beam with the predicted radius of the wave front. The effect of the improvement is more pronounced when the cutoff is placed in the Rayleigh zone that is for relatively large aperture of the antenna.

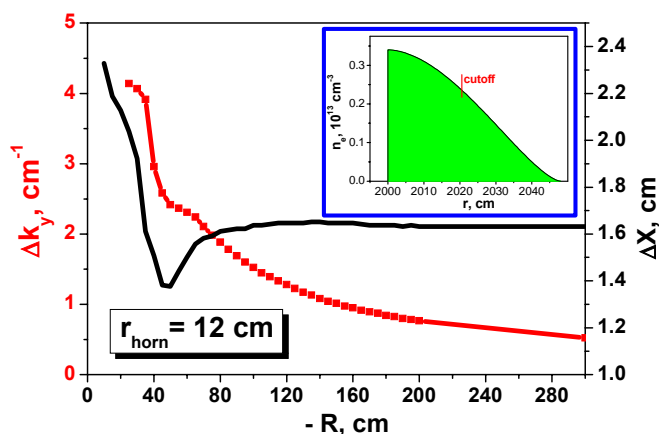


Fig.3 Spatial and wave number resolutions versus wave front radius R for background density distribution given in insert.

However the k -resolution turns out poorer than for the flat wave front. Therefore, a wave front radius reasonably follows from the trade off between the spatial resolution and k -resolution.

The fair resolution improvement can be achieved with use of two-antenna arrangement. The weighting functions computed for both monostatic and two-antenna arrangements are plotted in Fig.4 for comparison. One can see that with use of two antenna arrangement the probing and receiving antenna beams are not overlapped in the peripheral

In line with theoretical prediction [6] the spatial resolution improvement might be for the convergent beam even at stratified distribution of the background density. In Fig.3 the resolutions are shown as a function the wave front radius for ITER relevant distribution of the background density at plasma periphery. The spatial resolution is somewhat improved at the wave front radius equal to a distance from the antenna to the cutoff. However the k -resolution turns out

regions leading to narrowing of the weighting function. The latter most probably results in fair improvement of the resolutions illustrated in Fig.5. Further increasing of a distance between antennas transfers the Doppler reflectometry to a collective scattering diagnostics, in which effect of refraction has not essential importance.

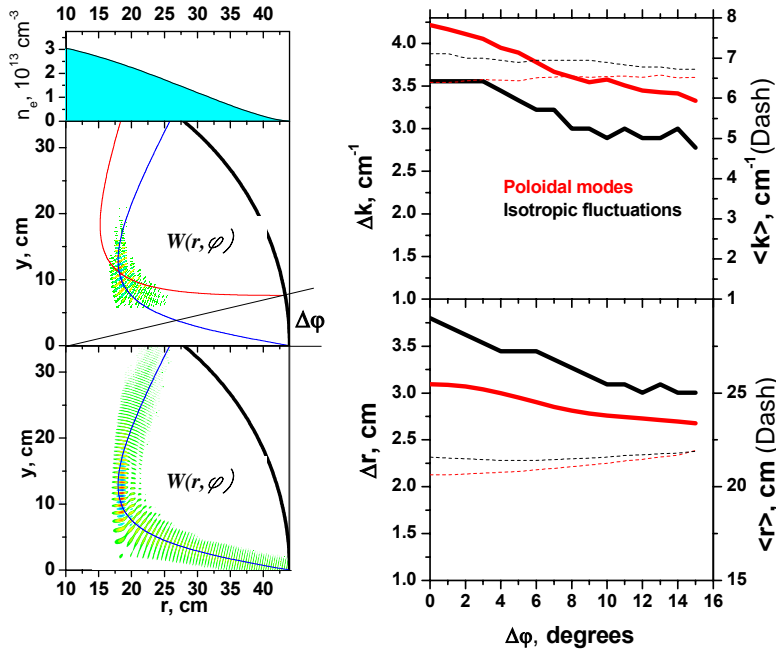


Fig. 4 2D plot of weighting function $W(r, \varphi)$ ($\alpha=10^\circ$) and background density $n(r)$ for monostatic $\varphi=0^\circ$ and two antenna arrangement $\varphi=10^\circ$. Spatial and wave number resolutions versus angular distance between antennas ($\varphi=10^\circ$). $\langle k \rangle$ is a selected k -value; $\langle r \rangle$ is radial position of scattering region.

beam fronts due to large amplitude MHD or/and ballooning modes is a disturbing factor to be analyzed in a first turn.

Acknowledgements.

This work was jointly supported by RFBR 02-02-17589 and INTAS-2001-2056.

Reference

- [1] – V.V.Bulanin, et.al., Proc. of 22nd EPS Conf. on Control. Fusion and Plasma Physics, (Bournemouth), Cont. Papers, (1995), Vol.19c, Part II, pp. 089-092
- [2] - X.L.Zou, et.al., Proc. 26th EPS Conf. on Control. Fusion and Plasma Physics, (Maastricht), (1999), p.1041
- [3] - V.V.Bulanin, et.al, Plasma Physics Reports, (2000), **26**, p.813
- [3] – M Hirsch., et.al., Plasma Phys. Control. Fusion, (2001), **43**, 1641
- [4] - G D Conway, et.al., Plasma Phys. Control. Fusion (2004) **46**, 951–970
- [5] - E Z Gusakov and A V Surkov, Plasma Phys. Control. Fusion (2004) **46**, 1143–1162

Summary and conclusion

The developed 2D code adequately describes the Doppler reflectometry in the conditions of tokamak experiment. Under a moderate cutoff curvature the resolutions may be improved significantly with use of the convergent microwave beams. The effect is more pronounced for relatively large aperture of an antenna. The code is appropriate for analyzing the two-antenna arrangement used to improve the diagnostics resolution. The problem still exists in proper consideration non-linear scattering. The influence of virtual distortion of

Nonlinear effects in the Doppler reflectometry (analytical theory and numerical simulations)

E.Z. Gusakov¹, S. Heuraux², F. da Silva³, A.V. Surkov¹

¹*Ioffe Physico-Technical Institute, Politekhnicheskaya 26, 194021 St.-Petersburg, Russia*

²*LPMIA, UMR 7040 Univ. Henri Poincare BP 239 F-54506 Vandoeuvre Cedex, France*

³*Associacao Euratom/IST-Centro de Fusao Nuclear, 1046-001 Lisboa, Portugal*

1. Introduction

One of widespread methods used at present for plasma poloidal velocity measurements is Doppler reflectometry [1–5]. This technique provides measuring fluctuations propagation poloidal velocity which is often shown to be dominated by plasma poloidal rotation velocity [3, 4]. This method is based on plasma probing with a microwave beam which is tilted with respect to the plasma density gradient. A back-scattered signal with frequency differing from the probing one is registered by a nearby standing or the same antenna. The information on the plasma poloidal rotation is obtained in this technique from the frequency shift of the backscattering spectrum which is supposed to originate from the Doppler effect due to the fluctuation rotation.

Spatial distribution of the scattering phenomena, which is usually assumed to occur in the cut-off vicinity, is the key issue for the diagnostic applications. In case of low turbulence level, when only single scattering is significant, this problem was investigated in the framework of linear theory numerically in [3] and analytically in [6–8]. The diagnostics locality in this case was shown to be better than for standard reflectometry. The approach used in [6–8] is based on the Born approximation. It assumed small enough amplitude of the fluctuations, which caused the scattering, to neglect a multiple scattering contribution to the received signal.

However this approximation can be incorrect in the plasma periphery where the turbulence amplitude is usually high, or in large plasma devices, where the probing ray trajectory is long. This is the case when the following criterion is satisfied [9, 10]

$$\frac{\omega_i^2}{c^2} \ell_{cx} x_c \left(\frac{\delta n}{n_c} \right)^2 \ln \frac{x_c}{\ell_{cx}} > 1$$

where n_c is the critical density corresponding to the probing frequency ω_i , x_c is the distance between the plasma and the cut-off, δn is the turbulence amplitude and ℓ_{cx} is the turbulence radial correlation length. This situation of the high turbulent density perturbation level, when the multiple forward scattering of the probing wave is dominant, was investigated analytically in [11]. It was shown there that even in this regime the diagnostics is able to measure the plasma poloidal velocity with a spatial resolution close to that of standard fluctuation reflectometry. Here we present the comparison of the analytical results of [11] with the full-wave modelling of the Doppler reflectometry.

2. The model considered

The consideration is performed in the frameworks of the analytical approach [11]. Its limitations are the following. The plasma is assumed to be large: $\lambda_0 \ll x_c$. The level of the turbulence is supposed to be modest

$$\frac{\delta n}{n_c} < \frac{\ell_{cx}}{x_c} \tag{1}$$

which provides the existence of the only one cut-off for the probing wave. The backscattering in radial and poloidal direction is neglected, which gives

$$\ell_{cx} > \left(\frac{c^2 x_c}{\omega_i^2} \right)^{1/3}, \quad \mathcal{K} \sin \theta > \ell_{cy}$$

where ℓ_{cy} is the turbulence poloidal correlation length, c is the light velocity, and $\mathcal{K} = \omega_i/c \cdot \sin \theta$ denotes the probing wavenumber poloidal component, where θ is the tilt angle. In addition, the analytical model is limited to the Gaussian antenna beams: $E \propto \exp[-y^2/(2\rho^2)]$, where ρ corresponds to the width of the antenna beam. All these assumptions allow us to take into account multiple small-angle scattering supposing arbitrary density and poloidal velocity profile, arbitrary turbulence spectra and statistically inhomogeneous turbulence.

For the sake of simplicity we consider the plasma slab with the linear density profile $n_e = n_c x/x_c$, perturbed by the statistically spatially homogeneous turbulence with Gaussian correlation function with characteristic length ℓ_c :

$$\langle \delta n(x, y) \delta n(x', y') \rangle = \delta n^2 \exp \left\{ -\frac{(x - x')^2 + (y - y')^2}{\ell_c^2} \right\} \quad (2)$$

In the code the turbulence was represented by the set of harmonics with amplitudes, chosen to provide (2), and random phases. The poloidal plasma flow is assumed to be homogeneous

$$\frac{dv}{dx} = 0$$

The results of [11] for this simplified model can be represented as follows. The registered signal power takes the form

$$\langle |A_s|^2 \rangle = \frac{P_i}{4} \frac{\exp \left[-\frac{2\mathcal{K}^2 \rho^2}{1 + \sigma \frac{2\rho^2}{\ell_c^2}} \right]}{\left\{ \left(1 + \sigma \frac{2\rho^2}{\ell_c^2} \right) \left[1 + \frac{c^2 x_c^2}{4\omega_i^2 \rho^4} \left(1 + \sigma_1 \frac{2\rho^2}{\ell_c^2} \right) \right] \right\}^{1/2}} \quad (3)$$

where P_i is the incident power and σ is the nonlinearity parameter [9]

$$\sigma = \sqrt{\pi} \frac{\omega_i^2}{c^2} \ell_c x_c \left(\frac{\delta n}{n_c} \right)^2 \left[1 + \ln \frac{8x_c}{\pi \ell_c} - \frac{\gamma}{2} \right], \quad \sigma_1 = \frac{\omega_i^2}{c^2} \left(\frac{\delta n}{n_c} \right)^2 \ell_c x_c$$

and $\gamma \simeq 0.577$ is the Euler constant.

One can easily see that due to the exponential suppression substantial signal can be registered only for the strong enough angular broadening of the probing beam

$$\delta k_y \simeq \frac{\sqrt{\sigma}}{\ell_c} \sim \mathcal{K}$$

Other suppressing factors $(1 + 2\sigma\rho^2/\ell_c^2)^{-1/2}$, $[1 + (1 + 2\sigma_1\rho^2/\ell_c^2) c^2 x_c^2 / (4\omega_i^2 \rho^4)]^{-1/2}$ are associated with the beam angular and spatial broadening correspondingly.

In accordance with [11] the Doppler reflectometry spectrum can be represented as

$$S(\omega) = \frac{\sqrt{2\pi}}{\delta\omega} \exp \left[-\frac{(\omega - \omega_i + \Delta\omega)^2}{2(\delta\omega)^2} \right]$$

where $\Delta\omega$ is the frequency shift

$$\Delta\omega = 2\mathcal{K}v \cdot \frac{2\sigma\rho^2/\ell_c^2}{1 + 2\sigma\rho^2/\ell_c^2} \quad (4)$$

which takes the form $\Delta\omega = 2\mathcal{K}v$ for $\sigma > \ell_c^2/(2\rho^2)$ and $\delta\omega$ is the spectral broadening:

$$(\delta\omega)^2 = \sigma \left(\langle \Omega^2 \rangle + \frac{v^2}{\ell_c^2} \cdot \frac{2}{1 + 2\sigma\rho^2/\ell_c^2} \right)$$

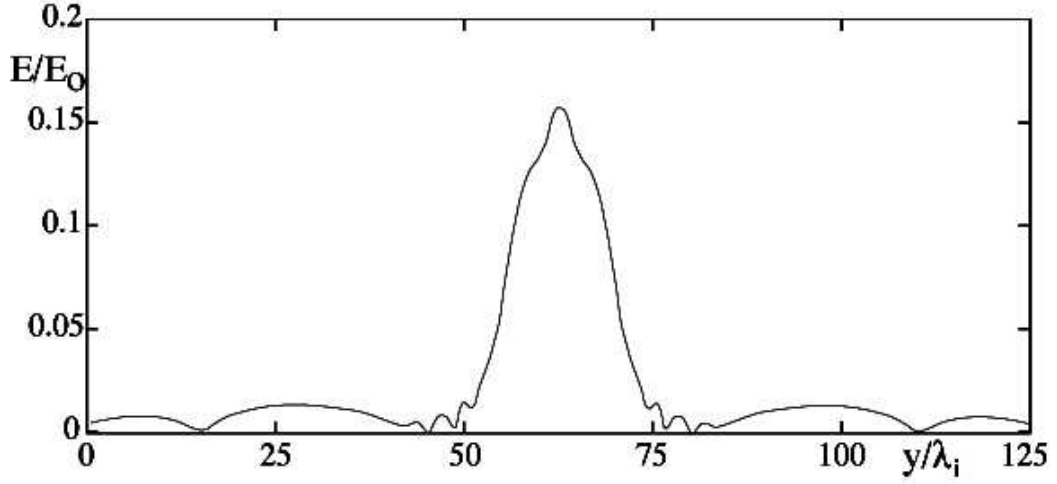


Figure 1: Absolute value of the antenna electric field on the plasma border vs. poloidal coordinate.

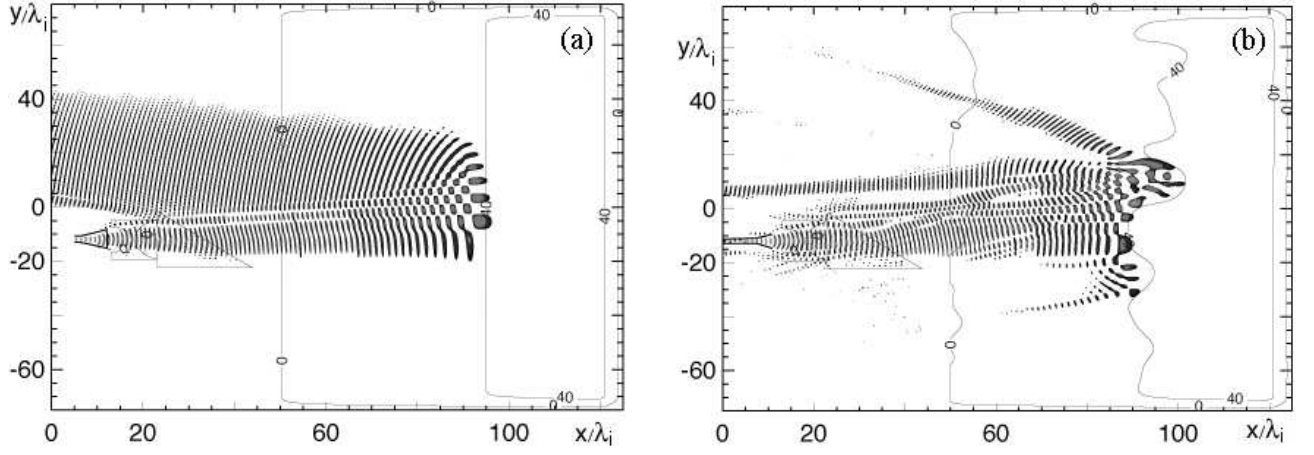


Figure 2: Absolute value of the antenna electric field in the plasma in the presence of the density fluctuations with r.m.s. amplitudes $\delta n/n_c = 0.1\%$ (a) and $\delta n/n_c = 10\%$ (b).

3. Full-wave simulation parameters and results

The probing wavelength was taken as $\lambda_i = 0.75$ cm, which corresponds to the probing frequency $f_i = 40$ MHz and critical density $n_c \simeq 2 \cdot 10^{13}$ cm $^{-3}$. The probing beam poloidal structure is represented in the figure 1.

The electric field in the plasma was calculated in the 2D rectangular area with dimensions $L_x = 150\lambda_i$, $L_y = 125\lambda_i$ in the presence of the homogeneous turbulence with correlation length $\ell_c = 4.5$ cm. The calculation results for different turbulence amplitudes are shown in the figure 2. It can be noted that the probing beam is completely distorted by the turbulence in case of $\delta n/n_c = 10\%$ (figure 2(b)).

The registered signal power is plotted in the figure 3(a) via turbulence amplitude. One can see the correspondence between the analytical expression (3) and the numerical calculation results for moderate turbulence amplitudes. Fast growth of the signal at the small turbulence amplitudes is associated with the decrease of exponential factor influence in (3). Following decrease of the signal corresponds to the influence of the denominators in (3), discussed above. The divergence of analytical formulae and numerical results in this region can be associated with the violation of the criterion (1).

The stationary structure, modelling the turbulence, moved in the poloidal direction with a velocity $v = 28.5$ km/s, imitating the plasma poloidal rotation. This results in the Doppler shift of the registered signal, which is plotted in the figure 3(b). It can be seen that the dependence of the spectrum shift on the turbulence amplitude, predicted by the analytical formula (4), is reproduced in the simulation results.

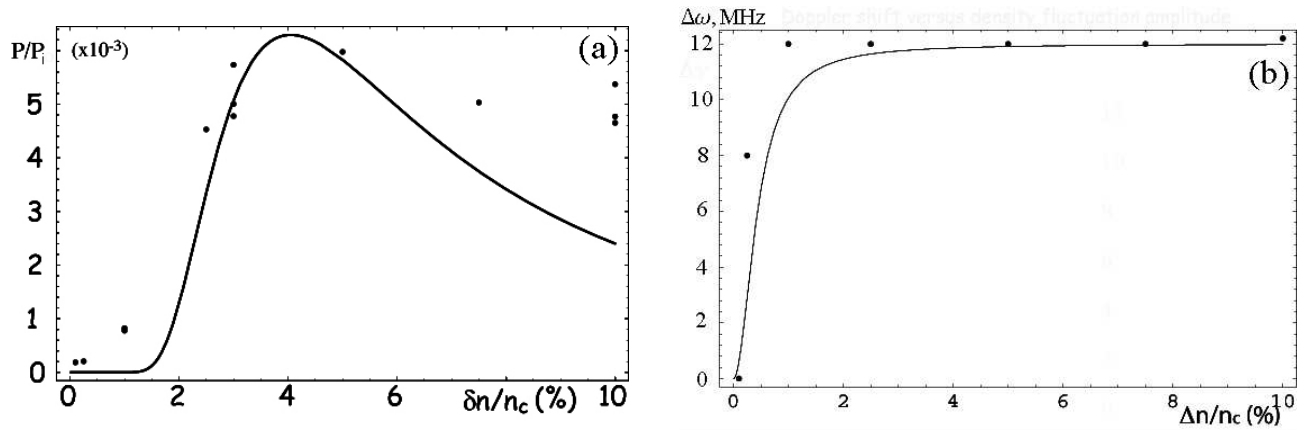


Figure 3: Registered signal power (a) and signal spectrum shift (b) vs. turbulence amplitude: analytical dependence (solid line) and simulation results (●).

4. Conclusion

Doppler reflectometry is considered in the nonlinear regime of dominating multiple forward scattering. Analytical expressions and full-wave simulation results for the power and spectrum shift of the registered signal are compared and shown to be in agreement in the region of analytical theory applicability.

The possibility to measure the fluctuation poloidal velocity with Doppler reflectometry technique even in regime of strong small-angle multi-scattering typical for large reactor-scale experiments is confirmed.

The work was supported by RFBR grants 04-02-16534, State support of leading scientific schools program (project no. 2159.2003.2), INTAS grant 01-2056 and NWO-RFBR grant 047.016.015. One of the authors (A.V.S.) is grateful to the Dynasty foundation for supporting his research.

References

1. Zou X L, Seak T F, Paume M, Chareau J M, Bottureau C and Leclert G 1999 *Proc. 26th EPS Conf. on Contr. Fusion and Plasma Physics (Maastricht)* ECA vol **23J** 1041
2. Bulanin V V, Lebedev S V, Levin L S and Roytershteyn V S 2000 *Plasma Phys. Rep.* **26** 813
3. Hirsch M, Holzhauser E, Baldzuhn J, Kurzan B and Scott B 2001 *Plasma Phys. Control. Fusion* **43** 1641
4. Conway G D, Schirmer J, Klenge S, Suttrop W, Holzhauser E and the ASDEX Upgrade Team 2004 *Plasma Phys. Control. Fusion* **46** 951
5. Hirsch M and Holzhauser E 2004 *Plasma Phys. Control. Fusion* **46** 593
6. Gusakov E Z and Yakovlev B O 2001 *Proc. 28th EPS Conf. on Contr. Fusion and Plasma Physics (Funchal)* ECA vol **25A** 361
7. Gusakov E Z and Surkov A V 2003 *Proc. 30th EPS Conference on Contr. Fusion and Plasma Physics (St.-Petersburg)* vol 27J (ECA) P-2.54.
8. Gusakov E Z and Surkov A V 2004 *Plasma Phys. Control. Fusion* **46** 1143
9. Denisov N G and Erukhimov L M 1966 *Geomagnetizm i Aeronomiya* **6** 695 (*In Russian*)
10. Gusakov E Z and Popov A Yu 2002 *Plasma Phys. Control. Fusion* **44** 2327
11. Gusakov E Z and Surkov A V 2005 *Plasma Phys. Control. Fusion* **47** (*To be published*)

Observation of coherent plasma flow perturbations using Doppler reflectometry on ASDEX Upgrade

G.D.Conway, B.Scott, J.Schirmer, M.Reich, A.Kendl¹ & ASDEX Upgrade Team

MPI Plasmaphysik, EURATOM-Association IPP, D-85748, Garching, Germany

¹*Institut für Theoretische Physik, Universität Innsbruck, A-6020, Innsbruck, Austria*

1. Introduction

By poloidally tilting the antenna of a microwave reflectometer, a Doppler frequency shift $f_D = u_{\perp} 2 \sin \theta / \lambda_o$ is induced in the reflected signal, which is proportional to the tilt angle θ and the perpendicular rotation velocity $u_{\perp} = v_{E \times B} + v_{ph}$ of the turbulence moving in the plasma [1]. Since u_{\perp} contains the $E \times B$ velocity, fluctuations in E_r will translate directly to f_D . Hence, in principle, the diagnostic can be used to measure \tilde{E}_r with high spatial and temporal resolution. f_D will also register fluctuations in B , v_{ph} or θ . However, $v_{ph} = 0$ since this requires a non-linear effect which is not evident. While MHD can modulate B and θ this effect can be detected since cutoff layer tilting will also modulate the reflected signal power which can be measured separately.

2. Analysis method

To extract fluctuations in f_D two techniques are used. A sliding FFT is applied to 20 MHz sampled I and Q signals from a dual channel V-band reflectometer [1] to produce time sequences of complex amplitude spectra. A weighted mean gives $f_D = \sum f.S(f) / \sum S(f)$ while the integrated spectra $A = \sum S(f)$ gives a measure of the density fluctuation amplitude at the selected k_{\perp} . An FFT of $f_D(t)$ then gives the \tilde{E}_r spectrum. Fig. 1 illustrates the measurement procedure. Alternatively, the instantaneous Doppler shift can be estimated from the differential phase $f_D(t) = \{\phi(t + \Delta t) - \phi(t)\} / \Delta t$ where ϕ is obtained from the Q/I signals. Although the reflectometer has a radial resolution of a few mm, the finite reflectometer beam diameter (\sim cm) limits the poloidal resolution to long wavelength E_r fluctuations. This is nevertheless ideal for studying zonal flows.

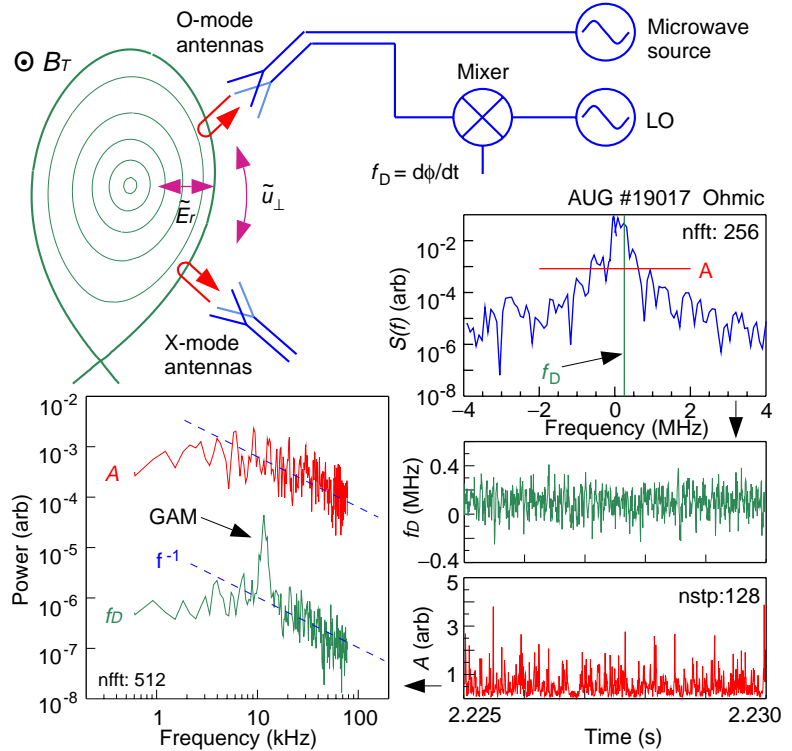


Figure 1: Schematic of measurement technique. Ohmic shot #19017 in X-mode at 60 GHz, $\rho_{pol} \approx 0.97$.

Although the reflectometer has a radial resolution of a few mm, the finite reflectometer beam diameter (\sim cm) limits the poloidal resolution to long wavelength E_r fluctuations. This is nevertheless ideal for studying zonal flows.

3. Flow perturbations

Zonal flows (ZF) and associated geodesic (GAM) oscillations are turbulence-generated time varying $E_r \times B$ rigid poloidal plasma flows with a $m = n = 0$ mode structure but finite radial extent, $k_r \neq 0$. They are of major interest for tokamak confinement since they are predicted to moderate drift-wave turbulence [2], and hence edge transport.

Detection of ZFs and GAMs is notoriously difficult since they have no magnetic feature, a negligible density perturbation and appear predominantly as low frequency (few kHz) coherent potential or radial electric field E_r fluctuations. Fig. 1 shows Doppler fluctuation data for an AUG ohmic shot which illustrates a narrow spectral peak in \tilde{f}_D but not in \tilde{A} .

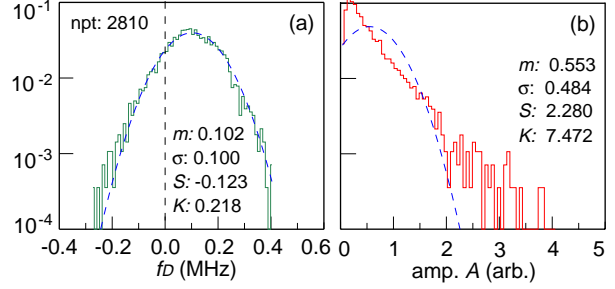


Figure 2: \tilde{f}_D and \tilde{A} pdf for ohmic #19017.

4. Results

Fig. 2 shows PDFs of f_D and A fluctuations for a typical ohmic discharge #19017 at $\rho_{pol} = 0.97$. \tilde{f}_D is nearly always Gaussian distributed while \tilde{A} is Rician or log-normal - typical of Radar signals. Their spectra, shown in fig. 1 are generally flat below ~ 10 kHz then roll-off with a spectral index $n \approx -1$, which reflects the underlying broad-band incoherent \tilde{E}_r background. A GAM oscillation when present appears as an exceptionally narrow dominant coherent peak around 5–20 kHz, even in the absence of MHD activity, with an amplitude of 1 to 2 orders of magnitude above the background.

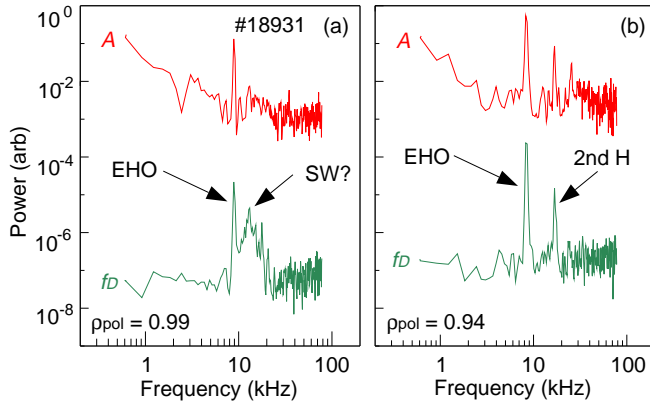


Figure 3: Effect of MHD in QH-mode shot #18931

If MHD is present then it appears in both f_D and A spectra as shown in fig. 3 for a QH-mode shot. Just inside the plasma boundary is a strong peak at 13 kHz in the f_D spectrum corresponding to a parallel ion sound wave (SW), while at the top of the density pedestal the Edge Harmonic Oscillation (EHO) at 7.9 kHz plus harmonics is dominant. Only the EHO appears in the Mirnov coil signals.

A variety of AUG ohmic, NBI L-mode and ECRH L-mode discharges have been investigated and a coherent single f_D spectral peak is normally observed in the low kHz range, close to the predicted GAM frequency. Theory [3] indicates that the GAM frequency should scale as $\omega_{GAM} = Gc_s/R$ where $c_s = \{k(T_e + T_i)/M\}^{1/2}$ is the ion acoustic speed and R the major radius. G is a scale factor of the order of 1. Experimentally f_{GAM} is indeed seen to scale linearly with the local $\sqrt{T_e + T_i}$, as shown in fig. 4, also with no obvious dependence on B_T or n_e - thus supporting the hypothesis that the oscillation is a GAM. T_e measurements are from ECE while T_i is from Li-beam CXRS when

available. When T_i is not available then it is scaled from T_e using similar shots. Fig. 4 shows considerable variation in the scaling constant G between various types of shots.

Both theory and modelling results suggest that the safety factor q and plasma shape (elongation) are also important parameters [3,4] in ZF behaviour. Experimentally f_{GAM} is seen to scale inversely with the elongation κ and directly with q_{95} . However, more data is required to fully determine all the parameter dependencies. Radially the GAM oscillation is only seen inside the plasma boundary (GAMs exist on closed field lines) in a narrow region coinciding with the edge density pedestal. This is the same region of high radial shear in the $E \times B$ velocity, as shown in fig. 5 for the ohmic shot #18813.

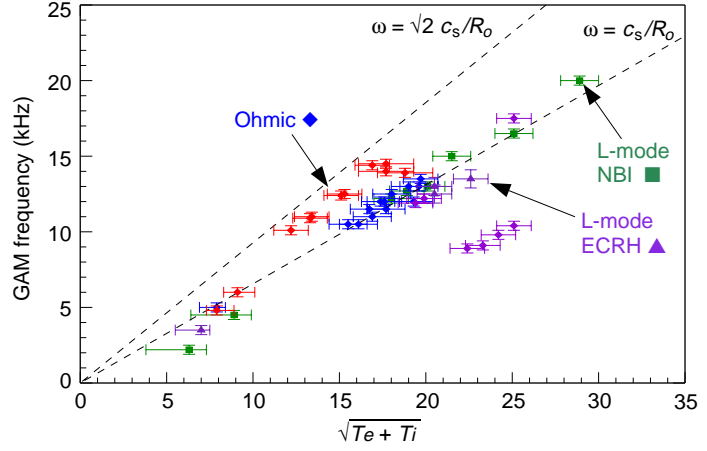


Figure 4: GAM frequency vs $\sqrt{T_e + T_i}$ for ohmic, NBI & ECRH L-modes.

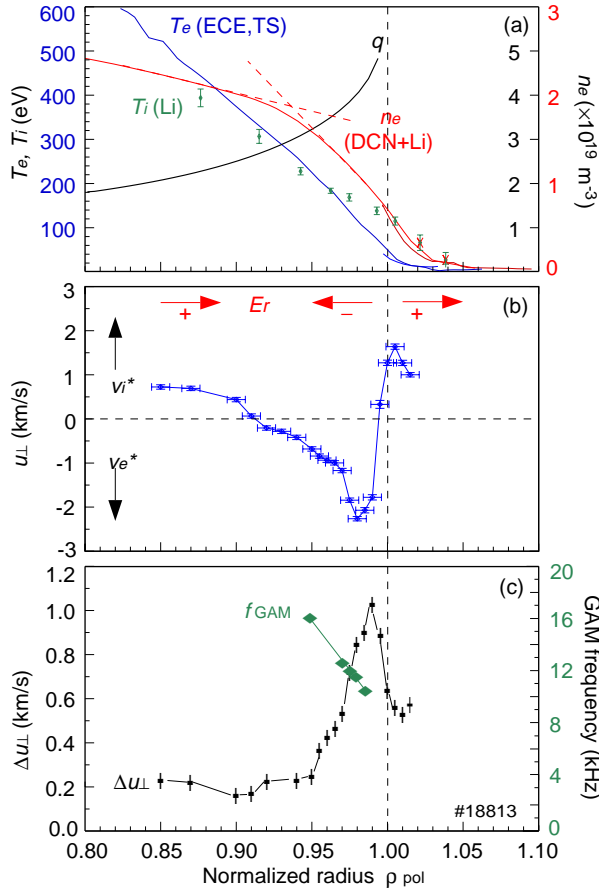


Figure 5: Radial profiles of (a) T_e , T_i , q and n_e , (b) u_{\perp} , (c) Δu_{\perp} and f_{GAM} for #18813.

The u_{\perp} velocity flows in the ion diamagnetic direction in the SOL but reverses inside the separatrix to form an E_r well across the density pedestal. The well depth increases in L and H-modes as the edge transport barrier strengthens - see [1] for further details. Just outside the E_r well is an increase in the overall f_D RMS fluctuation level. The GAM frequency increases with decreasing radius (as T_e and T_i rise) but stops at the top of the density pedestal.

To date no coherent f_D oscillations have been observed in the plasma core region. A GAM oscillation is not always found in the edge either. In highly collisional plasmas (high density and low temperature) GAMs are notably absent, which is consistent with collisional damping of ZF. Further, GAMs have so far not been observed in H-mode conditions, c.f. the QH-mode case in fig. 3. The GAM spectral peak intensity also appears to be intermittent. Fig. 6

shows a time resolved spectrogram of \tilde{f}_D where the 12 kHz GAM is modulated by 50%, as shown by the frequency integrated traces below. Possible explanations for the intermittency might include: a density variation sweeping the reflectometer cutoff across the radially localised GAM (however, the cutoff layer displacement to GAM radial width would need to be substantial, which is not observed) or the GAM position may be jumping radially, but again there is no evidence of T_e modulation in ECE. More plausibly, the GAM intensity envelope is time-modulated by the low frequency ZF, as is predicted by modelling results [5] and indicated by the counter modulation in the \tilde{A} level.

4. Discussion and conclusions

The measurements presented here demonstrate the possibility to measure E_r fluctuations in the tokamak edge region. Coherent modes have been observed in the perpendicular plasma flow in a range of ohmic and L-mode discharges, with no associated magnetic perturbation and negligible density fluctuation. The mode frequencies scale with the ion acoustic velocity. Two branches have been identified: parallel sound waves and Geodesic Acoustic Modes. However,

the “zero” frequency zonal flow has not yet been conclusively observed. GAMs are seen only in the plasma edge density gradient region and appear to be linked with the pedestal position. Coherent flow oscillations have not yet been found in the core plasma region. The GAM has a finite radial extent which is consistent with the expected $k_r \neq 0$. Confirmatory measurements are in progress using a second Doppler reflectometer channel to obtain the \tilde{f}_D radial correlation length directly. The poloidally displaced O-mode and X-mode antennas might also be used to check the $m = 0$ (potential) or $m = \pm 1$ (density) mode structure. L-mode data show notably larger GAMs, which may be expected considering the stronger E_r gradients and plasma vorticity present. The absence of GAMs in QH-modes may be related to the lower turbulence levels (less ZF drive) and/or the larger E_r shearing present. A more extensive presentation and discussion of these measurements may be found in a forthcoming paper [6].

5. References

- [1] G.D.Conway *et al*, Plasma Phys. Control. Fusion **46**, 951 (2004)
- [2] P.H.Diamond *et al*, Plasma Phys. Control. Fusion **47**, R35 (2005)
- [3] N.Winsor *et al*, Phys. Fluids **11**, 2448 (1968)
- [4] K.Hallatschek and D.Biskamp, Phys. Rev. Lett. **86**, 1223 (2001)
- [5] M.Ramisch *et al*, New J. Phys. **5**, 12 (2003)
- [6] G.D.Conway *et al*, Plasma Phys. Control. Fusion **47** (2005) In press.

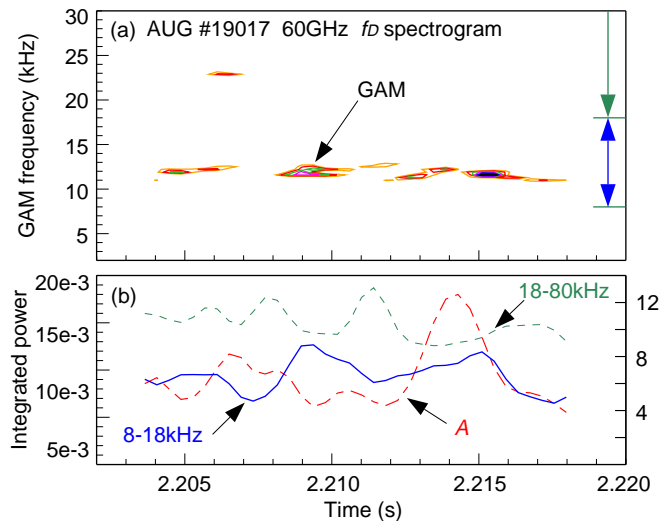


Figure 6: f_D spectrogram for ohmic #19017.

Radial Correlation Doppler Reflectometry on ASDEX Upgrade

J.Schirmer, G.D.Conway, H.Zohm, W.Suttrop, E. Holzhauser*, & ASDEX Upgrade Team

Max-Planck Institut für Plasmaphysik, Euratom-Association IPP, Garching, D-85748, Germany

*Institut für Plasmaforschung, Universität Stuttgart, Stuttgart, D-70569, Germany

Introduction

Radial correlation Doppler reflectometry is a new diagnostic technique which has been developed on ASDEX Upgrade. It allows for the measurement of several plasma properties such as the perpendicular rotation of the plasma (u_{\perp}), the radial electric field (E_r) and the radial electric field shear (dE_r/dr). The radial electric field shear in H-mode is believed to be responsible for the confinement improvement and reduction of anomalous transport observed [1] and hence, this measurement is of key interest. Presently, there is a lack of experimental E_r shear data available in tokamak devices and so a diagnostic which can provide such a measurement is valuable. In addition, the diagnostic is capable of measuring characteristics of the turbulence such as density fluctuations and the radial correlation lengths of the turbulence (L_r). By correlating the properties of the turbulence with the magnitude of the E_r shear, further insight can be gained about the plasma confinement. In this paper, several results from this new diagnostic technique will be presented, with particular focus on recent E_r shear and L_r measurements.

Technique

The correlation Doppler reflectometry system, installed on ASDEX Upgrade, consists of two identical V-Band heterodyne reflectometers with steppable launch frequencies (between 50 and 75 GHz) and selectable O or X-mode polarization [2]. In this technique, the two Doppler reflectometer channels are connected to the same antenna pair so that they launch microwaves with the same line of sight simultaneously into the plasma. The microwaves have different launch frequencies and therefore reflect from different radial positions in the plasma. From the Doppler shifts in the received microwave signals, one obtains the perpendicular rotation of the turbulence in the plasma (u_{\perp}). The velocity is given by $u_{\perp} = f_D \lambda / 2\sin\theta$ where f_D is the doppler shift, λ is the wavelength of the incident microwave and θ is the geometric tilt angle between the plasma flux surface normal and the incident microwave beam. u_{\perp} is the sum of the $E \times B$ velocity, $v_{E \times B}$, and the intrinsic phase velocity of the turbulence, v_{ph} . In the edge region for drift wave turbulence, v_{ph} is negligible [3] and hence, the radial electric field can be determined from the equation $E_r = -u_{\perp} B_{tot}$. Figure 1 shows an example of a radial electric field profile measured by Doppler reflectometry in an ohmic discharge [4]. The radial cutoff layer positions are evaluated from the

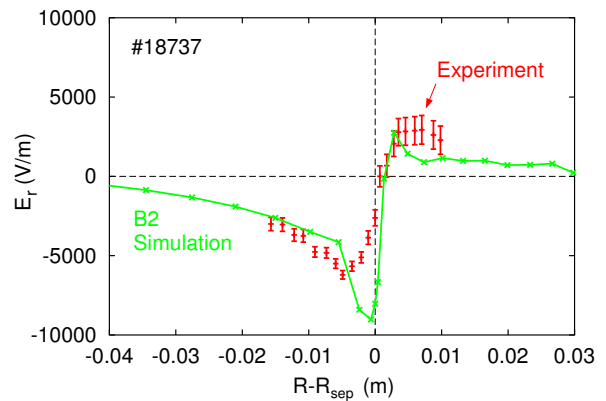
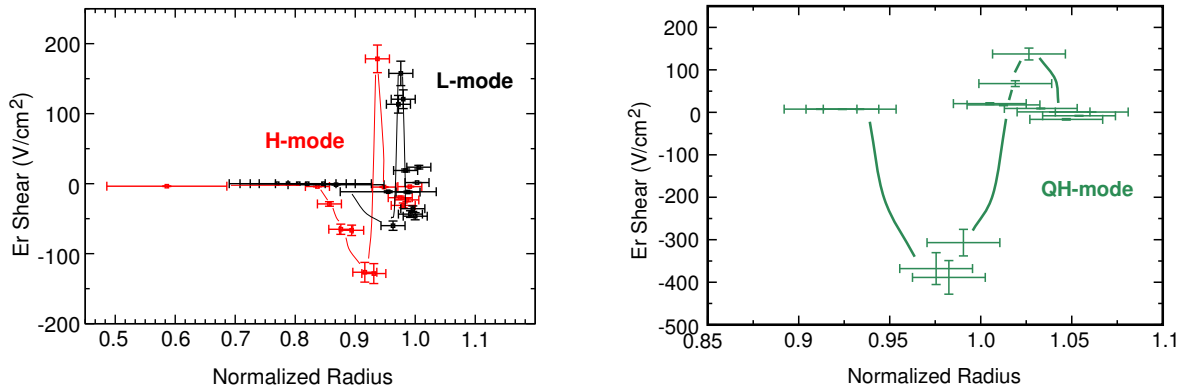


Figure 1: Radial Electric Field Profile in an Ohmic Discharge (#18737).

density profile and the magnetic field profile when using X-mode polarization. The n_e profile is obtained from other diagnostics such as Thomson-scattering, lithium beam and swept frequency profile reflectometry. Also shown in Figure 1 is the radial electric field modelled by the plasma fluid code B2 [5,6] for the same discharge. The code takes into account experimental density and temperature profiles as well as the drifts involved. The good agreement in both magnitude and position of the two profiles supports that the Doppler reflectometer is indeed measuring the E_r at the edge.

Two correlation measurement techniques have been developed: (1) Sweeping the two reflectometer channels but keeping the frequency difference between them fixed and then taking the difference between the two simultaneous E_r values divided by the channel radial separation gives a radial profile of the instantaneous E_r shear (dE_r/dr). Typically, a frequency sweep pattern of 1 GHz steps from 50 to 74 GHz in 100 ms with a fixed 2 GHz separation is used. (2) Alternatively, keeping the frequency of one reflectometer channel constant and sweeping the frequency of the second permits the correlation properties of the turbulence to be measured. Here, a sweep every 50 ms with a frequency difference between the two channels starting at 0.1 GHz (to avoid any cross talk between the two channels) and increasing logarithmically was found to be sufficient. The channel separation when the cross correlation between the two fluctuation signals drops to $1/e$ gives a measure of the spatial correlation of the turbulence (designated the radial correlation length, L_r) as a function of k_{\perp} .

Results: E_r Shear



(a) L-mode (#18103) versus H-mode (#17973)

(b) Quiescent H-mode (#18925)

Figure 2: dE_r/dr profiles showing enhanced edge shear in H and QH-modes. Note the different scale.

Figure 2 shows example E_r shear profiles measured during an L-mode, an ELMy H-mode and a Quiescent H-mode discharge. Three main observations can be made from these profiles. First, the shear is localized at the plasma edge and practically zero elsewhere. Second, the shear is positive near the separatrix and negative a few cm within the plasma edge coinciding with the pedestal. Thirdly, an increase of the negative edge shear is linked to an increase in plasma confinement. Typically at ASDEX Upgrade the maximum negative edge E_r shear measured in L-modes is between 0 and -75 V/cm^2 , in H-modes between -150 and -250 V/cm^2 and, in QH-modes between -400 and -500 V/cm^2 . Biglari, Diamond and Terry (BDT model) [7] predict that an increase in absolute shear suppresses density fluctuations and stabilizes

the turbulence. The data shown in Figure 2 is consistent with this model. Also, in Figure 2a, it can be seen that the H-mode E_r shear profile is shifted inwards in comparison to the L-mode profile. This may be due to the density pedestal which steepens and in this case moved inwards during the H-mode.

Results: Radial Correlation Lengths of the Turbulence

Radial correlation lengths of the turbulence (L_r) have also been measured using the Doppler correlation system. Recent results are presented here. With heterodyne and quadrature detection, there are a range of reflectometer fluctuation signals available to correlate. The reflectometer signals tested were the amplitude (A), phase (ϕ), homodyne in-phase ($I = A\cos\phi$), homodyne quadrature ($Q = A\sin\phi$), and complex ($I + iQ$) signals. It was found that the complex and homodyne signals consistently give larger L_r than the amplitude and phase signals [8]. This is most likely due to the fact that the homodyne and complex signals include both amplitude and phase information and therefore do not assign too much weight to either parameter, particularly during periods of low reflected power. As a result, the L_r measurements presented here are obtained by cross correlating the complex reflectometer signals.

Figure 3 shows how L_r varies with plasma position. The data was collected in the early L-mode phases of ASDEX Upgrade's Standard H-mode discharges. All plasma parameters were constant during the time the Doppler correlation data was collected in O-mode configuration. The figure shows L_r increasing into the plasma core, ranging from about 0.40 cm at $\rho_{pol} \approx 0.92$ to 1.75 cm at $\rho_{pol} \approx 0.35$. The magnitude of L_r is similar to those measured on DIII-D using a standard correlation reflectometer ($k_{\perp} = 0$) [9]. Note that the radial position of the core measurements will be corrected using TOR-BEAM raytracing calculations [10] to account for the strong beam refractive effects occurring in the plasma core. It is expected that the core L_r measurements will move radially outward.

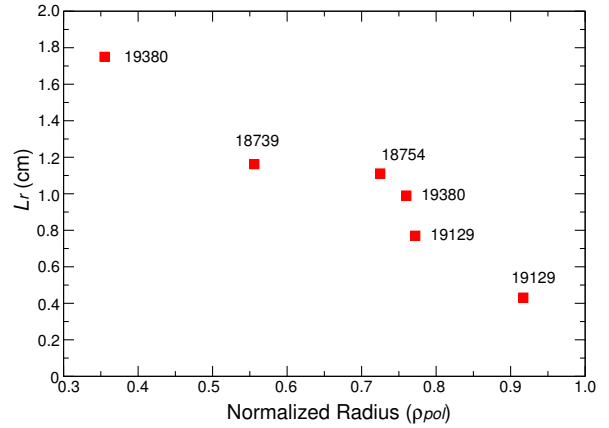


Figure 3: L_r measured as a function of normalized radius during L-mode phases in ASDEX Upgrade's Standard H-mode discharges (#18739-19380).

The relationship between L_r and the turbulent wavenumber k_{\perp} can also be examined with the correlation Doppler system since the tilted antennae of a Doppler reflectometer introduces a non-zero turbulent wavenumber, k_{\perp} . The wavenumber is given by the Bragg equation: $k_{\perp} = 4\pi \sin\theta/\lambda$ where θ is the geometric tilt angle between the plasma flux surface normal and the incident microwave beam and λ is the wavelength of the incident microwave. The antennae on ASDEX Upgrade are fixed in tilt angle so to vary k_{\perp} , the plasma shape is scanned from low to high triangularity. This was performed in two L-mode upper single null discharges (#19146 and #19148) and the results are shown in Figure 4. Surprisingly L_r increases with k_{\perp} . Simple theory predicts the opposite since one would expect smaller wavelengths (larger k_{\perp}) to probe smaller structures (smaller L_r). A possible reason for this unexpected trend is that by changing the plasma shape, the nature of the edge turbulence is changed. Previous measurements have shown that the radial electric field and its associated shear changes with plasma shape [11]. Another possibility is that the Doppler reflectometer is not measuring L_r alone but rather in addition some other component such as the poloidal correlation length L_{pol} .

To test these hypotheses, a repeat of this experiment is planned with a new tiltable antenna. This will allow the measurement to be performed under constant plasma conditions. As well, 2D Full Wave Finite Difference modelling of the reflectometer response has begun. The 2D code includes the experimental density, magnetic field and antenna characteristics during discharges #19146 and #19148. The overall goal will be to recreate the L_r experimental measurements and in particular, examine the dependence of L_r on k_{\perp} .

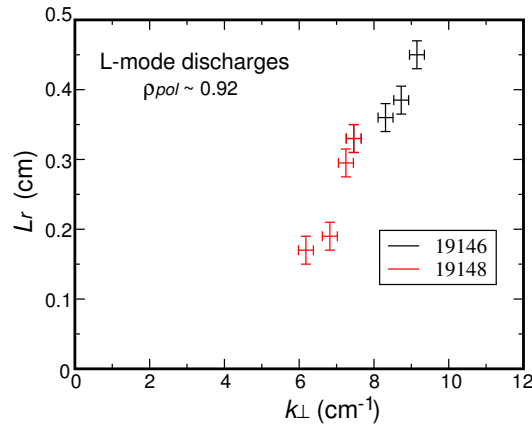


Figure 4: L_r measured as a function of the turbulent wavenumber k_{\perp} during L-mode discharges (#19146 and #19148)

Summary

In conclusion, using the new Doppler correlation reflectometer system on ASDEX Upgrade successful measurements of dE_r/dr and L_r have been made in various plasma scenarios. The edge E_r shear measurements show an increase in absolute value in H-modes and QH-modes. The L_r measurements show an increase of L_r into the plasma core as expected. However, the relationship between L_r and k_{\perp} give surprising results as L_r increases with k_{\perp} . This result has motivated an investigation using a 2D Full Wave Finite Difference code to simulate the reflectometer response and in particular recreate the experimental L_r measurements.

References

- [1] K. H. Burrell, *Phys. Plasmas* **4**, 1499 (1997).
- [2] G. D. Conway *et al*, *Plasma Phys. Control. Fusion* **46**, 951 (2004).
- [3] M. Hirsch *et al*, *Plasma Phys. Control. Fusion* **46**, 593 (2004).
- [4] L. D. Horton *et al*, *Nuclear Fusion* to be published (2005).
- [5] D. P. Coster *et al*, *Proc. of the 18th IAEA Conference, Fusion Energy, IAEA-CN-77/EXP5/32* (2000).
- [6] D. P. Coster *et al*, *Proc. of the 19th IAEA Conference, Fusion Energy, IAEA-CN-94/TH/P2-13* (2002).
- [7] H. Biglari *et al*, *Phys. Fluids B* **2**, 1 (1990).
- [8] J. Schirmer *et al*, *31st EPS Conference on Controlled Fusion and Plasma Physics*, P4.127 (2004).
- [9] T. L. Rhodes *et al*, *Phys. Plasmas* **9**, 2141 (2002).
- [10] E. Poli *et al*, *Computer Physics Communications* **136**, 90 (2001).
- [11] H. Meyer *et al*, *Nuclear Fusion* to be published (2005).

Core density fluctuations observed on Tore Supra by Doppler back-scattering: perpendicular velocity modification in high power ICRH experiments

P. Hennequin, C. Honoré, A. Truc, A. Quéméneur,
Laboratoire de Physique et Technologie des Plasmas, CNRS (UMR 7648)
Ecole Polytechnique, F-91128 Palaiseau cedex
C. Fenzi-Bonizec¹, C. Bourdelle¹, X. Garbet¹, G.T. Hoang¹
and the Tore Supra team

¹ Association Euratom-CEA, CEA/DSM/DRFC,
Centre de Cadarache, F-13108 St Paul lèz Durance cedex

Abstract

Backscattering of a microwave beam close to the cut-off allows for measurement of density fluctuations $\tilde{n}(\vec{k}_\perp)$ at a specified wave-number, selected by the scattering geometry $\vec{k}_\perp = -2\vec{k}_i$, where k_i is the beam wave-number at the reflection layer. On the system installed on Tore Supra, both the scattering wave-number k_\perp and the scattering localisation r/a can be changed during the shot for probing $.5 < r/a < .95$ and $2 < k < 15 \text{ cm}^{-1}$, owing to the steppable probing frequency and the motorised antenna. The perpendicular fluctuation velocity in the laboratory frame is obtained from the Doppler shift of the frequency spectrum $\Delta\omega = k_\perp v_\perp$. It is dominated by the plasma $E_r \times B$ velocity. In the core, the latter is mainly due to the projection of the toroidal velocity, as this is shown by comparison with measurements by charge exchange recombination spectroscopy. In the set of analysed Tore Supra ohmic and ICRH plasmas, the observed rotation is consistent with a poloidal velocity in the electron diamagnetic direction and/or a toroidal velocity in the counter current direction. Strong modification of velocity profiles and turbulence level are observed together with improved confinement in experiments with ICRH heating at high power and high concentration of minority ions. Preliminary results on associated wave number spectra will also be shown.

1 Introduction

Progress in understanding turbulence and anomalous transport requires localised measurements of turbulence characteristics, i.e. amplitude and typical length scales, or better the k spectrum, and their temporal dynamics. This is particularly the case for improved confinement regime where the improvement is generally not global (in space, in wavenumber, for ion or electron channel). In these regimes, the plasma velocity and its shear have been shown to play a crucial role and are important to be simultaneously measured with the fluctuation level. Furthermore, theoretical comprehension and modeling advances [1] now make detailed comparison with experiments meaningful [2]: knowledge of turbulent scales is especially crucial for identification of instabilities implicated that might have different drives and scales.

Taking advantage of both scattering and reflectometry technics, Doppler backscattering has emerged as a promising means giving access to fluctuations at a specific scale, and their velocity, in a volume small compared to plasma minor radius. It is based on the possibility to separately detect the field backscattered on fluctuations along the beam path from the field reflected at the cut-off layer (standard reflectometry), by launching the probing beam in oblique incidence with respect to the cut off layer. Fluctuations whose wavenumber matches the Bragg rule are selected $\vec{k}_f = -2\vec{k}_i$, where \vec{k}_i is the *local* probing wavevector. The localised swelling of the incident field at the cut-off, amplifies the scattering process and allows localisation of the scattering process near the cut-off layer. At the cutoff, the probing beam wave-vector is determined by its angle θ to the cut-off normal: $k_i = k_o \sin \theta$ (slab geometry) where k_o is the vacuum wavenumber. This techniques thus provides the instantaneous spatial Fourier analysis of density fluctuations, $\tilde{n}(\vec{k}, t) = \int_V n(\vec{r}, t) e^{i\vec{k}\cdot\vec{r}} d\vec{r}$, acting as a band pass filter in k -space around $\vec{k} = -2\vec{k}_i$ at the cut-off layer. The wavenumber selectivity Δk is related to the overlapping and shape of the probing and scattered beams. The turbulence frequency spectrum is Doppler shifted $\Delta\omega = \vec{k}_f \cdot \vec{v}_f$, that allows to determine the fluctuation velocity. Also referred to as Doppler reflectometry, it shares with standard fluctuation (CW) reflectometry good spatial and temporal resolution, easy access and low cost.

2 The Doppler back-scattering system on Tore Supra

The diagnostic has been designed to be able to measure the k -spectrum (from medium to small scale) and the velocity profiles of the fluctuations: exploring k and r space yields the choice of a tiltable antenna and a probing frequency in the V band (50-75 GHz range). This corresponds to O-mode cut-off density from 3.1 to $7 \cdot 10^{19} \text{ m}^{-3}$ suitable for enhanced performance regimes [3, 4].

The antenna pattern must be optimized to separate the reflected signal from the backscattered one and to get a good k selectivity. Gaussian beams have been preferred for their low divergence: a gaussian optics lens antenna associated with a corrugated horn, yields a beam waist of 40 mm (divergence 2.2° HPBW) The whole system is at 125 cm from the plasma (potential heavy heat load on non actively cooled components leads to limit plasma view angle from diagnostic ports, keeping away the windows and limiting their size). The antenna and the attached millimetric unit (see below) is tiltable and motorized, with an angular excursion from -1° to 10° (angle of the line of sight with respect to the last closed magnetic surface in the range -3° to 20°).

In O mode, the selected wave number at the cut-off is mainly poloidal. However, since the density fluctuations are nearly aligned along the magnetic field lines ($k_{\parallel} \ll k_{\perp}$), the beam wavevector should have a small toroidal component to fulfill the Bragg selection condition near the cut-off layer. The beam is thus launched with a small toroidal tilt angle so that the wavevector makes at the cut-off an angle ξ_k with the poloidal plane nearly equal to the pitch angle of the magnetic field lines (around 5° depending on the safety factor profile). This condition is not critical due to the beam slight divergence, but important to get a good sensitivity.

The actual incident angle varies with the plasma shape, cut-off layer position and refraction. Ray tracing is therefore needed to evaluate the reflection layer location r

from where the scattered signal is expected to come and k at the reflection layer. It is computed in 3D geometry with geometrical optics approximation [5], and takes into account the divergence of a gaussian beam: the beam is simulated with multiple rays diverging from the center ray, whose propagation is conditioned by its neighbors.

The microwave part of the system is based on a fluctuation reflectometer scheme with heterodyne detection with a single side band modulator (modulation frequency 80MHz, IQ detection) which allows for measuring the turbulence propagation velocity through the Doppler shift $S(k_{\perp}, \omega) \rightarrow \Delta\omega \sim k_{\perp} v_{\perp}$.

Choice has been made of stable source, a synthesizer, in the 12.5 to 19 GHz frequency range, with a typical switch time between steps smaller than 5 ms with a step duration from 5 ms, that can also be linearly swept in 5 ms typically. This signal is set to the 50 to 75 GHz range by use of an active multiplier which provides an output power of the order of 10 mW. It is then sent to the plasma through the high gain antenna via a high directivity coupler, to separate emission and reception signals. Modulation and demodulation are performed with the same quartz oscillator. A 12 bits VME system controls the data acquisition at 4 MHz acquisition rate, to account for the signal bandwidth expected (Doppler shift up to 1 MHz).

3 Probing frequency and tilt angle combined scans

Changing the probing frequency F changes both r/a and k and the same for θ . Thus obtaining radial profile at fixed k or wave-number dependence at fixed radius requires combined scans that are realised on a stationary phase of the plasma as shown in figure 1, by programing several sets of frequency steps during a tilt angle sweep. Figure 1(b) is a zoom showing the frequency steps timing: acquisition is triggered at each pre-set probing frequency step, recording typically 32k samples per step (10 steps require less than 200 ms), the whole pattern can be repeated several times during the shot; the angle sweep is sufficiently slow (.5 to 2°/s) to ensure that the angle has not changed much during the acquisition time (typically 8 ms).

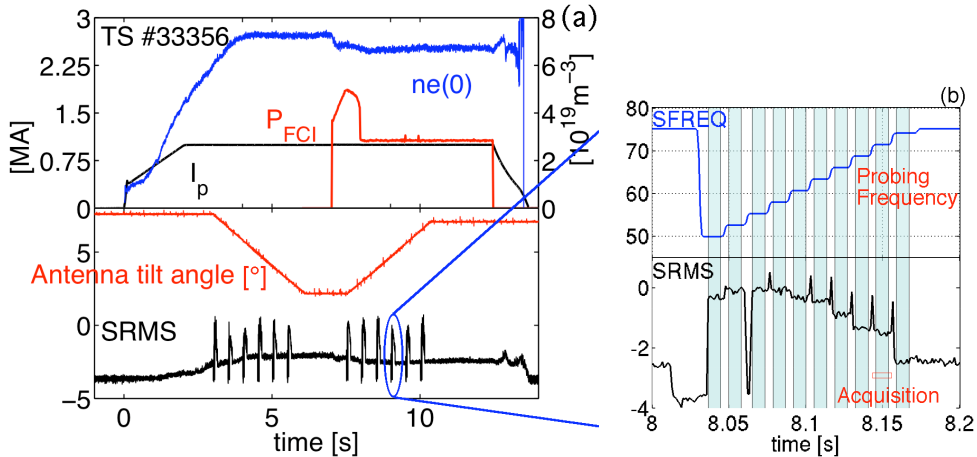
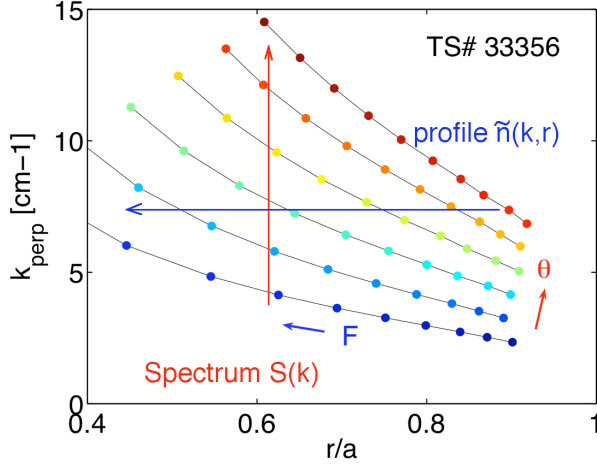


Figure 1: Combined probing frequency (in blue, b) and antenna tilt (red, a) scan scenarios during stationary plasma phase; black line is the back-scattered signal rms value

For each (F, θ) and plasma conditions, ray tracing is used to determine $(r/a, k)$ which map is shown on figure 2.



Density fluctuation profile can be measured for a fixed wave number (around $k_s = 8 \text{ cm}^{-1}$) from $r/a = 0.3$ to $r/a = 0.9$, and density fluctuation k spectrum can be obtained for a smaller region, for example around $r/a = 0.6$, range of k values is between $k_s = 4 \text{ cm}^{-1}$ and $k_s = 15 \text{ cm}^{-1}$. The access region both in k and real space highly depends on the plasma density profile, beam frequency and tilt angle combinations.

Figure 2: k_{\perp} versus r/a for the probing frequency and antenna tilt angle scan of figure 1

3.1 Doppler spectra vs r and k_{\perp}

Figure 3 shows the frequency spectra obtained for selected values of $r/a (\pm 0.05)$ and different k 's, for figure 1 plasma in the ohmic phase (a) and during ICRF heating at high power (b). The sign of the Doppler shift corresponds to the electron diamagnetic direction. There is no $f = 0$ component, i.e. the backscattered signal is separated from the reflected one, except for the magenta and black line of figure 3 (b), which corresponds to large values of the tilt angle. In these cases, the probing beam is deflected towards the wall, where it intersects metallic elements (ripple protection...) and is probably reflected and come back to the antenna experiencing forward scattering (and thus, frequency broadening). However, the Doppler shift increases with k as expected (see § 3.2). The spectrum width is rather small in the ohmic case, less than 100 kHz, increasing with k and heating power as previously observed on other tokamaks.

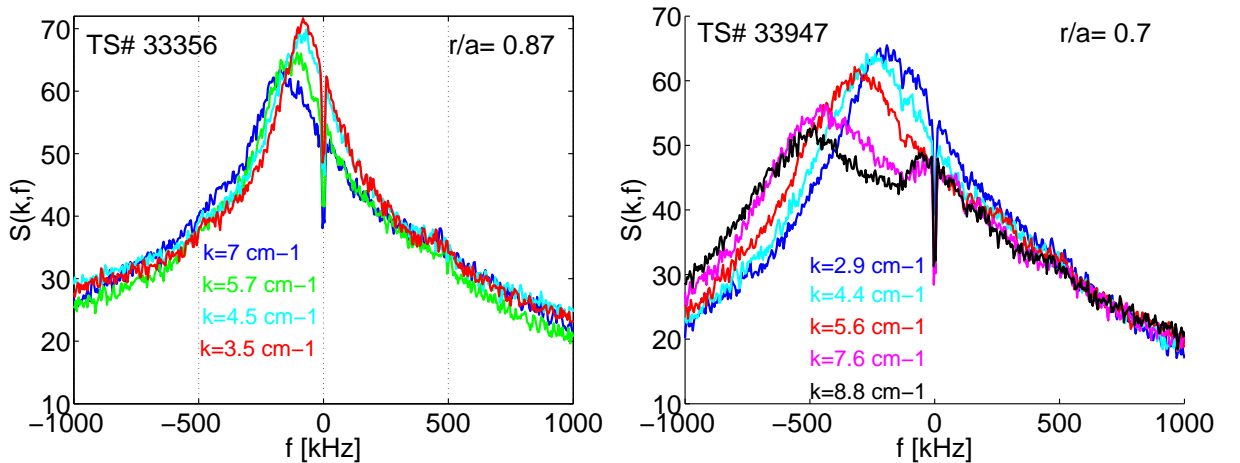


Figure 3: Frequency spectra at fixed r/a and various k for ohmic plasma, $n_l = 7 \cdot 10^{19} \text{ m}^{-2}$ (a) and during ICRH, $P = 8 \text{ MW}$, $n_l = 8 \cdot 10^{19} \text{ m}^{-2}$ (b).

3.2 Perpendicular fluctuation velocity radial profile

Fluctuation perpendicular velocity is derived from the Doppler shift, $v_{\perp} = \Delta\omega/k$ and is plotted as a function of k (figure 4(b)): fluctuation velocity very weakly depends on k

(within the error bar) as expected for fluctuation velocity dominated by the flow velocity, i.e. fluctuations play the role of tracers. The fluctuation perpendicular velocity profile (figure 4) is the derived (for $k = 4 \pm .5 \text{ cm}^{-1}$) for the ohmic and heating phase of figure 1. Values and shape are consistent with previous measurement in ohmic [6]. v_{\perp} decreases towards the center, and slightly to the edge. However the edge has not yet been probed in this configuration and requires high density plasmas (the smallest probing frequency, 50 MHz, corresponds to a density of $3 \cdot 10^{19} \text{ m}^{-3}$).

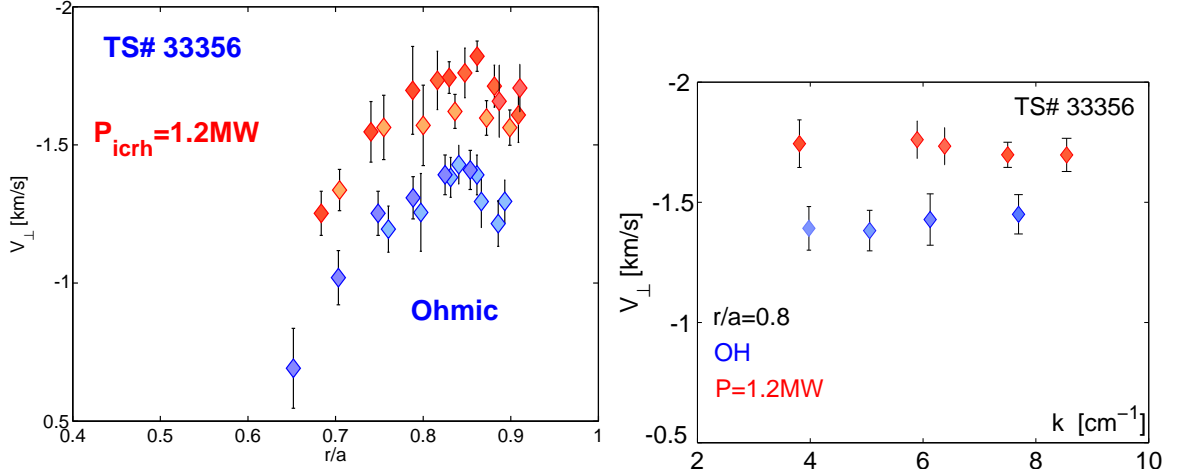


Figure 4: Fluctuation perpendicular velocity profile (at fixed $k = 4 \pm .5 \text{ cm}^{-1}$) for ohmic and heating phase, $n_l = 7 \cdot 10^{19} \text{ m}^{-2}$ (a), and its dependence with k at fixed radius (b).

3.3 Fluctuation k spectrum

The power spectral density $\propto \tilde{n}(\vec{k}_{\perp})$ is then evaluated as a function of k by integrating frequency spectra. The k -spectrum, plotted for a ohmic plasma at fixed radius in logarithmic scale (5a) is similar to observations from CO $_2$ laser scattering experiment on Tore Supra [10] with a spectral index ~ 3 at low k , increasing at higher k , or an exponential dependence as shown in semi-logarithmic plot (b).

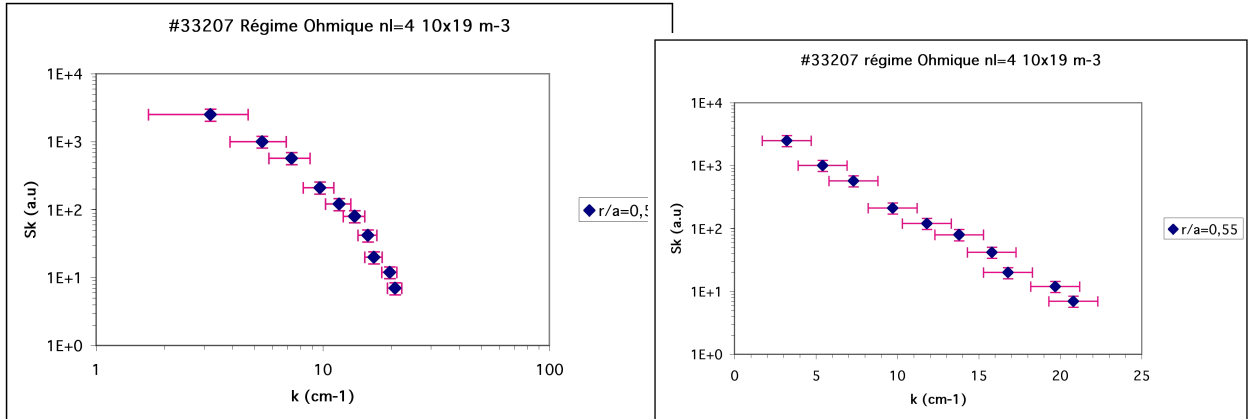
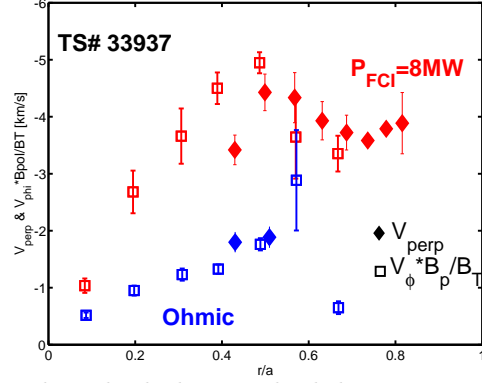


Figure 5: Fluctuation k spectra in ohmic plasmas.

4 fluctuation velocity compared with $V_{E \times B}$

The Doppler scattering experiment gives a measurement of the perpendicular fluctuation velocity in the laboratory frame: $v_{\perp} = V_{E \times B, \perp} + \langle \omega/k \rangle$. The radial component of the electric field generates the perpendicular component $V_{E \times B, \perp} = -E_r/B$. It can be derived from the radial projection of the force balance equation: $E_r = v_{\phi} B_{\theta} - v_{\theta} B_{\phi} - \nabla P_i / n q_i$.

The toroidal rotation velocity is measured by charge exchange recombination spectroscopy. Its contribution to $V_{E \times B, \perp} = -v_{\phi} B_{\theta} / B$ is compared to v_{\perp} in figure 6, showing close values in various plasma conditions, as observed with other Doppler reflectometry systems [7, 8, 9] *Figure 6: Profiles of fluctuation perpendicular velocity (closed symbol) and toroidal term $-v_{\phi} B_{\theta} / B$ during ohmic (blue) and heating phase (red), $n_l = 5.5 \cdot 10^{19} \text{ m}^{-2}$.*



The plasma scenario of figure 6 and 7 corresponds to high density, high heating power shots (8MW ICRH, 2MW LH) with a high concentration of minority ions (H). A good confinement (with an improvement factor H around 1.5) is observed as well as a strong spontaneous toroidal rotation (in the counter current direction). This is also seen from the large increase of the fluctuation velocity, up to 4 to 5 km/s and strong modification of the $V_{E \times B, \perp}$ profile, with a shearing zone around $r/a = 0.7$. Fluctuation levels are evaluated at different radii and show a drop for $r/a \leq 0.7$.

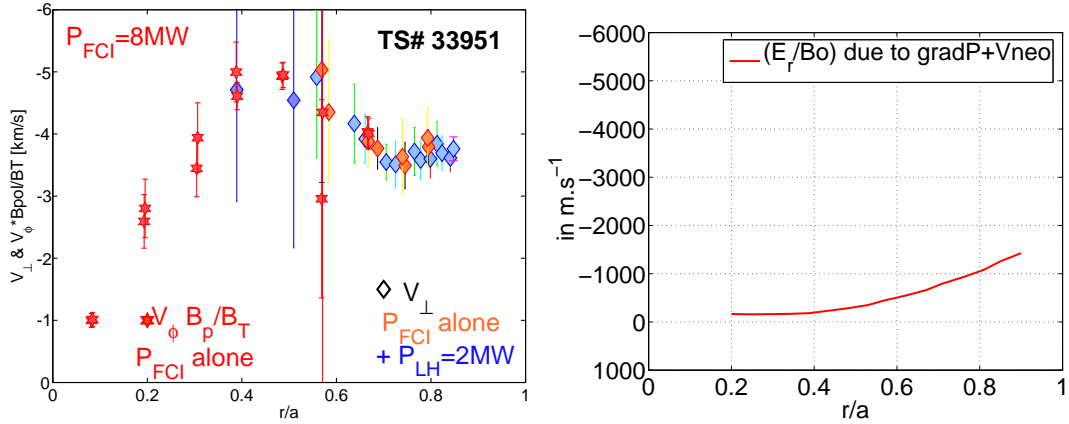


Figure 7: Profiles of fluctuation perpendicular velocity (diamonds) and $-v_{\phi} B_{\theta} / B$ (stars) (a) ; profiles of $v_{\theta} B_{\phi} / B$ and diamagnetic term (b).

Since the toroidal term of $V_{E \times B, \perp}$ dominates, small values of fluctuation phase velocity $\langle \omega/k \rangle_{flu}$ are expected. It should be of the order of the remaining part of the $E \times B$ velocity $\langle \omega/k \rangle \sim -v_{\theta} B_{\phi} / B + \nabla P_i / n q_i B$ which is plotted on figure 7(b), where the poloidal term v_{θ} is calculated from neoclassical evaluation. This part is seen to be rather small and of the order of ω_n^* , in the electron diamagnetic direction. This is consistent with linear stability code calculations (TEM around this frequency in this k range).

5 Conclusion and future plans

The Doppler scattering system is operating on Tore Supra since 2004 for measuring fluctuation perpendicular velocity profile, turbulence level, and k spectra in various plasma conditions: it can investigate particularly the role of the velocity shear and turbulence scales improved confinement regime; the impact of Te/Ti ratio or other non dimensional parameters on the level and the mean fluctuation frequency, their link to ion/electron modes; the link with the density peaking and thermo-diffusion; and electron transport related to small scale fluctuations.

On the diagnostic point of view, we are now testing X mode polarisation (105-150GHz) configuration, for a possible operation in both O/X mode. A faster acquisition (20 to 100MHz) is also under development for higher Doppler shift (in case of probing higher k) and also for developing instantaneous Doppler frequency evaluation from parametric analysis for dynamical and statistical analysis.

References

- [1] X. Garbet, Plasma Phys. Controlled Fusion, **43**, A251 (2001).
- [2] G D Conway, B Kurzan, B Scott, E Holzhauer and M Kaufmann, Plasma Phys. Control. Fusion, **44**, 451 (2002)
- [3] C. Honoré, J-M Chareau, P. Hennequin et al, *6th Int. Reflectometry Workshop*, San Diego (May 2003).
- [4] P. Hennequin, C. Honoré, A. Truc et al, Rev. Sci. Instrum., **75**, 3881 (2004)
- [5] C. Honoré, P. Hennequin, A. Truc, A? Quéméneur, *7th Int. Reflectometry Workshop*, IPP Garching (May 2005).
- [6] X. L. Zou, T. F. Seak, M. Paume, J.-M. Chareau, C. Bottereau, and G. Leclert. in *26th EPS Conf. on Contr. Fusion and Plasma Physics, Maastricht 1999*, Vol. 23J, 1041 (1999).
- [7] M. Hirsch, E. Holzhauer, E. Baldzun, and B. Scott, Rev. Sci. Instrum., **72**, 324 (2001).
- [8] M. Hirsch and E. Holzhauer, Plasma Phys. Controlled Fusion, **46**, 593 (2004).
- [9] G D Conway, J Schirmer, S Klenge, W Suttrop, E Holzhauer, Plasma Phys. Controlled Fusion, **46**, 951 (2004).
- [10] P Hennequin, R Sabot, C Honoré, G T Hoang, X Garbet, A Truc, C Fenzi and A Quéméneur. Plasma Phys. Controlled Fusion, **46**, B121 (2004).
- [11] V. Bulanin *et al.*, Plasma Physics reports, **26**, 813 (2000)
- [12] R. Sabot, C. Bottereau, J.-M. Chareau, F. Clairet, and M. Paume, Rev. Sci. Instrum., **75**, (2004)
- [13] A. Truc, A. Quéméneur, P. Hennequin, D. Grésillon, F. Gervais, C. Laviron, J. Olivain, S.K. Saha, and P. Devynck. Rev. Sci. Instrum., **63**, 3716 (1992).

Quasi-optical Gaussian Beam Tracing To Evaluate Doppler Back-scattering Conditions

C. Honoré, P. Hennequin, A. Truc, A. Quéméneur
Laboratoire de Physique et Technologie des Plasmas, CNRS (UMR 7648)
École Polytechnique, F-91128 Palaiseau cedex

Abstract

Microwave beam back-scattering near cutoff layer appears to be the most interesting diagnostic to observe density fluctuations time evolution for a given localization in the plasma and at a defined wave vector. It also provides perpendicular velocity. Scattering only occurs when the Bragg selection rule is fulfilled i.e. when the scattering wave vector is perpendicular to the magnetic field.

In order to evaluate these scattering conditions, ray tracing is required. In order to measure the angle between the magnetic field and the wave vector at the reflection, 3D geometry is necessary. Ripple effect on iso-index layer curve cannot be neglected. Scattering localization and wave vector resolution can be approached if single ray tracing is replaced with quasi-optical beam tracing. Optical propagation is still considered in the WKB approximation but the beam is described as multiple connected rays. The beam radial expansion due to diffraction is well described.

This approach allows to compute beam parameters for all data acquisition (50 / shot) and all shots (40 shots / day) during the following night on a recent personal computer with MatLab©.

1 Motivation

The Doppler back-scattering microwave diagnostic installed on Tore Supra is able to observe density fluctuations in the plasma core: ρ varies from 0.3 to 0.9, depending on plasma parameters. Density fluctuations are observed by an enhanced microwave back-scattering effect near the reflection layer (close to the cut-off). The microwave beam trajectory cannot be directly estimated. In order to know the scattering localization and wave vector in the reflection zone, wave propagation

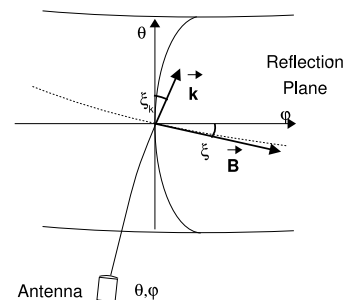


Figure 1: Poloidal section

evaluation is necessary.

It is also useful to estimate beam size and the wave vector resolution. Since the scattering efficiency is not a linear effect, they do not correspond to back-scattering resolution and expansion, but these beam characteristics give a first approach of back-scattering ones.

Density fluctuation properties should also be taken into account: For the diagnostic typical scattering wave-numbers range (3 to 20 cm^{-1}), density fluctuations are almost perpendicular to the magnetic field. This condition has to be verified in the scattering zone.

Since this beam propagation computation has to be done for each data acquisition sequence (in the order of 50 per shots), full wave simulation is not realistic. Ray tracing computation needs less time, but single ray integration is not sufficient to describe beam size evolution. Beam tracing, as multiple ray tracing is necessary.

In the first part, we expose the ray tracing integration with the complex eikonal method. This method is then applied to Doppler back-scattering in Tore Supra tokamak.

2 Beam tracing

The complex eikonal method to describe beam evolution in plasma is derived from the usual ray tracing method [1].

Eikonal function method for ray tracing

The plasma is described as a loss-less linear isotropic non-dispersive medium with an optical index $n^2(\mathbf{r})$. The incident wave is a monochromatic wave $E_\omega(\mathbf{r}, t) = E(\mathbf{r})e^{i\omega t}$, where ω is the wave pulsation. With these assumptions, the Helmholtz equation applies $\nabla^2 E + k_0^2 n^2 E = 0$.

With WKB approximation, valid when the local wavelength $\lambda(\mathbf{r})$ is much smaller than the electric field characteristic variation length $|E|/|\nabla E(\mathbf{r})|$, the zeroth order electric field approximation $E(\mathbf{r}) = E_0 e^{ik_0 S(\mathbf{r})}$ is considered. $S(\mathbf{r})$ is the eikonal function.

If this electric field expression is applied to the Helmholtz equation, the eikonal equation is deduced: $|\nabla S(\mathbf{r})|^2 = n^2(\mathbf{r})$. We introduce $\mathbf{k} = k_0 \nabla S$ as a intermediate variable. \mathbf{k} must then be an irrotational solution of the dispersion equation: $D(\mathbf{r}, \mathbf{k}, \omega) = k^2 - \frac{\omega^2}{C^2} n^2(\mathbf{r}) = 0$. The dispersion equation is solved by integrating rays along which the dispersion equation is satisfied:

$$\frac{d}{dt} \mathbf{r} = -\frac{\partial D}{\partial \mathbf{k}} / \frac{\partial D}{\partial \omega} = \frac{C^2}{\omega n^2} \mathbf{k} = \mathbf{v}_{group}$$

$$\frac{d}{dt} \mathbf{k} = \frac{\partial D}{\partial \mathbf{r}} / \frac{\partial D}{\partial \omega} = \frac{\omega}{2n^2} \nabla n^2$$

Complex eikonal to describe electric field envelope

The complex eikonal method was first proposed for inhomogeneous plasmas by S. Choudhary and L. B. Felsen [2]. This was extended to 3D vector field by E. Mazzucato [3]. Here we expose the more detailed application given by S. Nowak and A. Orefice [4, 5].

This method is generalized by considering complex form for the eikonal function: $S(\mathbf{r}) = R(\mathbf{r}) + iI(\mathbf{r})$. The eikonal imaginary part corresponds to the electric field spatial variation, where the real part corresponds to phase variations:

$$E(\mathbf{r}) = E_0 e^{k_0 I(\mathbf{r})} e^{ik_0 R(\mathbf{r})}$$

The eikonal equation still applies $|\nabla S(\mathbf{r})|^2 = n^2(\mathbf{r})$, but has real and imaginary parts:

$$|\nabla R|^2 - |\nabla I|^2 = n^2 \quad \nabla R \cdot \nabla I = 0$$

Once again, a dispersion equation is deduced by introducing $\mathbf{k} = k_0 \nabla R$.

$$D(\mathbf{r}, \mathbf{k}, \omega) = k^2 - \frac{\omega^2}{C^2} [n^2 + |\nabla I|^2] = 0$$

$$\mathbf{k} \cdot \nabla I = 0$$

The dispersion equation appears with an additional term $|\nabla I|^2$, and an additional condition $\mathbf{k} \cdot \nabla I = 0$. Since \mathbf{k} is tangential to the ray, this condition means $I(\mathbf{r})$ is constant along rays. It only depends on initial conditions. The complementary phase function $R(\mathbf{r})$, is constant along group wavefront.

Beam tracing consists in multiple ray tracing integration $i = 1 \dots n$. For each ray, I_i is given by initial conditions, but $|\nabla I(\mathbf{r})|^2$ varies. It will be estimated from neighbouring ray relative positions.

Gaussian beam description

For Gaussian beam, initial conditions are given in the beam waist plane ($z = 0$). The propagation direction is \mathbf{u}_z . The beam waist radius is w_0 . $M \times N$ rays are defined. M rays are in the beam radius direction: $r_{m=0 \dots M-1} = 1.6 w_0 \frac{m}{(M-1)}$ ($r = \sqrt{x^2 + y^2}$). N rays are regularly distributed around the beam: $\theta_{n=1 \dots N} = 2\pi \frac{n}{N}$. The initial conditions for ray tracing are given by ray positions and common wave vector:

$$\mathbf{r}_{m,n}(z = 0) = r_m (\cos \theta_n \mathbf{u}_x + \sin \theta_n \mathbf{u}_y)$$

$$\mathbf{k}_{m,n}(z = 0) = k_0 \mathbf{u}_z$$

By identifying the electric field envelope with its eikonal expression: $E(\mathbf{r}, z = 0) = E_0 e^{-r^2/w_0^2} = E_0 e^{k_0 I(\mathbf{r})} e^{ik_0 R(\mathbf{r})}$, initial values of I and R are given by: $I_{m,n} = -r_m^2/k_0 w_0^2$ and $R_{m,n}(z = 0) = 0$.

Each ray integration equations are:

$$\frac{d}{dt} \mathbf{r}_{m,n} = \frac{C^2}{\omega n^2} \mathbf{k}_{m,n}$$

$$\frac{d}{dt} \mathbf{k}_{m,n} = \frac{\omega}{2n^2} \nabla [n^2 + |\nabla I|^2]$$

Since $\nabla |\nabla I_{0,n}|^2 = 0$, for central ray ($m = 0$), ray tracing equations are the same as single ray tracing equations.

Runge Kutta integration

Rays can be integrated using adaptive step-size Runge-Kutta algorithm. Since $\nabla|\nabla I|^2$ term is computed from neighbouring rays, all rays are computed altogether with the same step. The step-size is then adapted to the most strained ray.

For region where the $n^2(\mathbf{r})$ function is not regular enough, like the plasma vacuum interface, Snell law is applied for affected rays.

Validation for Gaussian beam expansion in vacuum

Solutions of such beam tracing can be compared to paraxial analytic solution of Gaussian beam expansion in vacuum. In this case, the beam waist varies along propagation axis: $w(z) = w_0\sqrt{1+z^2/e^2}$ (where $e = \pi w_0^2/\lambda_0$). $w(z)$ is the distance between the central ray (where $E(\mathbf{r}) = E_0$) and the position where $E(\mathbf{r}) = E_0e^{-1}$.

Comparison between beam tracing and the analytical solutions shows they are very close. For beam initial waist equal to $w_0 = 40$ mm, over a distance over 2 m, the relative difference between both waists is less than $3 \cdot 10^{-4}$.

Analytical solution gives also phase wavefront radius variations along propagation axis ($R(z) = z(1+e^2/z^2)$). But this expression cannot be compared to the beam tracing, since the beam tracing only considers group velocity and not the phase velocity.

3 Plasma description

Plasma description

The plasma wave interaction is described with the cold plasma approximation.

Plasma equilibrium is described by major and minor radius, plasma height position, and Shafranov shift. More complete equilibrium description is forecast for the future.

Density profile is computed from central density n_0 and peaking coefficient p : $n(\rho) = n_0(1 - \rho^2)^p$. Experimental data spline interpolation is also possible, but profile irregularities can induce ray tracing integration instability.

Poloidal section description is extended to 3D with toroidal geometry. Ripple effect on equilibrium is taken into account.

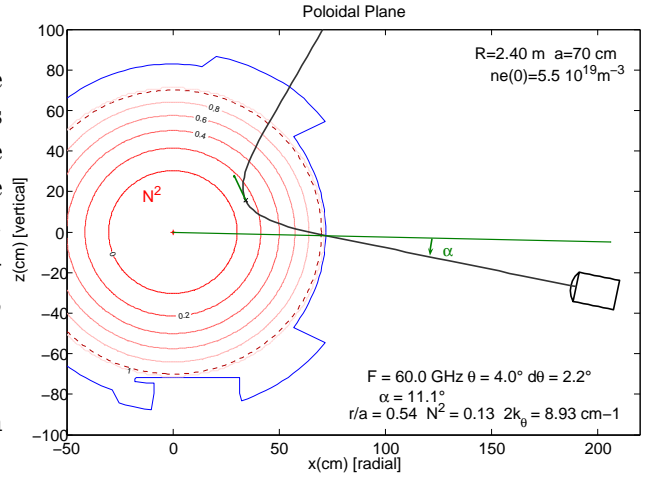


Figure 2: Ray tracing for cylindrical plasma

For X mode propagation, magnetic field is computed from simplified expression of the main toroidal and poloidal magnetic field, with first order paramagnetic, diamagnetic and ripple corrections.

The initial ray tracing program was developed in MatLab© by Y. Michelot, L. Colas and T.F. Seak (CEA-Euratom) as 2D single ray tracing.

Ray tracing validation for specific cylindrical plasma

Analytical solutions exist for single 2D ray tracing, for O mode propagation in a parabolic density profile ($n(\rho) = n_0(1 - \rho^2)$) with no Shafranov shift (Private communication by L. Colas).

For cylindrical symmetry, rk_θ is constant along the ray (it differs from slab geometry, where k_θ is constant).

Ray minimum radius ρ_{min} and corresponding poloidal wave-number $k_{\theta min}$ expressions are:

$$\rho_{min}^2 = \frac{\nu_0 - 1 + \sqrt{\nu_0^2 + 1 - 2\nu_0 \cos 2\alpha}}{2\nu_0}$$

$$k_{\theta min} = \frac{k_0 \sin 2\alpha}{\rho_{min}}$$

where $\nu_0 = n_0/\frac{\epsilon_0 m_e \omega_0^2}{q_e^2}$ is the density normalized to its critical value, and α is the angle between ray trajectory and plasma surface normal, where the ray enters the plasma (Figure 2).

The ray tracing results (given on figure 2) may be compared the corresponding analytical results: $\rho_{min} = 0.53$ and $2k_{\theta min} = 8.95 \text{ cm}^{-1}$. The relative difference is less than 2%. With the

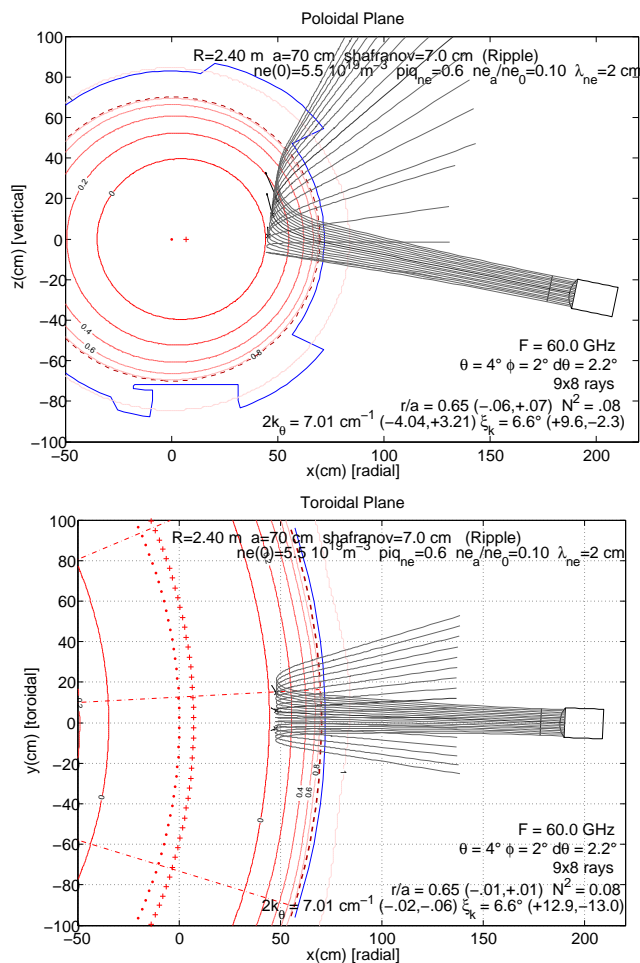


Figure 3: Poloidal and toroidal sections

slab approximation ($k_\theta = k_0 \sin \alpha$), we would get $2k_{\theta min} = 4.8 \text{ cm}^{-1}$. It is almost 50 % false in this example.

For more realistic plasma parameters, there is no analytical solutions. But since beam central ray tracing behaves like single ray tracing, the condition $k^2 = k_0^2 n^2(\mathbf{r})$ must apply along the central ray. This condition is verified during computation.

4 Beam tracing in Tore Supra plasma parameters

Figure 3 shows computation results corresponding to typical parameters for O mode 50-75 GHz Doppler back-scattering diagnostic on Tore Supra. Plasma central density is $5.5 \cdot 10^{19} \text{ m}^{-3}$. Density peaking coefficient is $p = 0.6$. Wave frequency is 60 GHz. Antenna poloidal tilt angle θ is 4.0° . In order to get scattering wave vector perpendicular to magnetic field, the antenna is also

toroidally tilted with $\varphi = 2^\circ$. The beam is represented by 9×8 rays. Figure 3 shows poloidal section (top) and the toroidal one (bottom). Wall inner limits are represented in blue. Red lines represent iso optical index lines. black curves show ray projection in the section. The legend of each figure show the localization and scattering wave-number at the central ray reflection (where the index is minimum). It also gives the scattering wave vector tilt angle ξ_k in the (θ, φ) plane (as defined on figure 1).

In order to estimate the resolution upon these quantities, we compare the results between the central ray and the rays initially distant by w_0 . For this case, the relative resolution on position is of the order of 10 to 20 %. The wave-number resolution is of the order of 30 to 50 %. For most studied cases, it appears that these wave-number and position resolutions are in the same ranges: $2\delta k_\theta = 3$ to 5 cm^{-1} , and $\delta \rho = .05$ to $.10$.

The ξ_k dispersion is quite high: 10° . It means that the beam should be perpendicular to the magnetic field.

References

- [1] S. Weinberg, *Eikonal Method in Magnetohydrodynamics*, The Physical Review, **126** (6) (1962), p1899-1909.
- [2] S. Choudhary & L. B. Felsen, *Asymptotic Theory for Inhomogeneous Waves*, IEEE transactions on Antennas and propagation, **AP-21** (6) (1973), p827-842.
- [3] E. Mazzucato, *Propagation of a Gaussian beam in a nonhomogeneous plasma*, Phys. Fluids B **1** (9) (1989), p1855-1859.
- [4] S. Nowak & A. Orefice, *Quasioptical treatment of electromagnetic Gaussian beams in inhomogeneous and anisotropic plasmas*, Phys. Fluids B, **5** (7) (1993), p1945-1954.
- [5] S. Nowak & A. Orefice, , Phys. Plasmas, **1** (5) (1994), p1242-1250.

Status of the Microwave Imaging Reflectometer at TEXTOR

M.J. van de Pol¹, E. Mazzucato², H.K. Park², T. Munsat³, C.W. Domier⁴,
N.C. Luhmann Jr.⁴, I.G.J. Classen¹, A.J.H. Donné¹, and the TEXTOR team⁵.

1. *FOM-Institute for Plasma Physics Rijnhuizen, Association EURATOM-FOM, The Netherlands, www.rijnh.nl**
2. *Princeton Plasma Physics Laboratory, Princeton, New Jersey, U.S.A.*
3. *University of Colorado at Boulder, Colorado, U.S.A.*
4. *University of California at Davis, Dept. of Applied Science, Davis, California, U.S.A.*
5. *Forschungszentrum Jülich GmbH, Institut für Plasmaphysik, Association EURATOM-FZJ, D-52425 Jülich, Germany**

** Partners in the Trilateral Euregio Cluster*

Abstract

Over the years, the efforts to develop Microwave Imaging Reflectometry (MIR) for nuclear fusion devices, have been extensively documented in the literature [1-9]. This paper intends to be a short overview of the MIR concept, the MIR instrumentation for TEXTOR, and preliminary results obtained so far.

1. Introduction

Reflectometry is a highly sensitive diagnostic for the localized measurement of density fluctuations in the core of tokamak plasmas. However, fluctuations (especially 2D fluctuations where the plasma permittivity varies both perpendicular and parallel to the direction of propagation of the probing beam) also complicate the interpretation of reflectometry data, due to the interference between reflected wave components.

A model that has been proposed to handle the effects of fluctuations on reflectometry measurements, describes the reflected field with a phase modulation that is caused by fluctuations mostly close to the cut-off layer and which magnitude is given by 1D geometric optics. Numerical studies [2, 4, 8] have shown this model to be valid when the amplitude of the fluctuations is smaller than a certain value, set by the spectrum of wave numbers. It has also been demonstrated that for an observer at the plasma edge, the reflected waves seem to originate from a “virtual” cutoff, located behind the actual cutoff. The reflected electromagnetic field consists of a group of scattered waves that propagate in various directions and a wave propagating in the direction of specular reflection. The amplitude of this specular reflection will decrease as the variance σ_ϕ^2 of the phase modulation becomes larger than unity. The scattered waves produce a complicated interference pattern when observed at a distance from the virtual cutoff layer larger than the diffraction length. Therefore, even when the above mentioned model is valid, the backward field needs necessarily to be measured as close as possible to the virtual cutoff. Experimentally, this could be achieved by collecting a significant part of the scattered waves by a large-aperture optical system and by imaging the object plane of the system, located at the virtual cutoff, onto a phase detector at the image plane. This concept has led to the development of the microwave imaging reflectometry (MIR) technique.

2. MIR instrumentation at TEXTOR

A MIR instrument has been developed for the TEXTOR tokamak. The layout of the diagnostic, which is combined with an Electron Cyclotron Emission Imaging (ECEI) receiver, to measure simultaneously electron density and temperature fluctuations, is shown in Figure 1. The ECEI part of the system is described elsewhere [10].

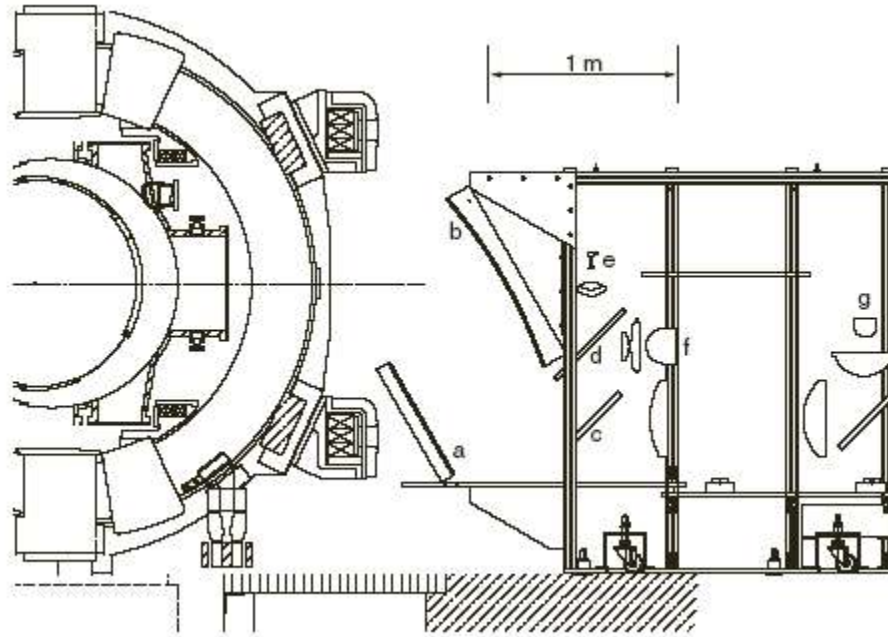


Figure 1: The combined MIR/ECEI system with the TEXTOR poloidal cross section.

The MIR employs large-aperture front-end optical components (the cylindrical mirrors a and b in Figure 1) to collect the reflected waves over an extended range of scattered angles. The limiting aperture is formed by the 42 cm \times 20 cm TEXTOR vacuum window. The same focusing mirrors are used to match the wave front curvature of the probing beam to the cutoff surface, thus improving the robustness of the system to variations of the location of the cutoff surface and reducing the effect of plasma refraction. A dichroic plate (c) is used to separate the higher frequency (> 95 GHz) ECEI signal from the lower frequency (< 90 GHz) MIR signal. Each subsystem has its own detector system, located at (g) and (f) respectively, including several lenses to improve the image quality and to match the image to the detector characteristics. A significant advantage of the imaging scheme is the possibility to perform multi-point measurements on an extended poloidal range of the cutoff surface by using a multi-element detector array. This way, the instrument will not only be able to perform measurements in the presence of poloidal fluctuations, but also of the poloidal fluctuations themselves.

The TEXTOR MIR instrument has a fixed frequency probing beam, launched in X-mode, of 88 GHz that covers a ≤ 15 cm poloidal range. The reflected waves are measured with a 16-channel detector array, leading to a spatial resolution of ~ 1 cm and a theoretical poloidal wavenumber k_{θ} resolution up to 3 cm^{-1} .

Before installation, the MIR instrument has been tested in the laboratory using a rotating corrugated reflecting target of known shape to simulate the fluctuating plasma reflection layer [6]. This test clearly illustrates the property of the MIR technique where the detection plane is moved to a location that is remote from the target surface and physically accessible for a detection system

3. Preliminary results

Figure 2 shows the results of a pilot experiment, where the electron density was ramped up during an Ohmic plasma discharge, to shift the virtual cutoff surface through and beyond the focal plane of the MIR optics [5]. The focal plane of the optics was held fixed, and all plasma parameters, apart from the density ramp, were held fixed. The figure shows I/Q plots from a single channel recorded over several 3 ms time windows during the density ramp. The striking difference between plots (a, d) and (b, c) is in the level of amplitude fluctuations. The smaller level of amplitude fluctuations in plots (b, c) is attributed to the in-focus condition of the virtual cutoff layer, as is confirmed by the agreement between the calculation of the virtual cutoff position and the position of the MIR focal plane. Remarkable is also the difference between the power spectra of the signal phase. When the cutoff is in-focus (Figure 2f), the phase power spectrum is dominated by large coherent MHD fluctuations, while the spectrum becomes a featureless $1/f^2$ spectrum when the focus goes out-of-focus (Figure 2e).

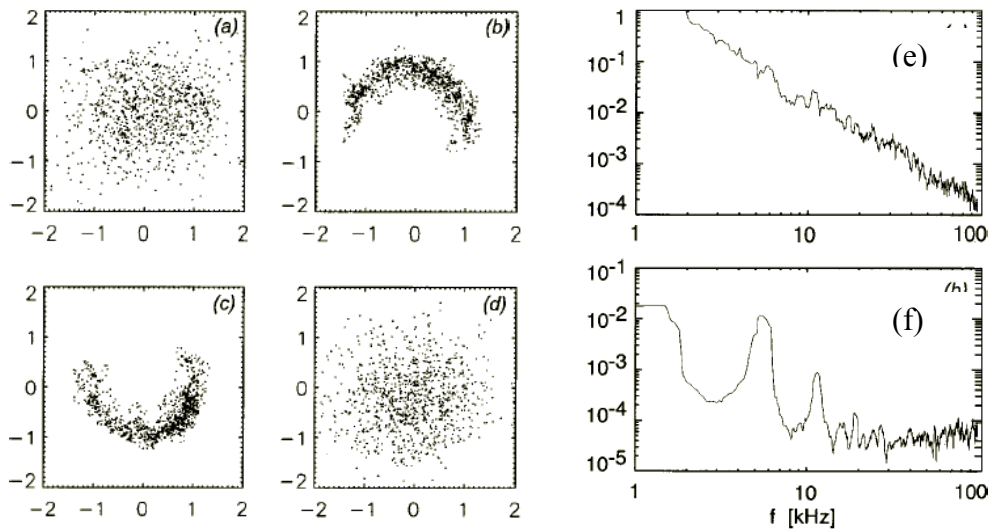


Figure 2: I/Q-plots of a single MIR channel during a density ramp in an Ohmic discharge (a, b, c and d) and its phase power spectra (e and f).

Recently, preliminary results on the measurement of phase spectral coherence, poloidal correlation lengths, poloidal wave number and poloidal phase velocity have been reported [9].

4. Discussion and conclusion

The latest version of the MIR system has been installed on TEXTOR in the summer of 2002. Due to a number of unforeseen and lengthy shutdowns, the experimental time that could be devoted to technical commissioning of the system was very limited. Moreover, during the few scheduled MIR test sessions, it has been very difficult to achieve the optimum plasma conditions. In the majority of test discharges, the system was out-of-focus, where the focal plane does not overlap the virtual cutoff. Obviously, more experimental time with improved plasma conditions is needed to fully explore the possibilities of MIR.

Recently, flexibility has been added to the MIR system to shift both the launching beam focal position and the detection system focal plane independently. Plans for the near future include the utilization of this flexibility to find optimum settings for both launching and receiving focal positions under optimized plasma parameters.

Acknowledgements

This work, supported by the European Communities under the contracts of Association between EURATOM/FOM and EURATOM/FZJ was carried out within the framework of the European Fusion Development Agreement, with financial support from the 'Nederlandse Organisatie voor Wetenschappelijk Onderzoek' (NWO), 'Forschungszentrum Jülich GmbH' and EURATOM. The views and opinions expressed herein do not necessarily reflect those of the European Commission. This work is also supported by the U.S. Department of Energy under contracts No. DE-FG03-95ER54295, DE-FG03-99ER54531 and DE-AC02-76-CHO-307.

References

- [1] E. Mazzucato and R. Nazikian, *Rev. Sci. Instrum.* **66** No. 2 (1995) 1237
- [2] E. Mazzucato, *Rev. Sci. Instrum.* **69** No. 4 (1998) 1691
- [3] E. Mazzucato, *Rev. Sci. Instrum.* **69** No. 6 (1998) 2201
- [4] E. Mazzucato, *Nucl. Fusion* **41**, No. 2 (2001) 203
- [5] E. Mazzucato et al., *Phys. of Plasmas* **9** No. 5 (2002) 1955
- [6] T. Munsat et al., *Plasma Phys. & Control. Fusion* **45** (2003) 469
- [7] T. Munsat et al., *Rev. Sci. Instrum.* **74** No. 2 (2003) 1426
- [8] E. Mazzucato, *Plasma Phys. Control. Fusion* **46** (2004) 1271
- [9] E. Mazzucato et al., *APS 2004*, Savannah, GA
- [10] J. Wang et al., *Rev. Sci. Instrum.* **75** No. 10 (2004) 3875

Simulation of optical and synthetic imaging using microwave reflectometry

G.J. Kramer, R. Nazikian and E. Valeo

Princeton Plasma Physics Laboratory, Princeton, NJ 08543-0451

2-D full-wave time-dependent simulations in full plasma geometry are presented which show that conventional reflectometry (without a lens) can be used to synthetically image density fluctuations in fusion plasmas under conditions where the parallel correlation length greatly exceeds the poloidal correlation length of the turbulence. The advantage of synthetic imaging is that the image can be produced without the need for a large lens of high optical quality, and each frequency that is launched can be independently imaged. A particularly simple arrangement, consisting of a single receiver located at the midpoint of a microwave beam propagating along the plasma midplane is shown to suffice for imaging purposes. However, as the ratio of the parallel to poloidal correlation length decreases, a poloidal array of receivers needs to be used to synthesize the image with high accuracy. Simulations using DIII-D relevant parameters show the similarity of synthetic and optical imaging in present day experiments.

A full report on synthetic imaging using microwave reflectometry is given in:
G.J. Kramer, R. Nazikian and E. Valeo, *Plasma Physics and Controlled Fusion* **46** (2004) L23-L29.

Experimental results from optical imaging in TFTR are shown in:
R. Nazikian, G.J. Kramer and E. Valeo, *Physics of Plasmas* **8** (2001) 1840-1855.

A description of the Full Wave Reflectometer code and an application of it can be found in:
E. Valeo, G.J. Kramer and R. Nazikian, *Plasma Physics and Controlled Fusion* **44** (2002) L1-L10.
G.J. Kramer, R. Nazikian and E. Valeo, *Plasma Physics and Controlled Fusion* **44** (2002) L11-L19.

IDENTIFICATION OF LOCAL ALFVÉN WAVE RESONANCES WITH REFLECTOMETRY AS A DIAGNOSTIC TOOL IN TOKAMAKS

A.G.El'fimov¹, R. M.O. Galvão¹, L. F. Ruchko¹, M.E.C.Manso² and A.A.Ivanov³

¹*Instituto de Física, Universidade de São Paulo, 05315-970, SP, Brazil*

²*Centro Fusão Nuclear-Instituto Superior Técnico, Av.Rovisco Pais, 1049-001, Lisboa, Portugal*

³*Keldysh Institute, Russian Academy of Sciences, Moscow, Russia*

Local Alfvén wave (LAW) resonances are excited in tokamaks by an externally driven electromagnetic field, below ion cyclotron frequency. We show that combination of small power deposition in LAW resonances, swept by plasma density variation or scanned by varying generator frequencies, in combination with detection of the density fluctuations in the LAW resonances by reflectometry can serve as diagnostic tool for identification of the effective ion mass number A_{ef} and q -profile in tokamaks. The idea is based on the simultaneous detection of the position of $m=\pm 1$ local AW resonances, which are excited by $M/N=\pm 1/\pm 2$ antenna modes, and $m=0$ generated by poloidal mode coupling effect in tokamaks. The $m=0$ resonance depends only on the effective ion mass number and does not depend on the q -profile, so that the mass number can be determined unambiguously. Then, we can determine q -factor at the position of $m=\pm 1$ LAW resonances. Using multifluid ALTOK code, we identify mass number in TCABR experiments and demonstrate the possibility of applying this method in Joint European Torus.

The idea of strong resonant absorption of RF fields, which are excited at the local Alfvén wave (LAW) resonance in magnetically confined inhomogeneous plasmas, is based on a series of the theoretical works carried out in seventh and eightieth (for example, [1-3]). LAW resonance excitation is defined by mode conversion of an externally driven RF field below the ion-cyclotron frequency, ω_{ci} , into the kinetic or electrostatic Alfvén wave (shear AW) at the Alfvén resonance layer where the resonance density can be determined by the equation in “cylindrical” form

$$k_{\parallel}^2 = \frac{\omega^2}{c_{Ai}^2} \left[\frac{A_i n_i / n_e}{1 - \omega^2 / \omega_{ci}^2} + \frac{A_z n_z / n_e}{1 - \omega^2 / \omega_{cz}^2} \right], \quad k_{\parallel} = \frac{B_t}{B_0 R_0} \left(N + \frac{m}{q(r)} \right), \quad c_{Ai} = \frac{B_0}{\sqrt{\mu_0 m_i n_e}} \quad (1)$$

where m and N are toroidal and poloidal wave numbers, q is the safety factor B_0 , B_t are the modulus and toroidal magnetic field, and A_z is the main impurity mass number. Eq. (1)

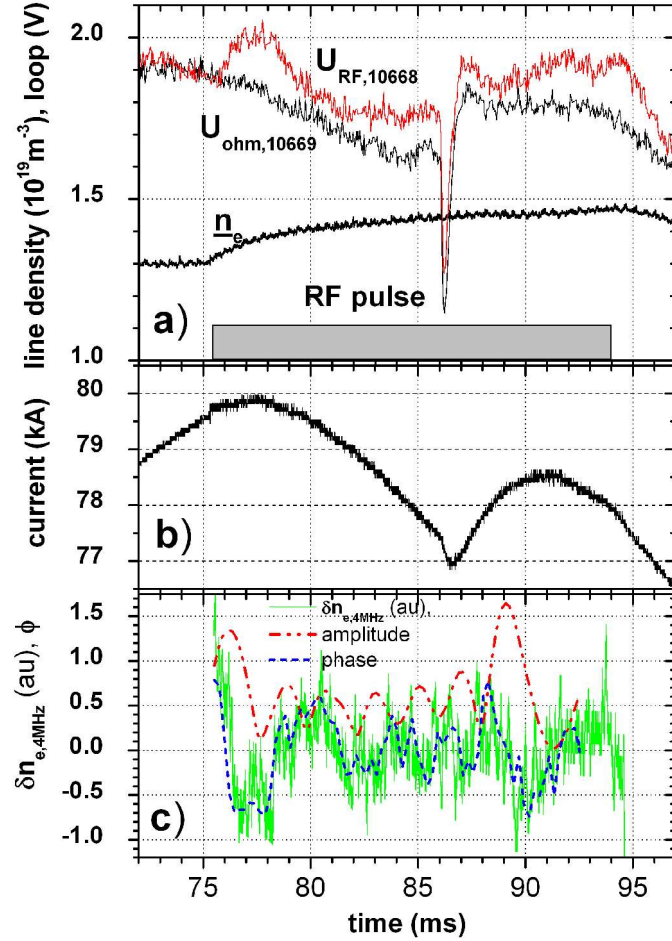
can be reduced to $\omega_A = c_A k_{\parallel} \ll \omega_{ci}$ in the low frequency limit, where $c_A = c_{Ai} / \sqrt{A_{ef}}$ is the

Alfvén velocity, $A_{ef} = (A_i n_i + A_z n_z) / n_e$ is effective mass number, and ω_{ci} is the ion cyclotron frequency. The continuous spectrum (1) of the LAW resonances is known as the Alfvén wave continuum. In the standard quasi cylindrical model for wave excitation in tokamak plasmas, the oscillating RF field is represented as a sum of harmonics $\exp[i(m\theta + N\phi - \omega t)]$. These fields are excited in the plasma by an antenna current sheet, $J_{\theta,\phi}(r, \theta, \phi, t) = \sum_M J_{\theta,\phi}(M, N) \delta(r-b) \exp[i(M\theta + N\phi - \omega t)]$. The antenna spectra of $J_{\theta,\phi}(M, N)$ driven in tokamaks are usually very wide both for the toroidal and poloidal wave numbers; however, a few harmonics can satisfy the LAW resonance conditions (1). Due to toroidal effects, the poloidal wave numbers m in the plasma may be different from M that are excited by the antenna. In particular, although $m=0$ LAW resonance can not be directly driven by an external antenna, poloidal mode coupling allows it to be excited as a satellite mode of $|m|=1$ LAW resonance, in tokamak plasmas. Indeed, that has been already demonstrated experimentally in TCA with a CO₂ laser interferometry [4] when it was operating in Lausanne. Recently, power deposition in $m=0$ local AW resonance has been also demonstrated by ECE heterodyne system in TCABR [5].

Moreover, AW can also be excited in a plasma as global Alfvén waves (GAW) [1-2] and toroidicity induced Alfvén eigenmodes (TAE) at the position of bifurcation of the LAW

resonances, for given N and different $m \neq 0$ numbers, with wave fields corresponding to the discrete eigenfunctions of the proper boundary value problem. Easy identification of these modes were explored as a diagnostic tool for definition of the effective ion mass number A_{ef} and q -profiles in a series of tokamak experiments (for example, [5-11]). This technique, called Magneto-Hydro-Dynamic (MHD) spectroscopy, is usually based on external measurements by magnetic probes and work in the active (AW excitation by an external antenna) and passive (using AW instabilities driven by accelerated ions in NB or ICR heating) regimes.

Fig.1. Time traces (70-97 ms) of the loop voltage and line averaged density (a), toroidal current (b), and amplitude and phase density oscillation measured with reflectometer (c) in the TCABR discharge with AW heating. The loop voltage in a control ohmic discharge # 10669 is also shown in (a), for comparison.



Recently, using a fixed frequency (32.4GHz) O-mode reflectometer, wave driven density fluctuations at the local

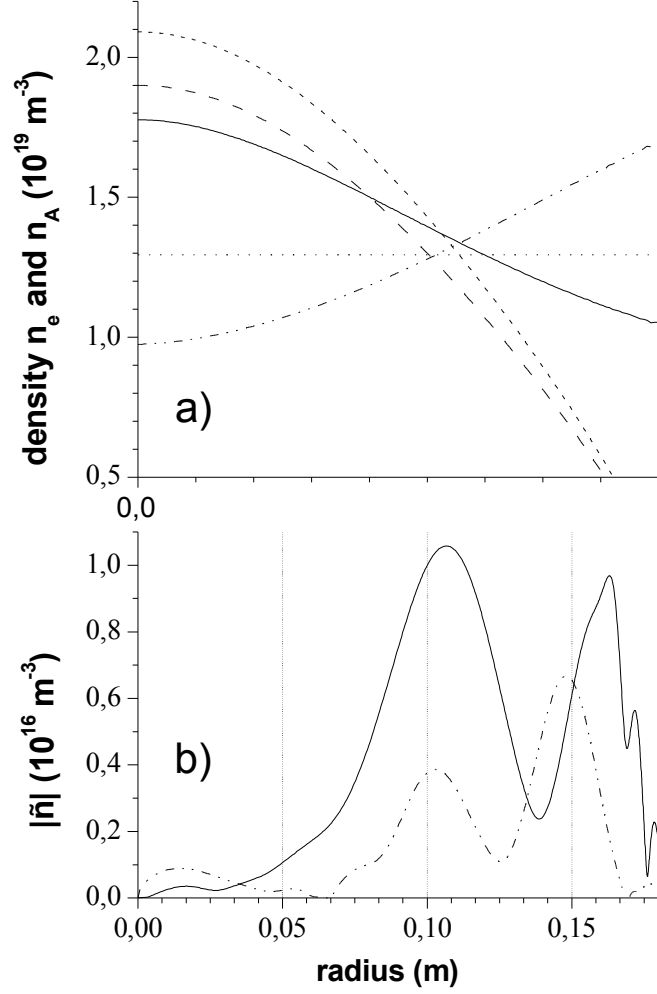
LAW resonance $m = \pm 1$, $N = -2, 3$ with frequency $f_A = 4$ MHz and relatively small power deposition of 30 kW were detected in the Tokamak Chauffage Alfvén Brésilien (TCABR) [12]. The LAW resonances were excited by a fixed AW frequency generator, which usually used for heating, together with a small density increase in these experiments. However, this density increase during RF pulse does not produce a relative sweeping of reflectometer reflection point over LAW resonance position, as follows from eq. (1)

$$n_A = \left[\frac{B_i}{4\pi m_i \omega R_0} \left(N + \frac{m}{q} \right) \right]^2 \left(\frac{n_i / n_e}{1 - \omega^2 / \omega_{ci}^2} + \frac{A_z n_z / n_e}{1 - \omega^2 / \omega_{cz}^2} \right)^{-1}; n_{\text{ref}} = \pi \frac{m_e}{e^2} f_{\text{ref}}^2 \quad (2)$$

Here $n_{\text{ref}} \approx 1.3 \cdot 10^{13} \text{ cm}^{-3}$ is the density at the reflection point, and n_A is the one at LAW resonance position. In Eq.(2), q factor and an impurity density variation may only allows to meet the condition $n_A = n_{\text{ref}}$.

In this paper, based upon results of calculations carried out with the two dimensional multi-fluid ALTOK code [13] and taking into account that the q variation was rather small during the RF pulse, we show that the average mass number could be determined in the experiments [14], and we discuss the possibility of frequency sweep of $m = 0, \pm 1$, $N = \pm 2$ LAW resonances, within the frequency band 0.5-0.9 MHz, to explore this effect in JET.

Fig.2. Plot of Alfvén radial density profile n_A for $A_{ef}=1.1$, $q_0=1.07$, $m/N=-1/3$ mode (dash-dot-dot line), and for $A_{ef}=1.17$, $q=1.08$, $m/N=-1/2$ (solid line), electron density distributions for $n=1.2 \times 10^{19} \text{ m}^{-3}$ (dashed) and $n=1.5 \times 10^{19} \text{ m}^{-3}$ (short dashed lines), the reflectometry cut off density in TCABR is marked by dotted line (a); amplitudes of the AW density fluctuations calculated with ALTOK for 4 MHz frequency $m/N=-1/3$ mode (dash-dot-dot line), respective to (a), and $m/N=-1/2$ (solid line) resonance for $n=1.5 \times 10^{19} \text{ m}^{-3}$ (b).



Plasma Model of TCABR and JET

The calculations with the ALTOK code have been carried out assuming circular, in TCABR, and D-shape cross-section ($\kappa=1.43$, $\delta=0.25$) in JET. To obtain good accuracy, 473×99 mesh

points are used in the numerical calculations. Here, we analyze the AW absorption in TCABR shot N°10668 [11] (minor radius $a=0.18\text{m}$, major radius $R_0=0.615\text{m}$, toroidal magnetic field $B=1.15\text{T}$, plasma current $I_p=78\text{-}80\text{ kA}$, with safety factor in the center $q_0=1-1.1$, line averaged plasma density $\bar{n}=1.2\text{-}1.5 \times 10^{19} \text{ m}^{-3}$ (gas hold hydrogen), central electron and ion temperatures $T_{e0}=450\text{ eV}$ and $T_{i0}=150\text{ eV}$). The TCABR antenna module has two groups of RF current carrying straps, which are positioned in two toroidal cross-sections separated toroidally by an angle about 22° , creating mainly the spectrum of the poloidal $M=\pm 1, \pm 2$ and toroidal $N=\pm 1, \pm 2, \pm 3 \dots$ modes. Their LAW resonances are strongly separated by choosing the generator frequency 4 MHz. In JET calculations, we use shot #60895 as a reference (minor radius $a=1.05\text{m}$, major radius $R_0=2.85\text{ m}$, toroidal magnetic field $B=1\text{ T}$, plasma current $I_p=1.2\text{ MA}$, safety factor $q(0)=1.1$, central plasma density $n_0=5 \times 10^{19} \text{ m}^{-3}$ (gas hold deuterium), central electron and ion temperatures $T_{e0}=3000$ and $T_{i0}=2000\text{ eV}$, respectively. The generator frequency has been swept in the band $f=0.2\text{-}0.5\text{ MHz}$. The antenna module is proposed to have two groups of RF current carrying straps. These groups are situated at two opposite toroidal positions creating mainly the spectrum of the poloidal $M=0, \pm 1, \pm 2$ and toroidal $N=\pm 2, \pm 4$ modes. The plasma profiles used in the code calculations are quasi parabolic temperature profile $T=T_0(I-\Psi)^{0.9}$, density profile of TCABR $n=n_0(I-\Psi)^{0.7}$, and of JET $n=n_0(I-\Psi)^{0.4}$, and current profile is $j=j_0(I-\Psi^{0.9})^{1.2}$, where Ψ is the normalized poloidal magnetic flux.

Identification of Local AW Resonance with Reflectometry

The density fluctuation rise in the LAW position can be detected by a reflectometer (for example, Ref.16-17). In the simple case, the relative amplitude of the density fluctuations $\delta n/n$ is proportional to the parallel component of the electric field, in accordance with Boltzmann distribution, and to the square root of the absorbed power density \tilde{p} ,

$$\frac{\delta n}{n_e} = \left| \frac{k_{\parallel} \varepsilon_{\parallel}^e}{4\pi e n_e} \tilde{E}_{\parallel} \right| \approx \left| \frac{e \tilde{E}_{\parallel}}{m_e k_{\parallel} v_{Te}^2} \right|; \quad |\tilde{E}_{\parallel}| = 2 \sqrt{\frac{\sqrt{8\pi} k_{\parallel}^3 v_{Te}^2}{\pi \omega_A^2 \omega_{pe}^2} \tilde{p}} \quad (3)$$

where n_e , v_{Te} , and ω_{pe} are the electron mass, thermal speed, and plasma frequency, respectively. For power density of 0.2 kW/m^3 at the resonance surface $r_A = 0.65(R-R_0)$ (or about of 1 kW of total absorbed power), we obtain $\delta n/n_e \approx 1.10^{-4}$, which is of the level that can be detected by a modern reflectometer (for example, Ref.13). The sensitivity of the system may be improved with locked frequency detection related to the AW frequency. In Fig.1, we show the time traces (70-100 ms) of the loop voltage, line averaged density, toroidal current, and respective amplitude of 4MHz oscillating phase measured with the 32.4 GHz O-mode reflectometer in TCABR discharge # 10668 with AW heating. The density trace during RF pulse was in accordance with the variation of the bolometry signal $\propto Z_{eff}^4 n^2 / T^{3/2}$ assuming that there is small Z_{eff} rise from 1.5 to 1.8, as found from ASTRA calculations, using the small loop voltage increase $\propto Z_{eff} / T^{3/2}$ and β_{eq} value at the beginning of the RF pulse (diminishing later) in comparison with the similar ohmic discharge # 10669. We observe that, consistently with the calculated increase in Z_{eff} , the loop voltage for discharge # 10668 shows a strong increase well correlated with the first spike in the density oscillation detected by reflectometer (the negative loop voltage spike at $t = 86 \text{ ms}$ is due to converting of different load resistors in the ohmic circuit to extend the plasma current). The central electron temperature does not increase during the RF pulse, as indicated by the ECE signal in this experiment. In Fig.1c, the observed maxima of the amplitude of 4 MHz microwave phase should be interpreted as local AW resonances for $m/N = -1/3$ ($A_{er}=1.1$), in the initial stage, and as a superposition with $m/N = -1/-2$ ($A_{er}=1.17$) in the final stage of the RF discharge # 10668.

Alfvén Wave Absorption in JET

The AW continuum is calculated for JET, using ALTOK code and parameters already specified. The results for $m=0, \pm 1, N=-2$ are shown in Fig.3(a) It is specially relevant to note that the continuum line for $m=0$ extends most of the inner region of plasma, for the 0.5- 1.0 MHz frequency band, offering the possibility to determine the effective mass number in JET through the detection of the LAW resonances by a reflectometry. Another possibility is related to detection of the $|m|=1$ LAW resonance. In Fig.3 b and c, we show specific dissipation profiles for these cases, as an example. The respective absorption profiles for 800 kHz and for 720 kHz frequencies are presented in Fig. 3 b and c, respectively, being both excited by the $M=-1, N=-2$ antenna. The absorption in Fig.3c is due to the GAW resonance of the $m/N=-1/-2$ mode. There is a correlation of the local AW resonance position of the $N=2$ and $m=0$ in Fig.3a with the first absorption spike at $R-R_0 = 0.8 a$ in Fig.3c, calculated for the $m=0$ mode. A typical absorption in the $m/N=-1/-2$ AW continuum is shown in Fig.3b for 800 kHz frequency. The power deposition profiles corresponding to these cases are shown in Fig.4. The half width of those spikes are 3% of the plasma minor radius, i.e., smaller than 4cm, and therefore offering good possibility for identification of the resonance position by reflectometry.

Discussion

To find out the effective mass number, the variation of the $m=0$ local AW resonance position, in accordance with sweeping the AW frequency, should be mapped by scanning

the reflectometry frequency, to identify the local AW density $n_A(r)$. Then, using the *cylindrical* equation (2) simplified for $\omega \ll \omega_{ci}$, we have

$$A_{ef}(r_A) = \frac{1}{4\pi m_i n_A(r_A)} \left[\frac{B_0}{2\pi f_A R_0} \left(N + \frac{m}{q(r_A)} \right) \right]^2 \quad (5)$$

where B_0 is the toroidal magnetic field on the magnetic axis, m_i is mass of the main plasma specie, f_A is the generator frequency at the moment of identification of the LAW resonance position, and n_A should be averaged over the magnetic surface where the LAW resonance is detected. A more precise option is to calculate AW continuum curve using exact equilibrium parameters and the main plasma specie mass with the ALTOK code (like shown in Fig.3a) and compare them with the code calculations using the n_A distribution over radius as found from the reflectometry measurements. Then, using the ratio of one curve to the other, we obtain the value of $\sqrt{A_{ef}(r)}$. Further, identifying radial position of the $m = -1, n = -2, 3$ AW resonances, we can find the *cylindrical* q from Eq. (5), which should be adjusted with the code calculations for different neighbor q profiles in the next step. Here, we note that identification of $m=0$ LAW spectrum has strong advantages for calculation the effective mass number in comparison with the other modes because the $m=0$ AW continuum does not depend on q -factor and it is not interrupted by TAE modes for low m .

Conclusion

- Using ALTOK code we find the mass number $A_{ef}=1.1-1.17$, in fixed frequency AW heating experiments in TCABR, where the density at the $m = -1, n = -2, 3$ local AW resonances was identified with a fixed frequency O-mode reflectometer.
- Calculations with ALTOK code show that AW frequency sweeping, in the band 0.2-0.5 MHz for $m=0, -1, N=-2$, accompanied by scanning the frequency of reflectometer, is quite viable scheme to identify the LAW resonance positions over the major part of the plasma cross section. Localization of the $m=0$ AW continuum helps to identify the effective mass number and q profile can be found from $m=\pm 1$ AW continuum in JET.
- Finally, we conclude that a combination of sweeping the frequency of the AW excitation system with sweeping of the reflectometer frequency may be a very powerful diagnostic tool to find effective mass number A_{ef} and q -profiles in tokamaks.

References

- [1] D. W. Ross, G. L. Chen and S. M. Mahajan *Phys. Fluids*, **25**, 652 (1982).
- [2] J. Vaclavik and K. Appert, *Nucl. Fusion*, **31**, 1945 (1991).
- [3] A.G. Elfimov, A.G. Kirov and V.P. Sidorov In: *High Frequency Plasma Heating*, edited by Litvak A.G (Transl. Series, AIP, New York, 1992) p. 239.
- [4] R. Bhen, G.A. Collins, J. B. Lister, H. Weisen *Plasma Phys. Contr. Fusion* **29**, 75 (1987)
- [5] R. M. O. Galvão et al, *30th EPS Conference on Plasma Phys. and Contr. Fusion*, 7-11 July 2003, St. Petersburg, Russia, ECA, 27A, P-4.50 (2003).
- [6] G.A. Collins, et al., *Plasma Phys. Contr. Fusion* **29**, 323 (1987).
- [7] J.P. Goedbloed, et al. *Plasma Phys. Contr. Fusion*, **35**, B277 (1994)
- [8] H. Holties, A. Fasoli, J.P. Goedbloed, *Phys. Plasmas*, **4**, 709 (1997)
- [9] J. B. Lister, L. Villard and G. de Rider, *Plasma Phys. Contr. Fusion*, **40**, 1635 (1998)
- [10] S. Sharapov et al., *Phys. Rev. Lett.*, **93** (2004) 165001
- [11] L. F. Ruchko, et al, *Rev. Scientific Instruments*, **75**, 655-660 (2004).
- [12] S. A. Galkin, A. A. Ivanov, S. Y. Medvedev, A. G. Elfimov. *Comp. Phys. Com.* **143**, 29 (2002).
- [13] G. D. Conway, G. Vayakis, J. A. Fessey, Bartlett, *Rev. Scientific Instruments*, **70**, 3921 (1999).

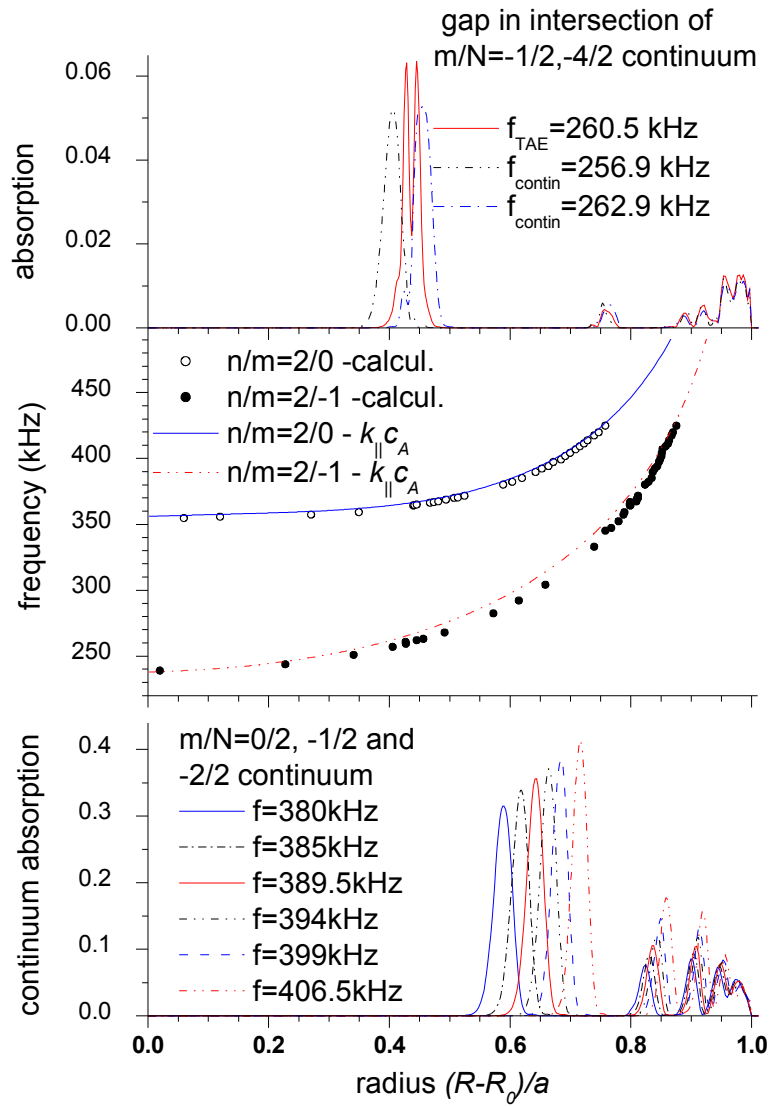


Fig.3. Plot of absorption profile for TAE mode in the gap $f=256.9\text{-}262.9 \text{ kHz}$ of $m/N=-1/2$ and $-4/2$ continuum (a), distribution of AW continuum frequency together with the position of some separate spikes of absorption for $m=0,-1$, $N=2$ (b), and absorption profile in the continuum band $f=380\text{-}406.5 \text{ kHz}$ (c) in JET.

Experimental studies of the registration of Alfvén wave resonances in the TCABR tokamak by the frequency scanning reflectometry

L. F. Ruchko, R. M. O. Galvão, A. G. Elfimov, J. I. Elizondo, E. Sanada,
Yu. K. Kuznetsov, A. M. M. Fonseca, V. Bellintani Jr, A. N. Fagundes,
I.C. Nascimento, and W. P. de Sá

Instituto de Física, Universidade de São Paulo, 05315-970, São Paulo, BRASIL

C.A.F. Varandas, M. Manso, P. Varela, and A. Silva

*Associação EURATOM/IST– Centro de Fusão Nuclear, Instituto Superior Técnico,
Av. Rovisco Pais 1, 1049-001, Lisbon, Portugal*

Abstract

The experimental studies of the application of the frequency scanning microwave reflectometry to the analysis of the local Alfvén wave (AW) resonances are presented. These resonances are excited close to the magnetic surfaces, at which the local plasma Alfvén velocity $C_A(r) = \frac{B}{\sqrt{\mu_0 m_i n_i(r) M_{eff}}}$ is equal to the phase velocity of the electromagnetic

wave, which is excited by the AW antenna system. These AW resonances manifest themselves as spatially radially localized plasma density oscillations at the AW frequency, and can be registered by the microwave scanning reflectometer technique. The experiments in the TCABR tokamak were carried out with the excitation of the AW modes $M=\pm 1$, $N=\pm 1, \pm 2, \pm 3$ at the frequency $f=4.5$ MHz. It is shown that the modulation of the reflectometer output signal at the AW frequency is increased when the position of the local Alfvén resonance is close to the plasma zone where the reflectometer microwave signal is reflected. The continuous sweeping of the reflectometer frequency in the course of the plasma discharge makes it possible to track the Alfvén zone position.

Introduction

Nowadays the microwave reflectometry is routinely used for probing the structure of magneto hydrodynamic and turbulent fluctuations in fusion plasmas due to their sensitivity to plasma density oscillations in the cutoff layer. Wide possibilities of this diagnostic technique can be realized by integrating it with AW excitation by external antennae. In this case coherent plasma density oscillations are excited in predefined plasma regions, and the registration of the related perturbations by the reflectometry technique can be used for diagnostic purposes.

The magnitude of plasma density oscillations in the course of the AW excitation has maximum value in the vicinity of the AW resonance layer. Its position can be found from the equation $\omega_{RF}^2 = k_{||}^2(r_A) C_A^2(r_A) (1 - \frac{\omega_{RF}^2}{\omega_{ci}^2})$, where $k_{||}(r) = \left(\frac{N}{R}\right) \left[1 + \frac{M}{Nq(r)}\right]$. (Here ω_{ci} is the effective cyclotron frequency taking into account impurities). The numerical calculations show that the density fluctuations are concentrated within few ion gyroradii of the resonance layer. It is seen that the localization of this zone depends both on the

frequency ω_{RF} and wave numbers M, N of the excited wave, and on the local plasma parameters $n_e(r), q(r), M_{eff}$. In the case of the O-mode reflectometer the AW dispersion in the plasma region, where the reflectometer signal is reflected, can be simplified [1]

$$\frac{N}{R} \left[1 + \frac{M}{Nq(r_A)} \right] \sqrt{\frac{m_e}{m_i M_{eff}}} = \omega \frac{\omega_{RF}}{c \omega_{ce} \sqrt{\left(1 - \frac{\omega_{RF}^2}{\omega_{ci}^2} \right)}}$$

It is seen that this expression does not depend on the plasma density explicitly, but only implicitly through $q(r_A)$. This fact helps us to identify the excited mode numbers M, N and to find the $q(r)$ values. For example, if plasma density increases in the course of discharge, the AW resonance zone moves to the plasma boundary, where $q(r_A)$ is larger. In this case, if AW modes with $M/N > 0$ are excited, the reflectometer will detect the increased AW modulation of the reflected signal at lower frequencies ω . This effect is not present for AW mode with $M=0$, which can be excited due to the toroidal effects.

Experimental setup

The experiments were carried out in the tokamak TCABR ($a=0.18\text{m}, R=0.61\text{m}, B=1.1\text{T}$). The basic parameters in this investigation were the following. Plasma current: $I_p = 70 - 95 \text{ kA}$; edge safety factor: $q(a) \approx 3.1 - 4$; line averaged plasma density: $\langle n_e \rangle = (0.9 - 1.5) \times 10^{19} \text{ m}^{-3}$; working gas: hydrogen. In the basic regime of operation, the AW antenna straps in the same toroidal cross-sections are fed by RF currents with $(0, \pi)$ phasing so that they can excite mainly the modes $M = \pm 1, N = \pm 1, \pm 2, \dots$. The RF power absorbed by the plasma was limited to $\tilde{P}_{RF} \leq 40 \text{ kW}$.

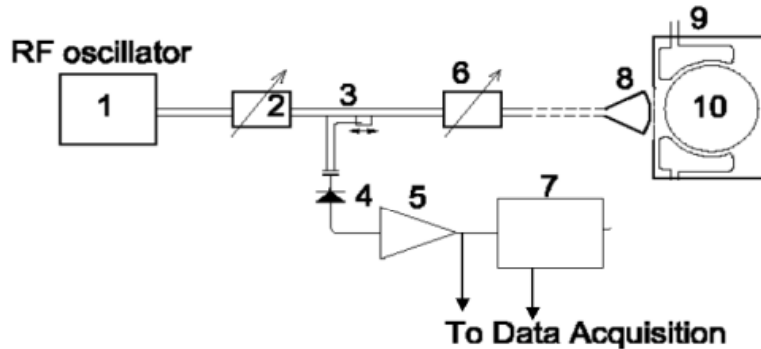


Fig.1 Schematic representation of the reflectometer diagnostic scheme: 1- microwave oscillator, $f=16 - 25.5 \text{ GHz}$, 2 - attenuator; 3 - directional coupler; 4 - diode detector; 5 - amplifier; 6 - phase shifter; 7 - resonance amplifier; 8 - horn antenna; 9 - RF Alfvén antennae, 10 - plasma column.

The registration of the AW driven density oscillations was carried out by a microwave reflectometer, which was developed in IST/CFN (Lisbon, Portugal), and operates at the frequency band of 16 to 25.5 GHz. Its scheme is shown in Fig.1

These rather low frequencies have limited the operational regimes of TCABR to low plasma densities, and only the plasma periphery was studied. The reflectometer was

adapted to the AW experiments in the TCABR. In order to register small signals in the AW frequency band, additional high sensitive selective amplifiers were constructed.

The output signal from the diode (4) is amplified by the wide band amplifier (5) and then is divided into two parts. One part is directed to VME through the low pass filter. This signal is used for plasma radial profile reconstruction. Second part is amplified by the selective amplifier (7) with pass-band frequency $f=(4.5\pm 0.5)$ MHz, which corresponds to the excited AW frequency. Then this signal is rectified, integrated with $\tau_{RC} \approx 5\mu\text{sec}$ and acquired by the VME. The VME sampling frequency was $f_s=3$ MHz. The data analysis includes the determination of the amplitude and spectral characteristics of these signals and their dependence on the variation of plasma current I_p and line averaged plasma density $\langle n(t) \rangle$.

Results

The registration of Alfvén wave resonances by microwave reflectometry was studied in the typical experimental conditions of the tokamak TCABR. Because of the low

frequency band of the reflectometer 16-25.5 GHz the initial rather low value of the line averaged plasma density

$\langle n \rangle \approx (0.9 - 1.2) \times 10^{19} \text{ m}^{-3}$ was chosen.

The typical traces of the plasma parameters are shown in Fig.2. The time window, in which the AW was excited, is shown in Fig.2(b).

In the course of the reflectometer frequency sweeping the amplitude of the diode signal is increased when the microwave cutoff zone coincides with AW resonance zone. In this case the continuous sweeping of the AW resonance zone will result in the repetitive increases of the diode signal for well defined reflectometer frequencies, which can change with the plasma parameters.

In the following data analysis the frequency modulating signal was transformed in the frequency-time plane and the contour lines of the amplitude of the diode signal were plotted in Fig.3. It is seen that maximum repetitive increases

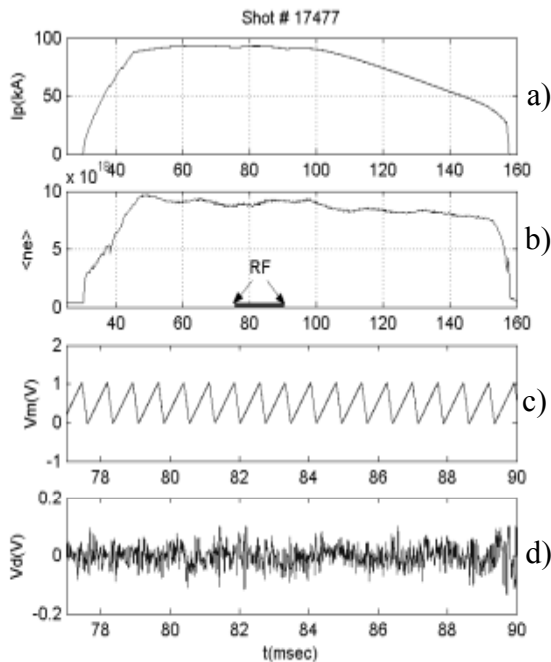


Fig.2 Shot #17477. a) - plasma current I_p ; b) - plasma density; c) - modulation signal ; and d) - diode signal at 4.5 MHz.

of the reflectometer signal occur at the frequencies $f \approx 20-20.5$ GHz. They correspond to increase of density oscillations induced by AW absorption near the resonant surface, which can be identified as $M=1, N=-2$ resonant surface.

Conclusions

Low frequency range of the reflectometer $f = 16-26.5$ GHz gives the possibility to study AW power deposition only at the plasma periphery in the low density regimes of the TCABR tokamak;

Experiments have shown that intensive density oscillations at the AW frequency are detected by the reflectometer close to the plasma boundary.

Selective excitation of the monochromatic AW with definite M , N and the utilization of the more wide range reflectometer is necessary for the implementation of this method for the plasma diagnostics.

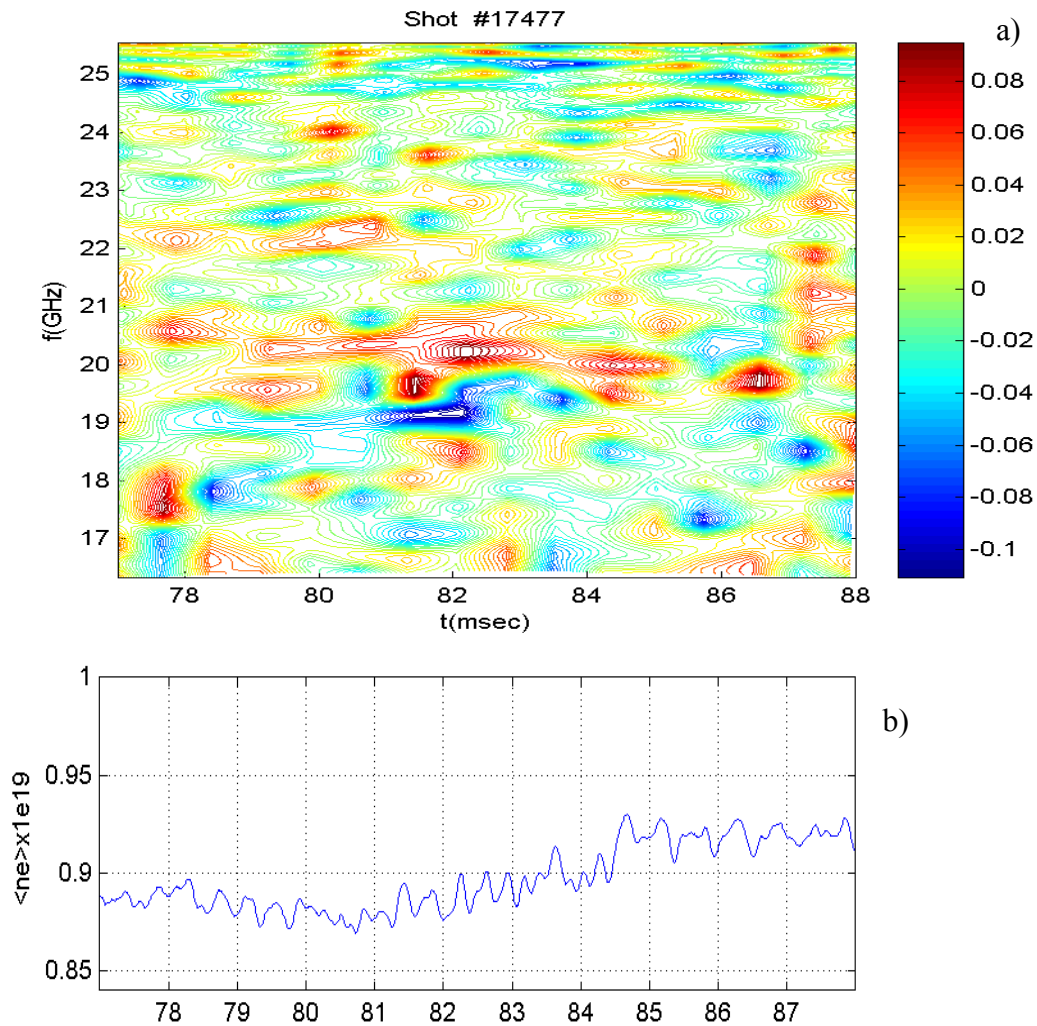


Fig.3 a) Contour plot of the AW signal from the reflectometer as function of the discharge time and of the reflectometer frequency.

b) line averaged plasma density $\langle n_e \rangle$

Acknowledgment

This work has been supported by The National Council for Scientific and Technological Development, The State of São Paulo Research Foundation, and The International Collaboration Council of University of São Paulo.

Referencies

- [1] L. F. Ruchko, R. M. O. Galvão, E. A. Lerche, A. G. Elfimov, V. Bellintani Jr, J. I. Elizondo, A. N. Fagundes, A. M. M. Fonseca, Yu.K. Kuznetsov, I. C. Nascimento, W. P. de Sá, E. Sanada, R. P.da Silva, R. Valencia, Rev. Sci. Instrum. **75**, 655 (2004).

Further development of reflectometry diagnostics for measurement of Alfvén Cascades on the JET tokamak

S. Hacquin¹, S. Sharapov², B. Alper², D. Borba¹, C. Boswell³,
J. Fessey², L. Meneses¹, M. Walsh² and the JET EFDA Contributors

¹*Associação EURATOM / IST, Centro de Fusão Nuclear, Lisboa, Portugal*

²*EURATOM / UKAEA Association, Culham Science Centre, UK*

³*MIT-PSFC, Cambridge, MA USA*

1. Introduction

A new class of Alfvén Eigenmodes, so-called Alfvén Cascades, was recently observed in the JT-60U, JET, TFTR and Alcator C-Mod tokamaks. The excitation and observation of these Alfvén Cascades is important for the diagnosis of advanced plasma scenarios. In addition to the determination of the magnetic field topology, the time evolution of the minimum of the safety factor – which is an useful parameter for the triggering of the internal transport barriers - can be inferred from their measurement. It was shown on TFTR that X-mode reflectometry could provide more information on the Alfvén Cascades than the external magnetic pick-up coils generally used for their detection ^[1]. On JET a new approach based on O-mode measurement in the interferometry regime proved to give an unprecedented clear picture of the Alfvén Cascades ^[2]. In this paper are discussed the main characteristics of the technique used and some illustrative results are presented.

2. Description of the fixed frequency multi-channel reflectometer diagnostic on JET

A 12-channel narrow-band reflectometer system probing the mid-plane plasma with the O-mode polarisation was used for density profile measurement on the JET tokamak ^[3]. This system now works with 10 channels at fixed frequencies (from 18.6 up to 69.6 GHz corresponding to the critical density range $0.43 - 6 \times 10^{19} \text{ m}^{-3}$) and is purely dedicated to study of the density fluctuations. Each channel uses two Gunn oscillators, whose frequency difference is maintained equal to 10.7 MHz by a phase-locked loop, for heterodyne detection. Each channel is also equipped with I/Q detection, thus allowing the determination of the amplitude and phase signals. I/Q data from up to 7 channels can be acquired with a digital

converter at a frequency rate of 1 MHz and for a maximum of 3s. In addition, another acquisition system offering the possibility of recording all the channels at a frequency rate of 2 MHz during all the discharges was recently implemented.

The advanced scenarios developed at JET generally lead to flat density profiles. In this case it is not possible to probe the core and the high field side regions of the plasma with O-mode reflectometry, since the probing waves cannot be reflected in these regions. This is illustrated on Figure 1, where the various frequencies of our multi-channel reflectometer are compared to the radial profile of plasma frequency for a typical JET discharge. From this figure it can be noticed that only the lowest probing frequencies (those lower than the maximum of the plasma frequency) are reflected by the plasma. This is the conventional use of a reflectometer but in these scenarios with flat density profiles the probing wave is reflected in the extreme edge region of the plasma (in the pedestal region) and consequently no information on the plasma core can be inferred. On the other hand, the probing frequencies higher than the maximum of the plasma frequency propagate without being reflected by the plasma. Reflected by the inner-wall, they come back to the detector after a round trip along the probing line of sight in the whole plasma region. In this situation, the reflectometer acts as an interferometer and all the plasma (including the core and high field side regions) can be probed. As shown in the next section, the interferometry regime proves to be quite efficient to observe MHD modes, such as the Alfvén cascades. Provided that the probing beam is launched perpendicularly to the inner-wall, the reflected beam is especially sensitive to the plasma fluctuations with a probing frequency approaching the plasma frequency.

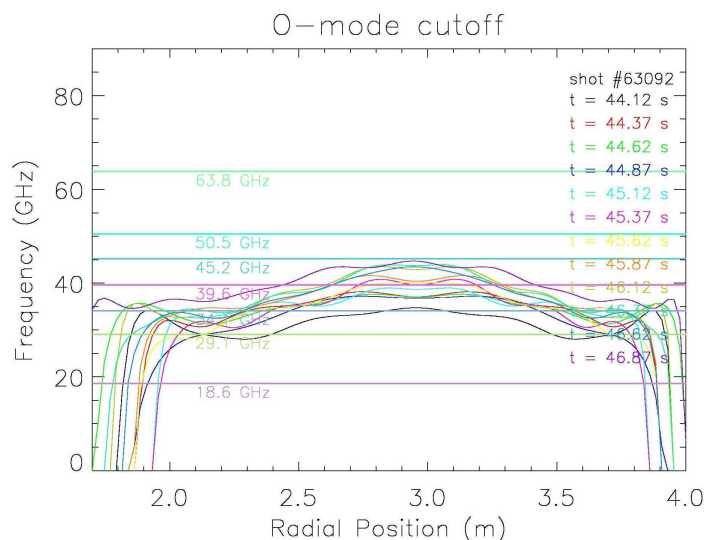


Figure 1: Frequencies of the different channels (horizontal lines) of the O-mode reflectometry diagnostic with respect to the plasma frequency at various times.

3. Measurements of Alfvén cascades in the interferometry regime

As discussed in [1], the density fluctuations induced by the Alfvén cascades are mainly localised in the high field side region so that only the channels in the interferometry regime (i.e. with probing frequency higher than the maximum of the plasma frequency) could detect them. In Figure 2 a spectrogram (sliding FFT) of the reflectometer “homodyne” signal $a(t) \times \sin(\phi(t))$ at frequency $f = 45.2$ GHz is depicted. From Figure 1, which corresponds to the same plasma discharge, we can notice that the diagnostic is in the interferometry regime during the time of interest (as the probing frequency $f = 45.2$ GHz is always higher than the plasma frequency maximum). Different classes of Alfvén Eigenmodes – such as the Alfvén Cascades (ACs) and the Toroidal Alfvén Eigenmodes (TAEs) in the 40-150 kHz range and the Elliptical Alfvén Eigenmodes (EAEs) in the 300-400 kHz range - can be observed in this spectrogram. In particular, the Alfvén cascades are detected with high time and frequency resolutions, far clearer than from other diagnostics as the magnetic pick-up coils and electron cyclotron emission radiometer. After calibration of the I and Q signals to remove the offsets and the amplitude and phase unbalance, the amplitude and phase signals can be extracted. A picture of the different Alfvén Eigenmodes as clear as in Figure 2 can still be obtained from the spectrograms of the amplitude and phase signals respectively.

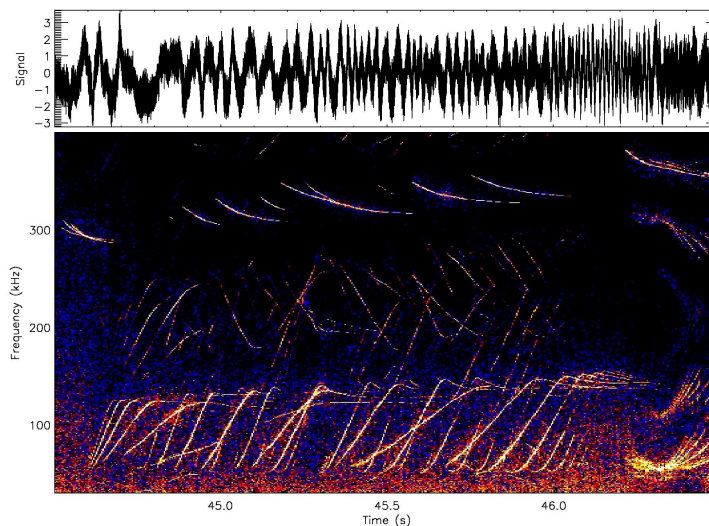


Figure 2: Observation of different classes of Alfvén Eigenmodes from the spectrogram of the homodyne signal (ACs / TAEs in the 40-150 kHz range and EAEs in the 300-400 kHz range)

Due to the high resolution of the interferometry-like measurements, the dynamics of the Alfvén cascades can be assessed. For instance, a clear Doppler shift of the frequency of the Alfvén cascades (up to 300 kHz) induced by the plasma toroidal rotation in the presence of strong neutral beam injection (NBI) heating was observed in [2]. As exemplified in Figure 3,

it was also shown that the Alfvén cascades, usually driven by super-Alfvénic ions accelerated with ion cyclotron resonance heating (ICRH), could also be driven by sub-Alfvénic ions in the presence of NBI.

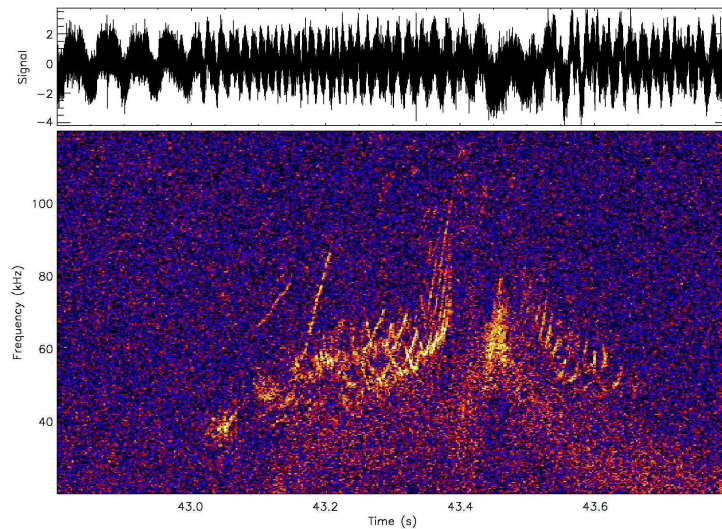


Figure 3: Observation of Alfvén cascades driven by NBI heating

4. Conclusions

When used in the interferometry regime, an O-mode multi-channel reflectometer diagnostic allows the measurement of the Alfvén Cascades on JET with high frequency and time resolution much clearer than from any other diagnostic, as for instance the magnetic pickup coils. However the Alfvén Cascades cannot be localised with this technique. In the next JET experimental campaigns (starting in November 2005), it is planned to complement these results with measurements in the reflectometry regime from the X-mode correlation reflectometer diagnostic using new low attenuation transmission lines.

Acknowledgements

The authors would like to thank R. Nazikian and G. Kramer for their useful advice. This work has been carried out in the frame of the Contract of Association between the European Atomic Energy Community and Instituto Superior Técnico (IST) and of the Contract of Associated Laboratory between Fundação para a Ciência e Tecnologia (FCT) and IST. The content of the publication is the sole responsibility of the authors and it does not necessarily represent the views of the Commission of the European Union or FCT or their services.

References:

- [1] R. Nazikian *et al*, *Physics Review Letters* **91**, 165001 (2004)
- [2] S. Sharapov *et al*, *Physics Review Letters* **93**, 125003 (2003)
- [3] A. Sips and G. Kramer, *Plasma Physics and Controlled Fusion*, **35**, 743 (1993)

FM-CW reflectometry for MHD activity measurements on Tore Supra

F. Clairet[&], S. Heuraux[€], G. Leclert[#], L. Vermare[&]

[&]*Association Euratom-CEA sur la fusion, DSM/DRFC/SCCP C.E. Cadarache, 13108 Saint-Paul-lès-Durance, France*

[€]*LPMIA, Université Henri Poincaré Nancy I, BP 239, 54506 Vandoeuvre-lès-Nancy, France*

[#]*LPIIM, CNRS-Université de Provence, Faculté de St Jérôme, case 321, 13397 Marseille, France*

Electronic mail : frederic.clairet@cea.fr

Abstract

In addition with traditional electron density radial profile measurements, fast frequency sweeping reflectometry technique can handle the fluctuations of the reflected signal to recover plasma density fluctuation measurements with a high spatial and temporal resolution. This paper illustrates how the large size turbulence related to magneto-hydrodynamic (MHD) activity and the associated magnetic islands can be recorded.

I. Introduction

Plasma turbulence is among the most important issues, which have to be addressed to appreciate the plasma equilibrium questions of magnetic fusion experiments. Problems of plasma discharge sustainment [1] can be destabilized by MHD activity, which can drive damaging fast electron towards the inner wall and/or conduct major plasma disruption. For example, plasma confinement regimes with full wave current drive experiment, specially used to achieve long duration plasma discharges, are particularly exposed to MHD stability problems. Innovative and comprehensible diagnostic measurements are required and reflectometry is a diagnostic permitting detailed research on this particular topic and benefits on a well-established technique.

II. Magnetic island and phase perturbation

Tore Supra is equipped with fast frequency sweeping (20 μ s) X-mode heterodyne reflectometers [2] dedicated to electron density profile measurements and covering the frequency range from 50 to 110 GHz. These reflectometers provide electron density profile measurements routinely and automatically on a shot to shot basis. Fast and repetitive sweeps (with 5 μ s dead time between sweeps), named burst mode technique, provide an equivalent sampling rate of 40 kHz at a given probing frequency and allow fast plasma events to be measured. The heterodyne and sine/cosine detection allows separate measurements of phase and amplitude of the reflected signal with a S/N sensitivity of about 40 dB. Reflectometry relies on the fact that, as an electromagnetic wave propagates through the plasma, its phase is shifted due to the departure of the local refractive index from the vacuum value. At a certain critical density corresponding to the cut-off layer, this refractive index goes to zero and then the probing wave is reflected. The plasma density fluctuations bring phase and amplitude fluctuations onto the recorded reflected signal. The presence of MHD activity can thus be

observed from the variation of the time of flight (ToF) $t = \frac{1}{2p} \frac{\partial f}{\partial F}$, because of the local flattening of the density profile produced by the magnetic islands (Fig.1).

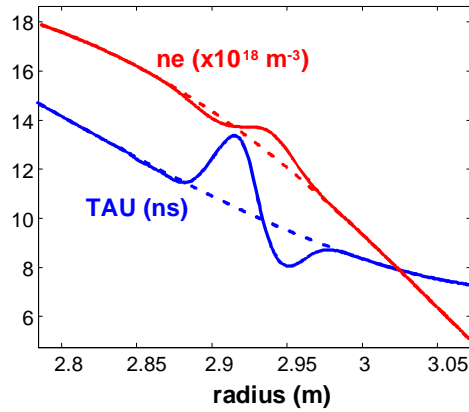


Figure 1 : Simulation of the time of flight response with a X-mode propagation for a perturbed (solid line) and non-perturbed density profile (dashed line).

Figure 2 is an experimental example of the variation of the ToF of the propagating probing wave. Thus, the derivative of the phase clearly exhibits the phase fluctuations induced by the density fluctuations.

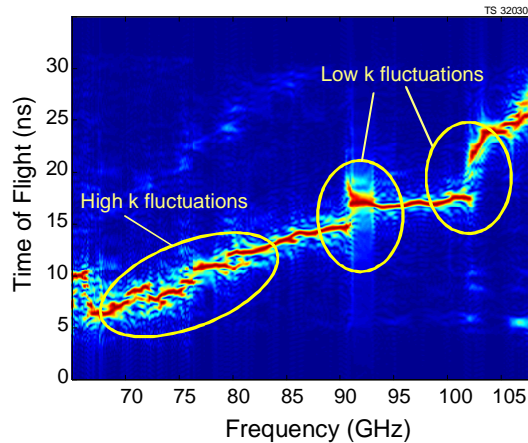


Figure 2 : Time of flight (phase derivative) of the probing electromagnetic wave propagating through the plasma. Two kinds of perturbations (large and small scale density fluctuations) can be identified.

Despite the continuous variation of the probing wavenumber value we will classify these fluctuations into two categories, large size (low k) due to large magnetic island of MHD activity and small size (high k) turbulence, which is analysed in [4].

III. Rational surface localisation

Tore Supra is particularly suited to perform long plasma duration over several minutes. The plasma current is then fully non inductive and totally sustained by the LHCD additional heating system. However, such discharges exhibit hollow current profiles with

double tearing modes sensitive to MHD activity and the control of the plasma current profile is thus challenging. Figure 3 illustrates the measurements of the low mode number MHD islands ($q=3/2$, $2/1$ and $3/1$) during such a plasma discharge. A comparison with plasma equilibrium code (CRONOS) (Fig. 3b) offered a valuable confrontation with measured data from FM-CW reflectometry.

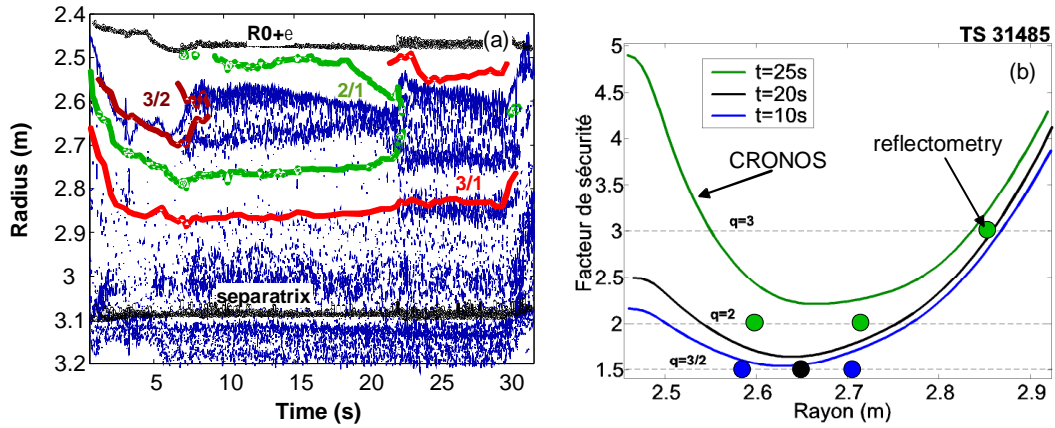


Figure 3 : a) ToF jumps recorded during the whole plasma discharge duration with low rational surfaces calculated from CRONOS superimposed. b) Comparison between CRONOS $q(r)$ hollow profile (solid lines) and measured radial positions of $q=3/2$, $2/1$ and $3/1$ rational surfaces using FM-CW reflectometry.

IV. Temporal dynamic of the MHD and magnetic island structure determination

High spatial and temporal resolution of fast sweep reflectometry makes possible to investigate dynamic of the MHD magnetic islands rotation up to 20 kHz [4]. Furthermore, an analysis of the amplitude variations of the reflected signal points out precious indications on their poloidal shape. There can be a particular interest in identifying modes with low values of the integers m and n in order to constraint equilibrium code during calculations of the plasma current profile.

Experimental observation and radial localisation of magnetic islands is performed through the detection of the major group delay jumps. Figure 4a and 4b illustrates the $q(r)$ profile evolution recorded by the reflectometry during a plasma current ramp-up experiment. Localised perturbations are radially detected and agree with the $q=2/1$ and $q=1/1$ rational surfaces calculated by the equilibrium code. However, at $t=9s$, the $q=2/1$ surface is no longer visible and it points out the limit of this method since magnetic islands have to be present into the plasma discharge to be recorded.

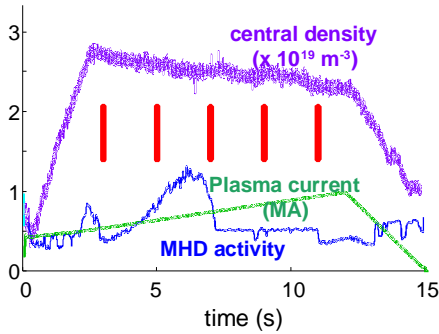


Figure 4a : Tore Supra plasma discharge where each vertical bars represent 1000 acquisitions of frequency sweeping during a current ramp-up.

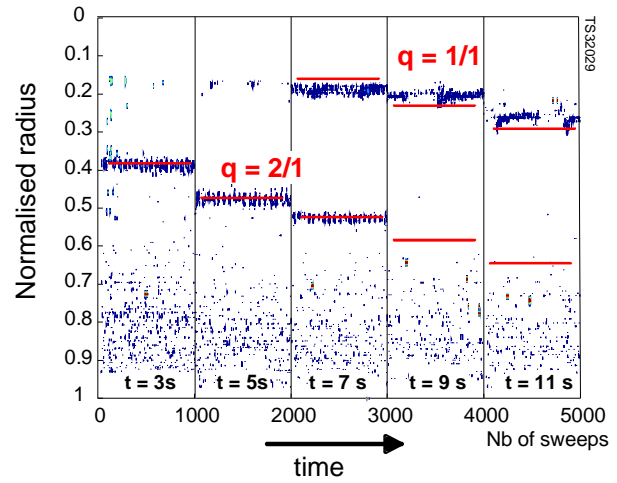


Figure 4b : Contour plot of detected ToF jumps that coincide with rational q safety factor value radial positions calculated with equilibrium code (horizontal red lines).

A detailed analysis of the reflected signal during the second burst of data at $t=5s$ exhibits clearly the dynamic of the island rotation of the $q = 2/1$ MHD mode. On figure 5 is shown the opposite phase oscillations of the phase derivative for probing frequencies on each side of the density plateau (as expected from figure 1); a significant loss of the amplitude of the reflected signal occurs when the reflectometer probes the O-point of the magnetic island.

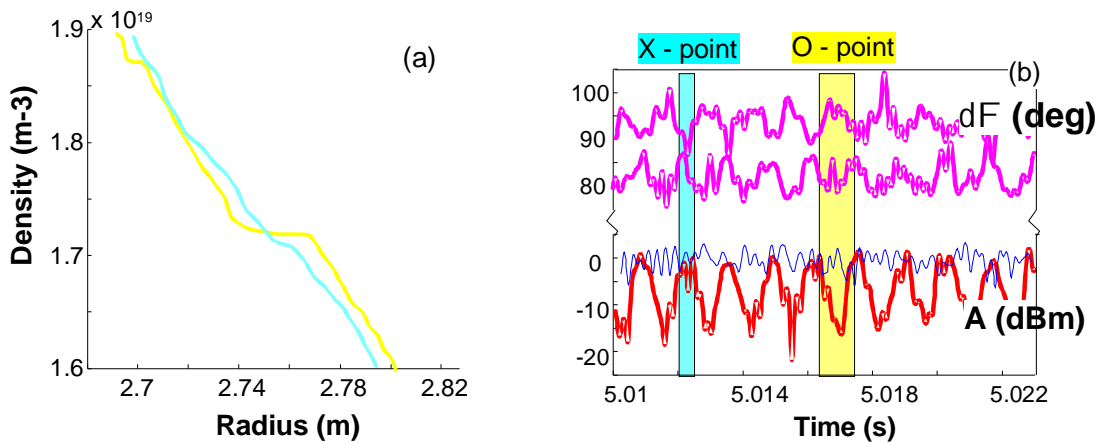


Figure 5 : a) Reconstructed density profiles when the reflectometer is probing the O point and the X point of the magnetic island. b) Perturbation of the phase derivative on both side of the density plateau and the corresponding reflected amplitude.

The time evolution of the above phase derivative and amplitude is Fourier analysed for each probing frequencies (Fig. 6). The radial position is retrieved from the reconstructed density profile, which is an averaged of the 1000 profiles over the burst period. The modulation of the amplitude at the plateau position strongly suggests the presence of a sub-structure inside the magnetic island, which has to be confirmed with 2D full wave propagating code.

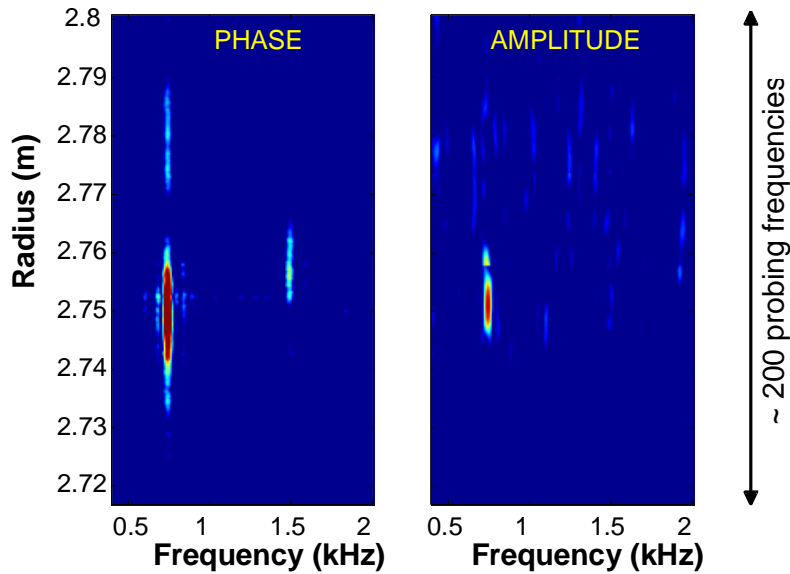


Figure 6 : Fourier analysis of the time evolution of the phase derivative and the amplitude of the reflected signal for probing frequencies between 92 and 100 GHz.

V. Summary

Fast frequency sweeping reflectometry has been routinely running to perform density profile measurements onto tokamak devices for many years now. Due to the high technical performances of Tore Supra set-up, accurate determination of the reflected phase signal is achieved with a high radial resolution. MHD activity can be clearly observed as long as magnetic islands are present into the plasma. This situation gives relevant experimental information to constrain the plasma current profile calculated from equilibrium codes. Very detailed analysis of the temporal dynamic and radial and poloidal shape of the magnetic islands is available with this technique.

References

- [1] P. Maget, F. Imbeaux, G. Huysmans, F. Clairet, Ph. Moreau, J.-L. Segui, L. Vermare, M. Ottaviani and M. Goniche *Nucl. Fusion* 45 No 2 (February 2005) 69-80.
- [2] Clairet F, Bottureau C, Chareau JM, Paume M and Sabot R 2001 *Plasma Phys. Control. Fusion* **43** 429.
- [3] S. Heuraux, L. Vermare, F. Clairet, G. Leclert, F. da Silva (*this workshop*).
- [4] Vermare L, Clairet F, Gabillet F, Sabot R, Sirinelli A, Heuraux S and Leclert G 2004 *Rev. Sci. Instrum.* **75** 3825.

Radial behaviour of density fluctuations deduced from FM-CW Tore Supra reflectometry data

S. Heuraux, L. Vermare[°], F. Clairet[°], G. Leclert[@], F. da Silva[#]

LPMIA, UMR-CNRS 7040, U H P, Nancy 1 BP 239, F-54506 Vandœuvre Cedex, France

[#]Association Euratom-CFN IST 1046-001 Lisboa, Portugal

[°]Association Euratom-CEA DRFC Cadarache, 13108 S' Paul les Durance, France

*[@]LPIIM, UMR-CNRS 6633, Université de Provence, Centre St-Jérôme
Case 321, 13397 Marseille Cedex 20 -France*

Introduction

On Tore Supra, FM-CW X-mode Reflectometry provides electron density profile routinely and automatically on the shot to shot basis [1]. It can provide, as well, localised information on the plasma fluctuations. Up to now the fixed frequency reflectometer was used to give good relative evolution and quantitative information if the local characteristic length of the fluctuations is known in the vicinity of the cut-off layer [2-3], as the refractive index gradient length, and assuming the corresponding wavelength can be associated to an oscillation of the cut-off. We explore here the possibility to obtain quantitative information about the radial evolution of the density fluctuation, either plasma turbulence, deduced from the wavenumber spectrum (k_f -spectrum) of the density fluctuation based on the analysis of the phase fluctuation of the reflected signal obtained during fast frequency sweeps [4]. To extract the density fluctuation profile from the X-mode reflectometer data, a new data processing method has been built taking the advantage that the local index gradient length is computed with the same data used for extracting the phase fluctuations more exactly from the time of flight fluctuations. This fact assures the coherency between the needed parameters used to extract the density fluctuation profile except for the magnetic field profile, which is provided by an equilibrium code or an analytical formula including all the corrections used to reconstruct the density profile [5]. After a brief recall of the basic physics processes and the aim of the method the data processing procedure is given. Then to validate this method and to determine the validity domain, simulations have been done. Finally, some examples of density fluctuation profile evolutions are shown as function of different parameters such as the plasma current in the ohmic shots, the central density and during ion cyclotron heating at different input power.

Basic physical processes and aim the method.

During the frequency sweep, each incident frequency *selects a wave number at a given radial position in the density gradient* owing to the Bragg selection rule $k_f = 2k(x)$ that relates the incident local wave number and the k_f component of the fluctuation spectrum. The results thus obtained show that all the wave numbers up to the Bragg detection limit ($k_f < 2k_o$ where k_o is the wave number in vacuum) contribute to the phase fluctuations in a wide k_f spectrum of the density fluctuations as shown previously on O-mode FM-CW reflectometer [4]. An important point has been put forward in the paper of Y. Lin *et al* [6], 1D simulations still remain useful, relevant and necessary to understand the

numerous physical processes involved in tokamak plasmas. The method relies upon between radial wave-number spectrum (k_r -spectrum) and phase fluctuation spectrum of the signal of a swept frequency reflectometer. Due to the Bragg selection rule $k_f = 2k(x)$ between the incident local wavenumber and the k_r -component of the fluctuation spectrum, every incident frequency *selects a wavenumber at a given radial position in the density gradient*. For O-mode reflectometry [2,7-8] analytical expressions of the phase variations induced by monochromatic density perturbations are then used to rely the phase spectrum to the density fluctuation spectrum under the Born approximation associated to monochromatic density perturbations. The phase perturbation varies as $\delta\phi \propto k_f^{-1/2}$: as expected for extended density perturbations [7], the main contribution comes from the small k_r , i.e. the vicinity of the cut-off layer. The local density gradient length L_n renormalises also the phase variation, $\delta\phi \propto L_n^{1/2}$. For X-mode reflectometry, there is no simple dependence of the phase on the wavenumber or gradient lengths except in the vicinity of the cut-off where $\delta\phi \propto k_f^{-1/2}$ like in O-mode. Thus a transfer function is needed to link the density fluctuation spectrum to the phase fluctuation spectrum. The way used to build the transfer function consists in the computation with a full-wave code [7,9] of the phase fluctuation spectrum $S_{\delta\phi}(k_r)$ from a known density fluctuation spectrum $S_{\delta n}(k_r)$ with the experimental magnetic field and density profiles. We can then compute the ratio $F_{tr} = S_{\delta n}(k_r)/S_{\delta\phi}(k_r)$ in the case of low density fluctuation amplitude. In order to access the absolute value of the density fluctuation, an integration over an appropriate range of $S_{\delta n}(k_r)$ is performed using the Parseval's theorem. The choice of the integration range in wavenumber k is determined by the fact that at very low wavenumber some contribution comes from poloidal wavenumber [9] and the upper bound in k by the ratio signal-noise or by the detection limit corresponding to the upper frequency of the probing wave. The signature and the role of the MHD activity (magnetic islands) have been discussed in the reference [4] for the Tore Supra O-mode reflectometer [10] and these conclusions can be extended to the X-mode reflectometer by substituting the density gradient length by the index gradient length.

Validation of the method by simulations and determination of the validity domain.

The simulations of the Tore Supra X-Mode reflectometers have been done with the experimental profiles except for density fluctuations with a given turbulent spectrum, which is built to reproduce as close as possible the knowing density fluctuation spectrum on Tore Supra. The data processing used is the same as those applied on the X-mode reflectometer data, which can be described as following: an average over 100 frequency sweeps is done to extract an averaged phase which is subtracted to the phase profile given by each single sweep. In order to obtain a phase fluctuation profile over the entire probing zone, a FFT is performed to determine the phase fluctuation spectrum (see Fig. 1). Then the transfer function obtained from the ratio of the input density fluctuation spectrum over the computed phase fluctuation spectrum is built for each sweep with experimental profiles and experimental parameters of the given shot as inputs of 1D full-wave code and applied on the phase fluctuation spectrum to recover the density fluctuation spectrum. The input density fluctuation spectrum has to be taken wide enough to be higher than the detection limit of the X-mode $k_f > 2 k_{omax}$ (k_{omax} the highest probing wavenumber). However, the method applied on the Tore Supra reflectometer data uses the spatial derivative of the phase (equivalent to the time of flight) to determine the wavenumber

spectrum. This spatial derivative introduces only a multiplication by k_r of the wavenumber spectrum after the FFT. This correction is directly taken into account in the transfer function.

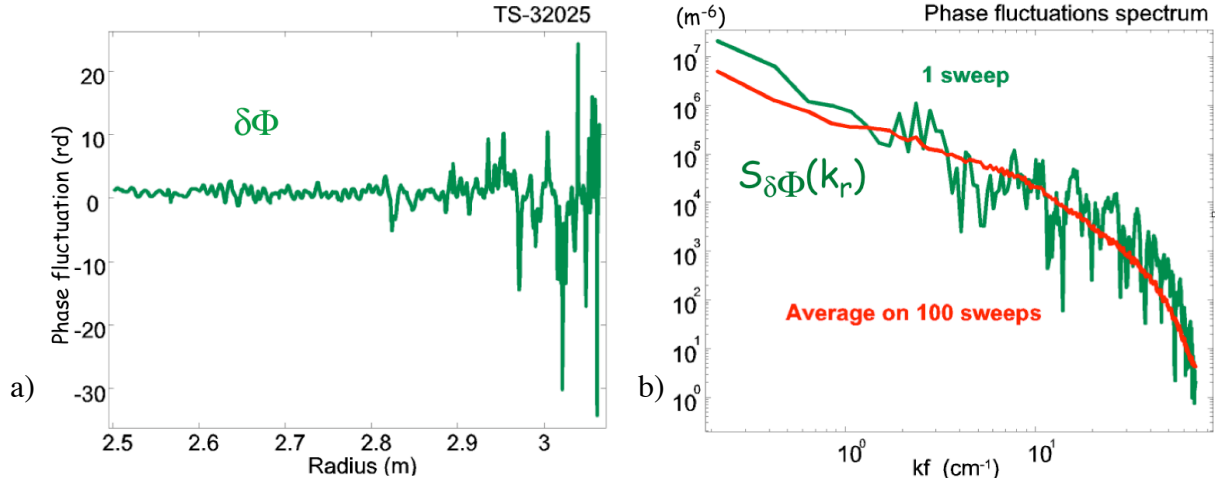


Figure 1: a) Phase fluctuation as a function of the major radius obtained from one sweep on V and W-band during the 32025th Tore Supra shot and b) the deduced radial wavenumber spectrum from Fourier transform for single sweep and an average spectrum over 100 sweeps.

This method has been tested over a wide set of simulations to determine its validity domain and its limits. At low-density fluctuation amplitude, the input density fluctuation spectrum is recovered up to the detection limit. Some distortion in the rebuilt spectrum appears for density fluctuation amplitude greater than 1-2 % in the Tore Supra-like cases. However the integral of the spectrum

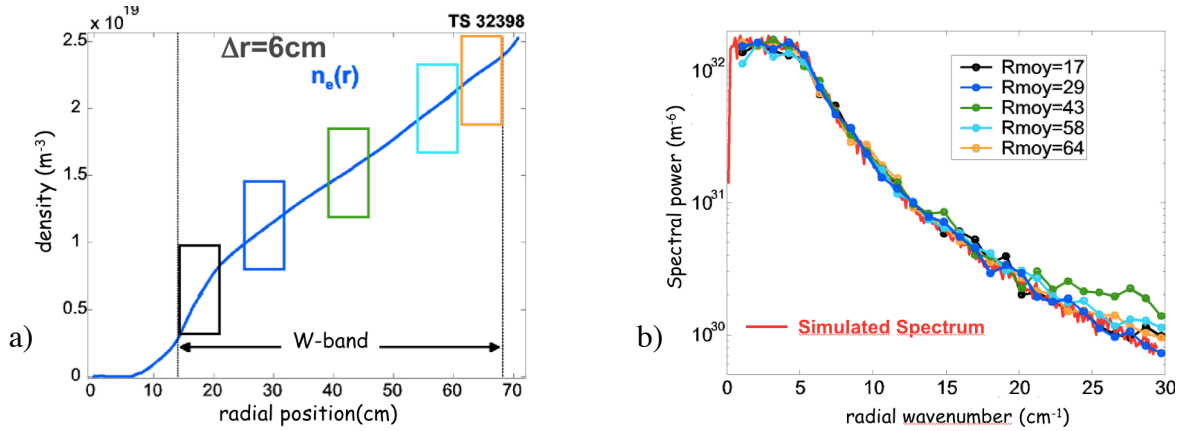


Figure 2: a) Density profile of the 32398th Tore Supra shot deduced from X-mode reflectometer and window positions used as inputs in the simulation and b) the deduced radial wavenumber spectra for different window positions in good agreement with input spectra at low turbulence level (<1%).

seems to be conserved up to 20-30% of the density fluctuation level at the edge. Up to this value only the shape of the spectrum is modified. Using the fact that the Bragg backscattering is localised, a sliding window applied on the phase fluctuation gives local information on the density fluctuation amplitude and spectrum. However, the width of sliding window Δr determines the range of wavenumber $[2\pi/\Delta r, k_{up} \text{ or } 2\pi/dr]$ used to reach the density fluctuation amplitude, where dr is the radial step and k_{up} is a chosen value of the wavenumber lower than $2\pi/dr$. In this case it is possible by using the Parseval's theorem to reach the radial evolution of the absolute density fluctuation amplitude. The simulations have shown this possibility and also another possibility to extract

information on the radial evolution of the wavenumber spectrum at low-density fluctuation level (see Fig. 2).

Some Experimental results deduced from the X-mode reflectometer data.

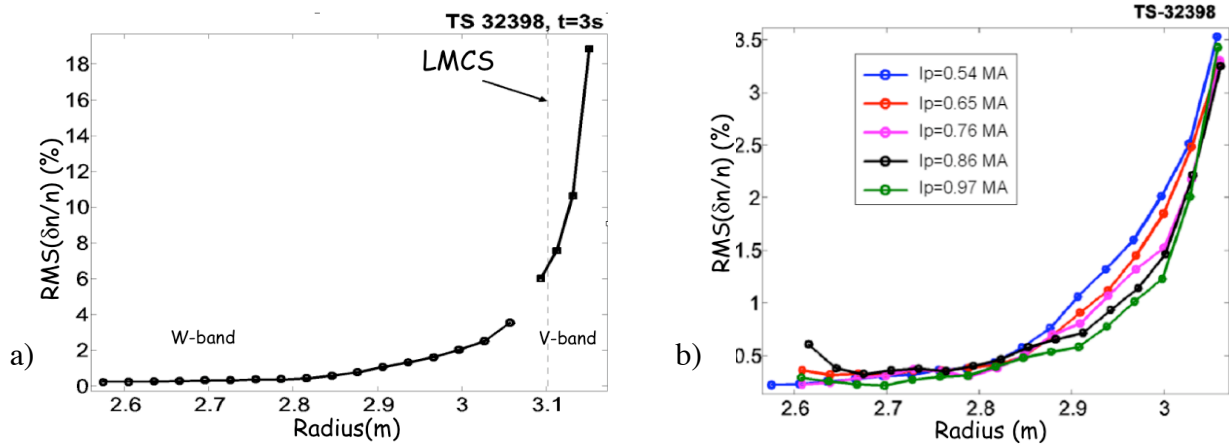


Figure 3: a) Radial evolution of the density fluctuation amplitude of the 32398th Tore Supra shot deduced from X-mode reflectometers on V and W-band and b) Evolution of density fluctuation profile for the same shot at different values of the plasma current in ohmic discharges.

Our method has been applied to the Tore Supra X-mode reflectometers to extract the radial profile of the density fluctuation over all the probing zone as shown on the figure 3a. A reduction of the relative density fluctuation amplitude is clearly seen in the gradient zone when the plasma current increases without significant change of the density profiles. This evolution follows the energy confinement time scale established [11]. This method using a transfer function is a very promising tool to access to the density fluctuation profile and to the wavenumber spectrum of the density fluctuation on a more restricted domain. The density fluctuation profile has been obtained also for different plasma conditions with or without heating.

References

- [1] F. Clairet, C. Bottureau, J.M. Chareau, M. Paume and R. Sabot, 2001 *Plasma Phys. Contro. Fusion* **43** 429; F. Clairet, C. Bottureau, J.M. Chareau and R. Sabot, *Rev. Sci. Instrum.*, **74**, 1481, (2003)].
- [2] R. Sabot, A. Sirinelli, F. Clairet, J.C. Giacalone, S. Heuraux, G. Leclert, J.L. Ségui, L. Vermare, 7th International Reflectometry Workshop 9-11 May Garching 2005 this proceeding.
- [3] E. Mazzucato and R. Nazikian, *Phys. Rev. Lett.* **71**, 1840 (1993).
- [4] S. Heuraux, S. Hacquin, F. da Silva, F. Clairet, R. Sabot et al, *Rev. Sci. Ins.* **74**, 1501 (2003).
- [5] A. Sirinelli, R. Sabot, JC. Giacalone et al, 7th Int. Reflec. Work. 9-11 May Garching 2005 this proceeding
- [6] Y. Lin, R. Nazikian, J.H. Irby, E.S. Marmor, *Plasma Phys. Cont. Fusion* **43** L1 (2001).
- [7] C. Fanack, I. Boucher, S. Heuraux, G. Leclert, F. Clairet et al, *Plasma Phys. Cont. Fusion* **38**, 1915 (1996).
- [8] B. B. Afeyan, A. E. Chou, and B. I. Cohen, *Plasma Phys. Contr. Fusion* **37**, 315 (1995).
- [9] S. Hacquin, S. Heuraux, F. Silva et al 29th EPS Conf. fusion & plasma phys; Montreux 17-21 June. ECA Vol. **26B** (2002) P5.094
- [10] P. Moreau , F. Clairet, J.M. Chareau, M. Paume and C. Laviron, *Rev. Sci. Instr.*, **71**, 74 (2000).
- [11] G. Hoang, B. Saoutic, L. Guizouand et al, *Nuclear Fusion* **40** 1869 (1998).

CORRELATION REFLECTOMETRY MEASUREMENTS IN T-10 TOKAMAK

V.A. Vershkov, D.A. Shelukhin, S.V. Soldatov, A.O. Urazbaev

Nuclear Fusion Institute, Russian Research Center “Kurchatov Institute”, Moscow, Russia

1. Introduction

Paper summarizes the results of turbulence investigation with correlation reflectometry (CR) in T-10 tokamak [1-7]. The main goal of the experimental program was identification of the physical mechanisms of the plasma turbulence. The T-10 diagnostic capabilities enable to investigate relatively long waves with $k_{\perp} \times \rho_i < 1$ due to low sensitivity for the wavelengths less than 1 cm. The investigations of turbulence physics supposed the determination of the temporal and spatial turbulence characteristics of density fluctuations. This was realized by means of the use of the correlation reflectometry, including poloidal, radial and long distance toroidal correlations. The restrictions of reflectometry are discussed in the second paper at this Workshop [7].

2. Experimental set up

The locations of (CR) antennas and T-10 limiters are shown in Fig.1. T-10 has circular plasma cross-section with the major and the minor radius of 1.5 and 0.3 m. respectively. The graphite permanent circular and movable rail limiters at radii 0.33 and 0.3 m defined the plasma column. The CR [3] was able to measure poloidal and radial turbulence characteristics. The CR had two antenna arrays, probing the plasma from the Low Field Side (LFS) and High Field Side (HFS). All antennas were aligned to the centre of the plasma column. It was possible to probe the plasma simultaneously from both the HFS and the LFS in order to measure the poloidal asymmetry of the turbulence and long distance poloidal and toroidal correlations [2,3]. The reflection of O-mode in the frequency range 22-78 GHz was covered with the four independent systems. The quadrature detectors were used to record the electric vector of the reflected waves. All signal processing was made in complex form. The available 8 ADCs with the sampling rate 800 kHz enable to record simultaneously the signals from four arbitrary antennas. The investigations of the radial and poloidal CR locality showed that for all radii sensitivity do not decrease significantly for the wave numbers $k_{\perp} < 3$, which is typical for T-10. The estimation of the turbulence velocity may be found from the ratio of the antennas reflection spots separation dx and the time delay of the two reflected signals Δt as $V = dx/\Delta t$. It should be stressed that due to the long extension of perturbation along the magnetic field line, the measured velocity principally always has poloidal and toroidal contributions.

3. Radial variations of turbulence characteristics

The OH and ECRH discharges show the distinct transition from the core turbulence to the SOL. Figure 2 presents the results of the complex poloidal correlation analysis. The typical amplitude Fourier spectrum of the first signal (top traces) and cross-spectra between two signals, including the poloidal cross-phase (middle) and

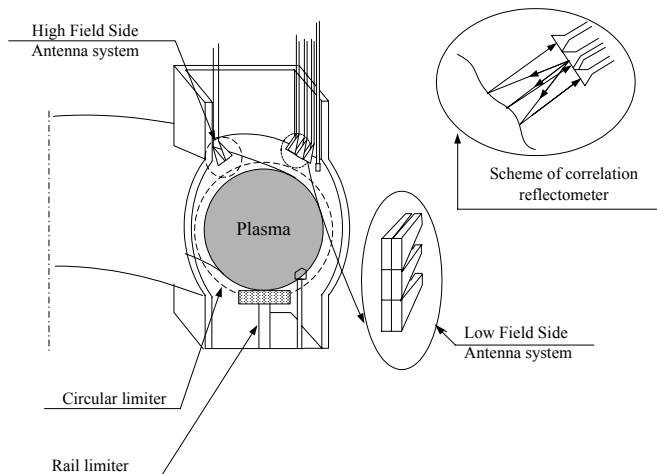


Figure 1. The schematics of correlation reflectometer diagnostics and limiters in the T-10

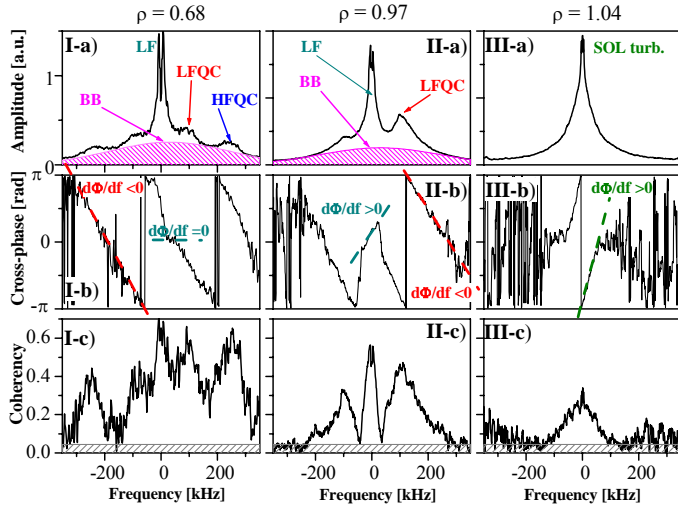


Figure 2. Typical spectra of CR signal from poloidally separated antennas from plasma center (left), reflection from the core edge plasma (middle) and SOL (right).

possible to distinguish five components in the core spectrum. The core edge turbulence retains only LF QC, while HF QC vanishes. In difference to the core, SOL fluctuations have a single spectral maximum at zero frequency and turbulence rotation changes the sign to the ion diamagnetic drift direction.

4. Characterization of turbulence types by radial correlations

Two quantities are obtained in the measurements of the radial correlation: the radial correlation length and the variation of the time delay with the radial separation. These data are presented in Fig. 3 for three turbulence types. The left column corresponds to LF, the middle one for the LF QC and the right one for the BB turbulence. It is clearly seen that BB has the shortest correlation length of 0.5 cm with zero time delay. It may arise due to the stochastic excitation of a single mode with high poloidal m number. In difference to BB, the radial correlation length of LF QC turbulence is the three times longer and the time delay is pronounced. This result can be formally treated as the radial propagation of QC with the velocity 2.3×10^3 m/s in addition to poloidal velocity 2.8×10^3 m/s. Nevertheless, the other hypothesis seems more real. It explains the observed phase shift of QC by rotation of helical “fingers”, inclined to the radial direction, which arise in 3D gyrokinetic simulations due to the toroidal coupling of several modes with close poloidal m numbers [10]. The LF has the longest correlation length about 4 cm. with zero time delay. These properties are similar to “streamers”, which arise in theory [11].

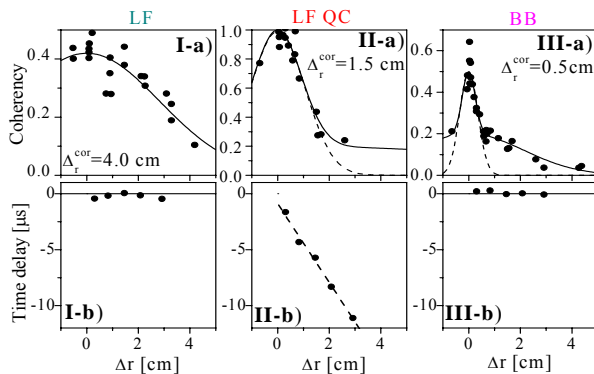


Figure 3. Coherency and radial time delay between the fluctuations at radially separated layers for LF, LF QC and BB oscillation.

coherency (bottom) are shown for the SOL, central and edge core regions. A pronounce difference is clearly seen. The core turbulence rotates in electron diamagnetic drift direction and has complex structure. It includes the background “Broad Band” (BB) fluctuation, High Frequency (HF) and Low Frequency (LF) “Quasi-Coherent” (QC) spectral maxima typically at frequencies 70-120 and 150-250 kHz respectively and “Low Frequency” (LF) peak at zero frequency. The special fluctuations at 20 – 30 kHz (not shown in Fig. 2) are also seen at low densities in core regions [1,4,6]. Therefore, it is

5. Specific modes in frequency range “15 - 30” kHz

The nearly monochromatic oscillations are typically observed in the frequency range 15 – 30 kHz with CR [1,4,6]. Similar phenomena had been observed, firstly in TEXT [21] and T-10 [1] and, recently in DIII-D, [12], CHS [13] and ASDEX-U [14]. The zero poloidal phase shift of the density fluctuations for this mode was measured by CR with poloidal angle separation of 5° and 55° . This means,

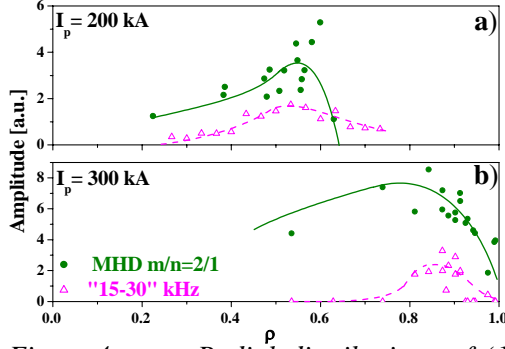


Figure 4. Radial distributions of ‘15 – 30’ kHz and MHD modes for discharges with plasma current 200 kA and 300 kA.

not consistent with the simple theory of “zonal flows”. The amplitude of the mode strongly localized near rational surfaces, especially $q=2$. Figure 4 shows the radial distribution of the mode and of the MHD $m/n=2/1$ density oscillations for two discharges with different $q(a)$ value. Clearly seen that mode located near $q=2$ region and shifted outward with the decrease of $q(a)$. Moreover, the mode has finite structure inside $m/n=2/1$ island [17].

6. Characterization of LF and HF Quasi-Coherent fluctuations

The typical core amplitude spectrum of fluctuations is shown in Fig. 2 exhibits two spectral maxima. The LF QC usually observed at 70-120 and HF QC at 150-250 kHz. The strong difference of their spatial structure was found in experiment [3]. The radial scan of $k_{\perp} \times \rho_i$ values for both QC types together with the linear growth rates of ITG [8], DTEM [8] and BRI [9] instabilities are presented in Fig. 5. Experiment showed only LF QC at the core edge ($0.8 < r/a < 1$), where only ITG is unstable, while in the plasma core both LF and HF QC maxima are seen in accordance with the increments of ITG and DTEM. It should be stressed that the appearance of HF QC at $r/a=0.8$ just coincides with the rise of DTEM growth rate. It is important that in core plasma the $k_{\perp} \times \rho_i$ values approach 0.3 for LF QC and 0.7 for HF QC as are expected from theoretical estimations for ITG and DTEM. The radial distributions of the amplitudes of both modes and values of linear growth rates are shown in Fig. 6 for the two phases of Ohmic discharge. The data of the left column was taken during the strong working gas influx at the density

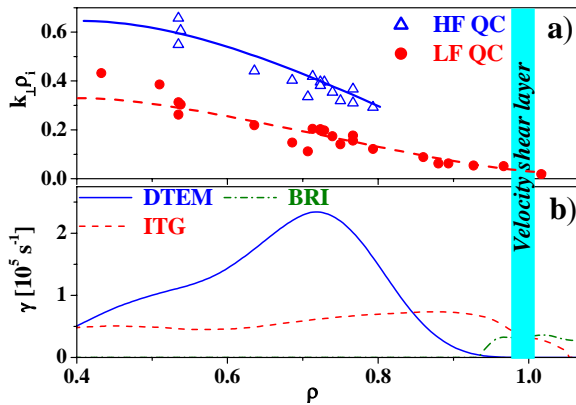


Figure 5. Radial distribution of $k_{\perp} \times \rho_i$ values for LF and HF QC oscillations (Top). Radial profiles of estimated growth rates of ITG, DTEM and BRI instabilities (Bottom).

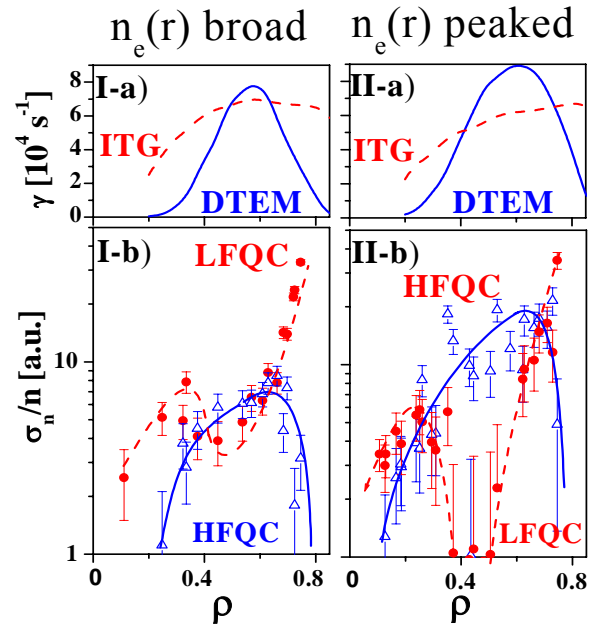


Figure 6. Top: Estimated growth rates of ITG and DTEM in two phases of Ohmic discharge: with broad plasma density profile (I, left) and peaked one (II, right). Bottom: amplitude of density fluctuations of LF and HF QC.

build up phase. The measured density profile is broad in this case. The right column corresponds to the stationary discharge conditions with more peaked density profile. The radial distribution of the LF QC amplitude is in good agreement with the growth rates values. The HF QC is maximal at $a/2$ at maximal DTEM increment. Figure 6 clearly show that after evolving of the discharge to the stationary conditions with more peaked density the LF QC is stabilized from 12 to 17.5 cm. This behavior again is consistent with stabilization of ITG by the density gradient. At the same time, the amplitude of HF QC is increased in accordance with DTEM growth rate increases. So both the radial behavior and reaction to the density peaking are consistent with ITG and DTEM instabilities. This correspondence is also supported by the values of $k_{\perp} \times \rho_i = 0.3$ for LF QC in core regions of discharges. Extremely wide scan was obtained by comparison of T-10, TEXTOR and FTU results in [5]. For $r=a/2$ all values were near to 0.3 in the wide range of magnetic field up to 8 T, as predicted for ITG instability.

7. Turbulence rotation

Figure 7 presents the radial dependence of turbulence parameters in the Ohmic discharge. Figure 7a shows the radial variation of the angular turbulence rotation and Fig. 7b the poloidal m numbers of the LF and HF QC turbulence. One can see that the angular turbulence rotation is remarkably constant over the whole plasma radii. Moreover it coincides with that of MHD $m/n=2/1$ island rotation. Figure 7b shows that poloidal m numbers are also constant. Thus the turbulence rotates over all radii like rigid body with the angular velocity of $m/n=2/1$ mode. It should be stressed that rigid body rotation together with the $m/n=2/1$ mode is the most general feature in OH discharges. It breaks in velocity shear layers and under additional toroidal momentum input with NBI heating in TEXTOR [5]. The turbulence rotation decreases during ECR heating.

8. Long distance toroidal correlations

The presence of the two antenna arrays separated poloidally at 55° gives possibility for observing long distance correlation along the torus, when the magnetic field line issued from one antenna, hit the sensitive spot of the other after one turn around major torus axis. The schematics of the possible resonant conditions are shown in Fig. 8 on the unfolding of the tokamak in toroidal/poloidal plane [2,3]. It is seen that in geometry of T-10 antennas toroidal correlations should be observed at the magnetic surfaces with $q = 0.87$ and $q = 1.18$, provided that the turbulence do not deviate strongly from the magnetic field line.

The first results were published in [2,3]. The new series of experiments were carried out in a special reflectometer configuration that eliminates the effect of parasitic cross-talk of

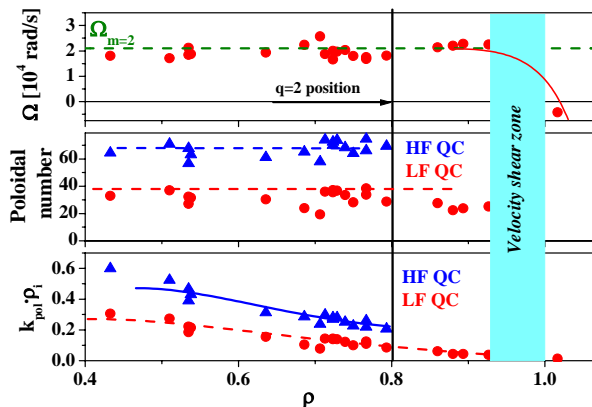


Figure 7. Radial profiles of turbulence angular velocity, poloidal m numbers for LF and HF QC oscillations and $k_{\perp} \times \rho_i$ values.

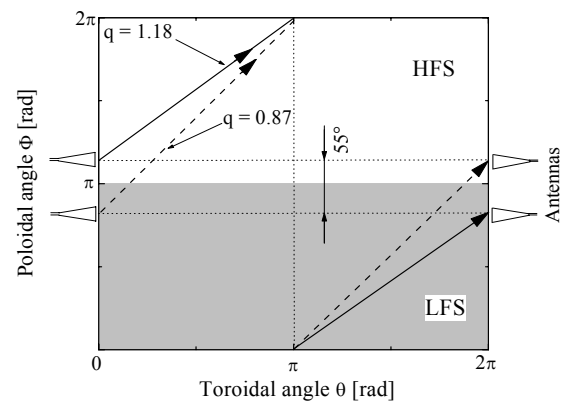


Figure 8. The schematics of the possible toroidal resonant conditions on the unfolding of T-10 tokamak in toroidal/poloidal plane.

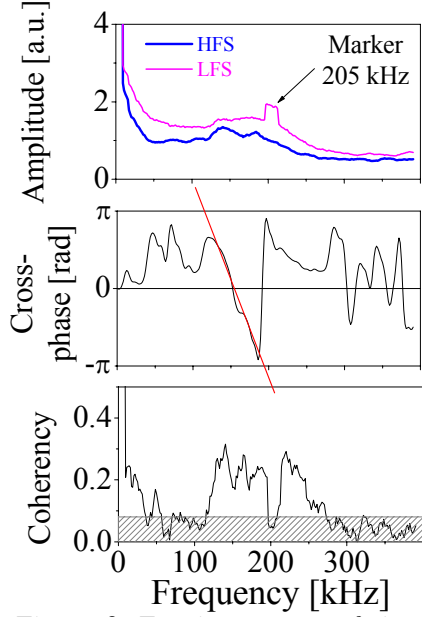


Figure 9. Fourier spectra of signal amplitude, cross-phase and coherency are shown for toroidal correlations at $q = 1.18$

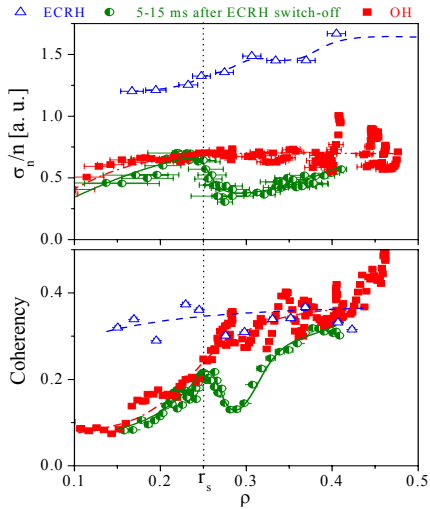


Figure 10 Radial profiles of density fluctuations amplitude and poloidal coherency in discharge with the e-ITB formation.

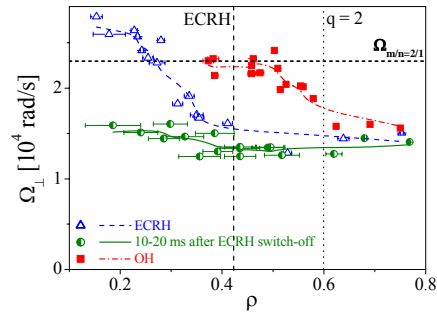


Figure 11. Radial profiles of turbulence velocity in discharge with the e-ITB formation after off-axis ECRH switch-off.

the antennas in one port. The experiments proved the previous data, taken with reflection layer near $q = 1$ radius [2,3].

The second resonant condition was also achieved in new experiments. The results for this case are shown in Fig. 9. The reflection radius was at $\rho \sim 0.45$ with the sawtooth inversion radius at $\rho \sim 0.2$, which guarantees the reflection well outside of the sawtooth mixing region. There were no special q measurements at the resonant conditions, but estimations of the current profile with the measured electron temperature gave the value close to $q = 1.18$. The cross-spectra in resonant conditions (maximum of cross-correlation) are shown in Fig. 9 a, b, c. One can see high coherency level after the one turn over the torus (≈ 10 m).

9. Turbulence behavior in transient e-ITB after the end of off-axis ECRH

The recent T-10 experiment with off-axis ECRH showed that the amplitude of density fluctuation in the center during ECRH are higher in 2-3 times then in OH phase, in spite of low $R/L_T=4$ (L_T -temperature scale length). The modeling with ASTRA code reveals the high influx of the neutrals to the plasma center. This is in good correlation with the strong increase of LF QC, which typically associated with high particles convection. Strong electron temperature gradient $R/L_T=16$ and local minimum of turbulence amplitude and coherency are observed at $r/a \sim 0.3$ 15 ms after ECRH switch off. This proves e-ITB formation. The radial distributions of the turbulence amplitude and poloidal coherency are shown in Fig. 10. The measured constancy of the angular rotation excludes the mechanism of the turbulence suppression with velocity shear (Fig. 11). One of the possible mechanism of ITB formation is the decrease of a number of rational surfaces near $q=1$ at low magnetic shear [7].

10. Conclusions

The experiments showed that poloidal, radial and toroidal correlations give important information about turbulence structure. The turbulence spectra retain the features of the linear instability in high OH confinement discharges. These features steadily vanish with the transition to strong non-linear regime with the increase of the heating power. The “Broad Band” turbulence with minimal radial scale arises due to stochastic excitation of a single high m mode, while “Quasi-Coherent” represent toroidal coupling of several modes. Experiment consistent with the existing of three different instabilities: in core - ITG (LF QC) and DTEM (HF QC); and

Ballooning Resistive Interchange in SOL; LF QC (ITG) typically associated with the regions with high level of particles fluxes at plasma edge and low density, or with flat density gradient in center zone; HF QC (DTEM), in difference, typical for low particles fluxes region and high electron temperature gradients; OH and ECRH discharges showed the transition from LF to HF QC with increase of density from low up to critical. Special modes near 15 – 30 kHz were observed with properties of Geodesic Acoustic Mode, which is the branch of “zonal flows”. However, its radial localization at rational surfaces contradicts to existing theories. The QC tend to rotate as a rigid body with velocity of MHD $m/n=2/1$ island. This work was supported Nuclear Science and technology Department of Minatom RF, Scientific School 1608.2003.2, RFBR (Grant 04-02-17567), NWO 047.016.015 and INTAS (Gr. 2001 - 2056).

-
- [1] V. A. Vershkov, et al, 21st EPS, 1994, Montpellier, France, V. 18 B, part III, p. 1192
 - [2] V.A. Vershkov et al, Nuclear Fusion (Yokohama Special Issue 2), **39** (1999) 1775.
 - [3]. V.A. Vershkov *et al* RSI, 1999, V. 70, N. 3, p. 2903.
 - [4] A.V. Melnikov et al, 30 EPS, St. Petersburg, Russia (2003) ECA Vol. 27A, P-3.114.
 - [5] Vershkov V, et al, 31 EPS Conf., London, UK, 2004, O2_06
 - [6] V.A.Vershkov *et al*, Proc. of 20th IAEA Fusion Energy Conference, Vilamoura, Portugal, 2004, ECA, Vienna 2005, IAEA-CN-116/OV/4-4
 - [7] D.A. Shelukhin *et al*, Proc. of 20th IAEA Fusion Energy Conference, Vilamoura, Portugal, 2004, ECA, Vienna 2005, IAEA-CN-116/ EX/P6-26.
 - [8] J. Weiland, H. Nordman, Nuclear Fusion, 31, (1991), 390
 - [9] M.V. Ossipenko, Nuclear Fusion, **43**, (2003) 1641.
 - [10] R. E. Waltz *et al* Phys. Plasmas **1**, 2229, (1994)
 - [11]. G. Manfredi et al, Plasma Phys. Contr. Fusion, **43**, (2001) 825-837.
 - [12]. G. R. McKee, et al, Physics of Plasmas, **10** ,(2003) 1712
 - [13] A. Fujisawa, 31 EPS Conf., London, UK, 2004, O2_04
 - [14] G. Conway, 31 EPS Conf., London, UK, 2004, P4_124
 - [15] T.S. Hahm, et al., Phys. Plasmas **6**, 922, (1999).
 - [16] N. Winsor, et al, Phys. Fluids, **11**, (1968) 2448
 - [17] S.V. Soldatov et al, Proc. 24 EPS, Berchtesgarden (1997), Vol. 21A, Part 2, p. 673.

Fluctuation measurements in TJ-II using a broadband fast frequency hopping reflectometer

T. Estrada, E. Blanco, L. Cupido*, M.E. Manso* and J. Sánchez

Laboratorio Nacional de Fusión, Asociación Euratom-CIEMAT, Madrid, Spain

*Associação Euratom-IST, CFN, Instituto Superior Técnico, 1096 Lisboa, Portugal

A broadband fast frequency hopping reflectometer designed for measuring plasma turbulence has been recently installed at TJ-II. The main feature of the reflectometer is its possibility to be tuned, within a fraction of a millisecond, to any selected frequency while keeping synchronized the Local and Radiofrequency oscillators with the same stability as a fixed frequency system would do. The system includes heterodyne detection. Reflectometry measurements have permitted the characterization of the velocity shear layer that develops spontaneously in the edge of TJ-II plasmas above a certain critical density. Simultaneously, a second velocity shear layer develops at inner radial locations that moves radially inwards when the plasma density further increases. The interpretation of these experimental results has been crosschecked with results obtained using a 2-dimensional full-wave code. Changes the spectra shape linked to low order rational surfaces in the rotational transform profile are also reported.

Reflectometer description

A broadband fast hopping reflectometer designed for measuring the plasma turbulence is in operation at TJ-II. The system works in the frequency range 33-50 GHz with propagation in extraordinary mode and uses heterodyne detection. A detailed description of the system can be found in [1]. The antennas are standard gain horn type with a 3dB beamwidth of about 20°. The antenna arrangement was designed to view the plasma perpendicularly to the cut-off layers, however a small misalignment may exist as it is seen in the measurements. The reflectometer covers the density range from about 0.3 to $1.5 \cdot 10^{19} \text{ m}^{-3}$, almost the whole density range of the TJ-II plasmas heated by ECH ($B=1 \text{ T}$, $f_{\text{ECH}}=53.2 \text{ GHz}$, $n_{\text{cut-off}}=1.75 \cdot 10^{19} \text{ m}^{-3}$). However, due to the shape of the ECH plasma density profiles (flat in the range $\rho < 0.6$) and to the low gradient of the magnetic field, the radial range covered by the reflectometer is limited in most cases to $\rho \geq 0.6$. Most of the experimental results discussed in the next sections refer to the spectra of the complex amplitude $Ae^{i\phi}$, but it is worth mentioning that the conclusions do not change when considering the complex phase $e^{i\phi}$.

Characterization of perpendicular velocity shear layers

As it has been recently reported [2] a perpendicular velocity shear layer develops spontaneously in the plasma edge of TJ-II above a certain plasma density. To study this phenomenon a set of experiments has been done modulating the plasma density around the critical value. In these experiments the plasma is created and heated by ECH with a total

power of about 400 kW. During the experiments the reflectometer is tuned to a low frequency (34 GHz) to probe a layer close to the Langmuir probe radial position ($\rho \geq 0.8$). The reversal in the perpendicular phase velocity measured by the Langmuir probes when the plasma density reaches the critical value is also seen in the reflectometer signal. Figure 1 shows the time evolution of the line density in a standard magnetic configuration discharge and the mean frequency of the complex amplitude spectra at $\rho \approx 0.8$. In this example, as the line density increases from 0.4 to 0.6 10^{19} m^{-3} , the perpendicular phase velocity measured by

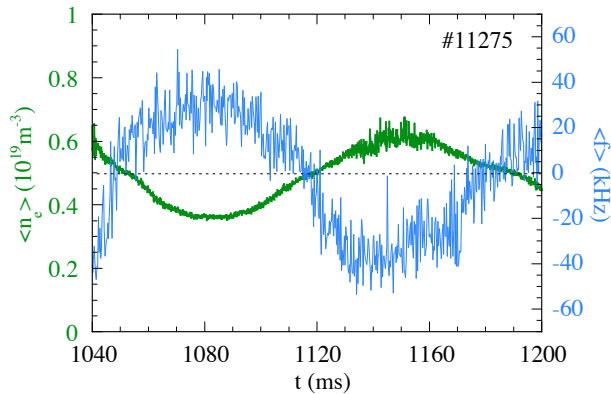


Figure 1. Time evolution of the density and mean frequency of the reflectometer signal spectra.

Langmuir probes reverses from $+10^3$ to -10^3 m/s [3]. The comparison of the reflectometer measurements with Langmuir probes results gives us information about the direction of the reflectometer misalignment. The misalignment in the antennas is such that negative/positive mean frequencies stand for rotation in the electron/ion diamagnetic direction (negative/positive radial electric field).

Experimentally, the behaviour of the turbulence rotation for inner radial locations has been studied changing the reflectometer probing frequency in a staircase mode during the discharge and changing the plasma density in a shot to basis. For plasma densities below the critical value, the mean frequency of the reflectometer signal spectrum is positive independently on the probing frequency. When the plasma density is slightly above the critical value the reversal in the perpendicular velocity is only seen for the lowest probing frequencies while the mean frequency of the reflectometer signal spectrum stays positive for the high probing frequencies. In these conditions the radial position where the perpendicular velocity reverses, computed as the radial location where the asymmetry changes sign, is located at $\rho \approx 0.8$. Increasing the plasma density further, this velocity shear layer moves to inner radial locations. As an example figure 2.a shows the staircase variation of the reflectometer probing frequency and the evolution of the line-averaged plasma density in three discharges with densities below (#11289), close (#11291) and above (#11294) the critical density ($\langle n_e \rangle \approx 0.5 \cdot 10^{19} \text{ m}^{-3}$). The mean frequency of the reflectometer signal spectrum as a function of the radial cut-off location is displayed in figure 2.b for these three discharges; also a fourth discharge with higher line density ($\langle n_e \rangle \approx 0.9 \cdot 10^{19} \text{ m}^{-3}$) is included. These measurements show that when the

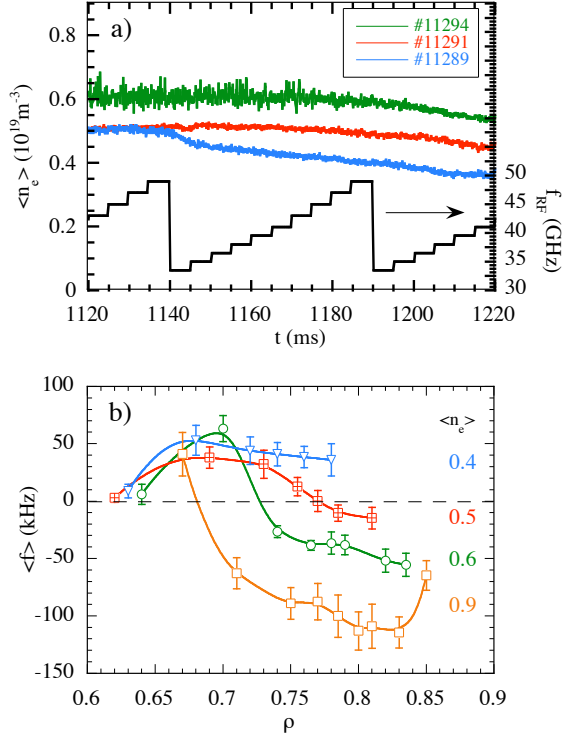


Figure 2: (a) Three discharges with densities close to the critical ($0.5 \cdot 10^{19} \text{m}^{-3}$) and staircase variation of the probing frequency, (b) Mean frequency of the spectra vs. cut-off radius in these discharges and in a fourth one with higher density.

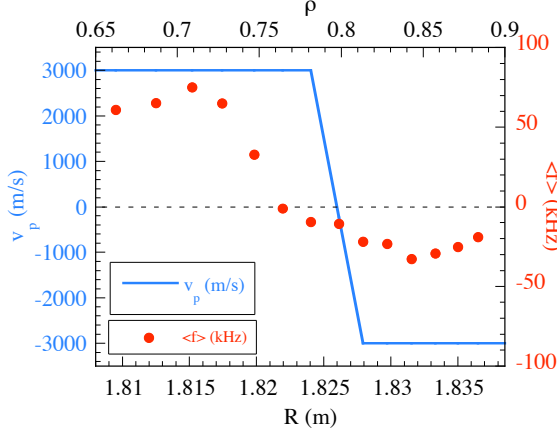


Figure 3: Perpendicular velocity and mean frequency of the simulated spectra as a function of the major and normalised radius.

$= -3000$ m/s at the plasma edge that changes linearly to $v_p = +3000$ m/s within a narrow region δx and stays constant further inside. The reflectometer signals are simulated for different probing frequencies within the band 33-50 GHz. The result for $\delta x = 4$ mm is displayed in figure 3. This figure shows the perpendicular rotation velocity and the mean frequency of the simulated complex amplitude spectra as a function of the major and normalised radius. These simulation results demonstrate the capability of the reflectometer to

velocity shear layer develops at the plasma edge, simultaneously, a second velocity shear layer appears at $\rho \approx 0.8$ that moves to inner radial locations when the plasma density further increases. HIBP measurements show that the inversion in the perpendicular rotation measured with the reflectometer may be dominated by the radial electric field. These results draw attention to the capability of the reflectometer to measure the inversion of the perpendicular rotation of the turbulence in a rather narrow radial region. This observation has been analysed using a two-dimensional full-wave numerical code [4]. As it is explained in [5] the code works with propagation in x-mode and incorporates the antennas arrangement of the experimental system. Realistic plasma shape and magnetic field distribution are introduced in the code using the theoretical magnetic surfaces of TJ-II. First numerical simulations indicate that asymmetric spectra are obtained for a misalignment as small as two degrees. Considering this tilt angle, we have studied the behaviour of the reflectometer signals in plasmas with a velocity shear layer localized in a very narrow region. For this study we consider a perpendicular velocity v_p

measure the velocity shear layer with a spatial resolution of about 1 cm, better than twice the probing wavelengths in vacuum (λ_0 : 0.7 – 0.8 cm).

Modification of the reflectometry signals spectra linked to rational surfaces

Modifications in the spectra have been observed in configurations having a low order rational surface in the rotational transform profile within the radial range covered by the reflectometer.

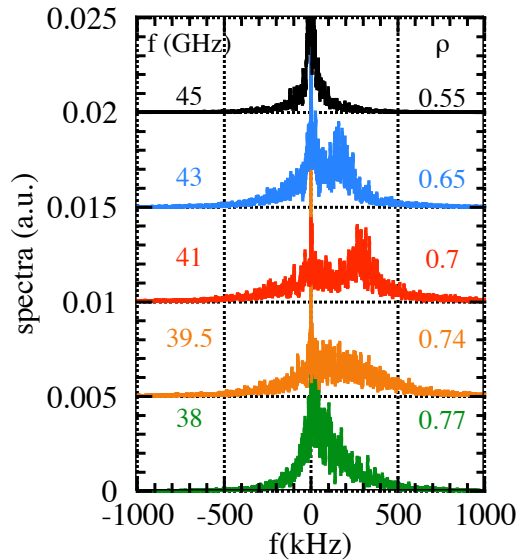


Figure 4: Spectra measured in a magnetic configuration with $\iota = 3/2$ at $\rho \approx 0.6$ (in vacuum)

An example is displayed in figure 4. The spectrum at the most internal radial location ($\rho = 0.55$) shows a coherent mode of about 10 kHz and the spectra modification appears for the adjacent probing frequencies (at $\rho = 0.65$ & 0.7). These measurements can be interpreted as a localized increase in the perpendicular rotation velocity of the fluctuations: due to the small misalignment of the antennas and to the long probing wavelengths, the perpendicular velocity should be as high as 15-20 km/s to reproduce the experimental spectra.

This phenomenon could be explained if we consider that the magnetic island produce an

enhancement in the electron diffusion higher than the ion diffusion and consequently the plasma reacts creating a positive radial electric field to preserve the ambipolarity. A similar phenomenon has been measured using the HIBP diagnostic during the formation of electron internal transport barriers triggered by low order rational surfaces [6]: the positive radial electric field increases in a factor of three in the central plasma region when the e-ITB forms.

Acknowledgments

This work has been partially funded by the Spanish Ministry of Science and Technology under project FTN2003-04431.

References

- [1] L. Cupido, J. Sánchez and T. Estrada. Rev. Sci. Instrum **75** (2004) 3865
- [2] C. Hidalgo, M.A. Pedrosa, L. García and A. Ware Phys. Rev. E **70** (2004) 067402
- [3] M.A. Pedrosa, C. Hidalgo, E. Calderón, T. Estrada et al. Plasma Phys. Control. Fusion **47** (2005)
- [4] E. Blanco, S. Heuraux, T. Estrada, J. Sánchez and L. Cupido. Rev. Sci. Instrum **75** (2004) 3822
- [5] E. Blanco, T. Estrada, S. Heuraux and J. Sánchez. These proceedings
- [6] T. Estrada, L. Krupnik, N. Dreval et al. Plasma Phys. Control. Fusion **46** (2004) 277

Density and fluctuation profiles obtained with the D-band reflectometer in Tore-Supra

A. Sirinelli, R. Sabot, J.-C. Giacalone, and F. Claret
Association Euratom-CEA, CEA/DSM/DRFC
Centre de Cadarache, 13108 Saint Paul lez Durance, France
(Dated: May 2005)

Up to now, density measurements in Tore-Supra using the reflectometry was available in the low field side (LFS). These measurements were achieved by two fast sweeps reflectometers covering the 50-110 GHz bands. In addition, a reflectometer has been set up in order to study density fluctuations in the core and in the high field side (HFS) using the 105-155 GHz band. A recent upgrade on this reflectometer allows it to perform fluctuations measurements at fixed frequency and density profiles in the same shot by switching between frequency steps and fast sweeps.

Density profiles covering the whole plasma using the 3 reflectometers is presented. The filtering treatments are described. The better knowledge of the core and HFS density allows a higher reliability in fluctuations measurements : both for the localisation of the cutoff layers and for the evaluation of the local index gradient length. Density fluctuation profiles enhanced by these new density profiles are shown.

I. INTRODUCTION

Reflectometry can perform density profiles or density fluctuation measurements. Most of the time, a reflectometer is dedicated to only one of these studies. The Tore-Supra D-band reflectometer has now the ability to perform both measurements. This paper will present the capability of this reflectometer to achieve these measurements. In a first part, the reflectometers used in Tore-Supra will be briefly described, the upgrade of the D-band one will be detailed. Then, the density profiles obtained with this new setup will be presented. Finally, the link between these new density profiles and the fluctuation localisation improvement will be explained.

II. EXPERIMENTAL SETUP

Tore-Supra is equipped with 4 reflectometers [1] : 2 profiles reflectometers covering the V and W bands, a fluctuation one on the D band and a Doppler setup [2] using the V band. The last one launches its waves in O-mode, while the others probe the plasma in X-mode. All the Tore-Supra reflectometers have the same design : an heterodyne detection achieved thanks to a Single Sideband Modulator (SSBM). This article will focus on the new evolutions of the D-band reflectometer.

This reflectometer was primary designed to study density fluctuations by doing steps of fixed probe frequencies. An upgrade has been achieved in September 2004 in order to let it make fast frequency sweeps for density profile measurements. Thanks to a fast switch, the D-band reflectometer can now perform during the same shot frequency steps and fast sweeps. Frequency steps are generated by an synthesizer which can do fast hopping : from 1 to 32 steps of 8 ms to 1 s. Acquisition is performed by a 1 MHz VME card. Fast frequency sweeps are produced by a VCO coupled with an arbitrary waveform generator. Sweeps length are typically from 60 to 100 μ s and the heterodyne signals are digitalised with a dedicated 100 MHz VME card. At least, during a shot, the D-band reflectometer produce up to 1000 density profiles and fluctuation measurements.

III. DENSITY PROFILE MEASUREMENTS

The heterodyne detection provides a complex signal : $S(t) = A(t) [\cos(\Phi(t)) + i \sin(\Phi(t))] = A(t) \exp(i\Phi(t))$. In order to perform a density profile reconstruction, the phase $\Phi(t)$ must be extracted from the complex signal which is treated and filtered. First of all, the waveguide dispersion and the vacuum propagation is removed using a wall reflection signal which is acquired before each shot. At this step, the window echo is also removed. A sliding filtering is then performed : using a sliding FFT, the beaten frequency is located during the sweep. The signal is then filtered along this beaten frequency. The width of the filter is automatically adapted function of the signal quality : when the beaten frequency is well defined, the filter is narrow. The phase is then extracted by unwrapping the angle of the complex signal. Finally, the density profiles are reconstructed with an inversion algorithm [3] taking account of the relativistic effects [4]. Initialisation of the profiles is done by using either the V-W band reflectometer or the interferometer.

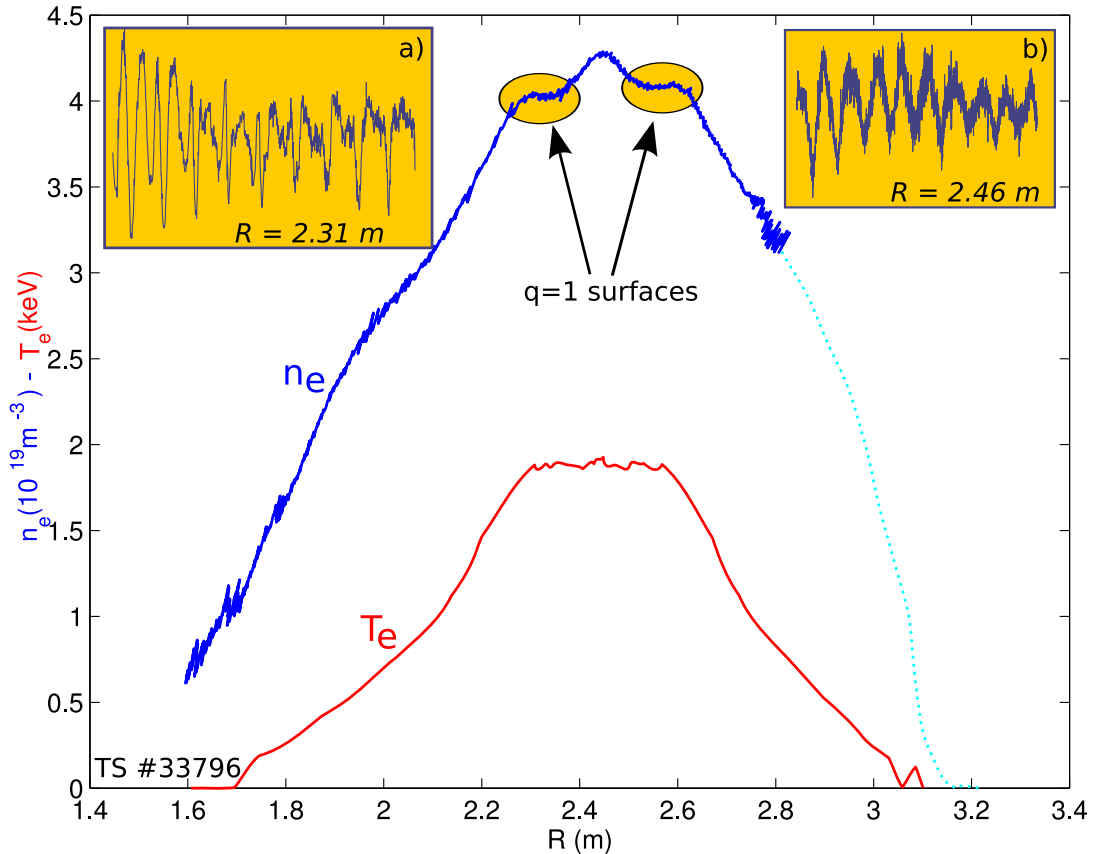


FIG. 1: Density profile in Tore-Supra during an ohmic phase.
 Plain line : D band reflectometer, dotted line : V-W band reflectometers
 a) and b) : fixed frequency measurements during the same shot with the D band reflectometer

The figure 1 shows a density profile covering almost the whole plasma. The dotted line represents the profile obtained with the V-W band reflectometers while the plain line is from the D-band reflectometer. The $q = 1$ surfaces are clearly visible on each side of the central hot core. The profile is more noisy at the beginning and the end of the band, due to a weakness of the VCO output. This profile is performed during MHD activity. During this shot, acquisition in fixed frequency mode is also available. The figures 1-a-b show these measurements at two different frequencies on both side of the centre. The large oscillations are the evidence of the presence of a coherent MHD mode. The shape of the hot core, most of the time localised in the centre of the plasma, is not yet well understood. Next upgrades of the reflectometer will permit higher temporal resolutions which should gave the ability to follow the MHD dynamic before a sawtooth crash.

IV. FLUCTUATIONS MEASUREMENT

The D-band reflectometer was primary designed to achieve fluctuation measurements. By launching different fixed probing frequencies, density fluctuations can be studied at different positions in the plasma. The link between phase measurement and density fluctuation is done by this relation :

$$\tilde{\Phi} \propto \sqrt{\frac{\pi k_0^2 L_\epsilon}{k_x}} \left(\frac{\tilde{n}}{n} \right)$$

where Φ is the phase measured by the reflectometer, k_0 the vacuum wavenumber of the probing frequency, L_ϵ the index gradient length close to the cutoff layer, k_x the wavenumber of the fluctuations and n the local density. In this article, we will assume the fluctuation spectrum is peaked around 1 cm^{-1} , so we will choose this value for k_x .

For a good fluctuation evaluation, L_ϵ has to be well calculate. This leads to a good accuracy in the density profile. In the past, we used the interferometer data. In Tore-Supra, there is only 5 chords for interferometry and density

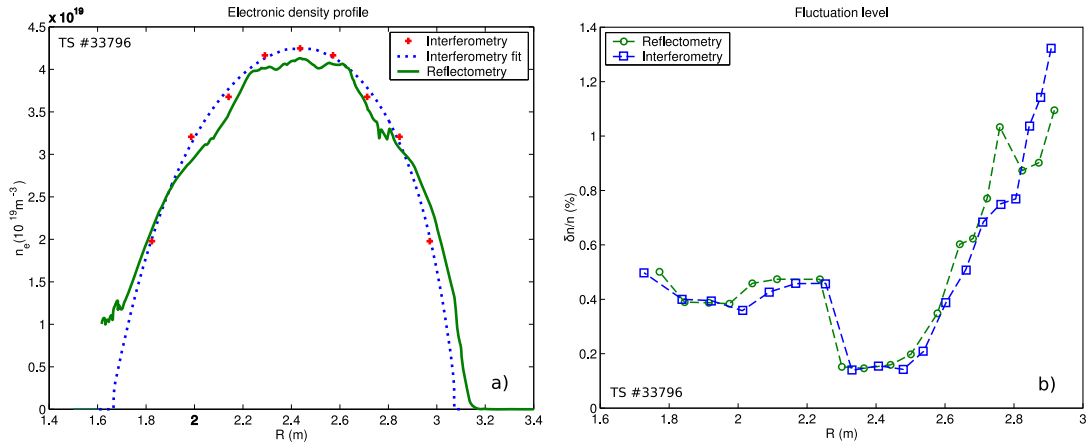


FIG. 2: a) Two measures of the density profile : interferometry and reflectometry
b) Fluctuation profiles : influence of the choice of the density profile for fluctuations interpretations

measurement is achieved from integral measures with assumptions on the plasma equilibrium. The figure 2(a) shows the same density profile measured with the reflectometry and interferometry. Reflectometry provides detailed profiles which permits better localisation of the measurements and better evaluations of the fluctuation levels.

In order to evaluate the impact of a better density profile for fluctuation measurements, we treat our fluctuations data using the interferometry profiles and the reflectometry ones. Results are shown on figure 2(b). Fluctuation levels have nearly the same amplitude but localisation can be shifted up to 5 cm. This enhancement of the localisation is important for the ρ -asymmetry fluctuation studies.

V. CONCLUSIONS

Last upgrade of the D-band reflectometer permits us to now have density profiles from reflectometry covering the whole plasma. Plasma centre is now nearly always covered by reflectometers in Tore-Supra. A better understanding of the core MHD dynamic is expected with the next enhancement. These accurate density profiles are also used to improve the evaluation and the localisation of the fluctuation measurements.

-
- [1] R. Sabot, F. Clairet, C. Honoré, C. Bottureau, J.-M. Chareau, F. Gabillet, P. Hennequin, S. Heurax, G. Leclert, A. Sirinelli, A. Truc, and L. Vermare. Advances of Reflectometry on Tore-Supra: From Edge Density Profile to Core Density Fluctuations. *International Journal of Infrared and Millimeter Waves*, 25(2):229–246, 2004.
 - [2] P. Hennequin, C. Honore, A. Truc, A. Quemeneur, N. Lemoine, J.-M. Chareau, and R. Sabot. Doppler backscattering system for measuring fluctuations and their perpendicular velocity on tore supra. *Review of Scientific Instruments*, 75(10):3881–3883, 2004.
 - [3] H. Bottollier-Curtet and G. Ichchenko. Microwave reflectometry with the extraordinary mode on tokamaks: Determination of the electron density profile of petula-b. *Review of Scientific Instruments*, 58(4):539–546, 1987.
 - [4] E. Mazzucato. Relativistic effects on microwave reflectometry. *Physics of Fluids B: Plasma Physics*, 4(10):3460–3461, 1992.

Fluctuation Measurements at TEXTOR during Operation of the Dynamic Ergodic Divertor (DED)

*A. Krämer-Flecken*¹, *S. Soldatov*^{1,2}, *H.R. Koslowski*¹, *M. Lehnen*¹, *Y. Liang*¹, *V. Vershkov*², *R. Wolf*¹, *O. Zimmermann*¹ and the TEXTOR-Team

¹Institut für Plasmaphysik, Forschungszentrum Jülich GmbH,
EURATOM Association, D-52425 Jülich, Germany*

²Nuclear Fusion Institute, Kurchatov Institute, Kurchatov Square, 123128 Moscow, Russia

1 The O-mode Reflectometry at TEXTOR

Since several years the heterodyne O-mode reflectometry system [1] at TEXTOR is in operation. It can investigate the plasma turbulence properties in a range of $0.84 \times 10^{19} \leq n_e \leq 1.74 \times 10^{19} \text{m}^{-3}$ using poloidal cross correlation techniques. The system consists of two phase coupled microwave generators with an intermediate frequency of 20MHz. The system is connected to two antennae arrays, one in the equatorial plane and the other one on top of the vessel. Each antennae system consists of 5 antennae, a launching antenna and four receiving and antennae. Since the power of the launching path is split and feeds both antennae arrays the system is capable to measure short correlation length with in one antennae array as well a long correlation length by using a combination of antennae from the upper and the equatorial position. The frequency of the reflectometer system can be varied in the range $26 \leq f \leq 37 \text{ GHz}$ on a shot to shot base. In Fig. 1 the scheme of system is shown. For the antennae and TEXTOR geometry the sensitivity in k_θ is restricted to $k_\theta \leq 4$.

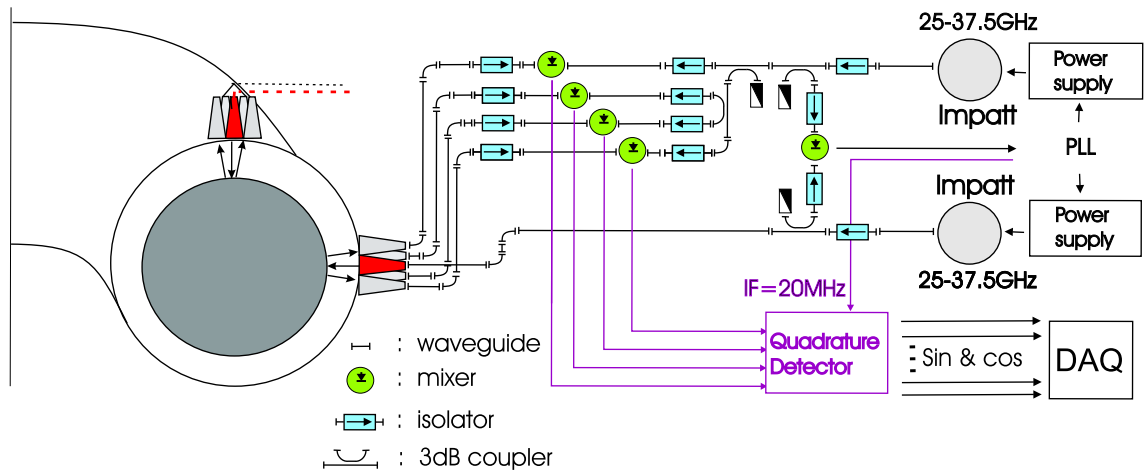


Figure 1: A sketch of the heterodyne O-mode reflectometry system operated at TEXTOR. The system operates with two antennae arrays in the equatorial plane and on top of the vessel. Short and long poloidal correlations can be investigated.

2 Turbulence during DED operation

The dynamic ergodic divertor (DED) [2] at TEXTOR consists of a set of 16 coils wrapped helically around the torus on the high field side (HFS). It generates a magnetic perturbation field which disturbs

*partner in the Trilateral Euregio Cluster

the plasma at the rational $q = 3$ surface. The DED can be operated in the 12/4 configuration and in the 3/1 configuration. For the 12/4 configuration the perturbation has a short radial range, whereas in the 3/1 configuration the perturbation has a large radial range. In 12/4 configuration the plasma is shifted to the HFS and the plasma parameters are such that the $q = 3$ surface is close to the plasma edge. For the typical plasma parameters used in 3/1 configuration the $q = 3$ surface is located in the gradient region. In both cases the properties of the turbulence are studied. The DED can be operated with different currents and frequencies according the needs of the experimentalists. Also the perturbation is generated at the HFS the turbulence is studied on the low field side (LFS) assuming that the perturbation is poloidally symmetric. The next sections discusses the results obtained in the one or the other configuration.

2.1 DED in 12/4 configuration

In this configuration the plasma is shifted to the HFS to enhance the effect of the near field of the DED on the plasma. With $I_p = 370$ kA and $B_t = 1.9$ T the $q = 3$ surface is found at the very edge

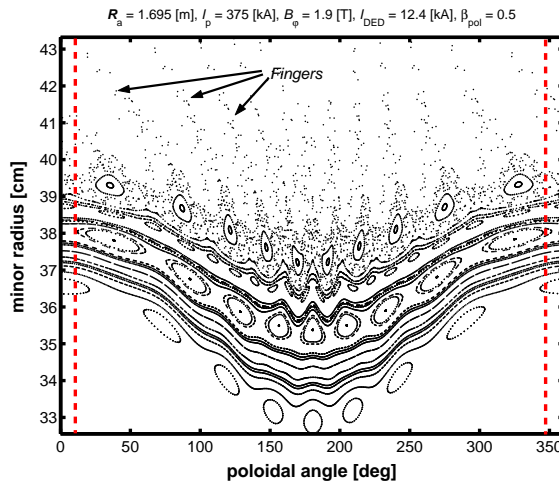


Figure 2: Poincare plot for the toroidal position of the reflectometer. The dashed line indicates the poloidal position of the reflectometer on the LFS. The HFS corresponds to $\Theta = 180^\circ$. Outside $r = 39$ cm the ergodic region is seen.

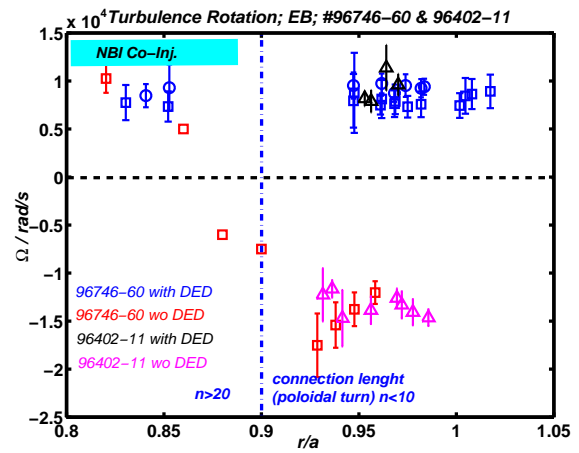


Figure 3: Turbulence rotation Ω for DED and non DED operation. The change of the rotation direction for $r/a \geq 0.9$ is clearly seen.

of the plasma. The onset of the DED creates a steep density and temperature gradient at the plasma edge, where the connection length to the wall are largely decreased and the last close flux surface is shifted inwards. In Fig. 2 the Poincare plot of the perturbation field [3] is shown. The position of the reflectometer measurements is indicated by dashed lines. In the observed slice, areas with increased connection length so called fingers are visible and intersecting the sight line of the reflectometer. The diameter of the fingers is $d \approx 1$ cm, however the reflectometer exhibits an increased coherency when measuring in the finger.

In Fig. 3 the turbulence rotation Ω_{turb} , calculated from quasi coherent [4] (QC) turbulence and low frequency (LF) turbulence, as function of r/a is shown for the case with and without DED. Without DED Ω stays constant at the plasma edge. In the radial region ($r/a \leq 0.9$), affected by substantial tangential neutral beam injection ($P_{NBI} = 800$ kW) in co-current direction, Ω_{turb} changes its rotation direction but keeping its magnitude. During DED operation, for $r/a \approx 0.9$, the poloidal connection length in units of poloidal turns n drops from $n \geq 20$ to $n \leq 10$ (indicated by the vertical dashed line in Fig. 3). There the rotation direction changes compared to the non DED case. The measurements of

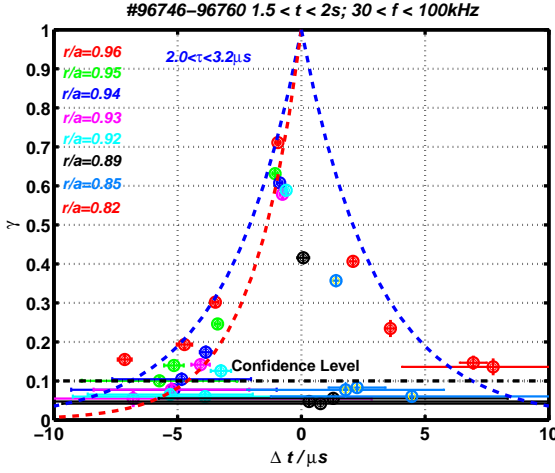


Figure 4: Decorrelation time for QC-turbulence without DED. For the ohmic edge the estimated decorrelation time is in between the dashed lines for $\tau = 2 \mu\text{s}$ and $\tau = 3 \mu\text{s}$ respectively. For NBI dominated plasmas (positive Δt) $\tau = 2 \mu\text{s}$ is estimated.

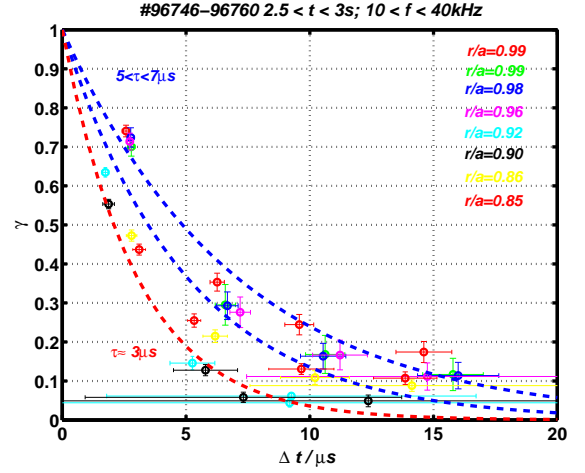


Figure 5: Decorrelation time for LF-turbulence with DED. An increase of τ_{turb} by a factor of two in the ergodic region is observed. Most of the measured values are between the blue dashed lines with $5 \leq \tau_{turb} \leq 7 \mu\text{s}$. For NBI dominated plasma $\tau_{turb} = 3 \mu\text{s}$ is found (red dashed line).

the poloidal plasma rotation from Doppler shifted carbon impurities, compared with Ω_{turb} , show also a change in the rotation direction at the plasma edge and yield within the error bars similar values. The change in the sign of the rotation as well as the absolute value confirms that the turbulence is frozen in the plasma. This opens the possibility for the calculation of the radial electric field (E_r) [5] according,

$$E_r = (\Omega \cdot r - v_{dia}) \cdot B \quad (1)$$

where v_{dia} is the diamagnetic velocity, and yields $80 \leq E_r \leq 100 \text{ V/cm}$ in the laminar region outside the last closed flux surface. This confirms earlier indication of an inward movement of the inversion point of E_r , observed at Tore Supra [6] with ergodic limiter operation.

Since the antennae set-up offers the possibility to measure the cross correlation for different antennae combination the turbulence decorrelation time τ_{turb} as well as the correlation length l_{turb} can be determined in none DED (Fig. 4) and DED (Fig. 5) plasmas. Without DED The QC- as well as LF-turbulence having the same Ω_{turb} yielding $2.0 \leq \tau_{turb} \leq 3.2 \mu\text{s}$. A decrease in τ_{turb} is observed in the transition layer where the rotation direction changes. When NBI injection dominates the plasma rotation (positive Δt), similar value for τ_{turb} is found compare with the ohmic plasma edge. With the DED $\tau_{turb} = 6 \pm 1 \mu\text{s}$ is estimated from the LF-turbulence in the divertor region. However for the innermost reflection layer dominated by NBI co-injection the decorrelation time drops to $\tau_{turb} = 2 \mu\text{s}$. The correlation length, for the innermost reflection layer of $l_{turb} = 0.008 \text{ m}$ and the outermost reflection layer of $l_{turb} = 0.013 \text{ m}$, is not changed significantly in cases with and without DED. Assuming a diffusion step width in the order of $D_{rw} = l_{turb}^2 / \tau_{turb}$ an indication for a decrease of the turbulent transport step width is obtained.

2.2 DED in 3/1 configuration

The plasma for the 3/1 configuration differs substantially from those in the 12/4 configuration. With $I_p = 300 \text{ kA}$ and $B_T = 2.25 \text{ T}$ $q_a = 4.8$ is achieved. Also the horizontal plasma position is kept constant. For the measurement of the toroidal plasma rotation, charge exchange spectroscopy CXRS

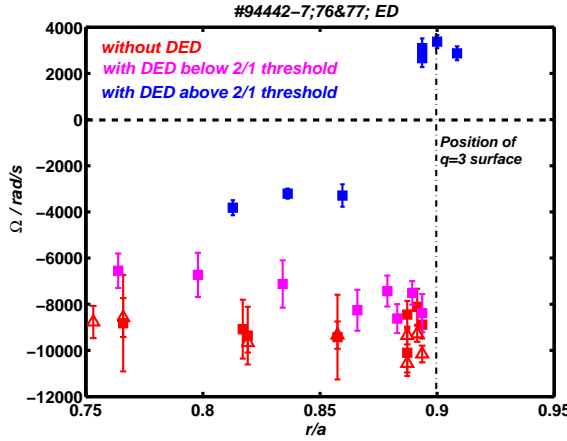


Figure 6: Ω_{turb} from LF-turbulence for three different cases: without DED (red); with DED below the threshold for the 2/1 island (magenta) and with DED and 2/1 island (blue). In addition the red open triangles display the data from the QC-turbulence.

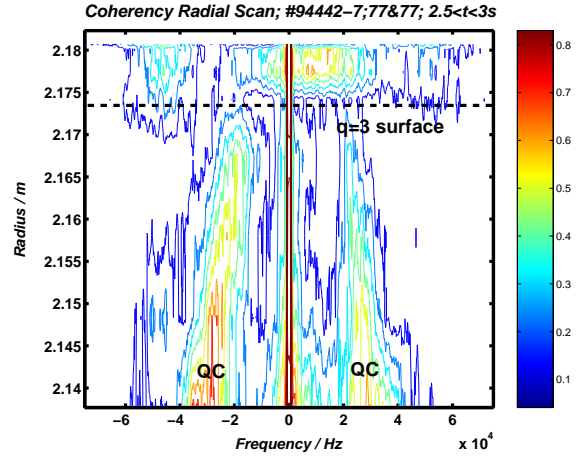


Figure 7: The radial progression of the coherency shows the decrease in frequency of the QC-turbulence. At the $q = 3$ surface LF-turbulence is generated.

at $P_{NBI} = 300$ kW is injected tangential in co-current direction. A main observation of the 3/1 configuration in dc operation is the generation of a large locked $m/n = 2/1$ mode in the plasma at a threshold of $I_{DED} = 0.8$ kA for those plasmas. For the experiments reported in this section I_{DED} was well below the threshold for the generation of a further $m/n = 3/1$ island, which is found at $I_{DED} = 2.4$ kA. The island width and position of the X- and O-point is estimated from SXR and ECE measurements. A width of $w = 0.06 - 0.08$ m is observed and the X-point is found close to the position of the reflectometry antennae array in the equatorial plane. The reflectometry observations are performed at the plasma boundary in the range $0.75 \leq r/a \leq 0.9$, well outside the $m/n = 2/1$ island. Within this radial range the electron temperature gradient decreases and the electron density gradient increases compared to the plasma without DED. From the coherency spectrum two main observations can be made (i) the reduction of the coherency with the onset of the locked mode and (ii) the decrease of the central frequency of the QC turbulence and the increase of the low frequency turbulence. From the calculation of the turbulence rotation Ω_{turb} at three different time slices within the discharge it is found that the Ω_{turb} is influenced first in the gradient region by a small but significant decrease with onset of the DED. With the onset of the locked mode Ω_{turb} is reduced to half of the value before mode onset and furthermore at the $q = 3$ surface the rotation direction changes (see Fig. 6). From the radial progression of the coherency (Fig. 7) the decrease of the QC-turbulence, in frequency and coherency, towards the $q = 3$ surface is clearly seen. Also the generation of the LF-turbulence rotating in a different direction in the vicinity of the $q = 3$ surface is seen. The radial electric field calculated from the turbulence rotation give $E_r \approx 40$ V/cm at the $q = 3$ surface. The change in Ω_{turb} goes along with a reduction in the density fluctuation level from 6% to nearly 3%.

Calculating the de-correlation time of the turbulence for the DED and the non DED plasma yields in the none DED case $\tau_{turb} = 7.0$ μ s for QC- as well as for the LF-turbulence, independent from the radial position of the measurement. The same analysis for the LF-turbulence applied to the DED plasma results in $\tau_{turb} = 17$ μ s, but only for reflection layers is close to the $q = 3$ surface. For reflection layer more far away from the $q = 3$ surface $\tau_{turb} \leq 2$ μ s is estimated. The correlation length in DED and non DED cases however shows no significant change as already observed in the plasmas with DED in

12/4 configuration. Therefore we conclude that for the 3/1 configuration an decreased diffusion step width for the turbulence is found, however this is only observed in the vicinity of the $q = 3$ surface.

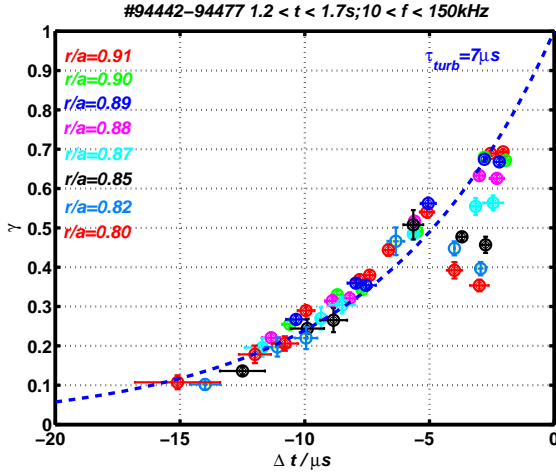


Figure 8: Estimation of the de-correlation time without DED. For the whole radial observation range $\tau_{Turb} = 7.0 \mu s$ is calculated.

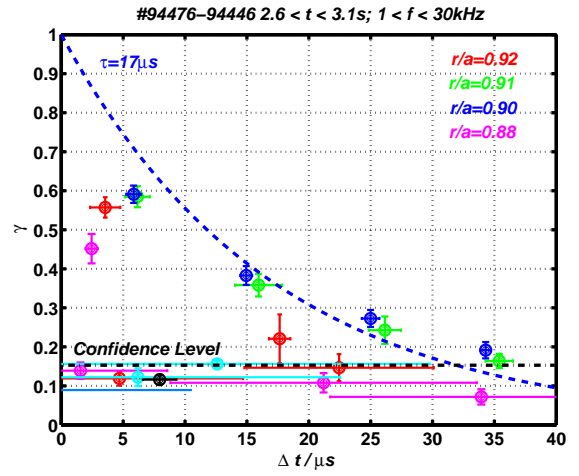


Figure 9: Only for the $f=27\text{GHz}$ and $f=28\text{GHz}$ the LF turbulence de-correlation time could be estimated. It is considerably larger (factor 2) compared to the non DED case.

3 Turbulence during slow rotating $m/n = 2/1$ islands

From the experiments in 3/1 configuration it is not clear whether the observed phenomena are due to the DED itself or due to the large generation of the $m/n = 2/1$ island. Therefore the turbulence properties for a pulse without DED and a large $m/n = 2/1$ island is studied. The plasma parameters for this pulse were the same as used as given in section 2.2. The reflection layer was located outside the island at $r/a \approx 0.9$. For this pulse the turbulence rotation and the 2/1 island rotation are determined and found to be of the same order as long as the mode does not start to lock. As soon as the island decreases in frequency ($f \leq 1400 \text{ Hz}$) and the width of the island increases ($w \geq 0.06 \text{ m}$) turbulence and 2/1 island rotation start to decouple. Whereas the 2/1 island rotation decreases the QC-turbulence vanishes and the LF-turbulence changes its sign. This observation extends measurements at T-10 and FTU where the 2/1 island rotation and the turbulence rotation are found of the same order, however in that cases the island width was smaller and island rotation was stable. The de-correlation time of the LF-turbulence changes from $10 \mu s$ to very small lifetime $\tau_{turb} \leq 2 \mu s$.

The experiment shows similar observations as in 3/1 configuration of the DED are made in the presence of large islands. Whereas in the DED operation the perturbation field itself together with the 2/1 island generates an ergodic layer with a small connection length, an intrinsic error field at TEXTOR or $m/n = 3/1$ island coupled together with the large 2/1 island seems to be responsible for the existence of an ergodic layer.

4 Summary

The O-mode reflectometer at TEXTOR is a good tool for the investigation of the DED induced effects at the plasma edge. It gives the possibility to measure the turbulence rotation, which is equal to the poloidal plasma rotation and to deduce with certain assumptions the radial electric field. Due to the

multi-horn set up also de-correlation times and correlation length can be estimated.

The experiments with the DED in the 12/4- and 3/1-configuration show similar turbulence features in the ergodic region as in the scrape off layer. In the amplitude spectrum the QC-turbulence vanishes and the rotation changes from electron diamagnetic to ion diamagnetic drift direction. The de-correlation time is increased with DED operation by a factor of 2 whereas the correlation length is nearly unchanged.

In the 3/1-configuration the main effect are not generated by the DED itself but due to the large $m/n = 2/1$ island which is generated at a certain DED current.

5 Acknowledgement

This work is supported by INTAS 2001–2056 grants.

References

- [1] A. Krämer-Flecken et al. Nucl. Fusion **44** (2004) 1143–1157
- [2] Special Issue: Dynamic Ergodic Divertor, Fusion Engineering and Design **37** (1997) 335
- [3] M.W. Jakubowski, S.S. Abdullaev, K.H. Finken and the TEXTOR Team Nucl. Fusion **44** No 6 (2004) S1-S11
- [4] V.A. Vershkov et al., *28th Conference on Contr. Fusion and Plasma Phys., Funchal*, ECA **25A** 2001 1413–1416
- [5] G.D. Conway et al., Plasma Phys. Control. Fusion **46** No 6 (June 2004) 951-970
- [6] J. Payan et al., Nucl. Fusion **35** (1995) 1357

Initial Density Fluctuation Measurements Using Fixed-Frequency Quadrature Reflectometers on DIII-D

G. Wang, W.A. Peebles, T.L. Rhodes, E.J. Doyle, N.A. Crocker, X. Nguyen,
L. Zeng, S. Kubota

*Department of Electrical Engineering and PSTI, University of California,
Los Angeles, California USA*

G.R. McKee

University of Wisconsin, Madison, Wisconsin USA

M.A. VanZeeland

Oak Ridge Institute for Science Education, Oak Ridge, Tennessee USA

Abstract

Two fixed-frequency (42 and 65 GHz) quadrature reflectometers have recently been installed on the DIII-D tokamak for density fluctuation measurements. Both systems have horns that can be orientated to launch and receive either O- or X-mode cutoffs in order to probe different regions of the plasma. The reconstructed phase information successfully identifies MHD activity. For an $m=3/n=2$ tearing mode, the calculated density fluctuation levels from reflectometry using a 1-D phase screen model agree well with Beam Emission Spectroscopy (BES) measurements. Initial comparison of turbulent density fluctuation spectra in the edge pedestal with BES shows qualitative similarity; however there are differences in the details, which are under further investigation.

I. Introduction

It has long been recognized that reflectometer density fluctuation measurements have numerous advantages, e.g. highly localized measurement, highly sensitive, flexible spatial coverage, non-perturbative, and it is now anticipated to play a much enhanced role in the harsh burning plasma environment in the next generation devices like ITER. Reflectometer density fluctuation diagnostics have not been completely understood so far [1] and have been the focus of intense investigation. Recently, two fixed-frequency (42 and 65 GHz) quadrature reflectometers have been installed on the DIII-D tokamak. In this paper, density fluctuation measurements of MHD activity, and turbulent density fluctuation measurements in the edge pedestal using these reflectometers are presented and directly compared to Beam Emission Spectroscopy (BES) measurements with similar location and localization. The results show that the calculated density fluctuation levels of an $m=3/n=2$ tearing mode from reflectometry using a 1-D phase screen model agree well with BES measurements. Initial comparison of turbulent density fluctuation spectra in the edge pedestal with BES shows qualitative similarity, however there are differences in the details, which are under further investigation.

II. Fixed-Frequency Quadrature Reflectometer System on DIII-D

Figure 1 is a schematic plot of one of the two similar fixed-frequency quadrature reflectometer systems on DIII-D. The second system is similar with the exception of a different frequency. Most of the microwave power from the source, a Gunn Oscillator, is launched into the plasma by passing through a directional coupler and 2 isolators which are used to prevent reflected power into the source. The received reflection from the plasma cutoff layer mixes with the local oscillation from

the source, and the quadrature mixer output provides the complex electric field, $E(t) = Ae^{i\phi(t)}$ i.e. $A(t)\cos\phi(t)$ and $A(t)\sin\phi(t)$ where ϕ i.e. is the phase delay between the launched microwave and its reflection from the plasma cutoff layer. The phase contains the density fluctuation information in the cutoff layer, e.g., the basic 1-D phase screen model predicts that the density fluctuation is proportional to the phase fluctuation, but they could have a more complicated relationship depending on the real geometry according to various models (see e.g. [1] and references therein).

The microwave and electronic components for each reflectometer are contained inside portable boxes. For initial tests, output waveguides are coupled to existing antennas normally used in the UCLA profile reflectometer systems [2]. Both systems have horns that can be orientated to launch and receive either O- or X-mode polarization in order to probe different regions of the plasma. The launch and receive antennas are in the outboard midplane of DIII-D.

A new algorithm [3] is applied to reconstruct the phase information from $A(t)\cos\phi(t)$ and $A(t)\sin\phi(t)$. It calculates the relative phase differences between two subsequent measurements and accumulates them to get the absolute phase. The method can be illustrated as follows. Assume two successive measurements (x_i, y_i) and (x_{i+1}, y_{i+1}) , where x_i and x_{i+1} are real parts (i.e. $A(t)\cos\phi(t)$), and y_i and y_{i+1} are imaginary parts (i.e. $A(t)\sin\phi(t)$), their phase difference can be derived [3] as:

$$\delta\phi = 2\sin^{-1} [(x_i y_{i+1} - y_{i+1} x_{i+1}) / \sqrt{\{(x_i + x_{i+1})^2 + (y_i + y_{i+1})^2\}(x_{i+1}^2 y_{i+1}^2)}}].$$

Note that this method can recover phase information if the phase variation between successive measurements is within $\pm\pi$, which can be compared to the normal method which recovers the phase between $-\pi/2$ and $\pi/2$. High data sampling rates (normally 10 or 25 MHz) are employed to avoid phase jumps exceeding 2π between successive measurements.

Beam Emission Spectroscopy (BES) [4] data will also be shown with similar location and localization for comparison in this paper. It measures a similar wave number range of $k_{\perp} \approx 0-3\text{cm}^{-1}$.

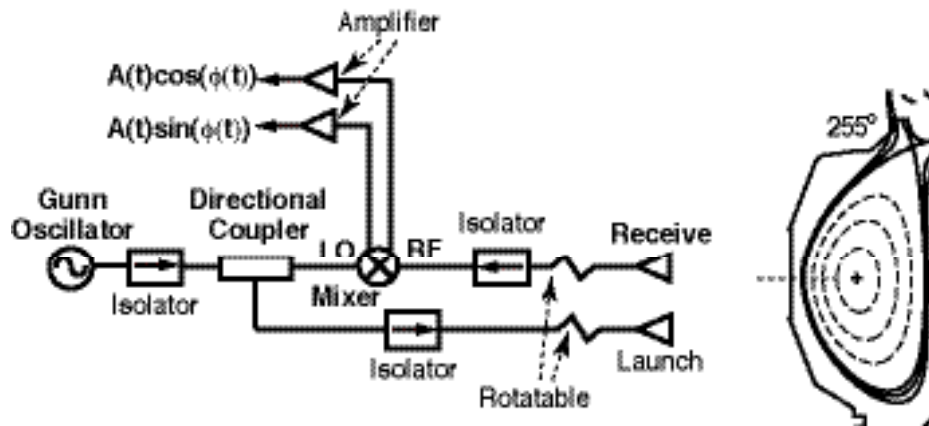


Figure 1 A schematic plot of quadrature reflectometers on DIII-D

III. Coherent Density Fluctuation Measurements

MHD activity (e.g. tearing modes and compressional Alfvén eigenmodes) has been successfully identified from the phase information. An example of detection of a tearing mode is shown in Figure 2.

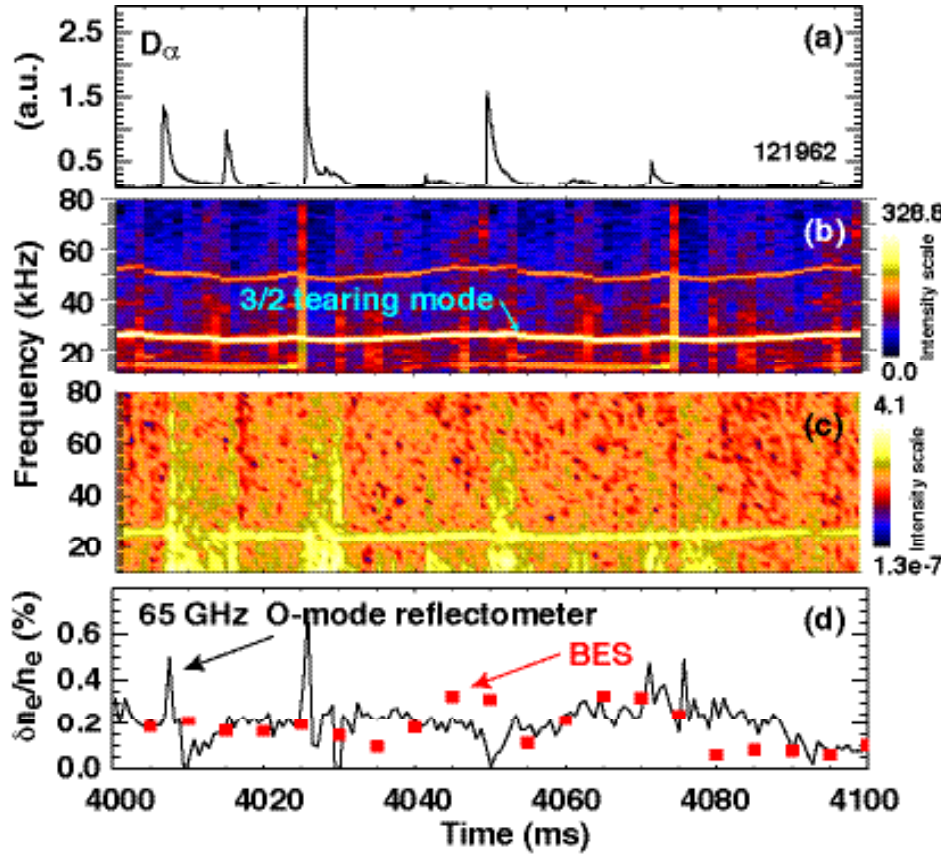


Figure 2 (a) Photodiode time history, contour plot of fluctuation spectrum (log scale) from (b) B from a magnetic loop, and (c) 65 GHz reflectometer at O-mode polarization, (d) density fluctuation levels versus time from reflectometer (solid line) and BES (filled rectangles).

Figure 2(b) is a contour plot of the magnetic fluctuation spectrum measured by a magnetic loop, showing the existence of an $m=3/n=2$ tearing mode (m and n are the poloidal and toroidal mode numbers respectively) between 25-30 kHz in the time window of 4000-4100 ms of shot 121962. This is an H-mode discharge with frequent ELMing activity as indicated by the photodiode time history in Figure 2 (a). Figure 2(c) is a contour plot of the phase fluctuation spectrum measured by 65 GHz reflectometer at O-mode polarization and clearly illustrates detection of the mode. It should be pointed out that from the Thomson Scattering density profile measurement between ELMs that the reflectometer detection locations are almost constant, i.e. at $\rho \sim 0.8$, but during the occurrence of the ELMs, the edge density profiles are affected and does cause the detection location to move radially inward/outward, as can be seen from the spectrum change in Figure 2(c), especially around 4010, 4028, 4052, and 4080 ms.

Using the basic 1-D phase screen model [1], the density fluctuation level induced by the mode can be calculated as $\delta n_e/n_e = \delta\phi/(2 k_o L_n)$, where $\delta\phi$ is the phase fluctuation level, k_o is the vacuum wave number of the source wave, and L_n is the density scale length. The solid curve in Figure 2 (d) is the result of the calculated density fluctuation level for the $m=3/n=2$ mode. With a time resolution of 0.655 ms, $\delta\phi$ is obtained from integrating the mode spectrum shown in Figure 2(c) over 22-30 kHz and subtracting the turbulent density fluctuation background which is calculated by integrating the spectrum over 30-38 kHz due to the fact that the spectrum is quite flat in the frequency range of 22-38 kHz. L_n is calculated from the Thomson scattering density measurement with 12.5 ms time resolution but interpolated to the time grid of $\delta\phi$. For comparison, measurements from BES were plotted as red rectangles with each averaged over a 10 ms time window. These BES measurements (and those shown in the following part of this paper) were obtained with the recently upgraded BES system [5]. The two diagnostics agree well with a few exceptions. The observed discrepancies could be related to 1) the possible uncertainty in the calculated turbulent density fluctuation background; 2) the afore mentioned effect of ELMs during which the actual L_n may have changed dramatically from the value interpolated from the sparse Thomson scattering density measurement; and 3) the mode amplitude has changed substantially as the detection location moves.

IV. Turbulent Density Fluctuation Measurements in Edge Pedestal Region

Initial analysis has also been done for the broadband density fluctuations in the edge pedestal. Figure 3(a) is a density profile measured by Thomson scattering, showing a case where the 65 GHz O-mode detection location is in the edge pedestal region. The raw data, $A(t)\cos\phi(t)$ and $A(t)\sin\phi(t)$ (data sampled at 25 MHz) are plotted in Figure 3(b) for $t=4000-4002$ ms. The figure shows a fairly well defined annulus, indicating a good phase measurement. The auto-power of the phase fluctuation for these data is plotted in Figure 3(c). The spectrum decays with an index of -3.3 in the frequency range of 85-800 kHz, again indicating non-random phase measurement (phase runaway would tend to increase the index to -1). Figure 3(d) shows the density fluctuation spectrum from BES measurement at the same location of $\rho\sim 0.8$ but averaged over a much longer time scale (4000-5000 ms). The plasma is in a steady-state condition in this time period. It is evident that the two diagnostics show qualitative similarity in the density fluctuation power spectrum, but a difference in the details can also be found. The difference might be due to several reasons, e.g., the 1-D phase screen model may not be applicable in this case, different instrument response and the difference of the averaging time windows of the two diagnostics, etc. For a better understanding, a 2-D full wave calculation [6] of the density fluctuation level and fluctuation spectrum is underway.

V. Summary and Conclusion

In summary, two fixed-frequency (42 and 65 GHz) quadrature reflectometers have recently been installed on the DIII-D tokamak for density fluctuation measurements. The reconstructed phase information successfully identifies MHD activity. For an $m=3/n=2$ tearing mode, the calculated density fluctuation levels using a 1-D phase screen model agree well with BES measurements. Initial comparison of turbulent density fluctuation spectra in the edge pedestal with BES shows qualitative similarity, however there are differences in the details. A 2-D full wave calculation of the density fluctuation level and fluctuation spectrum is underway for a better understanding.

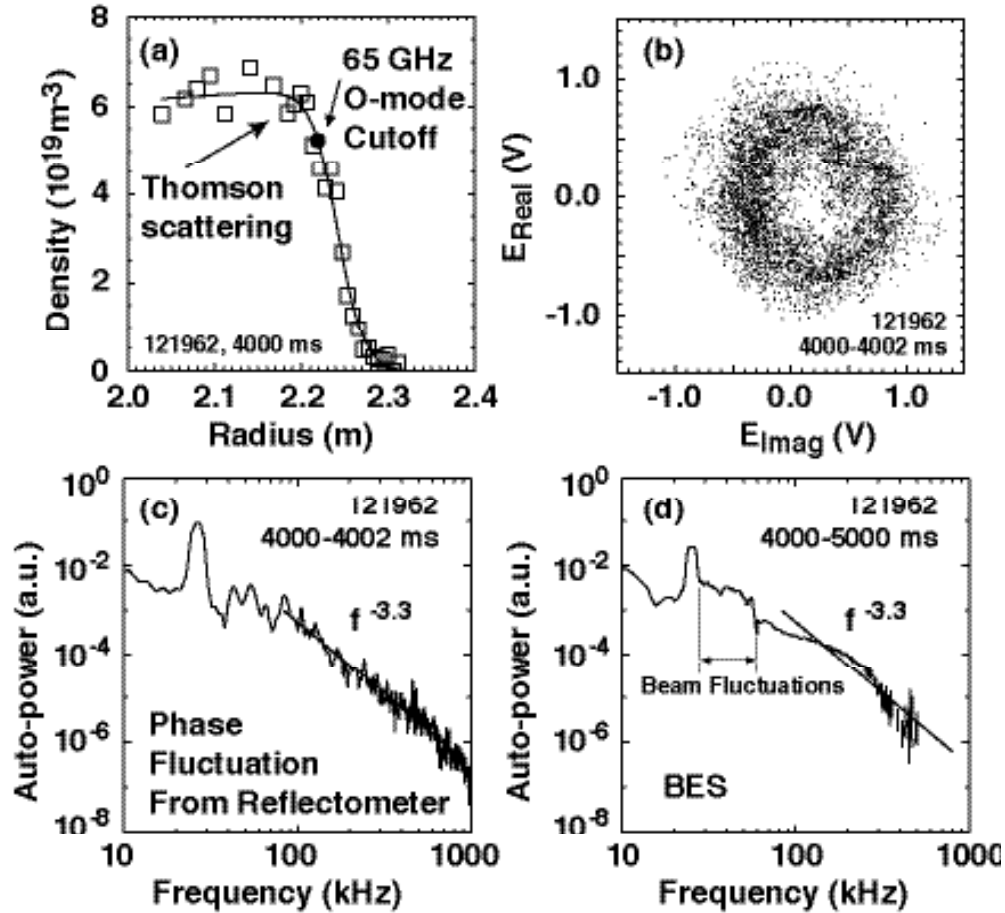


Figure 3 (a) Density profile from Thomson scattering measurement, (b) raw data $A(t)\cos\phi(t)$ and $A(t)\sin\phi(t)$, auto-power spectrum from (c) reflectometer, and (d) BES measurement where $f^{-3.3}$ line has been added for the reader's convenience in comparing with the data in Figure (c).

Acknowledgment

Work supported by US DOE Grant Nos. DE-FG03-01ER54615, DE-FG03-96ER54373, and DE-AC05-76OR00033.

References

- [1] R. Nazikian et al., Phys. Plasmas **8**, 1840 (2001).
- [2] G. Wang et al., Rev. Sci. Instrum. **75**, 3800 (2004).
- [3] S. Seo, Rev. Sci. Instrum. **76**, 036104 (2005).
- [4] G.R. McKee et al., Rev. Sci. Instrum. **70**, 913 (1999).
- [5] D.K. Gupta et al., Rev. Sci. Instrum. **75**, 3493 (2004).
- [6] R. Nazikian, G. Kramer, this proceeding (2005).

A new spectral analysis to study pellet triggered ELMs from broadband reflectometry at ASDEX Upgrade

L. Fattorini¹, M. E. Manso¹, P. T. Lang² and the ASDEX Upgrade Team²

¹ *Centro de Fusão Nuclear, Associação EURATOM / IST, Instituto Superior Técnico, Av. Rovisco Pais, P-1049-001 Lisboa, Portugal*

² *Max-Planck-Institut für Plasmaphysik, EURATOM Association, Boltzmannstr. 2, D-85748 Garching, Germany*

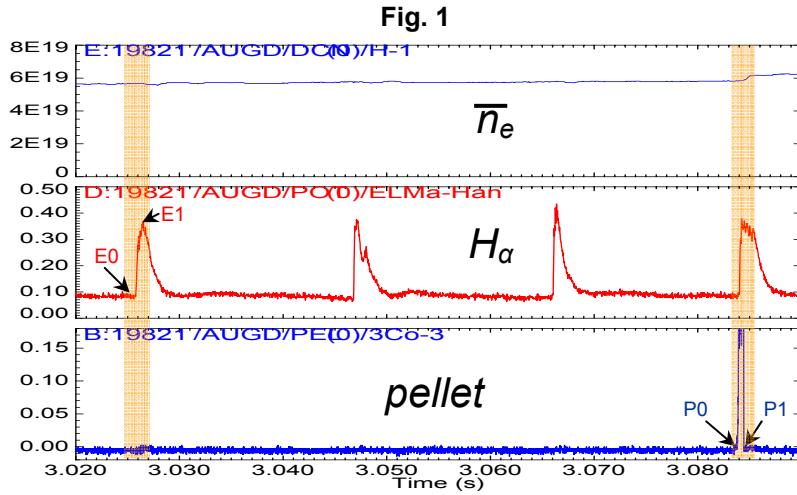
Introduction

The high-confinement mode (H-mode) is foreseen as the basic operation scenario for ITER. Unfortunately it usually drives transient, edge localized modes (ELMs), causing periodic expulsion of plasma energy and particles. In particular the type-I ELMs, can generate large energy losses from the main plasma, which can lead to unacceptably high heat power loads on the first wall elements, especially on the divertor target plates. ASDEX Upgrade is carrying out experimental studies to control the ELM frequency by mean of an appropriate technique in order to mitigate them. The most successful one was achieved triggering ELMs by cryogenic pellets that has also shown to be a promising technique to investigate ELM physics^[1]. Reflectometry, due to its high temporal and spatial resolution, is a diagnostic specially suited for this type of experiments. The ASDEX Upgrade FM-CW reflectometry system has 9 swept channels in K, Ka, Q, V and W frequency bands at the low field side (LFS) and in K, Ka, Q and V bands at the high field side (HFS), probing the plasma simultaneously. In swept mode these channels operate with a minimum repetition rate of 35 μ s and in fixed frequency mode with a sampling rate up to 1 MHz. Previous reflectometry analyses of pellet experiments were focused on the study of density profiles (especially at LFS) in the regions between ELMs, where profiles are not distorted by the ELM activity. Comparing intrinsic and triggered ELMs phases no significant differences were found. In order to understand the plasma behavior it became clear that it was necessary to analyze also the density changes occurring during both types of ELMs. For example, it was previously demonstrated that intrinsic ELMs in ASDEX Upgrade start to evolve at the LFS^[2] but no indications exist about the evolution of their triggered counterpart. Usually during ELMs strong perturbations are present at the plasma edge and profile evaluation can become difficult, especially at the peak of the ELM. For this reason it was necessary to develop a new method that could visualize in a simple and direct way detailed local profile changes, without the need to evaluate the density profile. The method uses the spectrogram derived from swept frequency data (basic information for density profile inversion) and gives the temporal evolution of spectrogram slices centered at selected plasma densities. In order to have the best time resolution, dedicated experiments were made with all the sweeps at the maximum repetition rate of 35 μ s (sweep duration 25 μ s), corresponding to a total data acquisition window of 107.24 ms (limitation imposed by present system memory). New information could also be obtained at higher densities (up to $1.2 \cdot 10^{-20} \text{ m}^{-3}$) after the recent improvement of the W-band channel at the LFS.

Novel method to analyze local density variations

The new method is based on the time evolution of slices of the reflected signal spectrograms taken at selected density layers. The spectrograms representing the spectral

content of the reflected signals (over the entire probed plasma region), are obtained with the simultaneous operation of the different swept channels. They are the basic tool to extract

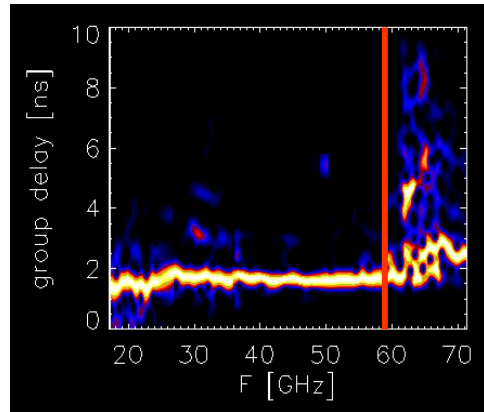


the group delay for profile evaluation and display also the spectral features due to plasma density perturbations, namely due to ELMs. Using spectrograms from consecutive sweeps it is possible to analyze the temporal evolution of the local spectra at selected probing frequencies (or densities). To illustrate the method we present

examples obtained in ASDEX Upgrade H-mode discharge #19821 (plasma current 1 MA, average density $8.8 \cdot 10^{-19} \text{ m}^{-3}$) where pellets were launched between 1.4 and 3.4 s with 5 Hz frequency and 240 m/s velocity. In fig. 1 are shown the time traces for average n_e , outer divertor H_α signal and the pellet ablation monitor signal between 3.020 and 3.090 s. The first three ELMs are intrinsic, the last one is triggered by pellet injection. An example of one of the spectrograms obtained between $t=3.025515 \text{ s}$ and $t=3.025865 \text{ s}$ (sweeps 730÷740) is depicted in fig. 2; in red it is marked the slice of the spectrogram at 59 GHz. The temporal evolution of the spectrogram slice at 59 GHz ($n_e=4.3 \cdot 10^{-19} \text{ m}^{-3}$) obtained from sweeps 730÷765, corresponding to the time interval $t=3.025515 \div 3.026740 \text{ s}$, is represented in fig.3. The three vertical lines correspond, respectively, to sweep 736 (65 μs before the ELM), sweep 748 (355 μs after the ELM) and sweep 761 (810 μs after the ELM). The response of the selected plasma layer to the onset of the intrinsic ELM at $t_{0,H\alpha}=3.025790 \text{ s}$ can be clearly seen from the figure. The increase of the group delay starting at sweep 740

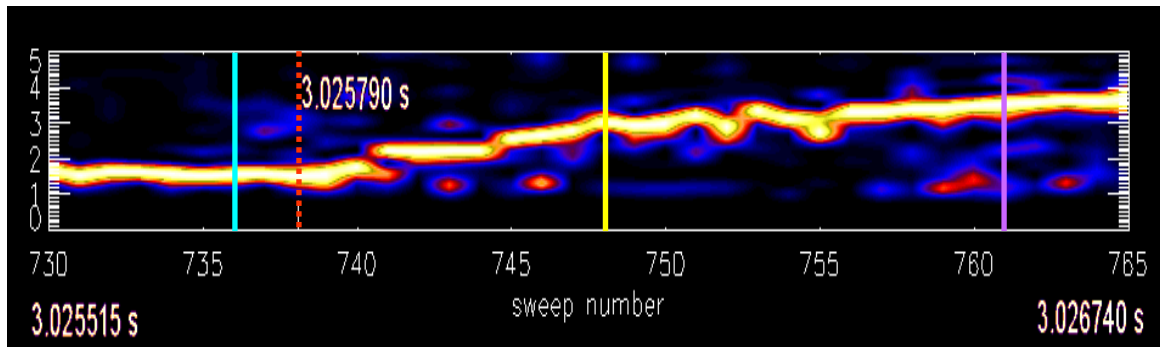
the group delay for profile evaluation and display also the spectral features due to plasma density perturbations, namely due to ELMs. Using spectrograms from consecutive sweeps it is possible to analyze the temporal evolution of the local spectra at selected probing frequencies (or densities). To illustrate the method we present examples obtained in

Fig. 2



can be clearly seen from the figure. The increase of the group delay starting at sweep 740

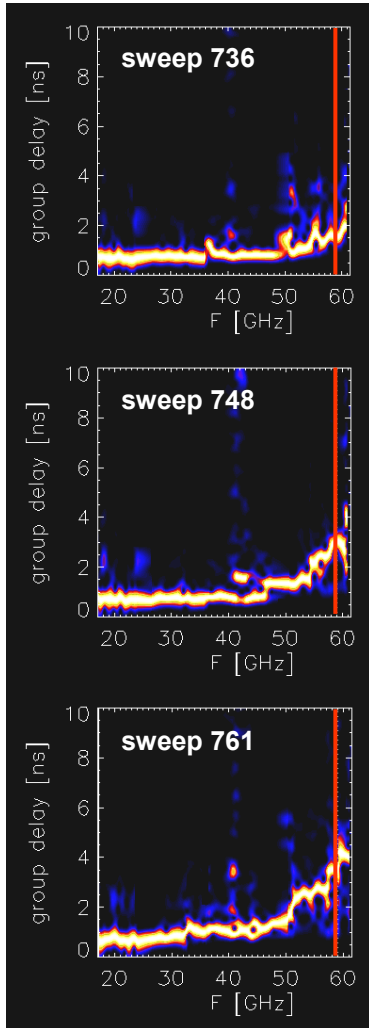
Fig. 3



($t=3.025865 \text{ s}$) indicates the inward movement of the density layer (away from the

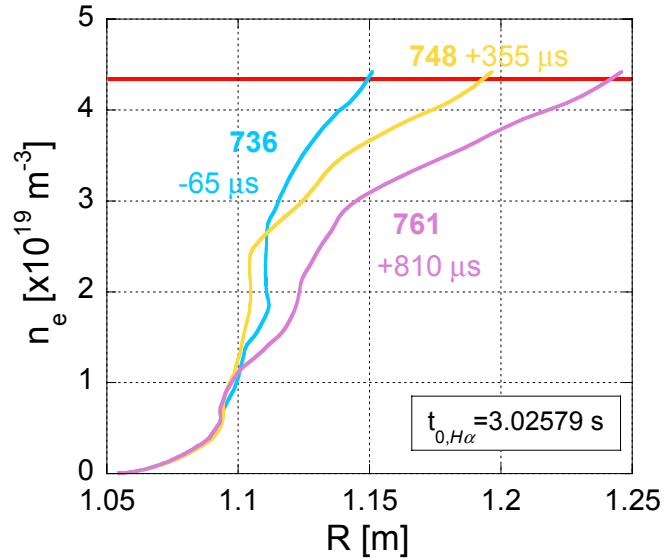
launching/receiving antenna) and therefore the density profile flattening caused by the ELM. It should be noted that, although important changes of the profile (group delay) occur

Fig. 4



and strong density perturbations are usually seen at the peak of the ELM, the selected plasma layer is not affected (spectral energy well concentrated around the group delay curve). To clarify the procedure, three of the thirty-six spectrograms utilized to perform the previous analysis are displayed in fig. 4 (they correspond to the sweeps indicated by the vertical lines in fig. 3). The slices at $F=59$ GHz are represented by the red vertical lines. The density profiles derived from these spectrograms (sweeps 736, 748 and 761) are shown in fig. 5, where the selected density layer is also indicated. It should be noted that only O-mode data was used

Fig. 5



to invert the profiles and the minimum probed density is $n_{el} \cong 0.45 \cdot 10^{-19} \text{ m}^{-3}$. Below that density the profiles are

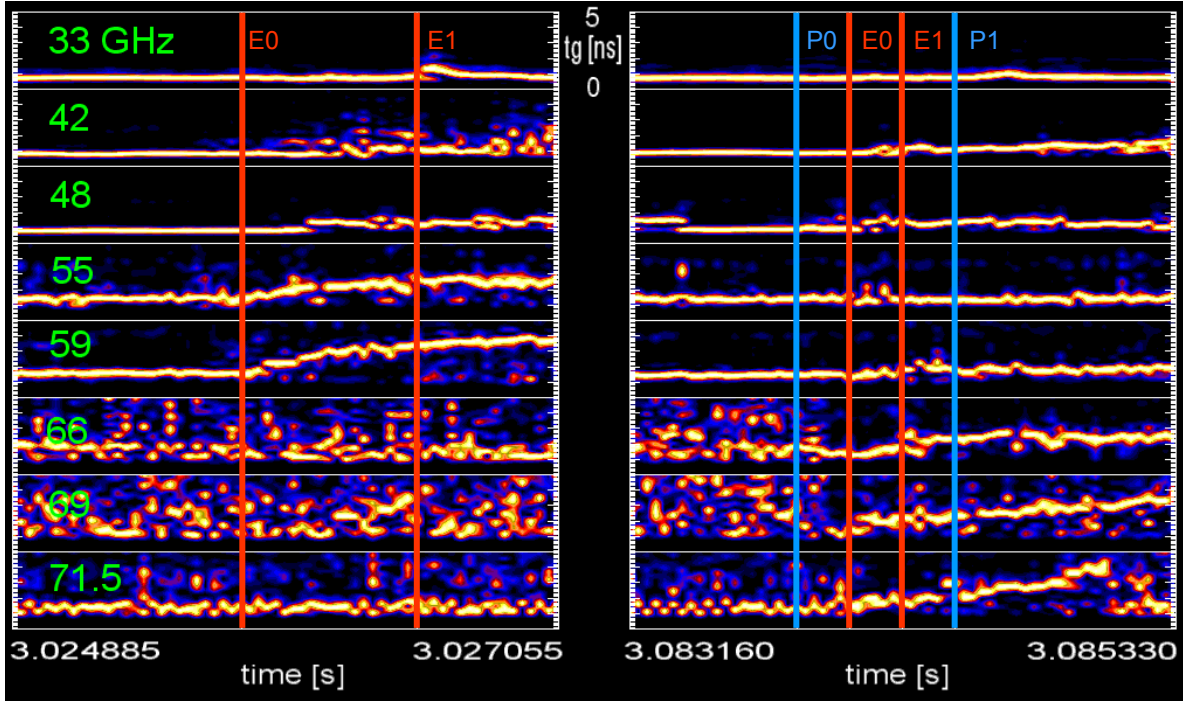
initialized using a linearly approximation of the group delay curve and a fixed position r_0 for the first plasma layer. Although this procedure introduces some errors in the absolute position of density profile, the errors are more significant closer to n_{el} and they decrease for higher densities.

Profile changes due to intrinsic and triggered ELMs

In the following we present the results concerning the first ELM (natural) and the fourth one (triggered) shown in fig. 1. With E0 and E1 we define, respectively, the beginning and the peak of the H_α signal. With P0 and P1 we indicate the beginning and the end of the pellet ablation in the plasma. We have chosen eight frequencies (density layers) and computed the temporal evolutions of eight group delay spectrograms slices (GDSS) for the intrinsic and the triggered ELM at the HFS (shown in fig. 6). For the intrinsic ELM (left part of fig.6) a clear inward movement is seen at plasma layers $n_e=3.8 \cdot 10^{-19} \text{ m}^{-3}$ and $n_e=4.3 \cdot 10^{-19} \text{ m}^{-3}$, corresponding to probing frequencies $F = 55$ GHz and $F = 59$ GHz. For frequencies 66 ($n_e=5.4 \cdot 10^{-19} \text{ m}^{-3}$), 69 ($n_e=5.9 \cdot 10^{-19} \text{ m}^{-3}$) and 71.5 GHz ($n_e=6.4 \cdot 10^{-19} \text{ m}^{-3}$) the reflected signal cannot be detected because the density is not sufficiently high to reflect the

probing microwaves. At 71.5 GHz the detected spectrum corresponds to the noise base line of the heterodyne detection. In the case of the pellet triggered ELM, we first notice that the movements of the plasma are shifted to higher frequencies (66, 69 and 71.5 GHz).

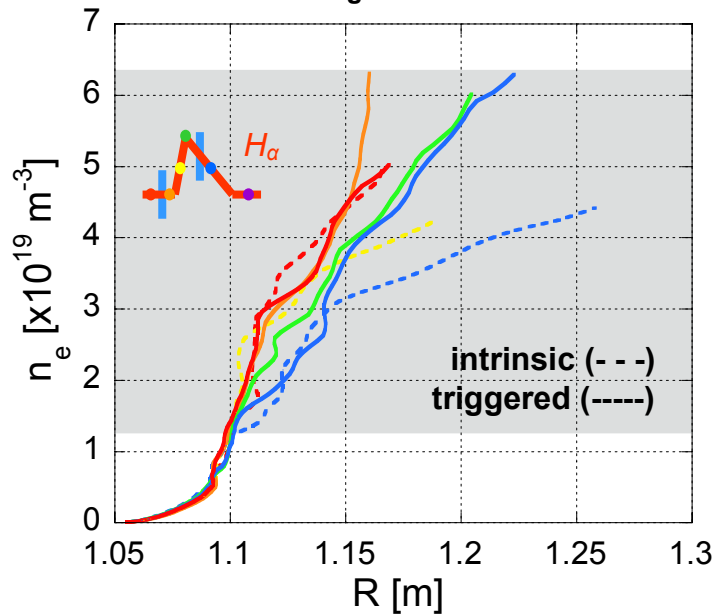
Fig. 6



Moreover for these three frequencies we can see that just after the pellet injection resulting in the peaking of the density profile at the HFS, the entire V band channel comes into operation. The GDSS plots also show how the density profile continues its flattening after the peaking of the H_α signal, E1.

In fig. 7 are shown the HFS density profiles corresponding to the main ELM phases. The plasma density profile is the same before the ELM and before the pellet injection (red line). Just after the pellet injection (orange line) the density peaking allows to measure the profile up to $n_e=6.4 \cdot 10^{-19} \text{ m}^{-3}$. In the phase after E1 the profile (blue line) is still flat but for the triggered ELM it is steeper; this is due to a double effect: the flattening due to the ELM and the density fuelling due to the pellet ablation. Phase between E0 and E1 (yellow line) and peak E1 (green line) are also depicted.

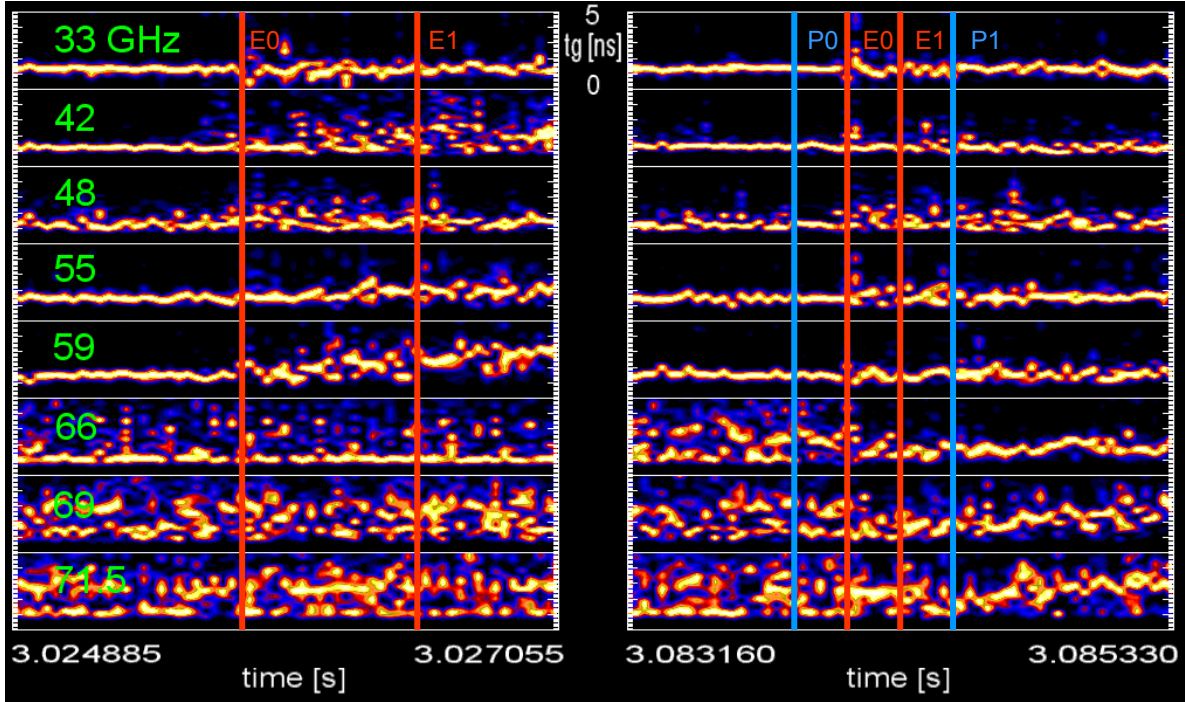
Fig. 7



Concerning the LFS (fig. 8) the general behavior is similar to the HFS except that all plasma layers are more turbulent after the beginning of the ELMs.

Moreover the density peaking due to the pellet injection is not immediate as it happens at the HFS. This is also confirmed from the LFS density profiles plotted in fig. 9.

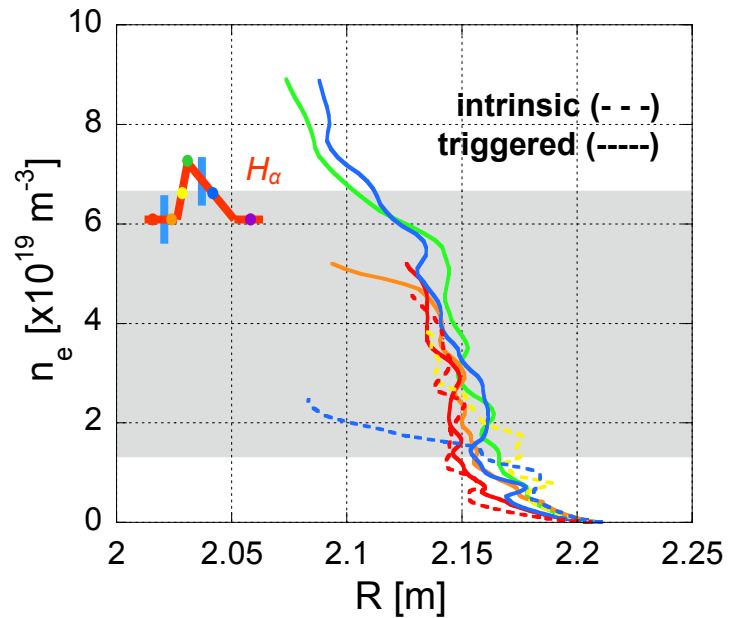
Fig. 8



Conclusions

The above study demonstrated that the new data analysis method has the advantage of a direct and simple evaluation (fully automatic). As it does not require the evaluation of the density profile, it is independent of any initialization procedure (O-mode operation only) or errors associated with X-mode (when X-mode is utilized to complement O-mode at the very edge). The method is very useful to track fast local profile changes and it can provide also the localization (in space and time) of density perturbations associated with fast plasma events, such as ELMs. It has the advantage that it can be used even when high resolution (25 μ s) single sweep density profiles are distorted due to plasma turbulence. The first analysis, here presented, clearly demonstrates how reflectometry can contribute to the study of the dynamics of intrinsic and triggered ELMs. This study seems to indicate that the two types of ELMs are very similar but to answer definitively this question more investigation is needed. For example it is important to detect where the

Fig. 9



triggered ELMS occur first, at HFS or at LFS? For this more dedicated plasma experiments are foreseen. The analysis of the space time evolution of the plasma turbulence during the two types of ELMS is another relevant issue.

Acknowledgments

This work has been carried out in the frame of the Contract of Association between the European Atomic Energy Community and Instituto Superior Técnico (IST) and of the Contract of Associated Laboratory between Fundação para a Ciência e Tecnologia (FCT) and IST. The content of the publication is the sole responsibility of the authors and it does not necessarily represent the views of the Commission of the European Union or FCT or their services.

[1] P. T. Lang et al., Nuclear Fusion **44**, 665

[2] I. Nunes et al., Nuclear Fusion **44**, 883

Scaling and inverse scaling of ASDEX Upgrade reflectometer data

M.Abel, G.D.Conway¹, H.Zohm¹ and ASDEX Upgrade Team¹

Institute of Physics, University of Potsdam, 14415 Potsdam, Germany

¹ *MPI Plasmaphysik, EURATOM-Association IPP, D-85748, Garching, Germany*

1. Introduction

The analysis, characterisation and explanation of turbulence and turbulent transport in plasmas is an important physical task to enhance fusion devices. At the same time it is of fundamental interest in physics as plasma turbulence is among the most complex systems currently investigated. In this paper we indicate how to use multifractal analysis as a tool to characterise turbulence. We apply the formalism of structure functions [Frisch(1995), del Castillo-Negrete et al.(2004)] and inverse structure functions [Jensen(1999), Biferale et al.(1999)] to edge reflectometer data from the ASDEX-Upgrade tokamak. The results for the multifractal spectrum can be used for comparison with results from numerical simulation and further for modelling turbulence in plasmas. Naturally, one important goal is the interpretation of the results in terms of basic turbulence theory. Below, we briefly present the data we used for analysis, and the multifractal formalism used. The results from analysis are presented in a compact way and finally, we close with a discussion.

2. The data

Data from two ASDEX Upgrade discharges were used, one with ohmic and (0.8 MW) ECRH L-mode phases #18726 (designated S1 in the following) at -2.4 T/0.8 MA with line ave. density of $7 \times 10^{19} \text{ m}^{-3}$, and one shot with a 2.5 MW NBI L-mode phase #19240 (S2) at -2.4 T/1.0 MA and $6 \times 10^{19} \text{ m}^{-3}$. Two heterodyne (I & Q) O-mode reflectometer signals were available in Q-band at 42 GHz and V-band at 55 GHz, giving two radial points per discharge at roughly normalised radii of 0.94 and 1.05. Schematically one has the following 6 signals:

| | Ohmic | L-mode |
|--------|-------|--------|
| V band | S1 | S1,S2 |
| Q band | S1 | S1,S2 |

The reflectometer signals displayed a small constant amounts of phase ramping during the periods of study, which was subtracted before analysis. The amplitude and phase signals were obtained from the I/Q signals in the usual way ($A = \sqrt{I^2 + Q^2}$ and $\Phi = \tan^{-1}(I/Q)$). The phase signal was then corrected for phase jumps. Fig. 1 shows an example of the Q-band phase signal during the ohmic stage of shot S1.

3. Multifractal analysis

The signals were analysed using the multifractal analysis techniques which have been developed in the frame of turbulence theory [Frisch(1995)], or statistical physics [Beck and Schlögl(1993)]. A turbulent signal typically does not follow a Gaussian distribution of the investigated quantities (in our case the density fluctuation as measured by reflectometry). Considering turbulence as an incremental process [Frisch(1995)], one is interested in the statistical properties of the increments of a signal s : $\Delta s(t) = s(t + \Delta t) - s(t)$. Its statistical properties characterise the underlying process and allow for stochastic modelling, e.g., by a fractional diffusion process. For statistical information one can determine the probability density function $P(\Delta s, \Delta t)$, or equivalently the

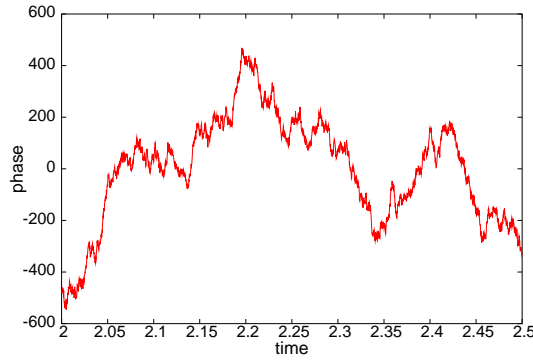


Figure 1: Phase signal S1, ohmic mode in Q-band. The base trend has been subtracted.

structure functions or moments of the increments, $S_p(\Delta t) = \langle (\Delta s)^p \rangle$. In a cascade process, non-Gaussianity of the increments is found in the moments scaling as:

$$S_p(\Delta t) \sim \Delta t^{\zeta(p)} \quad (1)$$

with $\zeta(p) = \alpha p$ a linear function for a fractal process and $\zeta(p)$ nonlinear for a multifractal. To determine $\zeta(p)$, the slope of $S_p(\Delta t)$ is determined in a log-log plot as

$$\log[S_p(\Delta t)] \sim \zeta(p) \cdot \log(\Delta t) . \quad (2)$$

Usually good scaling is observed in a certain range of scales, without that range different processes are dominant, e.g. at the scale where energy is fed to the system.

When the function ζ is known for all orders p the process is fully characterised in a statistical sense. The well-known Brownian motion in one dimension is a non-fractal process (i.e. an ensemble of trajectories fills space completely) with $S_{2p}(\Delta t) = 1 \cdot 3 \cdot \dots \cdot (2p-1)(D\Delta t)^p$, and $S_{2p-1} = 0$ i.e., $\zeta = 0.5p$.

In recent years a complementary approach has been suggested using the concept of exit-times, or residence times, respectively [Jensen(1999), Abel et al.(2000)]. The exit time is defined as the time the trajectory needs undergo a fluctuation of a given size Δs . With these times, one can calculate the corresponding statistics by the use of the so-called inverse structure functions, or exit-time moments

$$I_q(\Delta s) \sim \Delta s^{\xi(q)} . \quad (3)$$

The analog for the Brownian motion are the moments of the first passage times, where one calculates analytically $I_q = q \cdot IS_{q-1}(x) = q \cdot \dots \cdot 1(D\Delta s)^{-q}$ for all values of q [van Kampen(1992)]. A fractal/multifractal process can be characterised in terms of the inverse structure functions by the linear/nonlinear function $\xi(q)$. Depending on the situation one or the other method might be favourable.

Often, experimental data do not show perfect scaling, or have a very limited scaling range. In these cases, one can try to extract scaling exponents using the concept of extended self-similarity (ESS) [Benzi et al.(1993)]. Essentially, one assumes that individual structure functions behave similar, then one divides the common behaviour out by normalising to one structure function:

$$\frac{\log(S_{q+n})}{\log(S_q)} \sim \frac{\zeta(q+n)}{\zeta(q)} . \quad (4)$$

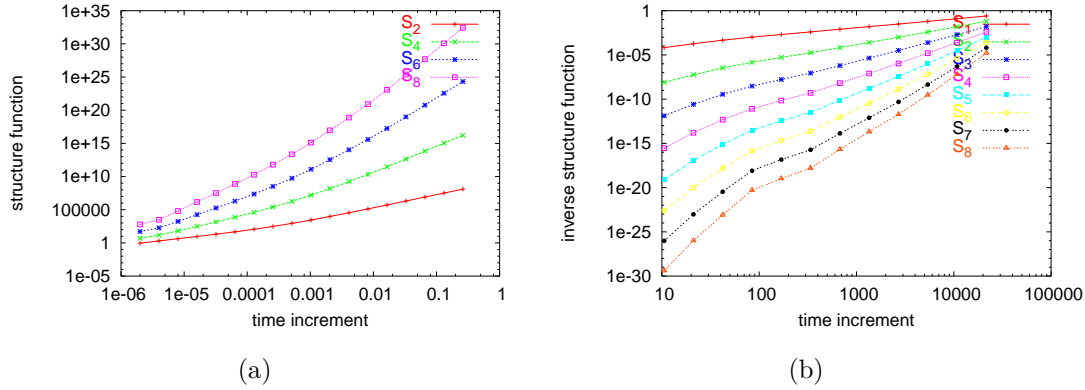


Figure 2: Log-log plot of a) Structure functions and b) inverse structure functions of various order for signal S1, L-mode, V-band measurement.

This way, a scaling relative to $\zeta(q)$ can be extracted.

4. Results

In this section, we will present the main results for the signals analyzed. We show results for all structure functions in the case of signal S1 in L mode/ V band measurement. Then, we give in one plot a comparison for the different signals and finally plot the multifractal spectrum as obtained from the data for structure functions and inverse structure functions.

For each constellation given in Table the structure functions $S_2 - S_8$ and the inverse structure functions $I_1 - I_8$ are calculated. As an example, in Fig. 2 a) the structure functions for signal S1, for L-mode and V-band are plotted. The corresponding result for the inverse structure function is shown in Fig. 2 b). We observe that for the usual structure functions, no scaling is found, rather the functions are curved, but as it occurs, in a similar way such that ESS is applicable. The inverse structure functions show two different scaling regions with slightly different slope, with a transitory region in between. This requires more detailed investigations, a possible reason are “unnatural” phase shifts from the conversion of the signal. It turns out that ESS does not scale away the effect.

In Fig. 3, a comparison of the ESS scaling for all investigated signals ($\log(S_4)$ vs. $\log(S_2)$) is shown. Clearly, the signals S1, Q-band and S1, V-band show very similar behaviour for ohmic or L-mode. Signal S2 does not collapse on the graphs for signal S1. The same behaviour is observed for the inverse structure functions.

To extract the multifractal spectrum, one must determine the slopes in graphs Fig. 3 a) and b). The corresponding local slopes are plotted in Fig. 4 a) and b). One obvious problem is the identification of the scaling region. This is almost an art, one typically has no good scaling for small and large values of the increment due to bad statistics and limits of the scaling. Only values are taken for which an approximately constant slope exists over 2 decades or more. The final spectrum for the structure functions is given in Fig. 5; it is clearly multifractal. At this point, further analysis is needed to ensure that the result is typical for the signals investigated .

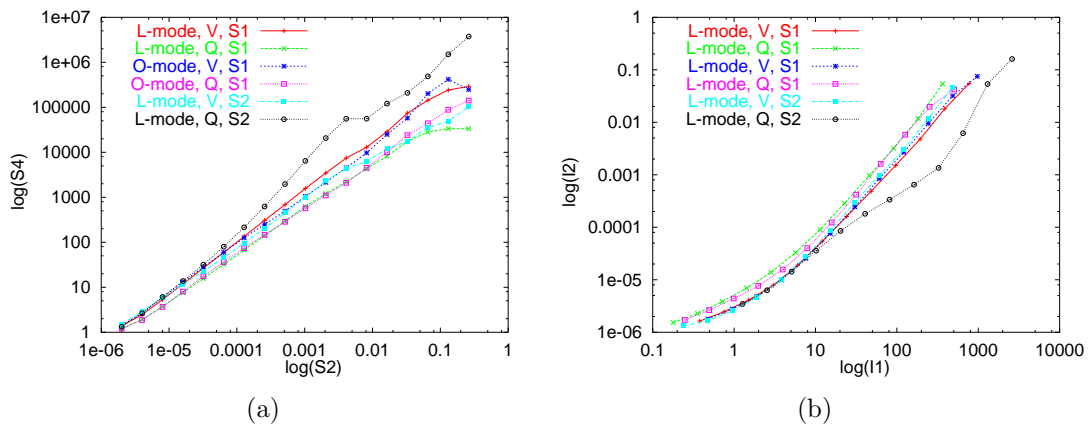


Figure 3: ESS applied to all signals investigated. For clarity, only $\log(S_4)$ is plotted versus $\log(S_2)$ for the structure functions and $\log(I_3)$ versus $\log(I_2)$ for the inverse structure functions. The other orders behave similarly. a) structure functions, b) inverse structure functions.

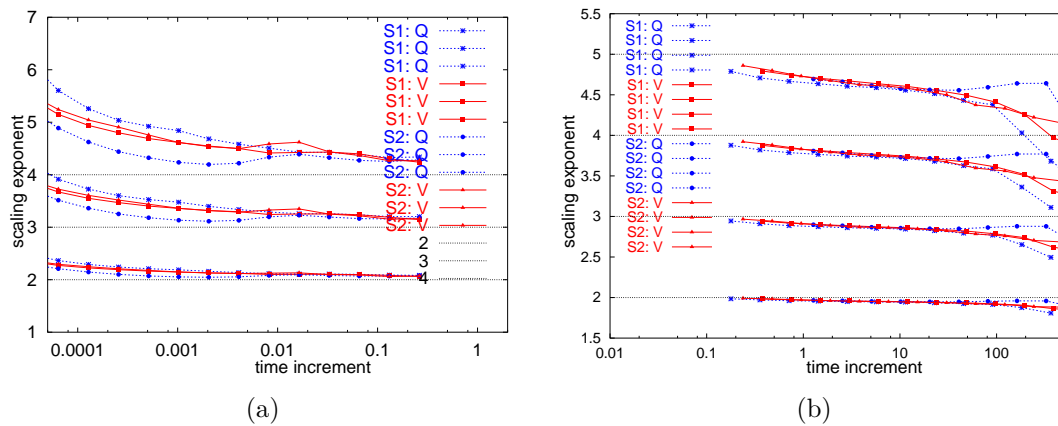


Figure 4: Scaling exponents as obtained from the signals (see legend). A normal, diffusive scaling corresponds to the straight lines at integer numbers. a) result for the usual structure functions, b) result for the inverse structure functions.

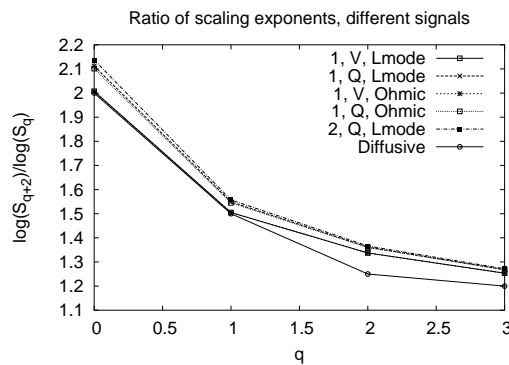


Figure 5: Multifractal spectrum as extracted from the slopes, cf. Fig. 4 a).

5. Discussion

The basis of the analysis is that fluctuations in a reflectometer phase signal represent localised density fluctuations at the point of reflection. An analysis of the fractal/multifractal behaviour of reflectometry edge data from ASDEX Upgrade show anomalous scaling for different confinement modes and radial positions. Clear multifractal behaviour is observed in the spectrum of scaling

In this contribution we showed that it is possible to apply the multifractal analysis to reflectometer data. In a first attempt we analyzed data with small amount of ramping. Problems concern artificial phase jumps which are physically not expected and a clear identification of scaling ranges. As a result we clearly find multifractal behavior in the spectrum of scaling exponents, which is different for different radial positions. The difference between ECRH L-mode and ohmic confinement seem to be less important than the radial position for the signal. The data from the NBI L-mode shot show a different behaviour, possibly due to the strong toroidal rotation. A more extensive analysis on a larger database of shots is required before further conclusions can be drawn. In the initial selection of data a small amount of phase ramping was present. Artificial phase jumps, which are physically not realistic, and the clear identification of scaling ranges are concern remaining to be resolved. Finally, a longer term goal is to use the spectrum of scaling exponents as input to numerical studies of turbulence and the signal propagation in a turbulent plasma.

6. References

- [Frisch(1995)] U. Frisch, *Turbulence: The legacy of A. N. Kolmogorov* (Cambridge Univ. Press, Cambridge, UK, 1995).
- [del Castillo-Negrete et al.(2004)] D. del Castillo-Negrete, B. A. Carreras, and V. E. Lynch, *Physics of Plasmas* **11**, 3854 (2004).
- [Jensen(1999)] M. Jensen, *Phys. Rev. Lett.* **83**, 76 (1999).
- [Biferale et al.(1999)] L. Biferale, M. Cencini, D. Vergni, and A. Vulpiani, *Phys. Rev. E.* **60**, R6295 (1999).
- [Beck and Schlögl(1993)] C. Beck and F. Schlögl, *Thermodynamics of chaotic systems* (Cambridge University Press, Cambridge, UK, 1993).
- [Abel et al.(2000)] M. Abel, L. Biferale, M. Cencini, M. Falcioni, D. Vergni, and A. Vulpiani, *Phys. Rev. Lett.* **84**, 6002 (2000a).
- [van Kampen(1992)] N. G. van Kampen, *Stochastic processes in physics and chemistry* (Elsevier, Amsterdam, 1992).
- [Benzi et al.(1993)] R. Benzi, S. Ciliberto, R. Tripicciono, C. Baudet, F. Massaioli, and S. Succi, *Phys. Rev. E* **48**, R29 (1993).

A dual source reflectometer for density profile and fluctuations measurements in Tore-Supra core

R. Sabot, A. Sirinelli, J.M Chareau, F. Clairet, J.C. Giacalone, L. Vermare,
P. Hennequin[#], S. Heuraux⁺, G. Leclert[°]

Association EURATOM/CEA, CEA/DSM/DRFC, CEA-Cadarache,
13108 Saint-Paul-lez-Durance, France

[#] Laboratoire de Physique et de Technologie des Plasmas, CNRS (UMR-7648),
Ecole Polytechnique, 91128 Palaiseau, France

⁺ Laboratoire de Physique des Milieux Ionisés, Université Henri Poincaré, BP 239,
54506 VANDOEUVRE Cedex, France

[°] LPIIM, CNRS (UMR 6633) - Université de Provence, 13397 Marseille Cedex 20, France

Abstract The stepped fixed frequency X-mode reflectometer operating between 105–160 GHz that was designed for density fluctuations measurement has been modified to measure the density profile. It runs now with two sources in parallel: a fast swept source and a frequency synthesizer to measure during the same shot the density profile and density fluctuations. Using fixed measurement, modes in the range 20-80 kHz have been detected in various plasma conditions and at various locations. The nature of these modes is still under investigation.

1. Introduction

Density fluctuation measurement from fixed frequency measurements asks for a precise density profile to locate precisely the cut-off layer [1]. The density gradient is also required to evaluate the level of density fluctuations from the phase fluctuation level using Bretz like expressions [2].

The 105-155 GHz X-mode heterodyne reflectometer that was designed for core density fluctuation measurements [3] can now measure during the shot density profile and density fluctuations. It operates with two sources: a frequency synthesiser for frequency steps and a fast swept VCO for density profile measurements. The reflectometer will be described briefly in this proceeding, a longer article will be submitted to Nuclear Fusion special issue on reflectometry that should appear in 2006.

2. Microwave set-up

2.1. Fluctuation measurements

The 105-155 GHz reflectometer (figure 1) is based on the set-up developed for Tore-Supra profile reflectometers: low frequency source, frequency multipliers and Single Side Band Modulator [4]. The 105-155 GHz multiplier is made of a V-band active quadrupler and a passive doubler. The output power is low: $-10 < P < 0$ dBm. A high performance single sideband modulator (SSBM) shifts the frequency ahead of the octupler for heterodyne detection. On the reference arm, a second quadrupler drives a second harmonic mixer. High gain Gaussian antennas (38 dB) were chosen to increase the reflected signal since the antennas are 2 meters from the plasma centre and to produce an almost parallel beam (divergence $\sim 1^\circ$ HPHW). With bistatic antennas parasitic reflections are minimised.

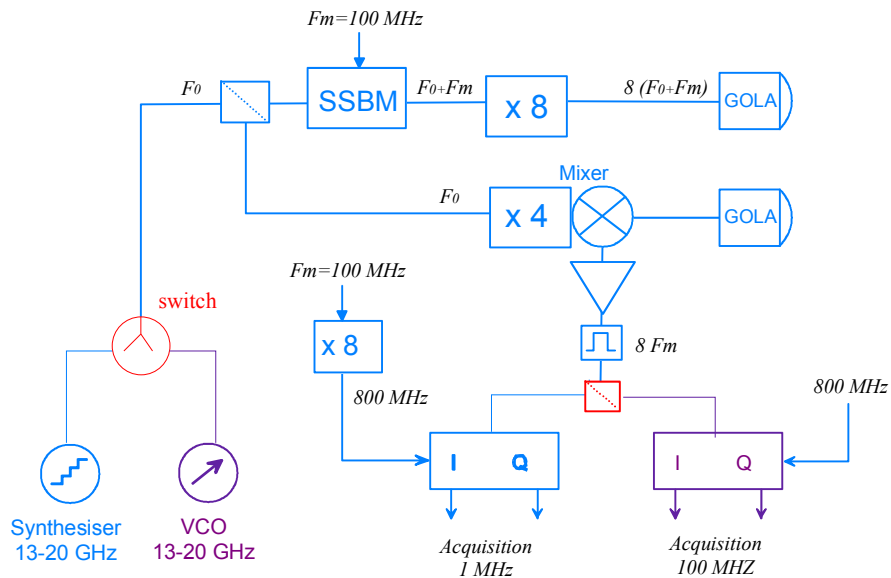


Figure 1: Microwave set-up for the 105-155 GHz reflectometer

The source should be very stable for fluctuations measurements because of the frequency multipliers. The source phase noise is indeed multiplied by 64, the square of the multiplication order. Frequency synthesisers are very suitable for fluctuation measurements. They have very low phase noise and can describe stair frequency pattern with 1 to 30 milliseconds between steps. A fast hopping synthesiser is currently used (dwell time below 1 ms), 15 steps of 8.2 ms are described in less than 200 ms. The phase noise after an inner wall reflection is only few degrees as shown figure 2. With a VCO, the phase noise is more than 180 degrees during an 8.2 ms step although the delay line is optimised for zero delay at outer plasma edge.

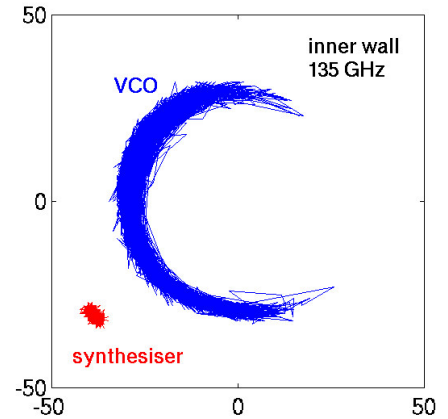


Figure 2: phase stability during 8.2 ms after inner wall reflection

2.2. Profile measurements

The VCO being not suitable for fluctuation measurements, the frequency synthesiser in swept mode was tested for profile measurements, but that was not a satisfying solution. The 5 millisecond sweeping time was too long and the synthesiser did not allow step and sweep mode operation in the same shot.

The frequency synthesiser being not suitable for profile measurements and VCO being too noisy for fluctuations measurements, we modify the reflectometer to run with two sources in parallel. The reflectometer uses also two acquisition systems. Fixed frequency measurements are recorded with a 1 MHz VME card. A 100 MHz acquisition is used for profile. Up to 1000 profiles equally sampled during the plasma discharge can be measured.

The VCO is usually swept in 60 to 100 microseconds to limit the beat frequency below 50 MHz. A microwave switch changes the source to the synthesiser at the time predefined for density fluctuations measurements.

The reconstruction relies on the Bottolier-Curtet method [5] and uses the density profile measured with the 50-110 GHz reflectometers or the interferometry diagnostic for initialisation. Combining the 3 X-mode reflectometers covering the band 50 to 150 GHz, the

density profile from the edge on the low field side up to the high field side can be measured if the magnetic field is high enough ($B > 3\text{T}$) [1].

A burst mode is now in operation fast profile evolution. The dwell time between two profiles can be reduced to $5\ \mu\text{s}$. This mode will be used for MHD studies like $q=1$ [6] and to compare to method proposed by S. Heuraux to measured density fluctuations from fast swept reflectometer [7] to the classic fixed frequency method.

3. Detection of high frequency modes

High frequency coherent mode in the range 30 to 80 kHz have been observed in various plasmas configuration (Ohmic, LH or ICRH heating) and at various locations (gradient zone on the low and/or the high field side, centre). Figure 3 shows the frequency spectrum of the complex signal for one of the best example in a high power discharge ($P_{\text{ICRH}}=4\text{MW} + P_{\text{LH}}=2\text{MW}$).

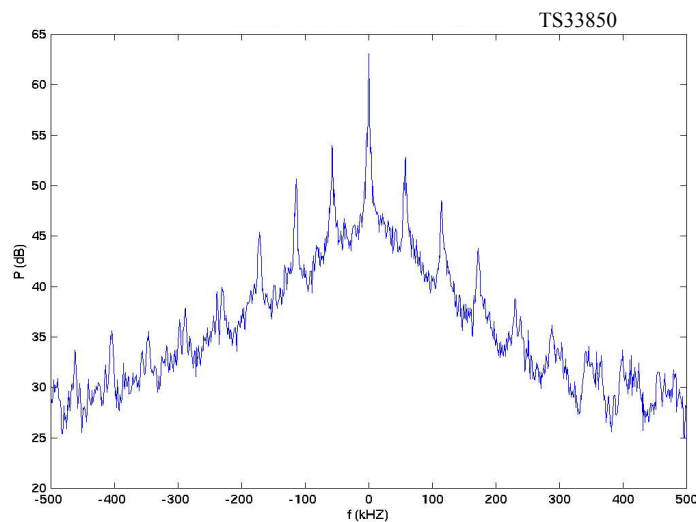


Figure 3: Example of a high frequency (54 kHz) mode detected in the centre ($r/a=0.06$)

On the frequency spectrum of the phase, harmonics of the mode are very low showing that they are Bessel harmonics on the complex signal. A radial movement of the cut-off layer thus probably causes these phase oscillation. In helium plasma, the frequency of these modes is lower, maybe an indication of a mass dependence.

The nature of the mode is still under investigations. The frequency range and the mass dependence could point to Geodesic Acoustic Modes [8] but theory predicts GAMS are stable in the core. It could also be coherent Ion Temperature Gradient modes, but in the centre, the temperature gradient is very low.

These modes are not Alfvén modes since Alfvén frequency in the core are much higher. At high power ICRH, they have been observed in the range 150-500 kHz with the 105-155 GHz reflectometer.

4. Conclusion

The microwave source incompatibility between agility for profile measurements and stability for fluctuation measurements was solved using two sources in parallel for the 105-155 GHz reflectometer. Commercially sources being imperfect, the reflectometry community needs a versatile source to measure with the same reflectometer the density profile and density fluctuations.

Although fast swept reflectometer can detect low MHD modes and a method has been developed to measure the level of fluctuations, only fixed frequency measurements can detect high frequency modes.

References

- [1] A. Sirinelli, et al., at this conference.
- [2] N. Bretz, Phys. Fluids B **4**, 2414 (1992).
- [3] R. Sabot, et al., 6th IRW, San Diego, 2003.
- [4] R. Sabot, et al., Int. J. Infrared Millim. Waves **25**, 229 (2004).
- [5] H. Bottolier-Curtet and G. Ichtchenko, Rev. Sci. Instrum. **58**, 539 (1987).
- [6] F. Clairet, et al., at this conference.
- [7] S. Heuraux, et al., at this conference.
- [8] P H Diamond, S-I Itoh, K Itoh and T S Hahm, Plasma Phys. Control. Fusion **47**, R35 (2005).

A user friendly interface for a fast wave solver in realistic plasma geometry

R.Nazikian

Princeton Plasma Physics Laboratory, Princeton, NJ 08543-0451, USA

This talk describes progress made at PPPL in developing a multi-user interface for large scale 2-D full wave reflectometer simulations in realistic plasma geometry. The software uses a JAVA interface and can be run from any WEB browser. A graphical interface guides the user through the necessary step to produce a batch job that executes potentially thousands of independent full wave runs on the PPPL PETREL cluster. The software then displays appropriate statistical analysis of the simulation results. It is intended that this tool be available to the international community for use in reflectometer data simulation and analysis. Suggestions for improvement and expansion in the capability of the code will be welcomed.

Reflectometry for Wendelstein 7-X

M. Hirsch, E. Holzhauser*, H.-J. Hartfuss

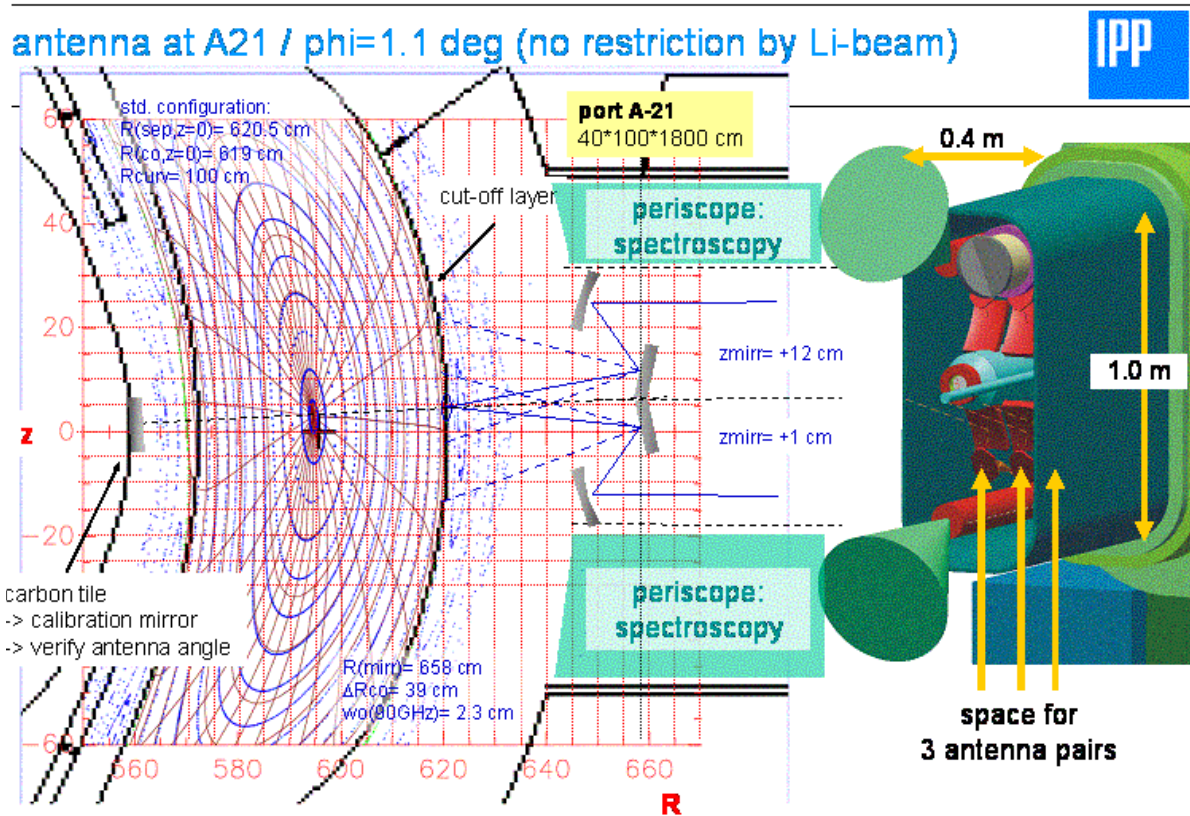
Max-Planck-Institut für Plasmaphysik, EURATOM Association, Greifswald, Germany

*Institut für Plasmaforschung, Universität Stuttgart, Stuttgart, Germany

The fully optimized stellarator Wendelstein 7 - X, now under construction in Greifswald, Germany, explores stellarator optimization and high-performance steady-state operation. In a first stage $P_{\text{ECRH}}=10$ MW for 30 min. planned. The diagnostic equipment (Hartfuss *et al* 1996) involves a reflectometry system dedicated to measure edge density profiles and to characterize density perturbations and their poloidal propagation velocity. Preparatory work such as design activities and the installation of a single antenna pair are included in the set of the so-called start-up diagnostics. First plasma operation is expected early 2012.

The position of the main reflectometer planned (Fig.1) is chosen such to minimize the curvature of the probed flux surfaces and where the B-field gradient increases continuously along the line-of sight like in a tokamak. The latter gives best access to the plasma core in x-mode either via the right-hand cut-off with low-field-side launch or via the left-hand cut-off launching at the same toroidal position from the high-field-side. In standard operation the local on-axis magnetic field is $B=2.59$ T with a variation of $2.35 \text{ T} < B < 2.94 \text{ T}$ along the sightline. Due to the strongly elongated plasma shape and the nearly vertical B_{mod} surfaces, the x-mode cut-off in the vicinity of the equatorial plane can be well approximated by the flux surfaces. Their *poloidal* curvature is low and varies as $80 \text{ cm} < R_{\text{curv}} < 100 \text{ cm}$ with cut-off layers $r/a > 0.5$. The *toroidal* curvature can be neglected. The variation of the conditions for reflectometry within the set of standard configurations of the stellarator vacuum magnetic field (Andreeva 2002) is small and neglected at this state of the design.

Expected cut-offs and resonances are given on Fig.2. For this design a density profile with central density $n(0) = 1 \cdot 10^{20} \text{ m}^{-3}$ and steep edge gradients is estimated based on W7-AS results. A reference cut-off layer is assumed to be at $(r-a) = -3$ cm in effective magnetic coordinates equivalent to $r/a = 0.94$ where the average minor radius $a = 52$ cm corresponding to the position of maximum velocity shear in an H-mode edge layer. Due to the elliptical plasma cross section the flux compression within the equatorial plane is about a factor of 2 such that one obtains $\Delta R \cong \Delta r_{\text{eff}} / 2$. Correspondingly the reference cut-off layer is located only 1.5 cm inside the separatrix. For the reference density profile this layer yields the x-mode cut-off for a frequency $f = 90$ GHz (center of the W-band) probing a density of $2.6 \cdot 10^{19} \text{ m}^{-3}$.



M Hirsch, IRW7, Garching 2005, p. 6

Fig.1: Flux surfaces (standard magnetic configuration) and plasma vessel contours at the diagnostic position $\Phi = 0, z = 0$. The port AEA21 (artists view on the right side) is shared with a variety of other diagnostics such as spectroscopy periscopes.

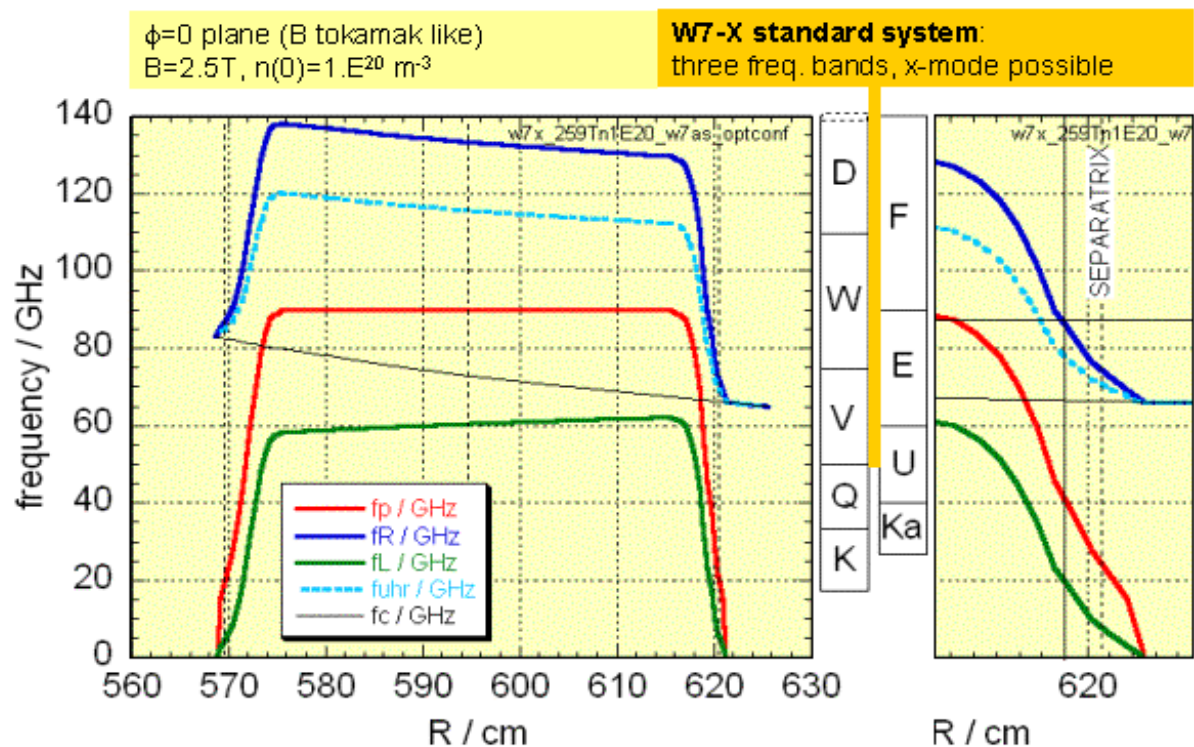


Fig.2 Cut-offs and resonances along the reflectometry sightline ($\Phi = 0, z = 0$) for a design density profile with $n(0) = 1 \cdot 10^{20} \text{ m}^{-3}$.

The diagnostic port AEA21 allows for three pairs of toroidally neighboured antenna pairs each with focussing elliptical mirrors with maximum diameter of 10 to 12 cm. Directly opposite on the high-field side carbon covered tiles at the inner vessel wall are designed as microwave mirrors (surface $10 \times 10 \text{ cm}^2$) in order to calibrate the time delay measurements (Fig.3). Thermal effects on their radial position are small: If during operation the plasma vessel heats up from 20 to 60 C° the tiles move radially outward by about 2.4 mm. The launching mirror positions are expected to remain almost unchanged as they are fastened to the flange which is assumed to stay at room temperature. These reflector tiles also would allow for an integrated HFS antenna - however with very restricted space available (about 3 cm to the vessel wall) (see Fig.3, left).

One of the antenna systems is planned to operate in an early state of W7-X operation. A high-directivity dual-antenna arrangement is proposed where the tilt angle of both sightlines with respect to the cut-off layer θ_{tilt} can be varied independently to provide flexibility. High-directivity can well be realized by a Gaussian antenna characteristic with nearly parallel wave fronts and a spot size taking into account the curvature of the reflecting layer: The latter yields a compromise between maximum number of perturbation maxima illuminated and minimum curvature within the spot (Hirsch and Holzhauser 2004). For example with $f = 90 \text{ GHz}$ probing a density of $2.6 \cdot 10^{19} \text{ m}^{-3}$ in x-mode and a tilt $\theta_{\text{tilt}} = 13.8 \text{ deg}$ which selects perturbations $K_{\perp} = 9 \text{ cm}^{-1}$ the calculated optimum beam width is $w_o^{\text{opt}} = 2.3 \text{ cm}$ (1/e-decay width of the E-field amplitude) resulting in a resolution of $(\Delta K_{\perp} / K_{\perp})^{-1} = 5.2$. The optimum beam waist varies as $w_o^{\text{opt}} \propto \sqrt{\rho \cdot \lambda}$ where ρ is the effective curvature radius and thus inherently fulfils the condition $w_o(\lambda) \propto \sqrt{\lambda}$ which allows for a broadband Gaussian optics with arbitrary mirror positions (Hirsch and Holzhauser 2005). A lower boundary $f > 70 \text{ GHz}$ arises only from the finite aperture which can be realized for the focussing mirrors within the port environment. To guide the beam in the long port to the vacuum flange a quasi-optical transmission line is planned which also has the advantage that there is no need for cooling waveguides. The variable antenna orientation is achieved by a steerable plane first mirror which decouples the sightline geometry - in particular the tilt angle - from the optimization of the spot size resulting from the second fixed elliptical mirror. Here the θ_{tilt} defines the selected density perturbations K_{\perp} via the Bragg condition whereas the spot size determines the spectral resolution ΔK . The steerable antenna sightlines allow for a number of different arrangements: a) *Density profile measurements* with separate antennas for signal launch and reception oriented to a common beam spot (bistatic arrangement), b) *conventional poloidal correlation reflectometry* where the two antennas are each oriented perpendicular to the cut-off layer probing long-wavelength perturbations such as MHD, c) *Doppler reflectometry* for a variety of different tilt angles θ_{tilt} with the two sightlines oriented in opposite poloidal directions such that the frequency shifts resulting from varying θ_{tilt} (induced by varying configuration or by MHD) can be separated from the Doppler shift resulting from a variation of the propagation velocity of the perturbations v_{\perp} (Hirsch and Holzhauser 2004). As two poloidally separate spots are probed this arrangement can be used for *poloidal correlation Doppler reflectometry* simultaneously. Poloidal correlation Doppler reflectometry measures the poloidal correlation length of small scale (finite K_{\perp}) perturbations and delivers a time-of-flight measurement which is the complementary method to determine the poloidal propagation velocity v_{\perp} (Hirsch and Holzhauser 2004). d) The K_{\perp} -spectrum of turbulence is obtained with the proposed system by means of a temporal scan of θ_{tilt} (see Hirsch

et al 2001, Hennequin *et al* 2005). Finally a *fast monitoring of the K_{\perp} -spectrum* is possible by simultaneously tracking the signal with two different values of θ_{tilt} which is of interest in the context of fast changes of the K_{\perp} -spectrum induced by shear flow for example. Limitations for the accessible θ_{tilt} arise from shadowing and crosstalk between the two antenna patterns involved.

integrated HFS-antenna: possible port access via AEC41

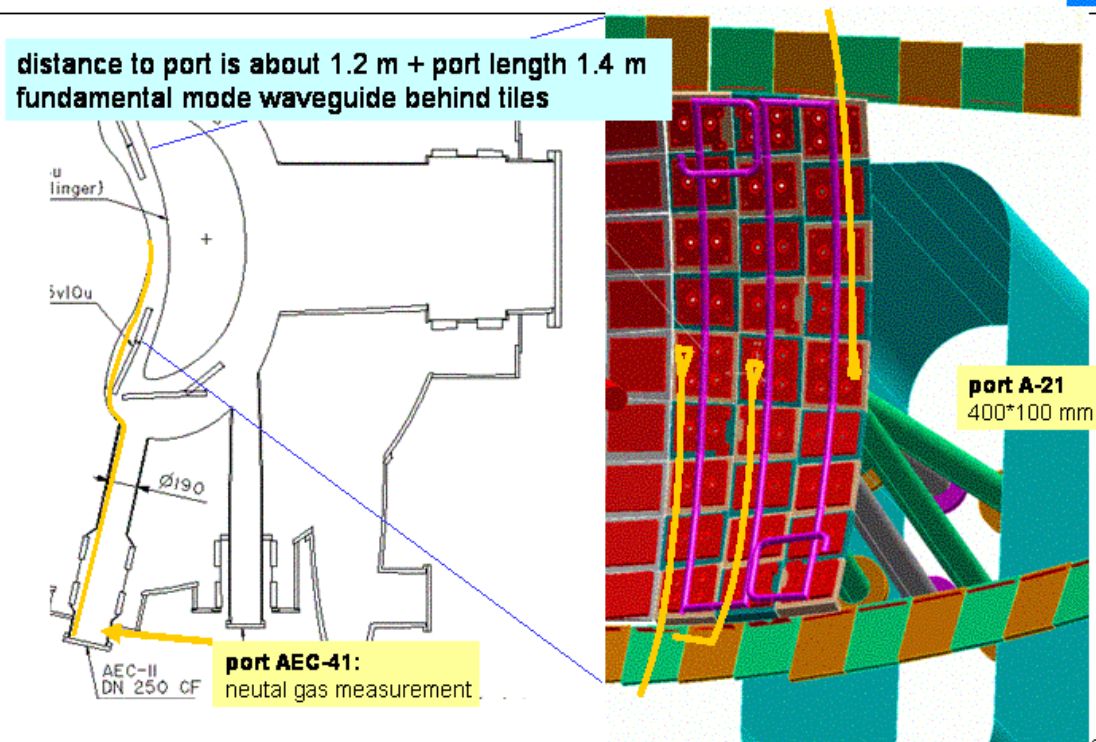


Fig. 3: Possible geometry for integration of a HFS antenna in the first-wall high-heatloads tiles (200 to 250 kW/m^2). The corresponding waveguides leading towards the next port distance to the port 1.2 m, portlength 1.4 m are indicated in yellow. In the right figure the tiles are shown from the high-field side (vessel wall omitted), CuCrZr cooling bodies in red, cooling pipes in purple. The graphite surface of the tiles right opposite the three antenna pairs is oriented as calibration mirrors for the time-of-flight measurement.

The antennas must withstand a heat-load of about $50 \text{ kW}/\text{m}^2$ which requires active cooling. The level of microwave stray radiation resulting from non-absorbed 140 GHz ECRH heating power is expected up to $100 \text{ kW}/\text{m}^2$ near the ECRH launching planes depending on heating scenarios and the position in the vessel considered (The reflectometry antennas are toroidally 72 deg apart from the ECRH launching plane). All in-vessel parts will be tested under these conditions in a test-chamber (Ullrich S. *et al* 2005).

Outside the vessel a bundle of oversized quasi-optical transmission lines are planned to guide the microwave signals to the diagnostic cabin right outside the bioshield (Fig.4). The single-path length is about 27 m, 5 mitre bends are necessary to account for radiation shielding and space requirements in the torus hall. In the diagnostic cabin quasi-optical beam splitters (Simonetto *et al* 2004) will offer the flexibility to adapt different transmitter/receiver

systems and use the full spectrum of reflectometry measurements.

reflectometry transmission line



-> diagnostic cabin outside bioshield (ground floor)

-> bundle of 6 quasi-optical oversized waveguides

single pass flange-to-receiver:

-> 5 metre bends

-> distance about 20 m

(see JET μ W-access: 8 bends, 36m)

-> radiation protection necessary at wall breakthrough

-> quasi optical beam splitters to adapt different transmitter / receiver systems

-> which windows at flange ?

AEA21 shared with:

-> Li-beam, launch

-> neutral gas measurement

-> VIS-Spec. upper / lower divertor

-> video X-point and divertor

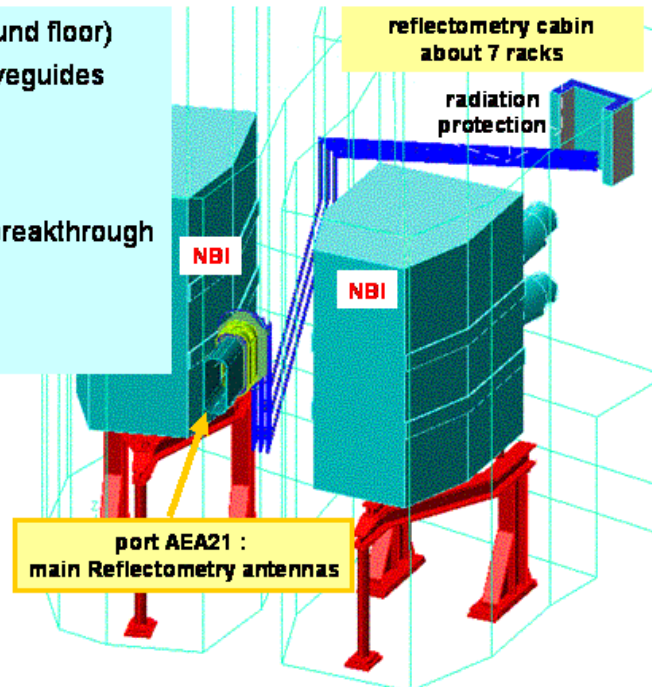
-> H-alpha: upper, lower divertor, inner wall

-> divertor thermography

-> BES (NBI 1 and 2)

-> LIF (alternative)

cooling port protection,



M. HIRSCH, IPP/117, Garching 2005, p. 5

Fig.4 Transmission lines to port AEA21. The bioshield (concrete with thickness 1.8 m) is omitted. From the diagnostic cabin outside only the radiation protection is shown.

REFERENCES

Hartfuss H.-J. *et al*, Rev. Sci. Instrum **68**, 1244 (1996).

Andreeva T., IPP Report III/270, May 2002.

Hirsch M. and Holzhauser E. to be submitted to Nuclear Fusion 2005

Hirsch M. and Holzhauser E. Plasma Phys. Control Fusion **46** (2004) 593-609

Hirsch M. *et al* Plasma Phys. Control Fusion **43** (2001) 1641-1660

Hennequin P. *et al* this workshop

Ullrich S. *Diploma Thesis* University of Greifswald, summary in Stellarator News 98, May 2005 available on the web: <http://www.ornl.gov/sci/fed/stelnews/>

Simonetto A. *et al*, Design of the Quasi Optical Interface System for JET's new Microwave Access, Proc. of 2004 29th Int. Conf. on Infrared and Millimeter Waves Karlsruhe, Germany, Sept 27-Oct 1, 2004, p 705, ed. by M. Thumm and W. Wiesbeck

Frequency hopping millimeter-wave reflectometry in ASDEX Upgrade

L. Cupido, S. Graça, L. Meneses, J. Santos, M. Manso, F. Serra

*Centro de Fusão Nuclear, Associação EURATOM/IST, Instituto Superior Técnico,
Av. Rovisco Pais, P-1049-001 Lisboa, Portugal*

Millimeter-wave reflectometers to perform density fluctuations measurements have been for quite a long time either fixed frequency (heterodyne and homodyne) systems in tunable or traditional multi-channel fixed frequency arrangements. Only recently novel systems were brought into operation with the ability to hop from frequency to frequency over a large bandwidth, during each plasma discharge, while retaining the quality of fixed frequency phase locked sources. The new hopping reflectometer system recently installed at ASDEX upgrade to study the radial distribution of turbulence characteristics is here briefly described and the proposed operation schemes envisaged are detailed.

1. Introduction

Millimeter-wave reflectometry has been used for a long time as a monitor for density fluctuations in fusion plasmas. In ASDEX Upgrade, density fluctuations were measured by fixed frequency homodyne and heterodyne systems, both in multi-channel fixed frequency arrangement. Homodyne swept systems to obtain density profiles cover the frequency range (18 – 100 GHz) and can be used also for density fluctuations studies [1]. Fixed frequency heterodyne systems are installed in Q (33 – 50 GHz) and V (50 – 75 GHz) band in O-mode propagation offer some advantages over homodyne systems: higher sensitivity as well as the ability to separate phase and amplitude at the receiver.

Recently, two broadband fast hopping mm-wave reflectometers were installed in Q and V bands to hop from frequency to frequency over a large bandwidth during each plasma discharge. These new heterodyne systems can cover the whole frequency band and have continuous spatial coverage by hopping from one frequency to another (measuring points can be selected as close as required). Its novel design avoids complex coupling elements required by multi-channel arrangement to feed several reflectometers into a single antenna system [2].

Due to the specific requirements of the new broadband fast hopping systems, the control software had to be upgraded. Actually, each band can operate, independently, on one of the two modes of operation: fixed frequency and frequency hopping. In fixed frequency mode, only one density layer is probed during the whole discharge. In hopping mode, several density layers are probed by hopping through the selected frequencies.

In the following sections, we describe the configuration of the ASDEX Upgrade frequency hopping system, the mm-wave hardware and the control software.

2. System configuration

The current configuration of the frequency hopping system is depicted in Fig. 1. It has three main blocks: mm-wave hardware, CAMAC crate and workstation “suref”. The mm-wave hardware generates the probing signals to the plasma and detects the reflected signals. The CAMAC crate hosts: two PPGs (Programmable Pulse Generator) and four Kynetic System

boards (ADCs) capable of acquiring 4 Mword of data with a sampling frequency of 500 kHz or 1 MHz. One PPG sends clock signals to mm-wave controllers triggering the transition to the next selected frequency while the other PPG sends clock signals to acquisition boards. The control software is running in the diagnostic workstation “suref” which programs the microcontrollers in the mm-wave hardware and configures PPGs and ADCs in the CAMAC crate.

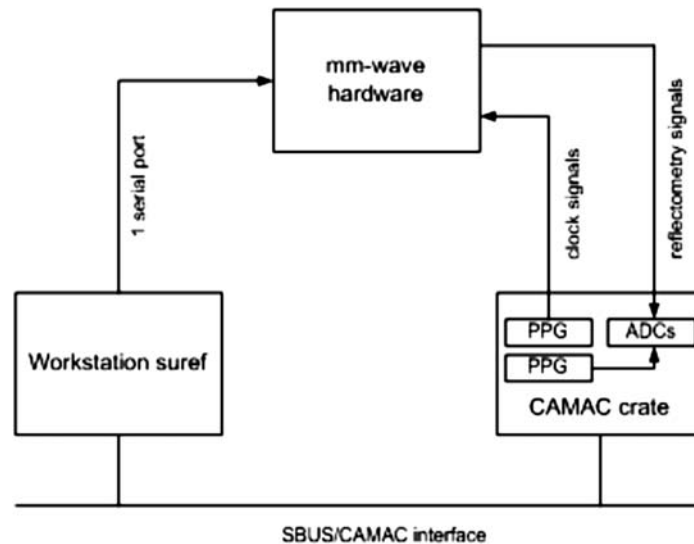


Fig. 1 Block diagram of the broadband fast hopping system in ASDEX Upgrade

3. Mm-wave hardware

The frequency hopping reflectometer has synthesized signal generation for both main signal and local oscillator signal and incorporates a receiver that maintains a coherent reception with in-phase and quadrature output signals (I and Q). The main feature of the system is its possibility to be tuned, within a fraction of a millisecond, to any selected frequency within a broad range of frequencies within a full waveguide band. To allow fast frequency switching fast frequency synthesizers are employed (CFN proprietary design).

The Q band system uses 8-12 GHz synthesizer while the V band employs 12-18 GHz. Each system uses two independent frequency synthesizers, one for the main signal and one for the local oscillator generator, ensuring a spurious and crosstalk free response in broad band operation.

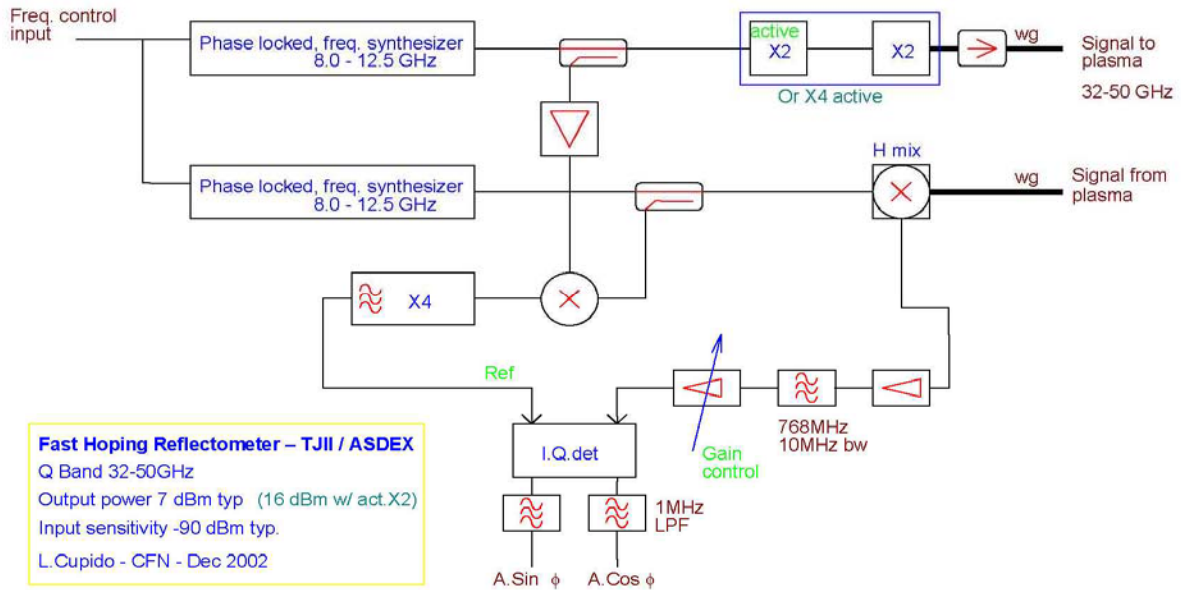


Fig. 2 Overall diagram in Q band

Each synthesizer uses a single agile hyper-abrupt tuned oscillator (HTO) within a phase locked loop (PLL) control loop. The output signal is generated by active or passive multipliers (or combination of both) and the reception uses a mixer or harmonic mixer. The phase reference signal, used for the coherent demodulation, was obtained by mixing down the main synthesizer outputs. In this way coherence is maximized and operation after frequency switching can happen as soon as the signals are within the IF filter bandwidth.

4. Control software

The control software is based on a client/server architecture [3] and configures the mm-wave hardware and the elements hosted in the CAMAC crate (PPGs and ADCs). The server developed in C++ runs in the workstation "suref" and accepts multiple connections from clients through TCP/IP (Transmission Communication Protocol/ Internet Protocol) protocol, however only one client can actually change the settings in the diagnostic. The client application has a Graphical User Interface written in C using Xforms library and can be executed in any computer. Due to the existing firewalls in IPP, the remote operation of the diagnostic in particular at CFN was enabled with the implementation of Secure Shell (SSH) tunneling protocol. A predefined protocol is used for exchanging messages between server and clients and was described in Ref. 4.

Due to the implementation of broadband fast hopping system in Q and V bands, two operation modes are now possible: fixed frequency and hopping. In fixed frequency mode, the operator introduces one frequency. In hopping frequency mode, the operator chooses a pattern of frequencies with a maximum of twenty frequencies, the period for probing each density layer and the number of repetitions of this pattern throughout the shot. Actually, only one PPG is available for two bands, so each band has the same number of frequencies, the same period and the same number of pattern repetitions. In both modes, the operator specifies the Intermediate Frequency (IF) gain in each band. When the server receives the configuration of the system, it programs the mm-wave hardware, the PPGs and ADCs in CAMAC crate.

For configuring IF gain and frequencies in mm-wave hardware, two microcontrollers (one for each band) are used and connected to the workstation “suref” through a serial port. A simple protocol is implemented to allow communication between server and microcontrollers.

The configuration of acquisition channels, acquisition rates, acquisition time windows and the sequence of pulses to trigger the frequency change in mm-wave hardware are written in a diagnostic shot-file-header (the header of a shot configuration file). A diagnostic program called RFL running in the workstation “suref” has two phases. In the first phase, prior to the shot initialization, RFL reads the shot-file header and sends information to PPGs and ADCs. In the second phase, at the end of the discharge and after the acquisition is finished, RFL reads the acquired data and builds a shot-file which it sends to the ASDEX Upgrade shot-file server.

5. Conclusion

In ASDEX Upgrade, the fast hopping frequency system is implemented for Q and V bands and the control software was upgraded to overcome these new changes and to make the diagnostic more flexible. Presently the new system is being commissioned and first results of the radial distribution of turbulence characteristics during the ongoing experimental campaign on ASDEX Upgrade are expected.

- [1] A. Silva et al., Rev. Sci. Instrum. **70**, 1072 (1999)
- [2] L. Cupido et al., Rev. Sci. Instrum. **75**, 3865 (2004)
- [3] V. Grossmann et al., Fusion Engineering and design **48**, 25 (2000)
- [4] S. Graca et al., Rev. Sci. Instrum. **75**, 3852 (2004)

JET Density Profile Reflectometer , new design.

L. Meneses, L.Cupido, A.A. Ferreira, M. Manso, L. Guimaraes
Associação Euratom/IST ,1049-001 Lisboa, Portugal.

New transmission lines and antennas have been recently installed at JET under the EFDA enhancement project "Millimeter Wave Access (MWA)" to meet the performance requirements of broadband reflectometry for density profile measurements. Taking advantage of this new facility a profile reflectometer is being developed. The new design consists of a fast swept FMCW reflectometer using coherent detection of the reflected signal. This reflectometer uses a single VCO oscillator as the main swept source and employs a heterodyne receiver configuration. Here we describe the operating principles of the new system and its expected performance taking in consideration the performance of the new waveguides and antennas. It is presented also the design topology for this swept reflectometer that is capable of operating on bistatic antenna arrangements over long waveguides using a local generated reference which are operating conditions that are likely to be those of ITER reflectometers.

Millimeter Wave Access (MWA)

A new transmission line and antennae have been recently installed at JET, under the EFDA enhancement project "Millimeter Wave Access (MWA)", it consists of four lines of corrugated waveguides for Reflectometry and two of circular waveguide for oblique ECE studies.

The main characteristics of the MWA for Reflectometry are [1]:

- 4 corrugated waveguides transmission lines
- Approximate 40 meters long – 9 Miter bends – Approx 260 nsec delay
- Bandwidth 60 to 160 GHz
- Antennae – Open Waveguide (Ø 31.8 mm) - *Gaussian beam*
- Antennae cluster with two rows of 3 antennae in the Toroidal direction
- Quasi Optical coupling to waveguide

With the installation of these new transmission lines and antennae a reduction of at least 20 dB on the losses is expected.

All the extraordinary mode propagation (X mode) JET reflectometers will be installed in these new lines (KG8b radial correlation).

A study of the reflecting conditions using ray tracing was performed for JET plasmas in order to evaluate the performance of the antennae cluster. As a result it was decided to use the central pair of antennae for all reflectometers; the four instruments of radial correlation measurements and the new profile reflectometer. For this we need to combine 5 systems to share the same antennae / waveguides with the use of Quasi Optical Combiners (QOB) [2].

The proposed arrangement of the QOBs is presented in fig 1

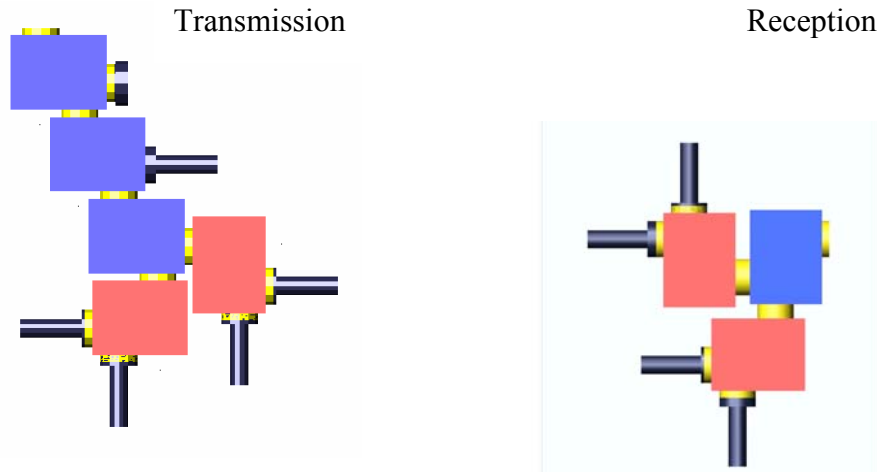


Figure 1 Quasi Optical box arrangement

The arrangement presented in figure 1, for frequencies we use allowed the operation of all instruments at the same time (50 -75 GHz FMCW, 76-78, 85-87, 92-96, 100-106 GHz radial correlation).

Diagnostic requirements

The requirements for the density profile Reflectometer summarized bellow:

- Measure the edge profile – X mode propagation
- Overcame plasma emission (1.5 Kev)
- 2 antennae setup
- Make use of existing parts, used in the past in other diagnostics:
 - Microwave (50 – 75 GHz)
 - Acquisition (CAMAC)
 - RF components

With the specified frequency range plasma with $8 \times 10^{19} \text{ m}^{-3}$ and magnetic field from 1.75 T could be probed and density profiles obtained for the plasma edge.

The suggested scenario is a consequence of the experience gained on previous attempts of density profiles measurements by FMCW (1995, 2001).

Design choices

The characteristics of the MWA and the diagnostic requirements presented above, lead to the design choices presented below that represent a ITER like scenario (long oversize waveguide and two antenna system).

- The use of two antennae
 - Local reference (LO) for down conversion
 - Delay compensation
 - Detection bandwidth limited due to plasma ECE emission
- Use only one VCO to minimize the detection bandwidth
- Use heterodyne detection with I and Q detection
- Output power $\leq 10 \text{ dBm}$

- With this set of characteristics two types of choices could be proposed for delay compensation;
 - in time (delay line)
 - in frequency (frequency offset)

The compensation in time could be done in waveguide (JET- KG3) [2], or in coaxial cable (Tore Supra) [3].

On this design we decided to use the frequency offset compensation.

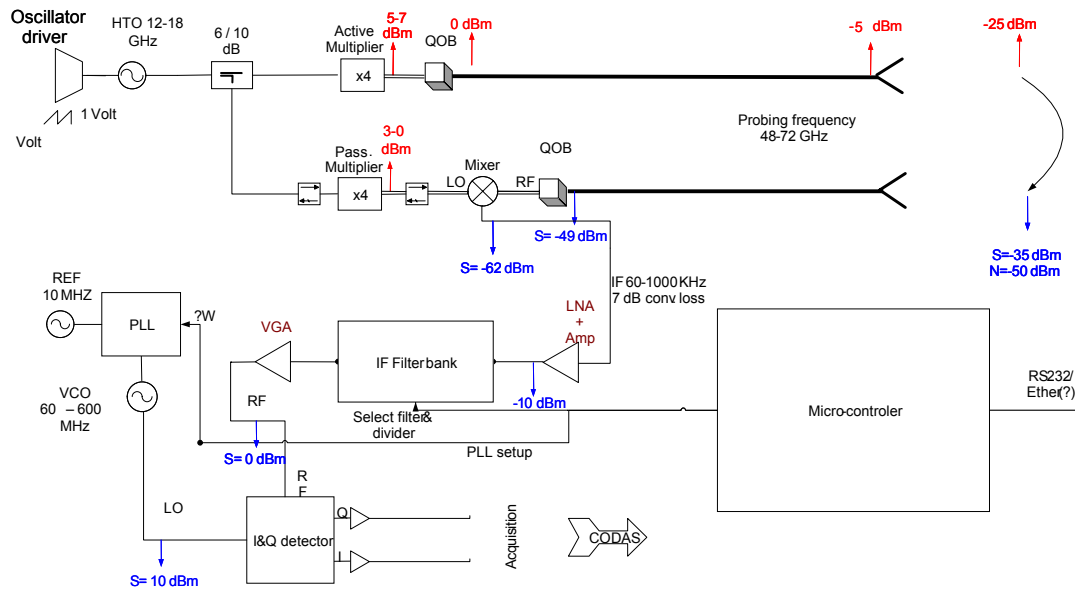


Figure 2 Proposed design for a new FMCW profile Reflectometer with auto coherent detection

With the proposed design we aim to compensate the time delay between the emission and reception of the generated signal and to generate an intermediate frequency (IF), necessary to have a heterodyne detection.

The local oscillator used for the IQ (In-phase and Quadrature) detection compensates for the time delay however the big advantage of such technique is the ability to place a virtual reference at any position from the plasma.

To minimize the plasma emission a narrow band filtering of 40 MHz band pass filter centered around 260 MHz will be used, we expect to have a signal to noise ratio great than 15 dBm, for an edge temperature of 1.5 Kev, However the IF bandwidth would be selected to guarantee a good signal to noise ratio (S/N).

Instrument main characteristics

The main characteristics of this new instrument are summarizing below.

- Using MWA to density profile measurements
 - Only central pair useful
 - 5 system installed sharing WG
- X mode operation (1.75 to 2.5 Tesla)
- Bi- static antennae
- Coherent I & Q detection
 - Phase and Amplitude detection
- Up to 128 profiles (1024 point 8 bit ADC 100MHz)

- Delay compensation by frequency conversion (approx. 260 nsec)
- Temporal resolution 35 μ sec
 - Sweep rate 25 μ sec
- Spatial resolution less 1 cm

Conclusions

- New design that takes advantage of the delay for IF conversion
- Less expensive than other designs
- Frequency compensation must be stable & precise (20 KHz resolution)
- The time delay compensation related to plasma position
 - Test with mirror
- Change in sweep rate → change frequency compensation

References

[1]- New Millimeter-Wave Access for JET Reflectometry and ECE, L. Cupido(1), et al – 23rd SOFT, Varena, Italy – 2004

[2] Simonetto A., Sozzi C., Cirant S., Bruschi A. and JET-EFDA contributors Design of the Quasi Optical Interface System for JET's new Microwave Access Proc. of 2004 Joint 29th Int. Conf. on Infrared and Millimeter Waves and 12th Int. Conf. on Terahertz Electronics - Karlsruhe (TH), Germany, Sept 27-Oct 1, 2004, IEEE Catalog 04EX857, ISBN 0-7803-8490-3 pg. 705 - Publisher: University of Karlsruhe - Editors: M. Thumm and W. Wiesbeck

[3] A C C Sips *et al* 1993 *Plasma Phys. Control. Fusion* **35** 743-755 - Analysis of reflectometry density profile measurements in JET - A C C Sips and G J Kramer JET Joint Undertaking, Abingdon, UK Print publication: Issue 6 (June 1993)

[4] F Clairat *et al* 2001 *Plasma Phys. Control. Fusion* **43** 429-441 - Edge density profile measurements by X-mode reflectometry on Tore Supra - F Clairat, C Bottereau, J M Chareau, M Paume and R Sabot - Association Euratom-CEA, Département de Recherches sur la Fusion Contrôlée, CEA Cadarache, 13108 Saint-Paul-Lez-Durance, France - Received 16 October 2000, in final form 19 December 2000 - Print publication: Issue 4 (April 2001)

COHERENT SIGNAL GENERATION AND DETECTION FOR MILLIMETER WAVE REFLECTOMETRY SYSTEMS

L. Cupido, L.Meneses, A.A.Ferreira

EURATOM/IST Association, Centro de Fusão Nuclear, Instituto Superior Técnico, 1049-001 Lisboa, Portugal

In view of the more demanding measurements to be performed on next fusion devices a new generation of reflectometer systems must be developed for both density profile and turbulence studies.

The new generation reflectometry systems should be able to integrate sweeping and hopping capabilities and should also cope with complex broadband transmission lines and bistatic antenna arrangements. Signal purity and stability becomes a very important issue when the use of compensation networks such as delay lines become impossible. This is the scenario for reflectometry on ITER using ultra broadband frequency operation, bistatic antenna arrangements and long corrugated waveguide lines.

The present paper describes a novel system for signal generation and detection (of both main plasma signal and local oscillator signals) capable of fast sweeping, frequency hopping as well as fixed frequency operation. It is based on a single synthesized source and utilizes several oscillators which are locked to a stable reference standard, resulting in line widths of few KHz at millimeter-wave frequencies.

This short paper summarizes the ongoing development effort undertaken at CFN-IST towards the next generation of reflectometers.

Introduction

Many millimeter wave signal generation devices and techniques have been used on plasma reflectometry diagnostics over the years. In most of the cases the broadest band possible was exploited in order to cover the maximum range of plasma densities, while in some other cases narrow band devices were used namely to achieve higher power and therefore the necessary signal to noise ratio. Sources that have been used range from the early BWO (backward-wave oscillator) to the modern frequency synthesizers, being the HTO (hyper-abrupt tuned oscillator, a voltage controlled oscillator using hyper-abrupt tuning diodes) the most widely used source.

Frequency synthesizers do employ internally HTO oscillators (when fast switching times are required) or YIG oscillators (when maximum signal purity is required) but locking to a stable and low phase noise reference.

The frequency generation for broad band has been using microwave signal generation followed by active and passive frequency multiplication into the millimeter wave bands since 1998[1].

The signal detection using phase and quadrature has the most desirable characteristics and usually requires an heterodyne receiver topology and as a consequence a matching LO (local oscillator) of similar performance is required.

In swept systems mainly two techniques have been used to ensure a good matching LO: *a)* the tracking oscillator technique (used at ASDEX upgrade main reflectometer[1] in bands V and W) - *b)* the SSB conversion to derive the offset LO (used at Tore Supra [2]).

A design using coherent signal generation and detection

Generating all signals (both RF and LO, plus the carrier for phase-quadrature detection) in a coherent manner gives the possibility of coherent phase/amplitude detection while maintaining the lowest phase noise possible. This however requires the main tunable signal to be synthesized, along with locked sources for all the auxiliary signals.

Synthesized frequency generation over a broad frequency range results also in calibrated frequency sweeps and also enables a fast frequency hopping mode of operation. Also, both conventional frequency hopping operation and fixed frequency operation will benefit from the very low phase noise of the synthesized source.

This topology also solves the requirement of a matched LO (without PLL (phase locked loop) drag that we may encounter at ASDEX like systems or the potential spurious and crosstalk problem that SSB converters may exhibit) since it will use only one synthesized source and derive all other signals by frequency conversion and frequency multiplication into the mmW(millimeter wave) range (30-300GHz).

The generation of the local reference becomes independent from the main signal and allows us to place it virtually at any distance from the plasma. This is particularly interesting while considering the bi-static antenna arrangements that we will encounter on ITER and we already have at JET if we consider using the recently installed MWA lines[3].

Why do we need it?

There are a few reasons why some of the usual topologies are not suitable for the next fusion machines such as ITER, namely the use of long lines and bi-static antenna arrangements, but also the number of systems that can operate on the same lines is limited by interference or interaction or simply by coupling power loss. A system with the proposed topology will operate in FM(frequency modulation, frequency sweep), FH(frequency hopping), FF(fixed frequency) modes and less access to the machine is required for transmission lines and antennas.

Also long waveguide runs will place problems on the coherency of the sources as the big round-trip delay will result difficult to compensate while using a conventional reflectometer. Note the phase noise above $1/t_{dt}$ will appear at output spectrum of the detected signals and compensating for that with a delay line may become unpractical, and

certainly, an identical line as delay line will be impossible. The use of a conventional delay line it will be possible but will not match well at all frequencies, and difficult to implement over large bandwidths.

There is also a need to have the output spectrum within a reasonable bandwidth to enable good quality/resolution data acquisition systems. By placing the reference virtually at any distance from the plasma we also shape the bandwidth of the acquired data which is a quite convenient feature when we deal with several types of signal to noise ratios and turbulent plasma scenarios.

The design challenge

In order to achieve the above outlined goals we do require a single broadband synthesized source capable of fast sweep and FF. Commercial units with the features required are not available on the market and specific custom designs tend to have excessive cost and still leave us to do all the fast control to set the frequencies according to the modes of operation. Also, disciplined ultra fast sweep is something we do not encounter on any synthesizer topology from the microwave industry.

The previous experience with the synthesized sources used on the frequency hopping systems at both ASDEX[4] and TJII-CIEMAT[5] encouraged us to develop our own solution of frequency synthesized source that could operate in the way described above.

The main difficulties are still to maintain a low phase noise, to operate within a broad band, and to perform a disciplined linear (or linearized) sweep.

While in broad band swept or hopping mode the system will be trigger activated and there will be no analog ramp frequency control.

The use of frequency conversion and multiplication is also something we must consider carefully in order to achieve low spurious content of the output signal (better than -40dBc was already proven to be possible during prototype tests done at CFN).

Low harmonics contents are depends on the last multiplier / amplifier and in this case the situation is not different from any other reflectometer topology. Also the high output power requirements will come from the use of broadband mmW MMIC(monolithic microwave integrated circuits) amplifiers that become available recently.

On figure 1.0 we can see a block diagram of the system under developments that shows the main synthesizer along with the fast digital electronics to control it the frequency converters and all the rest that configures a standard heterodyne reflectometer. Note the use of a locally generated signal reference for I.Q. Detection that allows us to relocate the bandwidth of acquired signals.

Reflectometer using coherent signal generation and IQ detection.

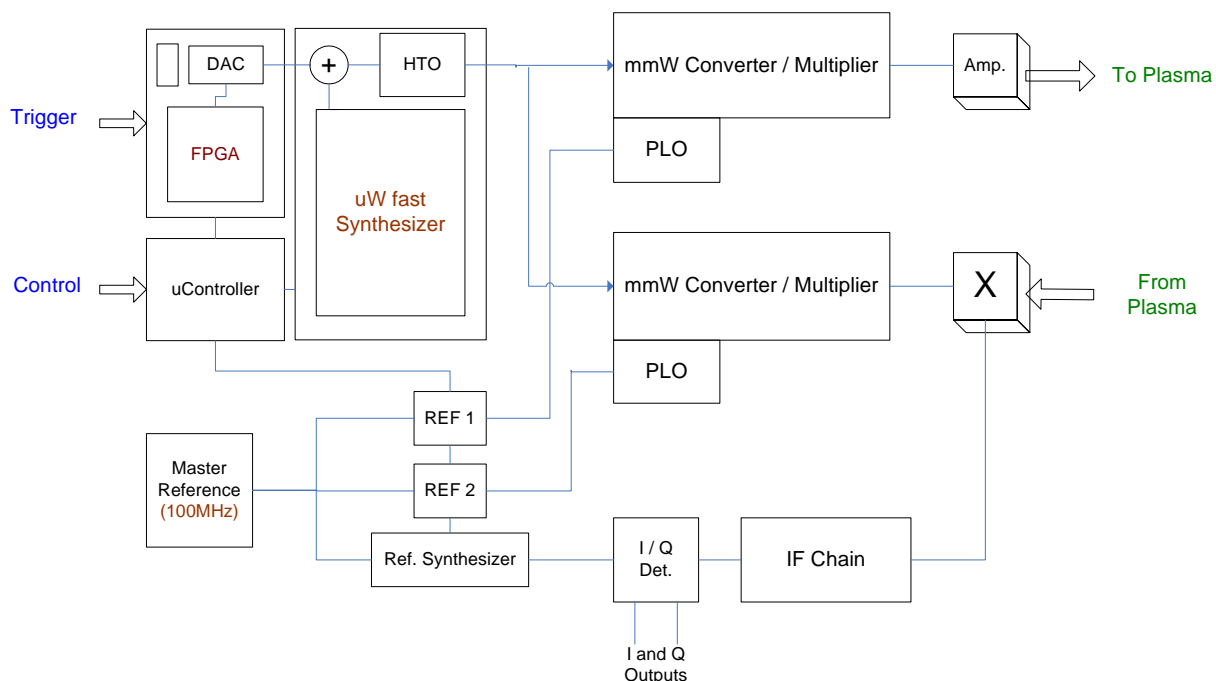


Figure 1 – Block diagram of the coherent reflectometer under development at CFN-IST

Conclusions

The present system is under development at CFN-IST and aims at the construction of a heterodyne reflectometer using phase-amplitude detection. It employs a topology with a single synthesizer for the main signal generation and can operate in fixed frequency, frequency hopping and fast frequency sweep modes of operation. It employs the latest technology and techniques in order to achieve clean signal generation.

It is particularly suited for the operation on long transmission lines and bi-static antenna arrangements as will be encountered on an ITER like scenario.

Presently (May 2005) a prototype is under construction at CFN-IST and it is expected to be tested on ASDEXup or at JET using the recently installed MWA lines.

[1] A. Silva et al., Rev. Sci. Instrum. v70, 1072 (1999)

[2] Ph. Moreau et al - Ultra Fast sweep heterodyne reflectometer on the Tore Supra tokamak – Review of scientific Instruments v71,1,Jan 2000

[3] New Millimeter-Wave Access for JET Reflectometry and ECE, L. Cupido(1), et al – 23rd SOFT, Varena, Italy – 2004

[4] L. Cupido et al. - Frequency Hopping Reflectometry in ASDEXupgrade” – IRW7

[5] L. Cupido, J. Sánchez and T. Estrada. - Frequency hopping millimeter wave reflectometer - Review of Scientific Instruments, 75, (10), 3865, 2004

Status and plans for reflectometry in ITER

G. Vayakis and C. Walker⁺ for the ITER International Team and Participant Teams
with contributions from
F. Clairet and R. Sabot (CEA)
V. Tribaldos, T. Estrada, E. Blanco, J. Sánchez (CIEMAT)
G.G. Denisov, V.I. Belousov et al
(Institute of Applied Physics of Russian Academy of Science, Nijni Novgorod)
F. Da Silva, P. Varela, M. E. Manso, L. Cupido, João Dias and Nuno Valverde (IST)
V.A. Vershkov, D.A. Shelukhin, S.V. Soldatov, A.O. Urazbaev, E.Yu. Frolov (KIAE)
S. Heurax (LPMIA, Université Henri Poincaré Nancy I Vandoeuvre France)

ITER IT, Naka Joint Work Site, Naka, Ibaraki 311-0193, Japan. ⁺ ITER IT, Garching JWS

I. Introduction

Reflectometry will be used in ITER to measure the density profile in the main plasma and divertor regions, and to measure the plasma position and shape in order to provide a reference for the magnetic diagnostics in long pulses. An outline description of a system to achieve these goals was compiled in 1997[1] and has since been updated [2-8]. It includes Low and High Field Side (HFS and LFS, respectively) O-mode systems for the measurement of the density profile in the main plasma, a LFS X-mode system for the edge profile, a HFS X mode system operating in the left hand cutoff to measure the core profile, a dedicated O-mode system for plasma shape measurement and a multi-band, multiple line of sight O-mode system to measure divertor density profiles.

Recently, as part of the preparations for ITER procurement, the systems have been re-organised, with development for the main plasma LFS and HFS systems now proceeding separately and a clear separation between the divertor interferometry and reflectometry being implemented. Engineering design work has begun in the ITER participant teams on the details of the implementation of the in-vessel waveguide runs that form part of the main plasma HFS launch systems and of the reflectometer for plasma position. Both these systems have to be procured relatively early as their assembly is linked with that of the ITER vessel.

For the LFS main plasma and divertor systems, which follow the standard port module approach, the process of defining the front-end functionality is not yet complete. As well as profile systems, two-point fluctuation and Doppler sub-systems are also planned for the main plasma, while multi-chord profile measurements in the region 15-300 GHz are envisaged for the divertor.

II. Role and limitations of reflectometry on ITER

Reflectometry is expected to be a major contributor for several measurements required for basic (Category 1a, [9]) and advanced (Cat. 1b) control of ITER, including plasma shape and position for long pulses, edge density profile, ELM density perturbation and divertor density, in addition to measurements for physics understanding (Cat 2), such as core density fluctuations and edge turbulence. It is also expected to make key contributions for other measurements in these categories, such as low (m,n) MHD activity, TAE and other perturbations with a high n core presence, core density profile and plasma rotation.

For measurements in the core, reflectometry is limited by poor access: X-mode launch from the LFS is constrained by absorption, but also by relativistic profile flattening (Figure 1); O-mode is limited by relativistic cutoff profile flattening for the standard flat ITER density profiles. Core access is, however, still possible using the HFS X mode left-hand cutoff. Direct measurements of

plasma rotation by reflectometry are not possible, but one can deduce the rotation velocity of the fluctuations rather reliably and investigate the detailed features of velocity shear layers [10].

For the divertor, mm-wave access is not an issue, but frequency range is: To deduce the LFS (outer) leg profile in O-mode, frequencies up to ~ 1 THz are needed, well past the limit of demonstrated swept reflectometry (which lies below 200 GHz) and beyond reasonable extrapolations of such swept systems (to 250 – 300 GHz). For this reason, a comb reflectometer has been assumed in the past for the divertor above 300 GHz [1,2].

Physical access to the plasma depends on the location of the antennas and is summarized in Figure 2. In all cases, the waveguide is routed through one of the ITER ports and in most cases at least part of the in vessel waveguide must be removed for port maintenance.

III. Progress with in-vessel systems

The reflectometer for plasma position and the HFS main plasma reflectometer include components mounted inside the ITER vessel, between the vessel inner wall and the neutron absorbing blanket. In addition to these systems, there are proposals for systems needing similar access, in particular a time-of-flight refractometer [11] to measure an analogue of line average density and a high-field-side antenna system for a collective scattering experiment [12]. All these systems have similar access problems and the design groups involved are in communication with each other.

Access to the inner wall is available through the ITER upper ports. The space available for waveguides is approximately 80 mm (tor.) by 15 mm (rad.) running in a poloidal plane on each side of the port centerline. This allows a pair of waveguides of ~ 23 mm x 12.5 mm ID to be fitted. Recently, this path has been improved by the removal of all but one toroidal bend, and the simplification of the exit path to just 7 bends in the poloidal plane, including just two flexible bends to take up thermal and other machine movements for which further optimization is clearly possible.

The curvature of the inner part of waveguide is imposed by the vessel and therefore the performance of this common component has to be investigated first. Direct mock-up tests of this line have been made at the KIAE and show that the performance is dominated by the 1st (90°) bend which will therefore require further optimization; the rest of the line is suitable for use between 18 and 120 GHz. Calculations at Nijni Novgorod show that the hyperbolic secant bend with a minimum radius in the range 100 – 125 mm might be suitable and a first inspection suggests that it can be fitted to the ITER blanket.

On the basis of results so far, it is expected that, for the full line, the performance in O-mode will be good and in X-mode acceptable. It seems even possible to design a “universal” transmission line with acceptable performance in X –mode (~ 9 to 90 GHz) and O-mode (~ 15 – 150 GHz) for full plasma access. This would allow greater flexibility in the use of the limited number of launch positions available, provided that a suitably versatile antenna can also be designed.

2D calculations are being used at KIAE and LPMIA jointly with IST to optimize the antenna. Preliminary results suggest that a simple antenna as originally proposed [1] is usable but that the gain is rather low for core access in X-L mode and the secondary reflections may limit the position reflectometer performance at small blanket-to-plasma distance. Further work is underway at IST and KIAE to quantify the performance of the transmission line and antenna.

A key variable in the designs is modification of the ITER blanket module. This is a thermally and mechanically stressed component with a composite (Be, Cu, Steel) first wall structure [9]. Present designs have assumed an available gap between blanket modules of up to 30 mm, which is then reduced to allow for blanket and antenna installation and manufacturing tolerances as well as vacuum and plasma sprayed insulation layers. This gap is achieved by local widening of the

nominal 10 mm gap and is also limited by local peaking of neutron irradiation levels in the TF coil insulator caused by the presence of the gap. The limits of this process are now being explored within the ITER IT with a view to accommodating higher gain designs, such as that proposed for the plasma position system. At the same time, engineering calculations are underway or planned in the EU and RF to investigate the thermal and electromagnetic loads for the various antenna proposals.

IV. Status of the main plasma reflectometer (LFS)

The main plasma reflectometry retains the high-redundancy universal waveguide approach outlined in the ITER 2001 design and previously described [1,2]. There are 6 waveguide pairs, with simple truncated waveguide antennas of 89.5 mm dia used for all functions. Multiple 90 or near 90° mitre bends are used to form in-port labyrinths and corrugated waveguide is used throughout for low loss transmission to ~ 300 GHz. The primary vacuum boundary now uses a combination of inclined quartz or similar window and a waveguide valve to satisfy ITER safety criteria and to allow for remote testing of the window.

The antennas (Figure 4) are provisionally grouped in two main clusters to give redundancy for profile measurements and a range of distances for poloidal and toroidal correlation measurements and mode studies. In addition there is an extra pair of lines for Doppler reflectometry measurements, inclined $\pm 7^\circ$ to the horizontal. This layout has not been optimized for the large set of measurements in principle possible from this location; this is expected to be the first task of the detailed design phase for this diagnostic. In particular, there are possibilities for imaging the gradient region plasma by a poloidal antenna array; this could lead to more robust profiles as well as a useful fluctuation diagnostic for a region of the plasma that has a strong impact on overall tokamak performance.

V. Status of the divertor reflectometer

The needs of ITER for divertor measurements arise from the critical nature of divertor performance on machine operation. The divertor design for ITER [1] assumes “semi-detached” operation with good control of the degree of detachment. It is also expected that the divertor in a reactor will be an expensive replaceable part, and ITER will be the only device that can be used to benchmark divertor codes in near-reactor conditions. At the same time, progress with divertor reflectometry worldwide has stagnated and it is not practical presently to design the combined reflectometer / interferometer envisaged previously [1], even though it is the only diagnostic able, in principle, to meet the resolution requirement across the divertor leg (3 mm). The present approach has been to divide functionally and physically, the interferometry from the reflectometry function and limit the reflectometry target density to below $\sim 10^{21} / \text{m}^3$ (~ 300 GHz). The implementation of a laser interferometer is under study [13] and an outline reflectometer system to cover a reduced density range from just one divertor port is planned within the ITER IT for the near future.

VI. Conclusions

In the last few years, there has been very encouraging progress with the ITER reflectometry designs for the in-vessel systems, that is, the reflectometer for plasma position and the reflectometer for the main plasma (HFS): The space allocation is known, preliminary designs exist, simulations and mockup tests are underway and there are plans to tests critical new measurement aspects (X-L mode HFS launch) to be tested on a tokamak (T-10). At the same time, the required engineering studies have been initiated, and the parties involved have agreed to collaborate closely. All these aspects bode well for the future of these systems, despite a number of yet to be resolved technical problems.

The ITER main reflectometer (LFS) remains essentially unchanged since 2001, although small technical improvements have been implemented, and the space allocation modified to allow a Doppler system. It is clearly feasible to provide an extensive system, and a workable, though not optimal, outline design example exists. However the detailed design of the front end is missing and, as there are many possibilities, the whole system is ready for review and update.

The divertor reflectometer remains an orphan in the parties despite the fact that it addresses key ITER needs. The resultant lack of progress has led to some space allocation reduction. On the present path, there is a high risk that this system may be implemented in a very reduced way, or not at all as (i) the system is not demonstrated (ii) the system will likely have to compete with other systems for late R&D funds. Any loss in projected divertor reflectometry performance directly degrades the only planned measurement of the density profile across the divertor leg.

References

[1] G. Vayakis et al, RSI 68 (1) 1997
 [2] G. Vayakis et al, in Diagnostics for Experimental Thermonuclear Fusion Reactors (Plenum Press, New York, P. Stott et al, eds.) p.97 (1998) [3] V. Vershkov et al, ibid. p. 107, [4] E.J. Doyle et al, ibid. p. 119, [5] N.L. Bretz et al, ibid. p. 129 [6] M. Manso et al, ibid. p. 139
 [7] G. Vayakis et al, in 23th International Conference on Infrared and Millimeter Waves Conference Digest, Parker and Smith (eds.), University of Essex, Colchester, U.K. (1998) pp. 287-289
 [8] G. Vayakis, "Status and prospects for reflectometry on ITER", talk at IRW6
 [9] ITER Plant Integration Document V1.0, J. How et al (Eds.) 2004 available through the ITER Team
 [10] Presentations at these proceedings
 [11] V. Zavariev, Private communication
 [12] F. Meo et al, RSI.75(10) p. 3585ff (2005)
 [13] D. Brower, private communication

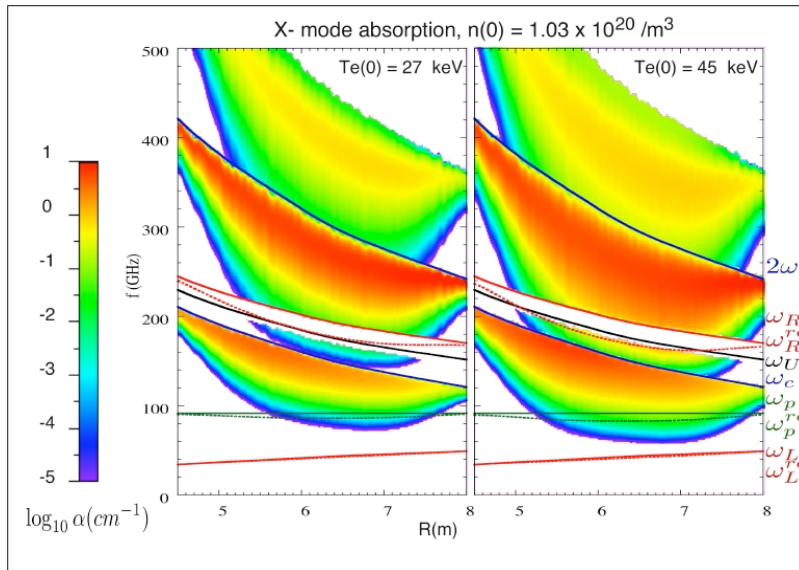


Figure 1: Absorption contours for X-mode propagation for two different peak core temperatures and flat density profiles.

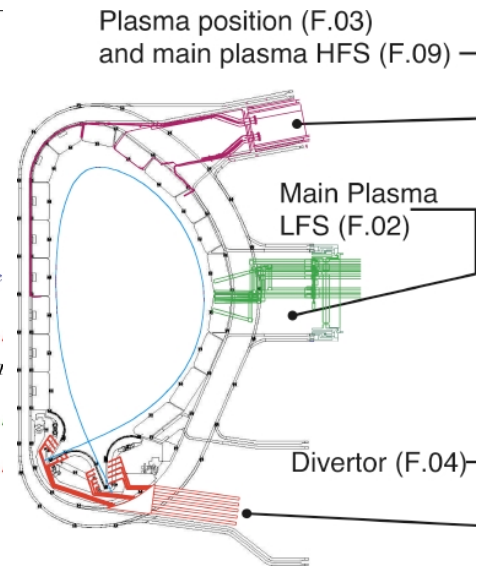


Figure 2: Access paths for ITER reflectometry systems reduced to one poloidal plane

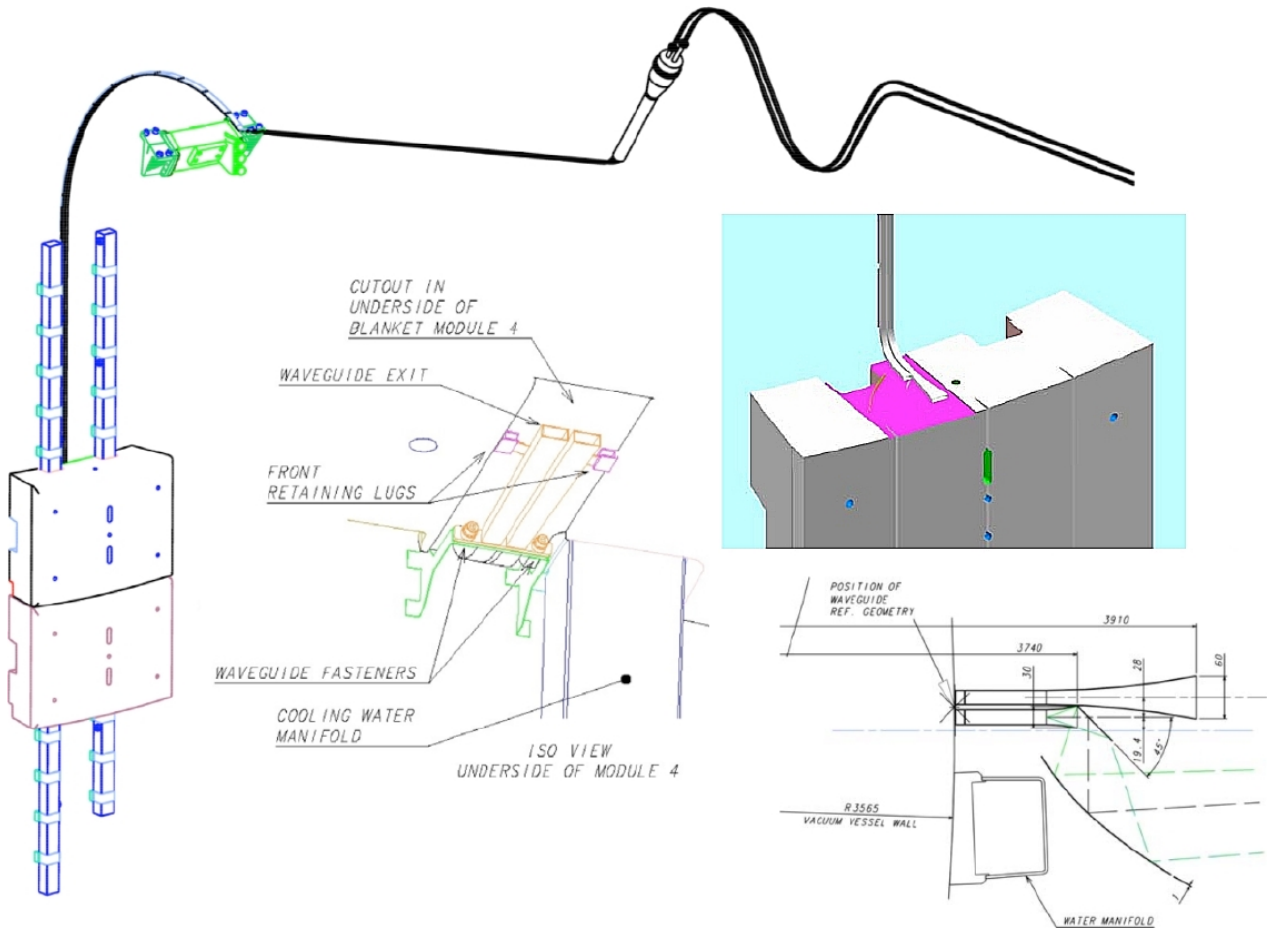


Figure 3: In-vessel waveguide for HFS access. Inset left: low gain truncated antennas from outline design. Inset right: Higher gain antenna proposal view (top) and horz. section (bottom)

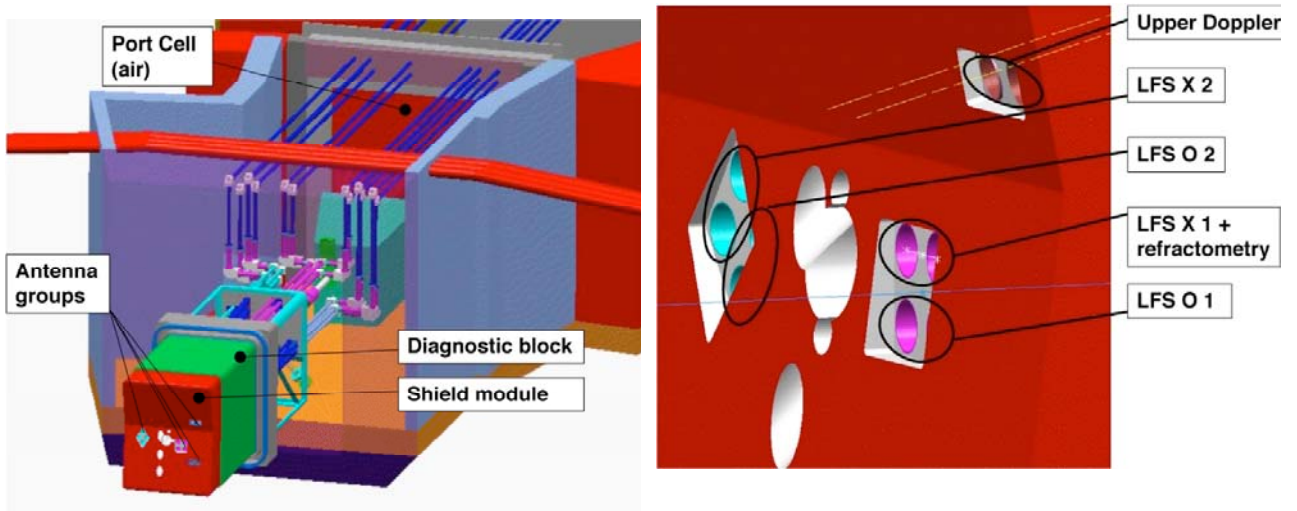


Figure 4: Antenna grouping at the front of the port. The lower Doppler pair is not shown.